DEVELOPMENT AND VALIDATION OF DATA SETS AND MONTE CARLO METHODS FOR ELECTRON/POSITRON TRANSPORT AT LOW AND MEDIUM ENERGIES

THÈSE N^{O} 3403 (2005)

PRÉSENTÉE À LA FACULTÉ SCIENCES DE BASE

Institut de physique de l'énergie et des particules

SECTION DE PHYSIQUE

ÉCOLE POLYTECHNIQUE FÉDÉRALE DE LAUSANNE

POUR L'OBTENTION DU GRADE DE DOCTEUR ÈS SCIENCES

PAR

Cezarina Elena NEGREANU

Physicienne diplômée de l'Université de Bucarest, Roumanie
et de nationalité roumaine

acceptée sur proposition du jury:

Prof. R. Chawla, directeur de thèse
Prof. M. Dingfelder, rapporteur
Dr O. Joneja, rapporteur
Prof. O. Schneider, rapporteur
Prof. M. Terrissol, rapporteur

Lausanne, EPFL
2005

"Composed out of scattered fragments
and snatches of movements."
– Beethoven –
"Symphony No. 9 in D minor, opus 125"

To my family.

Abstract

When exposed to ionising radiation, living tissue can potentially suffer somatic and genetic damage - effects depending mainly on the radiation dose or energy absorbed, the type of radiation, and the type and mass of cells affected. It is well known that large doses of radiation lead to high damage of the cell nucleus and additional cell structures, which results in harmful somatic effects, and even rapid death of the individual exposed, while at low doses, cancer is by far the most important possible consequence. Understanding the mechanisms by which low doses of radiation cause cell damage is thus of great significance, not only from this viewpoint but also from that of practical medical physics applications such as radiotherapy treatment planning.

Ionising radiation, such as electrons and positrons, begins to cause damage to the genome of a living cell by direct ionisation of atoms, thus depositing energy in the DNA double helix itself. The energy threshold for inducing strand-breaks by electrons, however, is around 7 eV, well below the energy levels required for direct ionization. The low-energy electrons that are set in motion around the tracks of energetic charged particles, for example, are responsible for a multitude of low-energy events (energy transfer of the order of 10 eV), which play a significant role in inducing molecular damage. Assessing the spatial configuration of energy transfer events and the deposited energy spectra, in regions of cellular and sub-cellular dimensions, can be aimed at via the application of appropriate Monte Carlo simulation tools. Such calculations depend primarily on an accurate knowledge of the production and subsequent slowing down of secondary electrons that form the basic structure of the charged particle track.

In the above context, an important requirement is the provision of detailed quantitative information concerning the interaction cross sections of electrons over an energy range extending down to low energies, i.e. including the sub-excitation domain. In addition, developing fast particle-transport simulation algorithms to cover the entire slowing down process efficiently is a key aspect. Thus, the present doctoral research has, as global goal, the development and validation of new Monte Carlo calculational tools for electron and positron transport in biological materials, both at high and low energies. More specifically, it aims at providing (i) a comprehensive and accurate set of appropriate cross section data, and (ii) a fast and reliable algorithm for the simulation of charged particle transport.

Thus, the first part of the thesis concerns the assessment, further development and validation of standard theoretical models for generating electron and positron cross sections to cover the main interactions of these particles with matter, in particular with the basic atomic components of biomaterials (water, bio-polymers, etc.). This has been done for bremsstrahlung, and both elastic and inelastic scattering, considering a wide range of atomic numbers and high up to thermal incident particle energies. In particular, the excitation cross sections for medium and low energies (down to 1 eV) have been derived by using a new formalism based on many-body field theory. The accuracy of the presently obtained data sets are assessed against other theoretical models, as also a large experimental database for each type of interaction, so that both a comprehensive coverage and adequate accuracies have been ensured for the cross section data sets generated.

In the second part of the thesis, an extension of the Monte Carlo code system PENELOPE is first undertaken such that use can be made of elastic scattering differential cross sections which have been made available in numerical form. Thereby, new computational routines (incorporated into the new code PENELAST) prepare the cross sections, needed for a given energy and scattering angle, by applying a fast and accurate sampling technique to a provided data set. The present development will allow various electron and positron cross section data libraries, appropriately formatted, to be used with PENELOPE for benchmarking purposes.

The development of a high calculation-speed (Class I) Monte Carlo tool for charged particle transport in biological materials has then been addressed. Thereby, a numerical algorithm for calculating the multiple-scattering angular distributions of high energy electrons and positrons is developed, based on the multiple-scattering theory of Lewis which accounts for energy losses within the continuous slowing down approximation. Partial-wave elastic scattering differential cross sections made available in numerical form, as indicated above, are used for the calculations, the inelastic scattering differential cross sections being obtained from the Sternheimer-Liljequist generalized oscillator strength model implemented in PENELOPE. The new code LEWIS has been used to calculate multiple-scattering angular distributions for given path lengths and can be readily adopted for Class I Monte Carlo simulations. The simultaneous generation of a large number of Legendre expansion coefficients is rendered possible, both rapidly and accurately. Results from LEWIS have been found to be in satisfactory agreement, both with detailed simulations carried out using PENELAST and with various sets of experimental data for high to medium energy electrons.

In brief, the present research represents a significant improvement in the quality of Monte Carlo modelling of charged particle slowing down processes, thus contributing to understanding the role of low-energy secondary electrons in radiation protection studies. It will also allow the further development of a complete Class I Monte Carlo code, which can then be reliably used in practical applications such as radiation treatment planning.

Version Abrégée

Un tissu vivant exposé au rayonnement ionisant peut potentiellement subir des dommages somatiques et génétiques qui dépendent principalement de la dose de rayonnement ou de l'énergie absorbée, du type de rayonnement, ainsi que du type et de la masse des cellules affectées. Il est bien connu que de fortes doses de rayonnement provoquent des dommages massifs du noyau et des structures additionnelles de la cellule, entraînant des effets somatiques importants qui peuvent aller jusqu'au décès rapide de l'individu exposé. A moindre doses, c'est le cancer qui est la conséquence la plus importante d'une exposition dans la majeure partie des cas. La compréhension des mécanismes par lesquels les faibles doses de rayonnement causent des dommages aux cellules est donc primordiale de ce point de vue, mais aussi dans l'optique d'applications médicales pratiques, telles que la planification des traitements radiothérapeutiques.

Le rayonnement ionisant, tel que les électrons et les positrons, commence par causer des dommages au génome d'une cellule vivante par ionisation directe des atomes et dépôt d'énergie dans la double spirale d'ADN elle-même. Cependant, le seuil d'énergie pour induire des ruptures de la chaîne d'ADN par les électrons (environs 7 eV) se situe largement en dessous les niveaux d'énergie requis pour une ionisation directe. Par exemple, les électrons de faible énergie, qui sont mis en mouvement aux abords des trajectoires des particules énergétiques chargées, induisent une multitude d'événements d'énergie réduite (transfert d'énergie de l'ordre de 10 eV), qui jouent un rôle significatif dans l'induction de dommages au niveau moléculaires. La caractérisation spatiale des phénomènes de transfert d'énergie et des dépôts énergétiques spectralement distribués dans les régions de dimension cellulaire et sub-cellulaire, peut être obtenue à travers la réalisation de simulations de Monte Carlo appropriées. De tels calculs sont principalement dépendent de la connaissance exacte de la production et du ralentissement des électrons secondaires, ces derniers représentant la majorité des particules chargées.

Dans ce contexte, une condition importante est la production d'informations quantitatives précises et complètes en rapport avec les sections efficaces d'interaction des électrons sur une gamme d'énergie englobant les basses énergies, c'est-à-dire incluant le domaine de "sub-excitation". Le développement des algorithmes rapides pour la simulation du transport des particules, est également essentiel pour pouvoir couvrir avec efficience le processus de ralentissement dans sa globalité. Par conséquent, ce travail de recherche doctoral a pour objectif général le développement et la validation de nouveaux outils de calculs stochastiques devant servir à la simulation du transport des électrons et des positrons de hautes et basses énergies dans des matériaux biologiques. Plus spécialement, il vise à fournir (i) un ensemble complet et précis de données des sections efficaces, et, (ii) un algorithme rapide et fiable pour la simulation du transport de particules chargées.

La première partie de la thèse concerne donc l'évaluation, le développement plus poussé et la validation des modèles théoriques standards permettant le calcul des sections efficaces associées au transport des électrons et des positrons. Ces investigations concernent la caractérisation des interactions principales de ces particules avec la matière, en particulier les composants atomiques de base des matières biologiques (eau, biopolymères, etc.). Ceci aussi bien pour le rayonnement de freinage ("Bremsstrahlung") que pour les réactions de diffusion élastique et inélastique en considérant un large éventail d'isotopes et de particules incidentes allant des basses aux hautes énergies. En particulier, les sections efficaces d'excitation pour des moyennes et basses énergies (jusqu'à 1 eV) ont été déduites en employant un formalisme inédite basé sur la théorie des champs à multi-corps. L'exactitude des bases de données obtenues dans cette recherche a été évaluée par comparaison avec d'autres modèles théoriques ainsi qu'avec une large base de données expérimentales, ceci pour chaque type d'interaction. Dans ces conditions, une évaluation appropriée des incertitudes des sections efficaces générées a été assurée.

Dans la deuxième partie de la thèse, une extension du code de Monte Carlo PENELOPE a d'abord été établie pour permettre l'utilisation des sections efficaces différentielles de diffusion élastiques disponibles sous forme numérique. Ainsi, de nouvelles routines (incorporées au nouveau code PENELAST) préparent les sections efficaces nécessaires, à une énergie et un angle de dispersion donnés, en appliquant une technique d'échantillonnage rapide et précise d'une base de données existante. En permettant l'emploi de différentes libraries de sections efficaces sous une forme adaptée pour le code PENELOPE, ce schéma de calcul pouvant dès lors être utilisé pour des exercices de validation ("Benchmarking").

Finalement, le développement d'un outil de calcul de type Monte Carlo de haute rapidité (outil de classe I) pour le transport des particules chargées dans des matériaux biologiques a été proposé. Dans ce but, un algorithme numérique pour calculer les distributions angulaires de diffusion multiple des électrons et des positrons de haute énergie a été développé. Cet algorithme est basé sur la théorie de diffusion-multiple de Lewis, qui prend en considération les pertes énergétiques dans l'approximation de ralentissement continu. Tandis que les sections efficaces différentielles de diffusion d'onde partielle sont entrées pour les calculs sous forme de données numéeriques adaptées, celles de diffusion inélastique sont obtenues à partir du modèle d'oscillateur généralisé de Sternheimer-Liljequist. Ce modèle est celui implémenté dans le code PENELOPE. Le nouveau code LEWIS a été utilisé pour calculer des distributions angulaires de diffusion multiple pour des longueurs de trajectoire données et peut, par conséquent, aisément être adopté pour des simulations Monte Carlo de classe I. La génération simultanée d'un grand nombre de coefficients d'expansion de Legendre est ainsi possible de manière rapide et précise. Les résultats provenant du code LEWIS ont présentés des accords satisfaisants avec des simulations détaillées utilisant des sections efficaces résultant du module PENELAST ainsi qu'avec différents groupes de données expérimentales pour des électrons allant des hautes jusqu'aux moyennes énergies.

En résumé, ce travail de recherche représente une amélioration significative pour la simulation par méthode de Monte Carlo des processus de ralentissement des particules chargées. En particulier, des apports significatifs sur la compréhension du rôle des électrons secondaires à énergie réduite dans les études de radioprotection ont été obtenus. Ces investigations permettront également le développement futur d'un code de Monte Carlo complet de classe I, code pouvant être utilisé de manière fiable dans le cadre d'applications pratiques, comme, par exemple, la planification de la radiothérapie.

Contents

1 Introduction and Motivation **1**

1.1 Interaction of Radiation with Living Matter 1

1.1.1 Radiation research in the past 1

1.1.2 Present state of knowledge 3

1.1.3 Challenges and research trends in radiation protection 6

1.2 Plan and Structure of the Thesis 8

1.2.1 Problems of Interest 8

1.2.2 Objectives and Structure 9

2 General Background **13**

2.1 DNA Structure 13

2.2 Radiation Induced Damage to DNA 16

2.2.1 DNA damage and carcinogenesis 16

2.2.2 Physico-chemical molecular mechanisms of primary DNA damage . . . 19

2.3 Modelling Tools and Procedures 25

2.3.1 Codes for calculation of cross section data 27

2.3.2 Monte Carlo codes 27

2.4 Description of the Tools Used and Further Developed 31

2.4.1 PSICRO code for cross section data calculation 31

2.4.2 Monte Carlo code system PENELOPE 35

3 Theoretical Models for the Generation of Interaction Cross Sections **39**

3.1 Bremsstrahlung Emission 39

3.1.1 Introduction 39

3.1.2 Analytical bremsstrahlung differential cross sections 42

3.1.3 Numerical representation of bremsstrahlung differential cross sections . 44

3.1.4 Theoretical models implemented in PSICRO for total bremsstrahlung data 47

3.2 Elastic Scattering of Charged Particles 50

3.2.1 Introduction 51

3.2.2 Partial-wave analysis method 52

3.2.3 Theoretical models implemented in PSICRO for the generation of elastic scattering data 56

3.3 Inelastic Scattering of Charged Particles 59

3.3.1 Introduction 60

3.3.2 Analytical models for ionisation cross sections 60

3.3.3 Theoretical models implemented in PSICRO for the generation of ionisation cross section data 62

3.3.4 Analytical models for excitation cross sections 64

3.3.5 Theoretical models implemented in PSICRO for the generation of excitation cross section data 65

3.4 Summary 71

4 Interaction Cross Section Data Generated with PSICRO and Their Validation 73

4.1 Bremsstrahlung Emission 73

4.2 Elastic scattering 74

4.2.1 Data generation and validation for energies above 10 eV 75

4.2.2 Data generation and validation for energies between 1 and 10 eV 82

4.3 Inelastic scattering 90

4.3.1 Ionisation cross section generation and validation 90

4.3.2 Excitation cross section generation and validation 100

4.4 Summary 103

5 PENELAST - Extension of the PENELOPE Code System 105

5.1 Introduction 105

5.2 Numerical Cross Section Data Tabulations 106

5.2.1 ELSEP - Numerical elastic scattering differential and integrated cross section tabulations 107

5.2.2 Differential and integrated inelastic scattering cross sections based on the optical data model. 111

5.2.3 Stopping power 115

5.2.4 Angular deflections 117

5.3 PENELAST Code Features 118

5.4 Mixed and Detailed Simulation of Angular Distributions and Energy Spectra of Electrons after a Given Path Length 124

5.5 Summary 127

6 A New Multiple-scattering Numerical Algorithm 129

6.1 Introduction 129

6.2 Multiple-scattering Theories 131

6.2.1 Goudsmit-Saunderson multiple-scattering distribution 131

6.2.2 Molière-Wentzel multiple-scattering distribution 133

6.2.3 Lewis multiple-scattering distribution 134

6.3 Numerical Implementation of Lewis Theory 135

6.4 Angular Distribution of Electrons after a Given Path Length: Comparison of Lewis, Wentzel-Molière and PENELAST 139

6.5 Angular Distribution of Electrons after a Given Path Length: Comparison of LEWIS with PENELAST and Experimantal Data 143

6.6 Angular Distribution of Electrons after a Given Path Length: Straggling Effects 145

6.6.1 Comparison of Lewis and PENELAST 145

6.6.2 A method to account for straggling effects in Lewis theory 148

6.7 Angular Distribution of Electrons after a Given Path Length: Effect of Inelastic Scattering on the Angular Deflections 150

6.7.1 Replacing Z by $Z^2 + Z$ 150

6.7.2 Calculation of transport coefficients 152

6.8 Summary 154

7 Summary, Main Results and Recommendations for Future Work 157

7.1 Summary 157

7.2 Main Results 159

7.2.1 Cross section data for Monte Carlo codes 159

7.2.2 Monte Carlo methods 160

7.3 Recommendations for further developments 161

A Examples of PSICRO Input and Output Files **163**

A.1 Example of PSICRO input 163

A.2 Example of PSICRO output 164

B Lagrange Interpolation and Cubic Spline Interpolation Methods **165**

B.1 Lagrange Interpolation 165

B.2 Cubic Spline Interpolation 166

C Properties of the Legendre Polynomials **167**

C.1 Legendre Polynomials 167

C.2 Associated Legendre Polynomials 169

D Additional Information on the PENELAST Code **171**

E The Code LEWIS **177**

References **181**

Acknowledgements **203**

Curriculum Vitae **205**

1 Introduction and Motivation

1.1 Interaction of Radiation with Living Matter

1.1.1 Radiation research in the past

Within just two years of the discovery of X-rays by the German scientist Wilhelm Röntgen on the 8^{th} of November 1895 [1], the biological effects of radiation had proven to be both beneficial, for the diagnosis and treatment of abnormal tissue, and harmful, for producing deleterious changes in normal tissue. A series of discoveries followed that helped to determine the nature of radiation, such as those of Antoine Becquerel [2] in 1896, Marie and Pierre Curie in 1898 (radioactive properties of uranium and radium), Joseph John Thomson in 1897 (discovery of β radiation), Irene Curie and François Joliot in 1931 (artificially induced radioactivity) [3] and James Chadwick in 1932 (discovery of the neutron) [4].

Since then, a continuous effort has been undertaken by the scientific and medical communities to apply ionizing radiation for the benefit of mankind. There has been a large spectrum of applications in this context, ranging from its use as a powerful medical diagnostic tool for many diseases to its important role in radiotherapy to treat most types of cancer. For the first 50 years, however, the principal application of radiation was clinical radiology, i.e. medical diagnosis based on the use of X-rays to produce radiographic images. The lack of precise methods to measure dose prevented the safe and effective use of radiation to treat disease. Important scientific and technical advances made in the second half of the 20th century helped extend widely the use of radiation in medicine and industry. For instance, in medicine, X-rays are nowadays used routinely for diagnosis in various form, e.g. computed tomography (CT) and 3-D digital imaging, as well as for interventional surgery and screening. Moreover, both γ radiation (mainly from radioactive isotopes) and X-rays find important applications in external and internal radiotherapy. Many examples exist also of the beneficial use of radiation in industry, such as the extensive utilization of radioisotopes for quality control and the sterilization of food and medical equipment.

Effective and safe use of radiation created the need to determine the effects of ionizing radiation in living tissue, which gave birth to the discipline of quantitative radiobiology. In 1927, the first measurements of mutation rates by Müller using X-rays demonstrated the dose-response relationship in the Drosophila fruit fly [5]. As a result of this work and others that followed, the initially crude qualitative methods, based mainly on skin tolerance to radiation measured by the severity of the resulting erythema, were gradually replaced with more accurate ones. These methods related damage to living tissue to the concept of absorbed radiation *dose*, $D(\mathrm{P})$, i.e. the mean energy deposited by the ionizing radiation in a mass of matter at a point P. This basic quantity is commonly used to characterise the effect of all kinds of radiation on living matter. For instance, Fig. 1 displays logarithmic curves of survival vs. dose, which characterize the survival of mammalian cells after exposure to ionizing radiation [6]. These curves are characterized by an initial shoulder at low doses indicating low cell sensitivity, followed by a logarithmic decline of the survival fraction as the dose increases. Different types of cells present distinctive curves depending on their 'radiosensitivity' to the form of radiation to which they are subjected. In this respect, early studies by Bergonié and Tribondeau [7] in 1906 already showed that actively dividing cell populations are more 'radiosensitive' than non-dividing ones. Later research found that the type and energy of the radiation were also important in determining how cells responded to it. In order to take into account these observations, the dose is modified by so-called *quality factors*, which account for the fact that the same dose can produce different effects in living matter depending on the type of radiation and of tissue in which the energy is deposited.

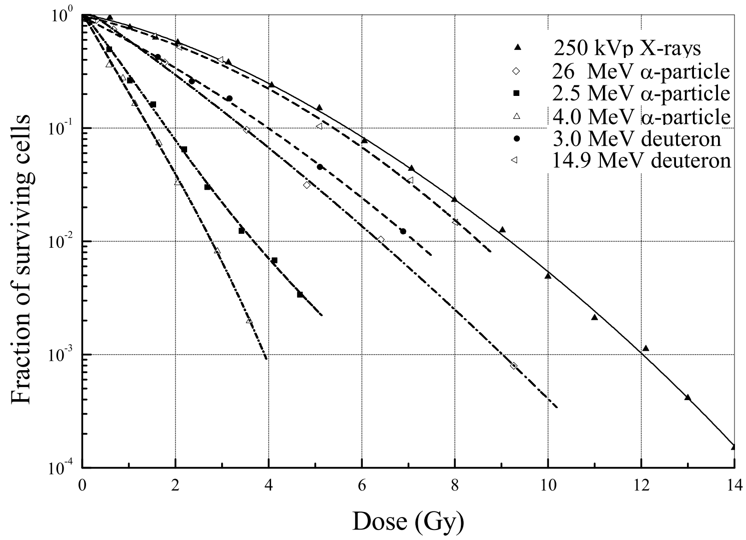

Figure 1: Biological effects on mammalian cells from exposures to different types of radiation [6].

An important discovery made in 1959 by Elkin and Sutton demonstrated that not all radiation damage is lethal for the cell, and that some repair is also possible [8]. Although the repair mechanism still remains to be described fully, scientists have proven that DNA (acronym for deoxyribonucleic acid, i.e. the genetic material of most organisms, whose structure in double helix was discovered in 1953 by James Watson and Francis Crick) is the principal target of radiation damage [9]. Over the past two decades, experimental [10-12] as well as theoretical work [13] has advanced significantly to address the issues related to the quantification and the description of the physical, chemical and biological mechanisms of initial damage to cellular and sub-cellular structures by ionizing radiation of different quality. It is now widely believed that the greater part of radiation damage that results in cell killing is a result of molecular damage to the DNA molecule, primarily in the form of single (ssb) and double (dsb) strand breaks, base damage and complex combinations within the cluster of damage. The cell's DNA repair mechanism can correct a single lesion, but closely spaced or complex lesions are likely to defeat its restorative abilities. Therefore, about a decade ago, cancer, the disease of DNA, was considered as the result of cumulative mutations that alter specific locations in a cell's DNA and, thus, change the particular proteins encoded by cancer-related genes at those spots. The last 25 years have recorded a continuing evolution in the need for developing mechanistic models that accurately describe the process of interaction of radiation with biological matter considering increasingly smaller volumes and, therewith, helping to interpret the results obtained in experimental studies of radiation biology.

On the practical side, the field of radiation protection was born from the need to control the dose-response relationship and limit the health effects at various ionizing radiation exposure rates. The most important achievement in this field has been the establishment of widely accepted radiation protection guiding principles, which have been set up for the protection of workers (occupational radiation protection) and the general public (public radiation protection) from the risks associated with radiation exposure. These principles are also applied for the safe exposure of people to moderate doses, i.e. medical radiation protection, used in medical diagnostics (e.g. X-rays, CT, nuclear medicine scans, etc.) and to the very high doses used in medical therapeutic treatments (e.g. radiation therapy for cancer patients). Since the first warning of possible adverse effects of X-rays in 1896 by Thomas Edison, William J. Morton, and Nikola Tesla, who independently reported eye irritations from experimentation with X-rays and fluorescent substances, many studies have been pursued in order to develop the appropriate monitoring instruments, physical controls, administrative procedures, and radioactive waste disposal practices necessary to help solve safely the entire spectrum of modern day radiation protection problems. As a result, exposures to man-made ionizing radiation from medical as well as from industrial activities can nowadays be reliably controlled. It is well known that an unavoidable level of ionizing radiation exists in the atmosphere from the minerals remaining since the very early formation of the planet or arising from cosmic rays. For human activities, basic principles are set to control or manage radiation exposures (both individual and collective to the workforce and the public) and releases of radioactive material to the environment to a level that is *as low as reasonably achievable* - ALARA. For example, in most developed countries, the estimates of all exposures show that, on average, doses from industrial activity plus weapons fallout represent a very small part of the total (1%). Doses from medical practices are greater (about 14%) and the remainder (about 85%) comes from natural sources. ALARA practices apply to virtually any toxic substance, but are made mandatory for radiation workers by the U.S. Nuclear Regulatory Commission (US NRC), and have been used as basis for similar regulations in other countries. On the other hand, procedures for the beneficial and safe use of radiation have been set for the medical field. *Safety Limits* to guide users of radiation have been recommended by the International Commission on Radiological Protection (ICRP).

1.1.2 Present state of knowledge

As shown in the previous section, the interaction of the particles in a beam of radiation, the so-called 'primary particles', with living matter has long been a focus of radiobiological research. In general, a beam of electromagnetic ionizing radiation consists of particles whose energies can range from those of high frequency γ-rays (in the MeV range, resulting from nuclear interactions) to those of lower energy X-rays (in the keV range, produced by atomic interactions or subatomic processes such as electron-positron annihilation). Other types of non-electromagnetic highly ionizing radiation are alpha particles, also known as alpha rays (two protons and two neutrons bound together to form fully ionized helium ions, He^{2+}), beta particles (high-energy electrons or positrons ejected from a nucleus in a beta decay process), and electrons, protons and heavy ions in high enegy accelerators. In terms of time scale, it is currently accepted that the interaction process between a particle of radiation and living matter involves at least 18 orders of magnitude. It ranges from the early events which determine the energy deposition after 10^{-15}s (during the so-called 'physical stage' of the interaction) to experimental detection of the effects of the interaction hours after the irradiation (the so-called ‘biological stage’). In terms of spatial description, about five orders of magnitude are involved, from atomic scale to the dimensions of a cell nucleus. Figure 2 shows schematically the time scale of the radiobiological processes [14]. Alpha particles are among the most damaging due to their greater mass and charge, followed by protons, beta particles and γ-rays. During the physical stage of interaction, primary particles can undergo several types of interactions. For example, high-energy photons (X- and γ-rays) can produce five major types of interactions, namely, coherent scattering, photoelectric effect, Compton scattering, pair production, and photo-disintegration. Electrons and positrons can undergo elastic collisions with atomic nuclei, inelastic collisions with atomic electrons (viz. ionisation and excitation), bremsstrahlung and positron annihilation. The probability of each particular type of interaction process depends on the primary particle energy.

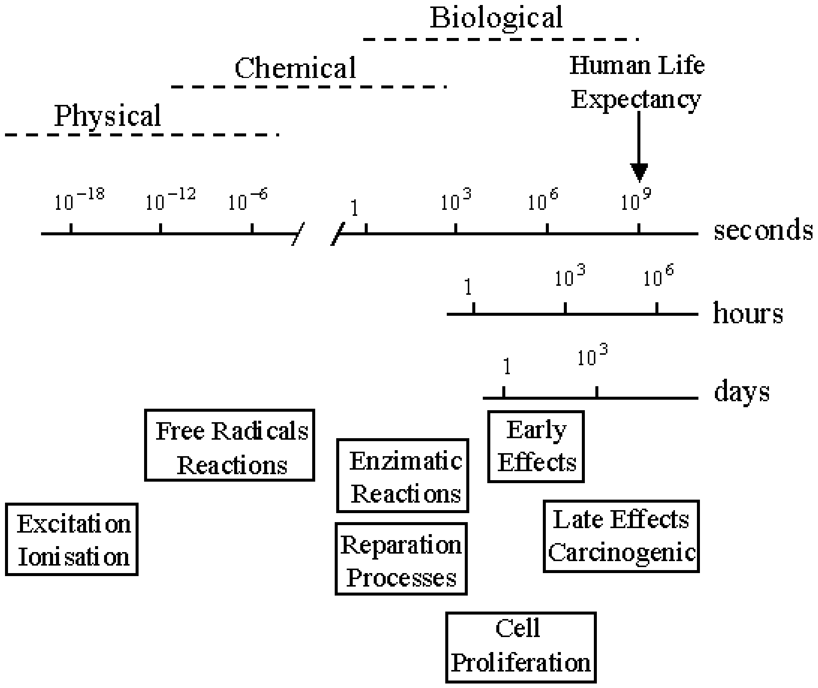

Figure 2: Time scales and stages of radiation interaction in radiobiology [14].

The fast ‘secondary particles’, produced by the primary particles that constitute the beam, lose their energy by a sequence of interactions with the medium which must also be fully accounted for. When the incident radiation consists of photons or electrons, most of the secondaries are electrons, the so-called δ-rays. As a result of ionization or excitation of the atomic orbital electrons, the secondary electrons attain thermal energies after about 10^{-11}s. According to the research studies prior to 2000, it was believed that DNA could be harmed only by secondary electrons with kinetic energy greater than 10 eV[1]. However, in more recent studies such that those on “radical attack” [15], it has been shown that an important part of the damage done to the DNA occurs during the chemical stage (see Fig. 2). It is during the chemical stage that

---

[1] The ionization energy of a hydrogen atom is 13.6 eV, so that a value of around 10 eV has been considered an approximate threshold.

the recombination reactions of primary free radicals (i.e. electrically neutral atoms having an unshared electron in the valence shell, which gives them a highly reactive character) such as $H^\bullet$ and $OH^\bullet$, resulting from ionizing radiation interacting with water molecules surrounding the DNA, take place. These experiments [15] have also demonstrated that the very low-energy electrons (3 eV) can break the DNA molecule's double helix by attaching to one of the strands of the molecule, which then loses a hydrogen atom or a larger fragment. The decay fragments can in turn damage the other DNA strand though chemical reactions. Therefore, in order to significantly increase the benefits of radiation therapy and the survival rates of cancer patients, special attention is currently being directed towards understanding the role of low-energy secondary electrons.

The accurate determination of ionisation and excitation events and, consequently, of the distribution of the secondary particles and their energy deposition (in particular the distribution of low-energy electrons, say lower than 100 eV), coupled with models to describe the chemical damage due to the radical formation process (occurring during the physico-chemical stage), can provide input to models describing other levels of radiation damage. This, in itself, can help to gain understanding of the relative importance of the different mechanisms causing DNA damage for various types of radiation. In this sense, theoretical atomic physics, in particular, makes available the instrumentation, the principles and the basic "data" for the consideration of chemical and biological effects of ionizing radiation [16]. In parallel, the development of new experimental techniques in fields such as microbiology, genetics, biochemistry and molecular biology has provided the means to study smaller and smaller biological entities, going from the whole organism, to cells, to genes and, finally, to the base sequence of DNA. In addition, computational methods, both analytical and stochastic, represent nowadays an invaluable tool for testing the assumptions on the intermediate steps of the process that leads to chromosome damage and other observable biological radiation effects that may be very difficult or impossible to ascertain with current experimental techniques. Thus, for example, studies carried out by Nikjoo *et al.* [13] and Ottolenghi *et al.* [17, 18] have shown that DNA double strand breaks (dsb) can exhibit various levels of complexity not experimentally detected, and that some dsb, which can be detected, are different at the molecular level, from what was thought previously.

Given the stochastic nature of radiation action at all stages, Monte Carlo (MC) methods have proven to be of great help to accurately simulate the various steps of radiobiological damage induction. In the context of developing computing methods for radiation protection and radiation dosimetry, the use of this technique yields quantities that estimate dose and energy deposition by sampling the track structure within the sensitive target volume (sub-cellular structures, cell, or group of cells). These quantities provide basic information about the structure of the statistical distributions of energy transfer on the scale of the simulated biological targets, and are thus capable of resolving some of the limitations encountered in analytical calculations and/or due to the barriers existing when developing new experimental techniques such as micro- and nano-dosimetry. Such information is very valuable for biophysical modelling [19, 20], e.g. in developing mechanistic DNA damage models, and can, subsequently, be correlated to models of biological response.

The MC calculation technique has, moreover, proven to be an invaluable tool for providing accurate simulations for radiation therapy. Since the first attempt to cure cancer by using radiation, dating back to the time of the discovery of X-rays [21], significant advances have been made in the application of radiation to cancer treatment. In fact, four common methods currently exist for the treatment of cancer, most of the time applied in a combined way: (a) surgery, i.e. the procedure of removal of cancerous tissue, (b) chemotherapy, i.e. the treatment of cancer by intravenous medication, (c) radiation or radiotherapy, i.e. the delivery of powerful X-rays, γ-rays, neutrons, protons or high-energy electrons and positrons to the site of the cancer with the result that the tumour eventually shrinks or disappears, and (d) biological therapy sometimes also called immunotherapy, biotherapy, or biological response modifier therapy, i.e. treatment to stimulate or restore the ability of the immune system to fight infections and other diseases. Radiation therapy may be performed either by using external radiation sources, i.e. external-beam radiation therapy (charged particle exposure by accelerator beams, neutron exposure by reactor beams), or by placing radioactive material in the body near cancer cells, i.e. internal radiation therapy, implant radiation, or brachytherapy. The goal is to maximize the dose at the tumour location while minimizing, at the same time, the exposure to the surrounding body tissue. Since radiation therapy is technically difficult and potentially dangerous, both approaches require careful treatment planning. In this context, the MC technique represents the state-of-the-art engine for the detailed 3D dose distribution calculations which need to be performed in routine clinical treatment planning.

1.1.3 Challenges and research trends in radiation protection

In spite of the considerable efforts made to date in radiation protection, the hazards stemming from the improper use of ionizing radiation in medical and industrial applications mentioned above have continued to arouse large public interest. As a result, more detailed studies have been launched recently, especially in relation to the carcinogenic and mutagenic effects of chronic exposure to very low doses. Despite the fact that ionizing radiation can be measured with great precision even at very low doses due to its physical characteristics, the initiation of damage at this level is much more difficult to quantify and cannot be easily correlated to macroscopic quantities. Thus, the classical concept of dose is difficult to apply at the cellular and DNA scales [22]. Current estimates of cancer risks following exposure to ionizing radiation are based on epidemiological studies of exposed human populations, principally the Japanese atomic bomb survivors. The predictions for low doses[2] and low dose rates are based on a linear extrapolation of the effect at relatively high doses[3] (the linear-no-threshold hypothesis[4]), taking a dose and dose rate dependent reduction factor into account as recommended by ICRP, NCRP (National Council on Radiation Protection - US), NRPB (National Radiological Protection Board - UK) and AECB (Atomic Energy Control Board - Canada).

It is in the above context that a project "Improved cancer risk quantification for environmental, medical and occupational exposures to low doses of ionizing radiation by mechanistic models", also called "Low Dose Risk Models", was implemented during the 5^{th} European Union Framework Programme (1999-2003) [23]. Similar research programs, such as "Health risks from exposure to low levels of ionizing radiation", currently in progress under US NRC coordination, have stemmed from the growing interest in the biological effects of all forms

---

[2] A cell may only be traversed by a single electron track over a long period of time, e.g. one year.

[3] A cell is traversed by multiple ionising tracks.

[4] The linear-no-threshold hypotesis for radiation induced cancer states that cancer risk increases as a linear function of dose. Thus, the smallest dose of radiation is theoretically capable of producing at least some cancer.

of radiation, including non-ionizing radiations (e.g. radiofrequency electromagnetic radiation and extremely low frequency electric and magnetic fields), on humans and other species. The main goal of these projects is to improve the understanding of the basic problem in radiation protection, especially the risk estimates after exposure to low doses of various types of ionizing radiation at dose rates that occur at work places (e.g. in the nuclear industry), in the normal living environment (from natural radioactivity, in aeroplanes, etc.), around nuclear facilities (through normal and accidental emissions) and in diagnostic medicine (as part of health care practice). Thus, the principal objectives of the "Low Dose Risk Models" programme have been the identification of general rules and broad data sets for developing and testing models of radiation health effects, refining the inherent assumptions, and identifying the new data and mechanisms which need to be included in the models. The project, consisting of five work packages, each with specific tasks, has comprised research studies which have aimed at:

- Critically evaluating the relevant physical, chemical, medical and statistical evidence, theories and data from basic and epidemiological studies; synthesising these into mechanistic models and important data needs.

- Developing mechanistic models for the induction of the primary damages to DNA, cells and organs by irradiation from various sources of ionizing radiation taking into account oxidative damages. The Paul Scherrer Institut (PSI, CH) participated with studies related to primary damage models and the framework of this activity has largely provided the prime motivation for the present thesis.

- Developing mechanistic models for the repair of these damages in DNA, membranes, etc., and for quantitative description of this repair for chromatin and chromosomal structures, as also for gene, cellular and organ functions (the lung, thyroid and bone).

- Developing improved mechanistic models of the multistep processes leading to radiogenic cancer taking normal oxidative processes into account, efforts being concentrated on the age and sex dependent dose-time-effect surfaces for the above mentioned organs.

- Based on the understanding acquired from the earlier four steps, making quantitative conclusions and recommendations for practical, operational radiation protection at places of work at nuclear installations, as well as for medical and natural radiation exposure, in order to evolve optimum health protection philosophies and radiation measurements strategies.

As regards medical radiation protection, new standards and guiding principles have been defined for medical physics practice in order to improve the quality of patient care. These standards recognize that the safe and effective practice of medical physics requires specific training, skills and special techniques to minimize the potential for unnecessary radiation exposure to individuals. In this sense, modelling experiments are conducted to accurately determine the input parameters of various treatment simulation models or to perform dose calculations. In particular, the application of MC techniques for routine clinical treatment planning has become a challenge for various producers of treatment planning systems. In order to achieve their successful implementation in commercial systems, additional requirements have been imposed such as a fast simulation time (below 10 minutes or, if possible real time calculations), precision in dose calculation (better than 1%), and the optimization of radiation field geometry (1mm) and dose ($< 1\%$). Such needs are addressed in the second part of the thesis, in which a new numerical algorithm is developed and implemented for fast and accurate simulation of charged particle transport in matter. This part has been carried out in collaboration with the radiation physics group of the University of Barcelona, Spain.

1.2 Plan and Structure of the Thesis

1.2.1 Problems of Interest

As indicated in Section 1.1, among the main objectives of radiation physics and radiation dosimetry for therapeutic purposes is the determination of the spatial distribution of energy deposition in living tissue when exposed to ionizing radiation. It is known that a high-energy particle of ionizing radiation does not inflict most of its damage by knocking atoms directly, but by releasing secondary electrons of very low energy (as low as 20 eV, comparable to a photon in the visible to ultraviolet range [24, 25]). In many practical situations, direct measurements are either not possible, or are too costly in terms of the time and effort necessary to achieve reasonable accuracy (e.g. in micro- and nanodosimetry applications for the investigation of radiation damage to sub-cellular structures). Besides, certain recent experiments have demonstrated that even very low-energy (few eV) electrons set off by ionizing radiation can break up key molecular compounds such as DNA and RNA (acronym for ribonucleic acid, structurally similar to a single strand of DNA, which transmits the genetic information from DNA to the cytoplasm and controls certain chemical processes in the cell). For example, a particle of 1 MeV energy can release as many as 40000 such low-energy electrons [15]. It is, therefore, important to provide detailed quantitative information concerning both physical and chemical aspects of radiation interactions with atoms and molecules, in order to extend the present knowledge related to the early effects of radiation in DNA damage induction.

In order to overcome experimental limitations of the type indicated above, sophisticated calculation methods, in particular MC simulation based on appropriate interaction cross sections and particle transport theories, are commonly used. The description of the penetration of a charged particle beam in matter is complex due to the usually very large interaction cross sections and, thus, the large number of possible long-range Coulomb interactions (e.g. inelastic with atomic electrons, elastic with the positively charged nucleus, and bremsstrahlung involving both the atomic electrons and the nucleus). The propagation of charged particles through matter in the course of their slowing down to thermal equilibrium can be efficiently simulated with the help of MC codes by using "condensed history" algorithms (e.g. Molière [26] in EGS4 [27] and GEANT3 [28], Goudsmit-Saunderson [29] in ETRAN [30] and MCNP [31], or mixed algorithms [32] in GEANT4 [33] and PENELOPE [34]). Such algorithms group together a large number of individual interactions using multiple-scattering theories for the elastic angular changes and stopping powers for the energy losses. Quantities such as the net displacement, energy loss and change of direction of a propagated particle are computed using appropriate sampling methods of the multiple-scattering probability distribution functions (PDFs). The accuracy of the calculation of these functions is limited by that of the adopted differential cross section (DCS) data and also by the approximations introduced in the multiple-scattering algorithms that are used for describing the cumulative effect of many interactions in one single step. The additional requirements imposed for the application of MC methods to routine medical treatment planning have addressed the problem of developing advanced MC algorithms which are fast running and, at the same time, able to perform very accurate dose calculations.

On other hand, due to the approximations made, condensed history models are not suitable for problems related, for example, to the damage to sub-cellular structures in radiation biology or to the dynamics of chemical reaction chains in radiation chemistry. For example, the continuous-slowing-down approximation assumes a continuous energy loss along a straight path length, so that interaction points of low energy transfer become indistinguishable. The key problem for the detailed understanding of the initialization of damage to DNA is the accurate knowledge of the spatial distribution of particle interactions, commonly known as the *track structure* [22]. For such calculations, interaction-by-interaction, or event-by-event, MC is required in order to simulate the detailed interaction of the radiation with individual cell structures. Although computationally very expensive, such codes (e.g. OREC [35-37], MOCA [22, 38, 39], KURBUC [40], CPA [41], PARTRAC [42-44] and PITS [45, 46], which are able to perform the calculation of various microdosimetric quantities) have already been developed. However, the cross sections needed to perform transport simulation in such detail are available only for water. PENELOPE [34] is the first widely available general purpose MC code system capable of transporting electrons and positrons through materials other than water by employing both fast, condensed history (for soft collisions) and detailed (for hard collisions) transport mechanisms. However, the representation of the cross sections and physics below 500 eV has remained somewhat uncertain because relevant refinements in the DCSs are usually neglected.

1.2.2 Objectives and Structure

Developments of MC methods in radiation physics have been made in the past decades in two broad sectors. Firstly, the advent of modern computers has made it possible to carry out MC simulations of electron transport at high energies (as pioneered by Berger [47]) with explicit consideration of complex geometries and non-uniform media. Secondly, low electron energy applications (initiated with the work of Paretzke [22]) have been addressed by considering the use of realistic cross sections, in particular for this energy domain. The present doctoral research aims at contributing towards the development and validation of new MC calculational tools for charged particle transport in biological materials at both high and low energies. As outlined above, a comprehensive and accurate set of appropriate cross section data, on one hand, and a fast and reliable simulation algorithm, on the other hand, are the essential requirements.

In order to obtain accurate angular distributions of the very low-energy secondary electrons scattered in various interaction processes, as well as to improve upon the current understanding of the mechanisms of the induction of primary physical, chemical and biological damage that lead to specific radiation effect end-points, the use of reliable cross section data has been continuously stressed by the physics research community [48]. In particular, the need has been underlined for a comprehensive coverage and the availability of a wide variety of data. Bearing in mind that the basic interaction physics models for energies below a few hundred eV are still open to question[5], the current research is considerably motivated by the strong need of having, at least, correct order-of-magnitude estimates. Thus, the first part of this thesis has been directed towards the assessment and further development of the existing elastic and inelastic scattering models for electrons and positrons over a wide range of atomic numbers and energies. Effectively, this part is devoted to the generation and validation of standard cross

---

[5] The theory of slow-electron interaction in condensed phase, especially in liquid matter, is still very poor.

section data that cover the main interactions of these particles with matter, in particular with the basic components of biological materials at energies down to about a few eV. Firstly, low-energy bremsstrahlung cross section data are calculated by an extrapolation method applied to the cross sections already available at higher energies. For elastic scattering in the medium and low energy range, the partial-wave analysis method is used, considering various descriptions of the interaction process. Then, ionisation cross sections, in the energy range near the threshold of ionisation, are calculated by using the Weizsäcker-Williams method. Finally, cross sections to model excitation interactions for medium and low energies (down to 1 eV) have been derived and generated by using a many-body field theory approach. The accuracy of the data sets thus obtained is assessed against other theoretical models, as also against the most recently reported experimental values, for a wide range of elements.

In the second part of the thesis, the extension of a widely used MC tool, viz. PENELOPE [34], is achieved to incorporate an external numerically calculated set of DCS data generated for certain angular and energy grids. This has required the development of a new computational tool which can prepare the cross section data needed, for any energy and scattering angle required, by making use of a fast, computationally efficient and accurate sampling technique. At the same time, the further development of fast MC simulation methods used to calculate detailed dose distributions in various materials, with elements ranging from Z=1 to 100 and covering the entire high to medium energy range, has also been addressed. In this context, a new computational algorithm, which can be implemented in any Class I MC code, is developed based on the multiple-scattering theory of Lewis [49]. Moreover, a new methodology to account for the inelastic scattering contribution to the calculation of multiple-scattering distributions is formulated. The performance and accuracy of this tool is tested by comparing its results with those of some of the most important multiple-scattering algorithms used by current-day MC codes, such as Molière [26] and Goudsmit-Saunderson [29]. The importance and interest in the use of such algorithms in MC codes is due to the possibility that they offer for the calculation of real-time charged particle transport in a computationally much more effective manner than direct simulation algorithms, while, at the same time, preserving to a great extent the accuracy of the results.

The present work is important for the future development of MC codes in radiation applications for two reasons. Firstly, it provides an in-depth assesment of the accuracy of currently available models for the calculation of electron and positron scattering cross section by neutral atoms, for different ranges of energies and mass numbers. The results of this analysis offer an insight into the appropriateness of the models as well as their deficiencies, especially for the low energy region. The second reason is the provision of standard tools that allow both the rapid use of any up-to-date cross section data set and the fast simulation of electron and positron transport (when implemented into a MC code). The detailed analysis of the currently applied multiple-scattering algorithms, carried out considering thereby radiation transport in different media and for various energy ranges, should also help answering questions regarding the validity of the approximations currently used to model different aspects of charged particle transport.

The present developments are expected to contribute, in particular, to the simulation of radiation interactions in volumes smaller than those in the micrometer range. The extension of MC calculations to very small scales will also increase their usefulness for certain novel radiation oncology applications, e.g. targeted radionuclide therapy (i.e. radiation therapy where cytotoxic radionuclides are linked to antibodies in order to deliver toxins directly to tumour targets), microbeam therapy (i.e. using synchrotron-generated arrays of parallel microplanar beams of X-rays), and proton and photon radiosurgery aimed at selectively damaging tumour cells. Thus, the results of the current research have implications for both the understanding of the biological effects of low levels of radiation, as well as for the improvement of radiation treatment procedures.

Following the present introduction, a detailed description of the interaction processes of ionizing radiation with biological matter is given in Chapter 2. Chapters 3 and 4 deal with the generation of bremsstrahlung, elastic, and inelastic scattering cross sections for electron and positron collisions with atoms (Z=1-100) in the energy range from 1 eV to 100 GeV. These two chapters outline, respectively, a) the standard theoretical models, together with the current developments, and b) representative results and their validation. Chapter 5 describes the methodology which has currently been developed for linking appropriate DCS input to the PENELOPE code system. The new numerical algorithm which implements the Lewis multiple-scattering theory for the calculation of the angular distributions of particles that have travelled a certain path length, is described in Chapter 6. Results obtained thereby are compared with experiments reported in the literature or, when this has not been possible, with distributions obtained from the simulation with the newly developed MC tool PENELAST. Finally, Chapter 7 summarizes the most important developments and findings of the present research and gives recommendations for future work.

2 General Background

This chapter introduces the principal background aspects of the research described in this thesis. Numerous studies have demonstrated, both in animals and in vitro, that ionizing radiation can produce irreversible damage to biological matter [50-52]. However, as already indicated in the introduction, somatic effects observed at high and low doses are qualitatively different. Whereas for high radiation exposures, direct damage to the nucleus and to other parts of the cell will cause serious damage to the body and even rapid death, at low doses, cancer is, by far, the most important possible consequence. In order to qualitatively and, especially, quantitatively understand the multi-step process of radiation induced damage that may lead to cancer, one needs to have a closer look at the constituents of biological matter, the most recent carcinogenesis models and the mechanisms involved in cell radiation damage. This is necessary in order to develop appropriate phenomenological and mechanistic models to describe the various interactions involved.

Sections 2.1 and 2.2 discuss, respectively, DNA structure and radiation damage to DNA. Computational tools and procedures are briefly reviewed in Section 2.3, while Section 2.4 presents, in somewhat greater detail, the tools applied and partly developed further during the current research work.

2.1 DNA Structure

The cell[6] represents the fundamental structural and functional unit of all living organisms, and has a diameter of 1-100 μm. Figure 3 shows the organization of an animal cell with the description of its internal structures called organelles. The nucleus contains the cell's genetic information encoded in the sequence of pairs of 4 bases (Adenine, Guanine, Citosine and

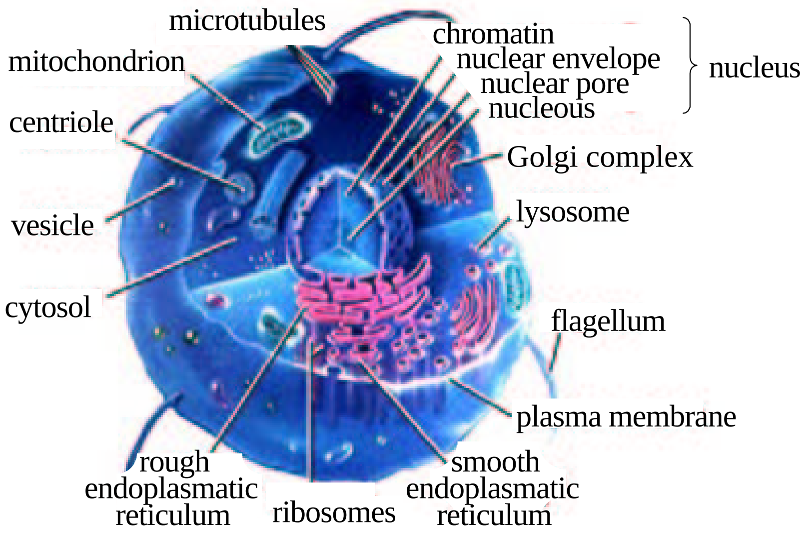

Figure 3: The structure of the cell.

---

[6] The name, given by Robert Hooke [53], comes from the Latin *cella*, a small room.

Thimine) which form the molecule of DNA. The DNA contains the complete set of instructions necessary to make an organism (human, animal, plant or other living thing) and to control the activity of the cells that form it. These instructions are known as the organism's genome, which consists of genes, i.e. sequences of DNA base pairs acting as a master 'blueprint' for cell development, differentiation and activity.

The human genome consists of tightly coiled threads of DNA and associated protein molecules, both forming the chromatin which is located in the cell nucleus. It is only during the cell division phase, when the nucleus prepares itself to divide, that chromatin strands coil and condense into thick separate structures, large enough to be seen through an optical microscope, called (metaphasic) chromosomes (from the Greek chroma = colour and soma = body). Thus, chromosomes represent the most critical part of the cell since they contain the genetic information and the instructions required for the cell to perform its function and to make copies of itself for reproduction purposes. It is also during the mitotic phase (M) of the cellular cycle, shown in Fig. 4a, that the largest damage with serious consequences to cell life can be produced. Different organisms contain different numbers of chromosomes; humans have 23 pairs of chromosomes, such that each pair is made up of homologous chromosomes.

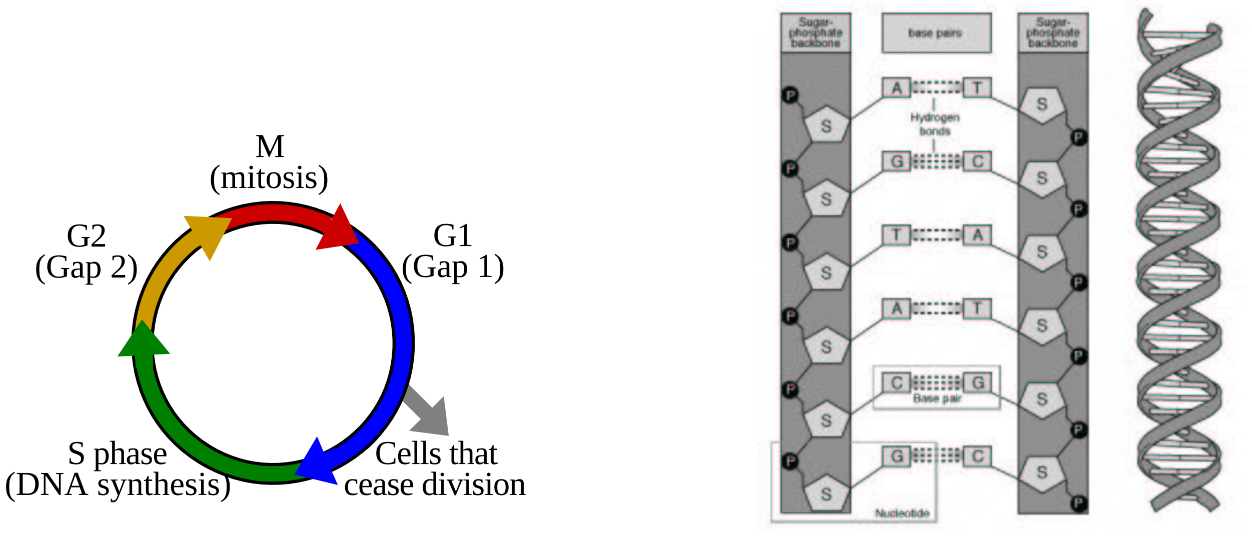

(a)

(b)

Figure 4: a) The cellular cycle, an ordered set of events, culminating in cell growth and division into two daughter cells: DNA synthesis (S), chromosome condensation, segregation and cell division (M), two non-consecutive distinct phases G1 (growth and preparation for replication) and G2 (preparation for the M-phase) of the life of a cell. b) The structure of DNA.

DNA, schematically shown in Fig. 4b, is a long polymer of deoxyribonucleotides with a molecular weight in humans of at least 1011 base pairs (bp) having the form of a double helix. The diameter of the DNA helix is 2nm and the vertical spacing per base pair is 0.34nm [54]. The DNA itself is surrounded by other biomolecules (proteins) and, of course, water. The structure of the DNA helix is stabilized by van der Waals forces, hydrogen bonds between complementary organic bases and hydrophobic interactions between the nitrogenous bases and the surrounding sheath of water. Despite their enormous size, all DNA molecules are made up entirely of three basic repeating units:

(1) deoxyribose, $C_5H_{10}O_4$, a pentose sugar with a five-member ring (four carbon atoms plus one oxygen; Fig. 5a). Hydroxyl groups are attached to two of the carbons in the ring. The fifth carbon and a hydroxyl group are attached to one of the two carbon atoms adjacent to the oxygen atom;

(2) a phosphate group PO_4^{3-} (Fig. 5b), which confers a negative charge to the molecule and links the pentose rings so that they form the two helices that constitute the basic skeleton of the DNA molecule;

(3) four different heterocyclic nitrogenous bases discovered in 1920 by P.A. Levene (Figs. 5c, 5d, 5e, 5f), viz. Adenine $C_5H_5N_5$ (A), Thymine $C_5H_6N_2O_2$ (T), Guanine $C_5H_5N_5O$ (G) and Cytosine $C_4H_5N_3O$ (C). They form complementary base pairs, i.e. A-T and G-C, joined by hydrogen bonds, that maintain linkage of the two strands of pentose-phosphate. The relative weakness of the hydrogen bond facilitates the separation of the strands during the replication process of cell division.

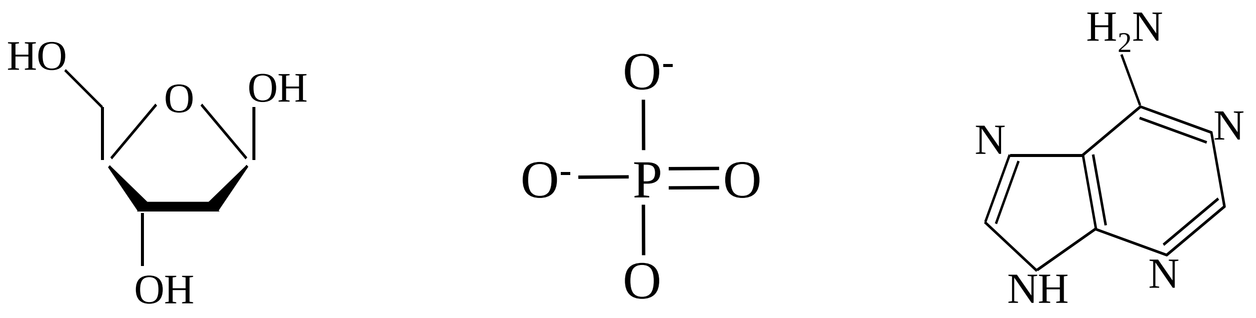

(a) Deoxyribose (b) Phosphate (c) Adenine

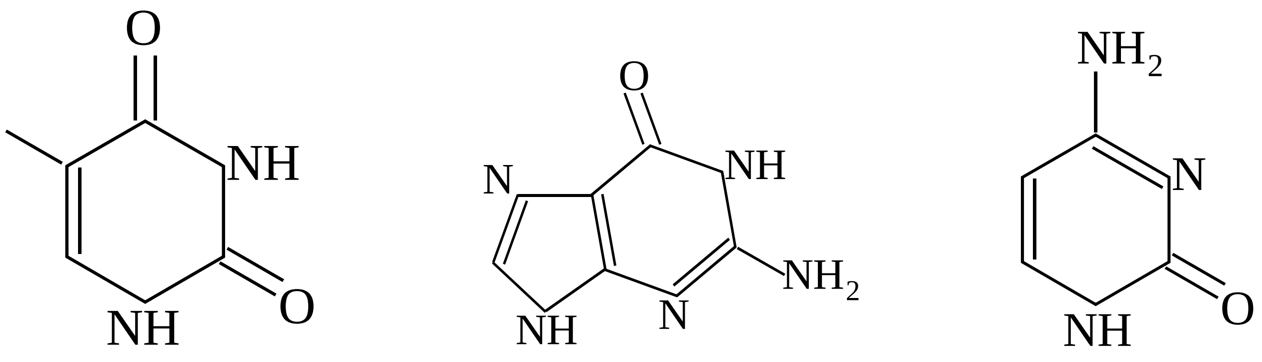

(d) Thymine (e) Guanine (f) Cytosine

Figure 5: The constituents of the fundamental chemical building block of DNA.

2.2 Radiation Induced Damage to DNA

When ionizing radiation interacts with the cell nucleus, it creates, as a result of an extremely complicated combination of physical, chemical and biological processes, singly damaged sites and clusters of strand breaks and base damage within one or two turns of the DNA (10 to 20 base pairs). The need to further study the damage to DNA caused by ionizing radiation arises from the proven capacity of such basic damage, when produced on distant parts of the DNA strand, to result in deleterious effects to the cell. Such effects can be mutations [55] (i.e. permanent, transmissible changes to the genetic material, usually DNA or RNA, of an organism), chromosome aberrations [56] (i.e. any deviation from the normal number or morphology of chromosomes such as deficiencies, duplications, translocations, inversions, etc., that lead to cell death or ill-adaptation), cell inactivation [57] and damage to the genome integrity [58]. In recent years, important advances have been made in the development of biophysical models that help to reliably predict the relation between the intensity of the irradiation measured by the dose and its observed biological response (e.g. radiation induced cancer). In particular, an intense research activity has been underway on the effects of low dose irradiation on DNA and the subsequent processes underlying radiation induced carcinogenesis (i.e. the process by which normal cells are transformed into cancerous cells).

2.2.1 DNA damage and carcinogenesis

There is much evidence that carcinogenesis in vivo, in humans and in other animals, is a multi-step process. The steps can be operationally described as initiation, promotion and progression. The initiation stage consists of the primary damage produced by the carcinogenic agent, e.g. ionizing radiation. During the promotion stage, additional secondary effects, that by themselves would not create cancer, are induced by the carcinogenic agent. Progression has to do with the development of the tumour. For most cancers, it is difficult to identify the initial cause. However, advances in the field of molecular biology in the last 20 years have opened the possibility of exploring the contribution of a particular DNA lesion to the carcinogenesis process, and to a certain extent, of predicting its behaviour. In what follows, the most plausible theories concerning the processes that connect the primary radiation induced DNA damage with the initiation of carcinogenesis and its progress until the metastatic phase are presented.

The spectrum of all possible radiation induced DNA lesions ($\sim 3^{60}$ different types if each configuration of base damage, strand break, and undamaged nucleotide in a 30-bp section of DNA is considered [59]) can be conveniently divided into two broad types of damage: simple lesions and complex lesions. Simple lesions are those which can be repaired by the cell independently of all other DNA damage in the cell. Single-strand breaks (SSBs), individual base damages, and some types of clustered damage sites may be considered as simple lesions. Complex lesions are lesions that can interact in a pairwise fashion with other DNA damage present. The interaction can result in another type of lethal, non-lethal, or potentially repairable damage, which can also be repaired or misrepaired independently of other damage in the cell. Double strand breaks (DSBs) are the prototypical example of a complex DNA lesion. The break-ends associated with two different DSBs may interact in pairwise fashion to form a lethal or non-lethal chromosome aberration. Alternatively, the break-ends associated with a single DSB may be misjoined through non-homologous end-joining (a type of DSB repair) to form a point mutation. Figure 6 indicates configurations of damage sites forming a SSB and a DSB. The intrinsic repair properties of each kind of configuration may, in principle, be different. For example, the repair of a SSB is less error-prone than the repair of a DSB. It is important to note that it has been estimated that $\sim 45\%$ of the SSBs formed by low-energy electrons are accompanied by additional base damage, i.e. they are in reality complex lesions [60].

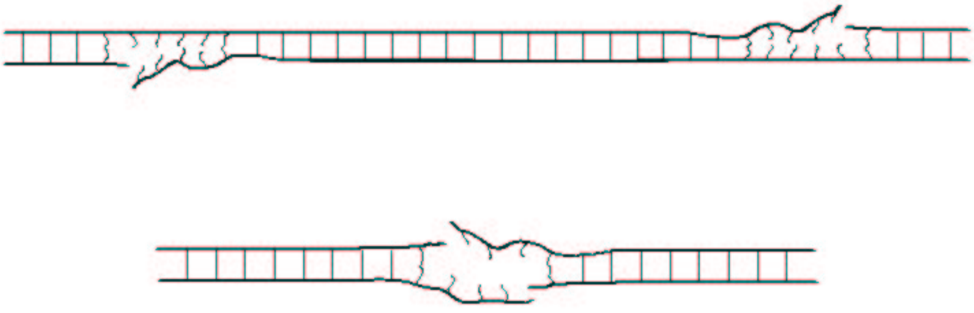

Figure 6: Single (top) and double (bottom) strand breaks. A double strand break is formed when two or more strand breaks are formed in opposite strands of DNA within about 10 to 20 base pairs of each other. The lines between strands of DNA represent hydrogen bonds between complementary base pairs.

For decades, the most widely accepted view of how cancer begins has been that cumulative mutations resulting from damage to the cell's DNA affect two kinds of cancer genes: the tumour suppressor genes, that normally restrain the ability of cells to divide, thus ensuring the integrity of the genome, and the oncogenes, that stimulate the cell to reproduce. Mutations in tumour suppressor genes cause growth-inhibiting proteins encoded by these genes to disappear, allowing the cell to survive and continue dividing in the absence of their signal. At the same time, mutations to oncogenes cause oncoproteins to become hyperactive, prompting the cell to grow ignoring the chemical message coming from the squeezed adjacent tissue that would normally stop the cell division. The excesses of oncoproteins and lack of tumour suppressor proteins lead mutant cells to reproduce excessively. After many rounds of mutations and expansion, one cell in the mass of mutants breaks free of all restrictions to its growth and the colony invades adjacent tissue in the host organ. In the last stage of its evolution, the cancer leaks metastatic cells into the bloodstream, which form new colonies at distant sites throughout the body and, thus, ultimately interfere with life-critical functions.

As the list of supposed cancer-related mutations has grown to more than 100 oncogenes and 15 tumour suppressors, and the rate at which such apparent molecular markers are being identified continues to increase rapidly, the oncogene/tumour suppressor gene hypothesis has been abandoned. More recently, three alternative theories have gained attention. One postulates a dramatic increase of the accumulations of random mutations (10^4 to 10^5 per cell) throughout the genomes of precancerous cells due to erroneous synthesis or repair of damaged DNA. Counting random mutations (scientists have to compare the genome of each individual cell letter by letter) has only recently become possible. The other two theories focus on the role of aneuploidy, i.e. the suite of large-scale chromosomal aberrations, including chromosomes with truncations, extensions or swapped segments. In the first theory, called 'early instability' and proposed by Lengauer *et al.* [61], 'master' genes, whose function is critical for cells to correctly reproduce, are disabled so that, when chromosomes duplicate during cell division, mistakes occur and the aberrations get worse with each generation. The second theory, called 'all-aneuploidy', put forth by Duesberg *et al.* [62], assumes that cells may become malignant before any master genes, oncogenes or tumour suppressor genes are mutated, the so called 'aneuploid cells'. Breaks appear in the double helix, destabilizing the genome further. The more aneuploid the cell, the more unstable it is, dying as a result. However, a few of these cells survive, acquiring a mix of aberrant chromosomes that convey one or more of the super powers of cancer cells and allow these to multiply into a precancerous tumour.

Although the theories presented above may not be completely independent, it is important to determine which of the ideas described above is more correct than others because they each make different predictions about the type of therapy that will succeed best against the most common and lethal types of cancer. For this reason, several topics such as modifications in chromosomes (cause and consequence), the role of telomeres (i.e. gene-free complexes of DNA and protein that protect the ends of each chromosome), possible signal molecules, damage to the cellular membrane and oxidative damage have been found to be of particular importance in the "Low Dose Risk Models" project [23].

From the discussion above, it is clear that modern carcinogenesis biological models point to the crucial role of damaged DNA in the origination of cancerous cells. Understanding how ionizing radiation interacts with living matter by studying the different mechanisms that lead to DNA damage, as well as the processes which, at different levels, result in biological effects (e.g. cancer), is of fundamental interest in the radiation research field. Therefore, the understanding of radiation induced carcinogenesis will greatly benefit from the development and validation of mechanistic models that accurately describe the interaction processes between ionizing radiation and living matter at all levels, especially in the cell's nucleus because of its relation to carcinogenesis, through damage induced to the DNA contained in it. Thus, detailed knowledge of the mechanisms leading to DNA damage can be expected to provide important insights into the relationship between dose (quantity, i.e. amount of energy deposited, and quality, i.e. type of radiation and energy) and the observed biological effects mentioned above. In this respect, several authors [63-65] have stressed the importance of appropriate modelling and simulation in the interpretation and prediction of radiation effects.

Mechanistic models represent an invaluable tool for testing the assumptions made for the intermediate interaction steps that lead from the initial DNA damage state to the observable biological radiation effects. For specific steps, most of our present understanding relies mostly on theoretical approaches such as, for example, for the early sub-picosecond events, the period between 10^{-15} and 10^{-12} seconds corresponding to the physico-chemical stage when radical formation takes place. This mainly involves low energy (< 20 eV) secondary electrons, and low energy (< 5 eV) secondary ion (and neutral) fragments. Only recent experiments have confirmed that the secondary electrons initiate DNA strand break formation via dissociative electron attachment[7]. However, the subsequent damage induced by these dissociative electron attachment ion fragments in DNA, or its basic components, is still unknown.

---

[7] decay channel of a transient negative ion (resonance) that leads to the production of a stable anion and a neutral radical.

Model development must also be supported by the development and application of appropriate experimental techniques that can provide the data necessary to test the validity of the model's predictions. Ottolenghi *et al.* [65] have pointed out that the formulation of more detailed models has often gone in parallel with the development and application of more accurate experimental techniques that can provide detailed information of not only the later stages of radiation damage, but also of the important intermediate steps. Such knowledge is very useful for refining and validating the mechanistic models proposed to quantify the effects of the interaction of radiation with the DNA molecule. This validation also contributes to make the models more accurate in their prediction capability and reduces the need for fitted parameters, which, in most cases, have no clear biophysical significance. A number of authors are currently carrying out intense research on this broad topic, e.g. [42-44,66-70]. These efforts can provide the tools necessary to reliably interpret experimental results, thus contributing to a more in-depth understanding of different DNA damage mechanisms (see Section 2.2.2). They can thereby also serve to guide for the development of more advanced experimental techniques, as well as the safe and effective planning of radiotherapy treatments.

2.2.2 Physico-chemical molecular mechanisms of primary DNA damage

In the living cell, ionizing radiation can cause primary DNA damage by either direct interaction (e.g. ionisation of DNA) or indirect (reaction of DNA with the free radicals formed in the neighbouring medium such as $OH^{\bullet}$, e^{-}_{aq}, $H^{\bullet}$, protein- and gluthatione-derived radicals). For quite some time, the extent to which one or the other mechanism controls the overall biological effects has been a matter of controversy. In terms of experimental evidence, most available data refer to DNA exposure under aqueous conditions and indicate that indirect interactions are the primary cause of DNA damage [71, 72], evaluated to be about 66% [73]. However, the magnitude of the effects produced by the scavenger intracellular material, present in the medium in the form of various proteins that influence the course of a chemical reaction by ready combination with free radicals, is yet unknown. In order to fill the gap between the early interaction events and the final biological effects described in the previous section, computer-aided modelling has proven to be a powerful technique for the accurate simulation of the various temporal stages of radiation interaction with living matter.

A: Direct interactions

The initiation of radiation damage to a living cell begins with the physical stage when, according to its energy, ionizing radiation interacts with biological molecules through various scattering and/or absorbing mechanisms. These processes take place in about 10^{-15}s. The radiation absorption mechanism not only provides the basis for radiation detection, it is also of particular importance in determining biological effects, because absorption of energy in the body tissue may result in physiological injury to the cell. Thus, a fraction of the kinetic energy of the incoming particle (in this case electron or positron) is deposited in the target medium during various interaction processes, therefore leading to a certain amount of particle energy loss. A quantity of central significance in all physics experiments involving accelerated particles and applications such as radiation diagnosis and therapy, is the *stopping power* of matter for penetrating charged particles, $(dE/ds)_{\mathrm{tot}}$, i.e. the mean energy loss per unit path length s:

$$\left(\frac{dE}{ds}\right)_{\mathrm{tot}} = \left(\frac{dE}{ds}\right)_{\mathrm{col}} + \left(\frac{dE}{ds}\right)_{\mathrm{rad}} \tag{1}$$

where $(dE/ds)_{\mathrm{col}}$ describes the collisional interactions such as ionisation and excitation, and $(dE/ds)_{\mathrm{rad}}$ gives the radiative losses such as bremsstrahlung.

- Ionisation, which is an interaction mechanism that results in the removal of one or more electrons from a given atomic or molecular shell, from valence orbitals to core levels, by transferring enough energy from the incoming particle to the target electron to overcome its binding energy. The atom or the molecule is left in an excited state which, depending on the electron's molecular bond, may determine further interaction or a break-up of the molecule. The electron released from its position may receive at the same time enough kinetic energy so as to induce further ionisation events, thereby losing energy and being slowed down. For this reason, the ionisation process represents the most important mechanism in inducing primary DNA damage.

- Excitation, in which a system such as an atom or a molecule receives enough energy from the incoming particle to change into a configuration of higher energy (lower binding energy) than its ground state. In an excitation process, no ions are produced (or no electrons released). The lifetime of a system in an excited state is usually short. Depending on the characteristics and energy of the electron's molecular bond, molecular break-up may occur. The excited atom will eventually lose its excess energy by spontaneous or induced emission of a quantum of energy (such as a photon or a phonon), which usually undergoes other absorptive processes locally, or by molecular break-up. Thus, the excitation process plays an important role in the energy range below the ionisation threshold, and it can provide new insights into low-energy physics phenomena.

- Bremsstrahlung, which is a radiative energy-loss process resulting from the change in velocity of a free charged particle, such as en electron, when accelerated in the field of the atomic nucleus and the atomic electrons. Since bremsstrahlung is not quantized, photons of any wavelength from 0 to the energy of the free particle can be emitted. The bremsstrahlung process is enhanced for high-Z materials, with large Coulomb forces, and for high-energy electrons, which undergo more interactions before all their energy is lost.

A fundamental concept in particle interaction processes, which will be employed throughout the thesis, is the scattering cross section, i.e. the "effective" cross sectional area for interaction. The cross section takes on a statistical nature when a beam of particles is aimed at a target which is much smaller than the beam size, like in the Rutherford scattering experiment [74]. Thus, its value gives the time-independent probability for the occurrence of a particular interaction process between an incoming particle and the target (e.g. atom). Further, we consider a beam of monoenergetic electrons with energy E_0 and momentum κ_0, directed along the z-axis. The electron beam of N_{e} particles/(a.u[8].)^2 per second is uniformly incident on N_{t} target particles considered at rest and placed at the origin of the coordinate system. Then,

---

[8] A system of units of measurement used in atomic physics for describing the properties of electrons. The atomic units have been chosen such that the fundamental electron properties, the electron rest mass ($\mathrm{m_e}$), the elementary charge (e), Planck's constant divided by 2π ($\hbar$), and 4π times the permittivity of free space ($4\pi\epsilon_0$), are all equal to one atomic unit. In this system, Bohr radius is the atomic unit of length (a_0 =

the number of particles $N_{\rm i}$ with energies between $E_{\rm i}$ and $E_{\rm i} + {\rm d}E_{\rm i}$ scattered per second into the solid angle element ${\rm d}\Omega$, about the solid angle Ω determined by the polar and azimuthal angles (θ, ϕ) which define the direction of scattering relative to the incident direction, is given by

$$N_{\rm i}{\rm d}E_{\rm i}{\rm d}\Omega = d^2\sigma_{\rm p}(E_0, E_{\rm i}, \Omega)N_{\rm e}N_{\rm t} \tag{2}$$

where the index p denotes a particular interaction process leading to the final state i. The quantity ${\rm d}^3\sigma_{\rm p}/{\rm d}E_{\rm i}{\rm d}\Omega$ is known as the doubly-differential cross section (DDCS). By integrating over all angles of the scattered electron, the single-DCS, ${\rm d}\sigma_{\rm p}/{\rm d}E_{\rm i}$, can be obtained as

$$\begin{aligned}\frac{{\rm d}\sigma_{\rm p}(E_0, E_{\rm i})}{{\rm d}E_{\rm i}} = \int {\rm d}\Omega_{\rm i}\frac{{\rm d}^2\sigma_{\rm p}(E_0, E_{\rm i}, \theta, \phi)}{{\rm d}\Omega_{\rm i}{\rm d}E_{\rm i}} &= \int_0^\pi {\rm d}\theta \int_0^{2\pi} {\rm d}\phi\frac{{\rm d}\sigma_{\rm p}(E_0, E_{\rm i}, \theta, \phi)}{{\rm d}\Omega}\sin\theta \\ &= 2\pi\int_0^\pi \frac{{\rm d}\sigma_{\rm p}(E_0, E_{\rm i}, \theta)}{{\rm d}\Omega}\sin\theta{\rm d}\theta,\end{aligned} \tag{3}$$

The integration of the single DCS over the energy loss profile yields the integral scattering cross section, $\sigma_{\rm p}(E_0)$,

$$\sigma_{\rm p}(E_0) = \int {\rm d}E_{\rm i}\frac{{\rm d}\sigma_{\rm p}(E_0, E_{\rm i})}{{\rm d}E_{\rm i}}, \tag{4}$$

as function of the incident beam energy, E_0, for the interaction process p.

The total cross section is obtained by summing over all interaction processes p (e.g. ionisation, excitation, bremsstrahlung) and integrating over all scattering angles and energies:

$$\sigma_{\rm T}(E_0) = \sum_{\rm p}\int\int \frac{{\rm d}^3\sigma_{\rm p}(E_0, E_{\rm i}, \Omega)}{{\rm d}E_{\rm i}{\rm d}\Omega}{\rm d}\Omega{\rm d}E_{\rm i}. \tag{5}$$

Cross sections are obtained by experimental measurements and also calculated with suitable analytical models. Thus, the instrumentation and the experimental techniques used for measuring interaction cross sections of atoms and molecules by electron impact[9] have continuously evolved since the first attempts at the quantitative characterization of the scattering of electrons by atoms in 1921 by Ramsauer [75]. The significant achievements made, thanks to the use of improved techniques, have strongly motivated the development of quantum collision theory, which has, in turn, produced suitable analytical models to be used for describing individual processes which were averaged out in previous measurements.

The interaction processes defined above between an incident radiation beam and a target material result in an energy loss of the incident particle which is characterized by the linear-energy-transfer, LET, defined as the average energy deposited along the track of a particle per unit length. This parameter is, therefore, directly related to the dose. The concept of

---

$h^2/4\pi^2me^2 = 0.529177249\AA$) and Hartree is the Coulomb repulsion between two electrons separated by one bohr (1 hartree= e^2/a_0)

[9] Experimentally, the concept of electron impact is applied to the situation in which atoms or molecules in the vapour phase are bombarded with a beam of high-energy electron and their *impacts* are then recorded in a mass analyser as a spectrum of positive ions separated on the basis of mass/charge.

absorbed dose is used by various models for the calculation of the yields for DNA strand breaks due to direct interactions [76-79]. In these models, simple element track structure and stopping power theory are combined with a detailed three-dimensional geometrical model of the DNA molecules, in order to calculate the average energy deposition by fast charged particles. The distribution of the resulting states of molecular ionisation and excitation is taken as a Poisson distribution, given the stochastic nature of the energy deposition process during this physical stage (see Chapter 1). Despite the success of these relatively simple models to predict measured absolute yields of strand breaks from direct energy deposition, it is essential to consider more detailed mechanistic and molecular approaches and a higher degree of sophistication in modelling biological targets. It has thus become of prime importance to increase our understanding about radiation action mechanisms at various stages, in order to obtain an accurate picture about the hazard of low-LET radiation and the validity of the no-threshold hypothesis for radiation risk assessment.

Secondary particles generated after an interaction process such as those mentioned above, undergo further interactions with the biological matter until they reach equilibrium with the surrounding temperature. This takes about 10^{-12}s, a period called the pre-thermalization or the physico-chemical stage. At this stage, little is known about the way very low energy electrons further interact with the DNA molecule. Recent experimental measurements by Märk *et al.* [80] have demonstrated, by considering the scattering of low energy electrons by gaseous uracil, thymine, cytosine and deoxyribose, that even electrons with 'nearly zero' energy destroy deoxyribose very efficiently, producing a number of fragment ions. The electrons seem to exert their destructive power by attaching to one of the DNA's component molecules and thus causing the resulting negative ion to break down. Moreover, when using cloro-uracil, a compound similar to those used in chemotherapy, it has been shown that the effectiveness to breakup molecules by low-energy electrons increases about 100 times compared to the situation of ordinary uracil. Although experiments with actual DNA molecules in vivo with numerous closely attached water molecules indicate rather different effects than those using dilute uracil gas, the results concerning the effectiveness of low-energy electrons to damage the DNA molecule do certainly justify further studies. From the discussion above, it is clear that in order to be able to describe the detailed interactions of ionizing radiation at the molecular level, needed to calculate DNA strand break yields, extensive sets of DCSs, also for the low-energy domain, are required.

B: Indirect Interactions

The indirect action of ionizing radiation in biological systems, on the other hand, involves the radiation chemistry of liquid water molecules that surround DNA strands. During exposure to radiation, the primary products of water radiolysis are generated with a non-uniform spatial distribution owing to the inhomogeneous distribution of the initial energy loss. As a result of the energy deposition in the water molecules, ions (H^+, OH^-) as well as new chemical species, e.g. free radicals such as hydroxyl ($OH^\bullet$) and hydrogen ($H^\bullet$) radicals, are generated within the cellular complex:

$$H_2O \overset{rad}{\rightarrow} H_2O^+ + e^- \qquad \text{ionisation}$$

$$H_2O^+ \longrightarrow H^+ + OH^\bullet \qquad \text{hydroxyl radical formation}$$

$$e^- + H_2O \longrightarrow H_2O^- \longrightarrow H^\bullet + OH^- \qquad \text{hydrogen radical formation}$$

A free radical is an atom or a group of atoms with an unsatisfied electron valence pair. For this reason, radicals are electrophilic and unusually reactive, strongly oxidizing species capable of causing a wide range of biological damage. At this point in the time-scale, the basic physical mechanism is the diffusion of free radicals that may further react chemically resulting in biological damage. In water, free radicals can readily recombine to electronic and orbital neutrality. However, additional reactions occur (viz. radical transfer) that maintain a high concentration of free radicals:

$$\begin{aligned} H^\bullet + H^\bullet &\longrightarrow H_2 \qquad \text{hydrogen radical dimerization} \\ OH^\bullet + OH^\bullet &\longrightarrow H_2O_2 \qquad \text{toxic peroxid dimer} \\ H^\bullet + OH^\bullet &\longrightarrow H_2O \qquad \text{recombination} \\ H_2O + H^\bullet &\longrightarrow H_2 + OH^\bullet \qquad \text{radical transfer} \end{aligned}$$

Although the overall chemical stage in an irradiated cell can persist as long as a second or more, the early chemical events are also very fast processes spanning a range of time from 10^{-12} to 10^{-6}s. It is believed that almost all the damage not directly caused during the physical interaction process, which results mainly in double strand breaks, is due to the attack of the highly reactive hydroxyl radicals on the DNA chain [9]. They do so by extracting hydrogen from the deoxyribose group. In a similar manner, the organic matter, symbolized by RH, reacts with water radiolysis products in the following way:

$$\begin{aligned} OH^\bullet + RH &\longrightarrow R^\bullet + H_2O \\ H^\bullet + RH &\longrightarrow R^\bullet + H_2 \end{aligned}$$

Absorption of a sufficient energy in a direct ionizing process may also lead to radical formation that results in bond breaks:

$$\begin{aligned} RH &\overset{rad}{\rightarrow} RH^+ + e^- \\ RH^+ &\longrightarrow R^\bullet + H^+ \end{aligned}$$

The sensitizing effect of dissolved oxygen [81, 82] was already recognized by Schwarz, and some years later Gray *et al.* [83] measured the influence of oxygen concentration on the response of tissue to radiation. It is now well known that reactive oxygen species with greater stability and lifetimes are also created in the interaction of ionizing radiation with water or biological molecules:

$$\begin{aligned} H^\bullet + O_2 &\longrightarrow HO_2^\bullet \qquad \text{hydroperoxy free radical} \\ R^\bullet + O_2 &\longrightarrow RO_2^\bullet \qquad \text{organic peroxy free radical} \\ RO_2^\bullet + RH &\longrightarrow RO_2H + R^\bullet \end{aligned}$$

The last reaction is particularly important because it shows how, in addition, the organic peroxy free radical plays a role in transferring the radical from molecule to molecule, thereby causing damage at each encounter. Thus, a cumulative effect can occur, greater than a single ionisation or a broken bond.

In spite of the accumulated knowledge on radical formation and chemistry briefly introduced above, a series of important questions remain to be answered to fully understand the various stages of DNA radiation damage especially the role of low-energy electrons (i.e. track ends). To date, it has been shown that low-energy electrons in liquid water can influence the chemistry in a radiation track in the following ways:

(1) thermalized electrons can be captured by biologically active molecule such as DNA bases and form molecular hydrogen which cannot be suppressed by hydrated electrons or H-atom scavengers [84, 85];

(2) the large inelastic cross section at low energies would imply that $OH^{\bullet}$ radicals, yielded by each ionisation and excitation, are later moved apart, before the chemistry simulation starts. So far, there is no evidence for highly mobile H_2O^+ ions or electronic excitations extended over a number of molecules;

(3) low-energy electrons can cause optically forbidden molecular transitions which often have markedly different chemistry. Thus, the spin state of the radicals produced in an event can have a significant effect on the yields of scavenging [86-90];

(4) thermalized electrons influence the rates and yields of reactions between the hydrated electrons and the $OH^{\bullet}$ radicals or the H^+ ions; so far, the probability distributions of the electron thermalization range calculated using experimental energy loss cross sections for amorphous ice, differ from those obtained experimentally [91, 92];

(5) the final stage in the life of the low-energy electron - its immobilization by solvation [93-97] or by capture [98, 99] - can occur before the thermalization process is complete; solvated electrons are known to react only with the DNA bases (adenine, guanine, thymine and cytosine), which leads to point mutations.

Several theoretical approaches exist also for the calculation of the yields of the chemical species produced as a result of water radiolysis [100-102]. Advances in computer technology have allowed detailed studies that combine computer-generated track structure simulation, the stochastic treatment of species production and diffusion, and detailed DNA representation [67]. Moreover, modification of the indirect DNA damage effect due to the additional interaction with a radical scavenger, has been properly accounted for. The purpose of such complicated models is to discover how the chemical nature of radiation damage can be understood in terms of the fundamental physical processes involved.

Although the latest developed models overcome some of the detailed simulation difficulties through parameterization, additional aspects need to be considered according to Green *et al.* [87]. For instance, in the opinion of these authors, it is not possible to obtain an accurate picture of a radiation track without solving the problems related to the scattering and transport of low-energy electrons in condensed media. This may involve the reformulation of models currently used for electron scattering at low energies and the explicit incorporation of spin effects on spur[10] kinetics. Presently, one accounts for the latter by means of experimental

---

[10] isolated cluster such as free radicals

reactivity constants which permit the calculation of track structures that incorporate the optically forbidden transitions induced by low-energy electrons. No track model available is able to perform this by considering highly detailed information, and therefore, the development of more accurate models for track structure predictions becomes an interesting area for future research. The detailed modelling of the five low-energy interaction mechanisms listed above could also provide additional information that can be included in comprehensive biophysical simulation codes.

To this end, track structure has become an important tool in the modelling and calculation of the early effects of radiation in DNA damage induction and provides the experimentalists with the challenge of identifying the complex lesions influencing the damage processing until the final expression of malignancy. So far, the parameter sets used in the simulation codes developed by different research groups are in agreement with experimental data, but mixing of the different descriptions leads to unrealistic results [103]. This has indicated a strict interrelation of the various steps in the modelling of radiobiological damage induction. Presently, there are still important gaps between what is provided by a typical track structure code (the statistical distributions) and what is required to start the chemical model [64]. In this sense, the detailed physical behaviour of low-energy electrons in condensed matter, and the way this is translated into an initial configuration for a chemistry model with an adequate degree of certainty, remain to be addressed fully. In some cases, for example, the spin states of the clusters of radicals may also play a role in the chemistry, and hence, the need to understand such additional mechanisms of radiation damage and improve/generalize current microdosimetry concepts to include all significant effects at the nanometer scale. Although problems such as those listed above are not addressed in the present doctoral research, it is quite clear that the achievable accuracy in the calculation of the spatial distribution of the low-energy electrons themselves depends directly on the adequacy of the interaction cross sections and the particle transport algorithms employed.

2.3 Modelling Tools and Procedures

The various reported computational techniques used for dosimetric calculations depend on the size and spatial resolution of the sources and targets, considered in conjunction with the type and energy range of the radiation [104, 105]. As the dimensions of the target decrease from the centimeters of human organs to micrometers of small tumours and nanometers of cell and nuclear DNA, a different approach for the determination of the radiation dose is required. Thus, for the whole organ or for sources or targets bigger than some centimeters, the most important computational effort, concerning mainly diagnostic imaging and radioprotection purposes, is in the field of photon dosimetry. On the millimeter scale, on the other hand, photons can often be disregarded and β-particle or electron dosimetry is generally reported. As compared to other numerical and analytical approaches, direct calculations applying MC techniques are often considered at this level, because they allow media of inhomogeneous densities to be taken into account as well as the full simulation of the stochastic variation of particle-hits and energy deposition under extreme geometric conditions. At the nanometer level, viz. for single-cell dosimetry, α-particle and electrons (low-range β-particles or Auger electrons) are the principal radiation examined to study energy deposition in cell nuclei. At the DNA level, microdosimetric studies of Auger electrons and α-particles are often connected with the development of mechanistic models that describe the effects of the interaction of ionizing radiation with biological matter and give reliable predictions of the relation between dose and biological response measured in experiments. In order to understand cancer destruction, different MC codes are sometimes linked together considering detailed models, which separately take into account the physical, physico-chemical and chemical steps.

In spite of the advanced computational facilities available today, detailed studies of radiation transport properties based on analytical solutions of the Boltzmann transport equation still encounter considerable difficulties as soon as one departs from photons in homogeneous media or when finite geometries are involved. As an exact analytical solution is impossible without making gross approximations such as ignoring energy-loss straggling, large-angle single scattering and bremsstrahlung production, the MC technique has become a very powerful alternative to deal with transport processes due to its ability to accurately simulate the entire range of conditions encountered in almost any calculation concerning radiation transport. Thus, ever since the first publication in 1949 [106], MC methods have been successfully applied for quantitative analysis in surface electron spectroscopy [107-109], positron surface spectroscopy [110], electron microscopy [111], electron energy-loss spectroscopy [112], electron probe microanalysis [113], and for the design and quantitative use of radiation detectors [114]. Radiation dosimetry and radiotherapy [115] clearly represent a field in which accurate knowledge of radiation transport is required and also one which plays an important sociological role. Thus, MC methods are nowadays extensively used for radiation dose calculations due to their ability to accurately predict dose for the entire range of conditions encountered, for example, in the treatment of cancer. The true power of the MC method is reflected when the radiation is transported from one medium into another, across complex shaped boundaries. This method can correctly characterize beams of photons, electrons and neutrons emerging from linear accelerators, as well as characterize the photons and electrons emerging from Auger (^{32}P, ^{89}Sr, ^{89}SrCl$_2$, ^{125}I, ^{153}Sm) or α-particles from brachytherapy (^{210}Po, ^{226}Ra, ^{238}Pu, ^{241}Am, ^{252}Cf) sources. It can further accurately simulate the transport of particles through beam shaping devices or source shielding devices. The transport of the resulting particles through the patient may then similarly be simulated, taking into account surface irregularities and the internal structure of the patient, including any metallic implants and prostheses, to determine the deposited dose.

The MC method has thus proven to be the most direct and, at the same time, the most versatile tool for the simulation of a great number of primary particle transport events, called histories, in matter. Various MC codes, based on detailed analytical models for the cross section calculation and sophisticated particle transport theories, have been developed in recent years to suit relatively well the different types of irradiation conditions encountered in practice and via appropriate modelling of the structure of the irradiated system. The importance of improving upon the present physics models and the accuracy of the cross section data has, however, been stressed upon, especially in the energy range below 100 eV. Furthermore, the need has also been pointed out for developing algorithms that can treat the transport of particles in materials in a more efficient way. In the following subsections, examples of the basic tools currently available are briefly described. Those used in the course of the present doctoral research are presented in somewhat greater detail in Section 2.4.

2.3.1 Codes for calculation of cross section data

The code PSICRO [116-118] has been developed at PSI in order to calculate different types of differential and integrated scattering cross sections (e.g. elastic, inelastic, bremsstrahlung) and other data (e.g. secondary particle energy and angular distributions), for various charged particles (e.g. electrons, positrons, protons and heavy-ions) in the energy range from 1 eV to 100 GeV for neutral atoms of $Z = 1 - 100$. Details of the physics algorithms implemented for the calculation of cross section data will be given in Chapter 3, together with the developments made during this thesis work. The code consists of a source file (the main program and a number of 133 subroutines) and several numerical data files. The description of the structure, of the arguments requested by the input file and of the operation of the code is made in the next section. Examples of input and output files are given in Appendix A.

The program ELSEPA (ELastic Scattering of Electrons and Positrons by Atoms) [119, 120] is a Fortran77 code used for the calculation of the elastic scattering of electrons and positrons by atoms and positive ions. ELSEPA implements robust numerical solution methods and computes differential and integrated cross sections, and scattering amplitudes. This code has been developed by the radiation physics group of the University of Barcelona, Spain. A detailed description of the physics models behind, their numerical implementation and of representative results obtained are also provided.

2.3.2 Monte Carlo codes

The MC particle transport codes available today can be divided into two classes: one dedicated to research and development (are very accurate but require a long simulation time) and a second category of codes suitable for therapy treatment planning (have the advantage of being quite fast). In the research area, codes are developed for particle transport either at the macrometer level (i.e. general purpose MC codes), or at the micrometer and nanometer level (i.e. track structure MC codes). These are illustrated by the examples given below.

A: Track structure MC codes

Track structure MC simulations provide stochastic geometric patterns of energy deposition depending on the energy and type of particles, which determine the distribution of energy transfers in the irradiated medium [121]. A simulated microscopic track structure is formed by a series of energy losses of the primary particle and all the subsequent particles resulting from their interaction with matter along the path of the particles. The use of this technique yields quantities which estimate dose and energy deposition by sampling the track structure within the sensitive target volume (cell, sub-cellular structure or group of cells). These quantities provide basic information about the structure of the statistical distributions of energy transfers on the scale of simulated biological targets, and are thus theoretically capable of resolving the limitations encountered in analytical calculations. Such information is very valuable for biophysical modelling [19, 20] and can be correlated to models of biological response or used as basic information relevant to mechanistic biophysical modelling, e.g. DNA damage models.

Particle track structure calculations are applied, in particular, at low energies (where the number of electron interactions per track is relatively small, say, up to few hundred) for the simulation of the track ends of electrons which are important in radiation biology. However, relativistic energies are also of interest, especially concerning the effects of high-energy heavy ions from galactic cosmic rays (HZE particles) in space radiation physics. Such calculations specify every interaction, ionisation or excitation process, in terms of spatial coordinates, the amount of energy transferred, and the emission angle for leaving particles. To achieve such a degree of detail, reliable interaction cross sections are needed, and these are obtained from experimental data or from theoretical models. The lack of accurate basic physical data and the corresponding uncertainties for the energies and the biological media of interest are the main imitations of track structure calculations. The cross sections needed for transport simulations in cellular and subcellular sized regions of matter are usually available only for water. Work on this topic is currently an active area of research [23,122-131]. In the past few years, work has been also carried out to calculate elastic and inelastic scattering cross sections for the DNA bases [132, 133].

Recently, improvements have been reported in track structure simulation codes, which make possible an event-by-event description of tracks for photons, electrons and light ions in liquid water, along with the addition of the time-dependent chemical development of tracks [134]. These codes offer advantages over other approaches because they allow to consider all stochastic aspects of radiation-induced DNA damage. The application of such tools to the simulation of the irradiation of a cell nucleus, assisted by up-to-date cross section data for liquid water, detailed target description that considers the atomic structure of DNA, and advanced models that can account for the link between the physical and chemical stages of DNA damage, could provide a valuable detailed description of the status of DNA in the cell nucleus after irradiation. Such information could then be used as input for models that simulate damage at the chromosome level up to 10^{-6}s after irradiation [65].

As an example, a series of MC codes such as OREC [36], MOCA [22, 38, 39], KURBUC [40], and CPA [41], have been developed in order to carry out track structure MC simulations and are appropriate for performing detailed radiation-induced DNA damage analyses based on stochastic energy deposition patterns. A revised version of the code OREC, renamed NOREC Semenenko03, has been also made available, in which the original elastic scattering cross sections are replaced by the current ones from the National Institute of Standards and Technology (NIST). Such codes have proved to be suitable for incorporating various models that can describe the processes taking place during the physical, physico-chemical and chemical stages leading to DNA damage.

The biophysical code PARTRAC [42-44,131,136,137] couples detailed simulation descriptions of both the physical and chemical stages of track structures of photons and electrons in liquid water. This code can treat targets at five levels of organization, from nucleotides to chromatin-fibre loops, which can be connected to build the chromosome structure. The information provided by the code is very diverse and includes yields of single and double strand breaks, distribution of DNA fragment lengths, yield of specific mutations, etc.

B: General purpose MC codes

Other available MC codes that can be used for particle tracking and energy deposition in micro-scale, and even more specifically in macro-scale targets, are GEANT [33], GEANT-PSI [28] (developed from the original Fortran code GEANT (version 3.15)), EGS4 [27], MCNP [31] and PENELOPE [34].

At present, the simulation of high-energy (above 1 MeV) charged particle transport is not feasible using detailed track structure MC codes if the particle slows down all the way until reaching the thermal equilibrium. Instead, one of two different types of algorithms are employed, viz. either condensed history (Berger's Class I procedures [47]), which model the continuous slowing down of the interacting particles in matter, or mixed (Class II [47, 138]), which combine continuous slowing down with detailed simulation of the interaction of the particles with matter. Class I algorithms (ETRAN [30], ITS system [139], MCNP [31]) rely on major predetermined energy steps to simulate the interactions, with an equidistant ratio for the energy before and after a step. The emission of electrons due to ionisation, as well as of γ-rays due to bremsstrahlung, is determined by randomly selecting the reaction type at the end of each substep. Both the energy loss and the angular deflection of the particle, after travelling a predetermined step, are sampled from multiple-scattering probability distribution functions. The main drawback of Class I algorithms is when dealing with interfaces. In order to better deal with this problem, Class II algorithms (EGS4 [27], GEANT [33], PENELOPE [34]) introduce a cut-off value so that only collisions with energy-loss and angular deflection below this cut-off are grouped together and described with the help of multiple-scattering theories. The rest are called "catastrophic" (hard) collisions and are simulated in detail (event-by-event). For instance, in GEANT [33], the step length corresponding to the distance between hard events, is determined by a "reduced" cross section for ionisation. With these "reduced" cross sections, the emission of electrons is considered only above a given energy cut-off so that the Class II algorithm enables a purely stochastic emission of electrons. The energy of the low-energy electrons is included into the energy straggling and deposited locally at each energy step. In order to improve the calculational efficiency and accuracy of MC simulations, the development and implementation of a new multiple-scattering algorithm, which accounts also for the effect of inelastic scattering on the multiple-scattering distributions, has been considered necessary. A few examples of general-purpose MC codes are given below.

• Although not strictly a track structure code, the object-oriented simulation system code GEANT [33], developed and maintained by CERN, is a general-purpose program that can also provide a detailed description of energy deposition and model the different stages of DNA damage. Its capabilities include a very powerful kernel, extensive but transparent physics models and several auxiliary capabilities (e.g. the ability to visualize the detector, particle trajectories and hits, etc.). The code has been designed for considering elements, compounds and mixtures and a variable spatial grid. It can handle 50 particle types (gamma, electron, positron, proton, etc.) and 62 ions (^{6}Li, ^{12}C, ^{88}Sr, ^{31}P, ^{238}U, etc.). Photons and neutrons are transported in a detailed manner, and the condensed history method based on the Class II algorithm is employed for charged particle tracking. The energy limits for photon and charged particle transport lie between 250 eV and 10 TeV. Atomic cross section data libraries, for photons (EPDL - *Evaluated Photon Data Library*) [145] and electrons (EEDL - *(Evaluated Electron Data Library)* [146], were developed at Lawrence Livermore National Laboratory (LLNL). Photon data include coherent and incoherent scattering, total photo-effect, photo-ionisation by sub-shell, pair and triplet production and, for electrons and positrons, the data contain elastic scattering, ionisation, excitation, bremsstrahlung and annihilation into one or two photons (for positrons).

• The Fortran code GEANT-PSI [28], based on the GEANT v. 3.15, is maintained and upgraded at PSI. The code is essentially identical in its performance to the current CERN version in most respects, except that new data libraries have been attached that provide the possibility to go down to 1 eV for photons, electrons and positrons. In addition, detailed simulation of charged particle transport can be performed. Efforts have been made during the present research to bring down the energy limit to 1 eV [116-118].

- EGS4 i.e. Electron-Gamma-Shower [27], originally developed at the Stanford Linear Accelerator Center (US) for high-energy physics applications and extended later in collaboration with the National Research Council of Canada (NRC) to lower energy applications, is actually a general purpose package for MC simulation of the coupled transport of electrons and photons in an arbitrary geometry for particle energies from a few keV (1 keV for gamma and 10 keV for charged particles) up to several TeV. The EGS code is sometimes referred to as the 'de facto' standard tool for clinical radiation dosimetry. It is designed for radiation transport in any element, compound or mixture and for macrometer as well as micrometer ranges of grid intervals. The data preparation package, PEGS4, creates data to be used by the code, using cross section tables for elements Z=1 to 100. Both photons and charged particles are transported in steps of random length rather than in discrete steps. The implemented transport procedures are the detailed method for simulating photon interactions and the Class II algorithm for condensed history tracking of charged particles (purely stochastic emission of particles). EGS4 can also simulate the transport of particles in magnetic or electric fields by implementing a specially designed subprogram to take into account the influence of these fields.

- MCNP [31], i.e. MC N-Particle, has been developed and maintained at the University of California, Los Alamos National Laboratory. The code can be used for neutrons (0 - 20 MeV, with data available up to 150 MeV for many nuclides), photons (with initial energy from 1 keV to 100 GeV) and electrons (1 keV - 1 GeV), or coupled neutron/photon/electron transport, including also the capability to calculate eigenvalues for critical systems. The code treats an arbitrary three-dimensional configuration of materials - any type of element, compound mixture - in geometric cells bounded by first- and second-degree elliptical tori, for macrometer as well as for micrometer ranges of grid intervals. For photons, the code accounts for incoherent and coherent scattering, the possibility of fluorescent emission after photoelectric absorption, absorption by pair production with local emission of annihilation radiation, and bremsstrahlung. The transport procedure includes a detailed simulation method for photon interactions and the Class I algorithm for condensed history tracking of charged particles. An extensive collection of cross section data based on LLNL libraries is the important standard feature which makes MCNP very competitive.

- PENELOPE [34], acronym for PENetration and Energy LOss of Positron and Electrons, is a code system for the MC simulation of electron, positron and photon transport in arbitrary materials composed of elements with atomic numbers from 1 to 92, and which is developed and maintained at the University of Barcelona [140-142]. The code is designed for the radiation tracking of photons with initial energy from 1 keV to 1 GeV and electrons from 100 eV to 1 GeV. The ability to transport charged particles to low energies and through materials other than water, opens up the possibility of using PENELOPE, a general-purpose MC code system, for applications in micro- and nanometer ranges of grid intervals. The atomic cross section data are based on very detailed physics models for coherent and incoherent scattering, total photoeffect and pair production (for photon data), elastic and inelastic scattering and bremsstrahlung (for electrons and positrons). The code uses a detailed simulation method for the transport of photons and both detailed as well as so-called mixed (Class II) simulation algorithms for charged particle transport simulations [140, 141]. For these reasons, PENELOPE can be particularly useful for applications that are computationally too intensive for even-by-event MC, e.g. *in vivo* microdosimetry of spatially complex distributions of radioisotopes inside the human body. PENELOPE is described in greater detail in Section 2.4.2, while in Chapter 5 of the thesis we present the new modifications and updates implemented in the code in order to obtain a rapid and accurate assessment of the DCSs available in tabular format for given incident energy and angular scattering grids.

C: MC codes for therapy treatment planning

PEREGRINE [143] is an example of the second category of MC codes, viz. those designed specifically for radiation therapy treatment planning. Developed and maintained by Lawrence Livermore National Laboratory, PEREGRINE is a 3D MC code meant to calculate dose distributions for photon, electron, fast neutron and proton therapy by directly simulating particle transport through both the beam delivery system and the patient. CT Scans are used for the exact location of the tumour and sensitive structures, and maps of the density and elemental composition of all materials in the vicinity of the beam are derived with both high accuracy and high spatial resolution. The code uses LLNL cross section data libraries, the world's most extensive nuclear and atomic cross section databases (ENDL - *(Evaluated Nuclear Data Library)* [144], EPDL [145], EEDL [146]), which were extended for the PEREGRINE project to 250 MeV for biologically important elements (for proton and fast neutron therapy applications). Dose algorithms to treat sources from first principles are implemented. Each given accelerator, together with collimators, apertures, blocks and wedges, is fully modelled during a PEREGRINE calculation to ensure accurate representation of the radiation source.

2.4 Description of the Tools Used and Further Developed

In this section, the structure of the code PSICRO [116, 117], used and currently further developed for calculation and validation of cross section data, and the code PENELOPE [34], used for MC simulation of charged particle transport in various materials, are described in somewhat greater detail. In the case of PSICRO, emphasis is placed on the low-energy aspects (down to 1 eV incident particle energy) related to the present research.

2.4.1 PSICRO code for cross section data calculation

The program package PSICRO, developed at PSI and further extended in the course of this thesis, has been used for the generation of cross section data, and of angular and energy spectra for electrons and positrons scattered by neutral atoms of atomic numbers between Z=1 and 100. The code consists of a collection of FORTRAN77 subroutines, integrated through a main driver program, that implement the physical models described further in Chapter 3. A set of numerical data files containing evaluated data for different types of electron and positron interactions are also combined through an input file in the manner required by the input data stream of PSICRO. Based on these models and on the evaluated databases, PSICRO generates differential and integrated cross sections in a format that can be used by MC simulation codes.

The main parts of the code PSICRO are indicated in Fig. 7 and described briefly below (the flowchart also gives additional information about the calls to the individual subroutines):

`PSICRO.F`: contains the main program and the subroutines that implement the physical models for the calculation of differential and integrated elastic, inelastic and bremsstrahlung cross sections for electrons and positrons scattered by atoms with atomic number from Z=1 to 100. In addition, cross sections for positron annihilation, which takes place at very low energies, are also calculated by this program.

`PSICRO.IN`: input file for the code PSICRO, which combines the evaluated datasets and also contains the details of the type of calculation to be performed (an example of `PSICRO.IN` is given in Appendix A). The code input arguments and the different options available are described in Table 1.

Table 1: Input arguments of the code PSICRO. Their values specify the name of the output file, the date, the type of projectile, and the atomic numbers of the first and the last elements for which the calculation of the cross section data is made.

Argument	Values	Description
ELDL		Output library name
IDATC		The date
IPART	2	positron
	3	electron
	4	proton
	5	α-particle
NELEM1	1 - 100	Z - of first element
NELEM1	1 - 100	Z - of last element
IZ		Number of atom of Z=IZ
IRHO		1 - Condensed density to be taken from `PSICRO.RHO` file.
		2 - Gaseous(vapour) density to be taken from `PSICRO.RHO` file.

`PSICRO.RHO`: file containing the potentials and material densities; this file also has the atomic weight of the target atom IZ.

`EADL.DIR`, `EADL.BIN`: Evaluated Atomic relaxation Data Library [147], external direct and binary file including data to describe the relaxation back to neutrality of ionized atoms (due to either photoionization or electroionization), during which photons (fluorescence X-rays) and electrons (Auger and Coster-Kronig) are emitted (e.g. number of subshells, number of electrons, binding energies, kinetic energies of electrons and subshell radii).

`EEDL.DIR`, `EEDL.BIN`: Evaluated Electron interaction Data Library [146], external direct and binary file including data to describe the transport of electrons (elastic scattering, bremsstrahlung, excitation, and electroionization subshell cross sections), as well as the initial generation of secondary particles, such as the primary photon due to bremmstrahlung, as well as the primary electron due to inelastic scattering and electroionization.

`EPDL.DIR`, `EPDL.BIN`: Evaluated Photon interaction Data Library [145], external direct and binary file including data to describe the transport of photons (photoionization, photoexcita-

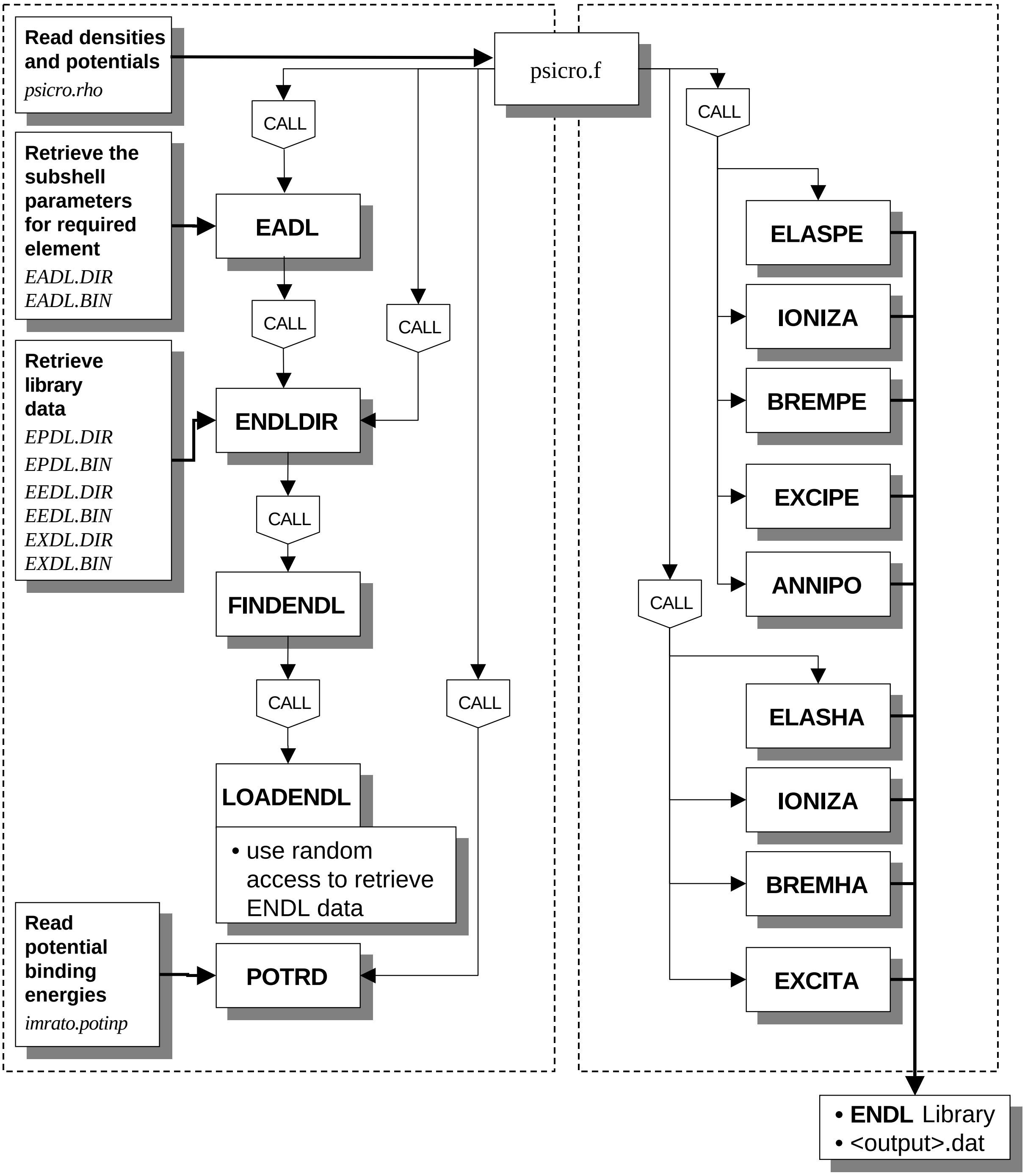

Figure 7: Flowchart of the cross section generation code PSICRO.

tion, coherent and incoherent scattering, and pair and triplet production cross sections).

`EXDL.DIR`, `EXDL.BIN`: Evaluated Excitation Data Library, external direct and binary file including data to describe photoexcitation lines.

The evaluated data libraries described above span atomic numbers from 1 to 100 and cover incident particle energies ranging from 10 eV to 100 GeV. As the main purpose of these libraries is to furnish data for particle transport calculations, these files have been originally released by LLNL for external distribution in a machine independent format. In a complete coupled electron-photon transport analysis, results from all the data files are required. Details of the physical models which describe the interaction of electrons and positrons with groundstate free atoms are given in Chapter 3. Their numerical implementation in the code PSICRO is realised in five main subroutines, namely `ELASPE`, `IONIZA`, `BREMPE`, `EXCIPE`, and, for positrons, `ANNIPO`. The description of the structure of these subroutines for each interaction will also be provided in greater detail by Chapter 3.

Subroutine `ELASPE` calculates elastic scattering cross sections and angular distributions for an incident electron or positron, and a target atom of a given atomic number Z, atomic mass A and density ρ (electrons per unit volume). In the low energy range from 1 eV to 1 MeV, the relativistic (Dirac) partial wave analysis is applied. At higher energies, at which the partial wave model would yield extremely large numbers for the required partial shifts, a factored cross section, in which the screening effect is treated separately from relativistic and spin effects is used. Thus, `ELASPE` makes use of two additional subroutines: `PWADIR` for partial wave analysis, `MOTT` for Mott-to-Rutherford calculations, when the partial wave model cannot be used (for further details see Chapter 3). The physical models applicable to elastic scattering of protons and alpha particles is implemented in the coresponding subroutine, `ELASHA`.

Subroutine `IONIZA` calculates cross sections and energy distributions for ionisation by a positron or electron in an element of atomic number Z. For this it employs the Weizsäcker-Williams method. For a proton or alpha particle, the corresponding subroutine is `IONIZA`.

Bremsstrahlung data for a positron or electron in the electrostatic field of an element of atomic number Z are obtained in the subroutine `BREMPE`. For protons or alpha particles, the corresponding subroutine is `BREMHA`.

Subroutine `EXCIPE` generates excitation cross sections for electrons and positrons, and the average energies and angles of the photons and scattered electrons/positrons for elements based on their atomic number Z, atomic mass A and density ρ. For a proton or alpha particle, the corresponding subroutine is `EXCITA`.

For positrons, anihilation cross sections into one (with the K-shell bound electrons only) or two photons in an element of atomic number Z are generated by the subroutine `ANNIPO`.

The calculations are coordinated by the main program in `PSICRO.F` which, based on the information in `PSICRO.IN`, manages the input of evaluated data, selects the appropriate models to use and, finally, outputs the information required by the input options in Table 1.

The calculated results are delivered in two types of outputs files: a library of data generated in the Evaluated Livermore Data Library (ELDL) format, and a text file, with the extension .DAT, containing tables of differential and integrated cross section data in ASCII format. The size of the data tables included in the output files has been minimised by presenting only those values that are required to allow log-log interpolation between the tabulated values for all quantities with an accuracy of 1%. For coupled electron/positron-photon calculations, the newly generated ENDL file is completely consistent with the EPDL97 [145] and EADL [147] libraries. Therefore, these cross section files can be further used with various MC codes, e.g. PARTRAC, GEANT, etc.

2.4.2 Monte Carlo code system PENELOPE

As mentioned in the introduction, various applications in radiation chemistry and radiobiology have shown the necessity to simulate the details of the tortuous paths of very low-energy electrons in condensed matter [101, 134]. When confronted with a large number of interactions, or with complex 3-dimensional geometries, the code system PENELOPE offers the possibility of high simulation efficiency and accuracy. To achieve this goal, 'hard' collisions (large angle and large energy-transfer events) of electrons and positrons are simulated in a detailed manner, i.e. interaction by interaction, while 'soft' interactions are treated in a condensed form by using multiple-scattering theory [138], refined by using a continuous slowing down approximation (CSDA) model which accounts for energy straggling [141].

This section describes the main physical characteristics of the models used by PENELOPE to describe the transport of electrons and photons in matter. Various comments on the selection of algorithm parameters used in order to safely minimize the simulation time are made.

A complete PENELOPE application consists of the PENELOPE transport kernel, a series of Fortran77 routines that have to be called from the main program, and a set of user-supplied routines to record the location of energy transfer events, control the overall evolution of particle tracks and determine the geometry of the materials used in the simulation. For the simulation of the particle transport and interaction, PENELOPE uses a mixed (Class II) simulation algorithm, i.e. it simulates in detail (interaction by interaction) the effect of the so-called hard colisions (i.e. those collisions that dramatically change the direction and energy of the electron) and it uses multiple-scattering theories to describe the effect of the remaining, soft collisions. Moreover, PENELOPE uses the random hinge method, i.e. the global effect of the soft collisions between two hard events is simulated as a single artificial soft scattering event. The physical models and the cross sections implemented in PENELOPE have been described in detail elsewhere [140-142]. In order to achieve a high computational efficiency, PENELOPE uses a DCS model that has a physically reasonable shape, can be easily sampled by MC methods, and gives the correct behaviour for track segments formed by at least 15-20 hard collisions [141]. Sampling from the relevant cross sections, as well as the temporary storage of the secondary particles created during the transport of the primaries, are both automatically and transparently handled.

Coupled electron-photon transport simulations can be controlled by the user in PENELOPE with the help of several input parameters [141]: W_{CC} - the cutoff energy for hard inelastic collisions, W_{CR} - the cutoff energy for hard radiative events, as also C_1, and C_2 which determine the distance between hard elastic collisions (i.e. they can be selected in such a way that all events are treated as hard collisions). Hard elastic collisions are those with scattering angles θ greater than a given threshold θ_{c}.

The simulation of soft elastic scattering in PENELOPE is defined by specifying the mean free path $\lambda_{\rm el}^{(\rm h)}$ between hard elastic events defined by

$$\frac{1}{\lambda_{\rm el}^{(\rm h)}} = \mathcal{N} 2\pi \int_{\theta_{\rm c}}^{\pi} \frac{{\rm d}\sigma_{\rm el}(\theta)}{{\rm d}\Omega} \sin\theta \, {\rm d}\theta. \tag{6}$$

This equation determines the angle $\theta_{\rm c}$ as a function of $\lambda_{\rm el}^{(\rm h)}$. A convenient way to select the mean free path $\lambda_{\rm el}^{(\rm h)}$ is

$$\lambda_{\rm el}^{(\rm h)}(E) = \max\left\{\lambda_{\rm el}(E), C_1 \lambda_{\rm el,1}(E)\right\}, \tag{7}$$

where C_1 is a small constant (say, less than ~ 0.1) and $\lambda_{\rm el,1}$ is the elastic first transport mean freepath. The mean angular deflection in a path length $\lambda_{\rm el}^{(\rm h)}$ is

$$1 - \langle\cos\chi\rangle = 1 - \exp(-\lambda_{\rm el}^{(\rm h)}/\lambda_{\rm el,1}) \simeq C_1. \tag{8}$$

PENELOPE uses the following distribution $F_{\rm a}(\mu; s)$ to generate angular deflections in artificial soft elastic scattering events

$$F_{\rm a}(\mu; s) = a U_{0,{\rm b}}(\mu) + (1-a) U_{{\rm b},1}(\mu) \tag{9}$$

where $U_{\rm u,v}(x)$ denotes the normalized uniform distribution in the interval (u, v),

$$U_{\rm u,v}(x) = \begin{cases} 1/(v-u) & \text{if } u \le x \le v, \\ 0 & \text{otherwise.} \end{cases} \tag{10}$$

The parameters a and b are

$$b = \frac{2\langle\mu\rangle^{(\rm s)} - 3\langle\mu^2\rangle^{(\rm s)}}{1 - 2\langle\mu\rangle^{(\rm s)}}, \qquad a = 1 - 2\langle\mu\rangle^{(\rm s)} + b. \tag{11}$$

This simple distribution can be used when the number of hard collisions per electron track is large enough, say larger than ~ 10. By selecting a small value of the parameter C_1, this condition can be satisfied. The internal parameter `DSMAX` also defines the maximum allowed step length.

Soft stopping interactions are those with energy loss $W < W_{\rm CC}$ and emission of bremsstrahlung photons with $W < W_{\rm CR}$, where $W_{\rm CC}$ and $W_{\rm CR}$ are cutoff values. The quantities that define the algorithm for the simulation of soft energy loss are the mean free paths $\lambda_{\rm in}^{(\rm h)}$ and $\lambda_{\rm br}^{(\rm h)}$ between hard collisions and hard radiative events, respectively, the stopping power $S_{\rm s}$ and the energy straggling parameter $\Omega_{\rm s}^2$ associated with soft interactions. These quantities are given by

$$\lambda_{\rm in}^{(\rm h)}(E) = \left(\mathcal{N} \int_{W_{\rm cc}}^{E} \frac{{\rm d}\sigma_{\rm in}}{{\rm d}W} \, {\rm d}W\right)^{-1}, \tag{12}$$

$$\lambda_{\rm br}^{(\rm h)}(E) = \left(\mathcal{N} \int_{W_{\rm cr}}^{E} \frac{{\rm d}\sigma_{\rm br}}{{\rm d}W} \, {\rm d}W\right)^{-1}, \tag{13}$$

$$S_{\rm s}(E) = \mathcal{N} \int_0^{W_{\rm cc}} W \frac{{\rm d}\sigma_{\rm in}}{{\rm d}W} \, {\rm d}W + \mathcal{N} \int_0^{W_{\rm cr}} W \frac{{\rm d}\sigma_{\rm br}}{{\rm d}W} \, {\rm d}W \tag{14}$$

and

$$\Omega_{\mathrm{s}}^2(E) = \mathcal{N}\int_0^{W_{\mathrm{cc}}} W^2 \frac{\mathrm{d}\sigma_{\mathrm{in}}}{\mathrm{d}W}\,\mathrm{d}W + \mathcal{N}\int_0^{W_{\mathrm{cr}}} W^2 \frac{\mathrm{d}\sigma_{\mathrm{br}}}{\mathrm{d}W}\,\mathrm{d}W. \tag{15}$$

When the cutoff energies are small, straggling due to soft interactions is small and can be neglected. In spite of this, PENELOPE incorporates energy straggling due to soft interactions that allows us to use large cutoff energies W_{cc} and W_{cr} and therefore speed up the simulation process without distorting the energy distributions. The details of the distribution from which PENELOPE generates straggling can be found in the PENELOPE report (p.135) [34].

When soft energy-loss is considered, the mean free path $\lambda_{\mathrm{T}}^{(\mathrm{h})}$ varies with energy and may change along a single step. To overcome this difficulty, we can limit the length of the step to make sure that the average energy loss is much smaller than the kinetic energy E at the beginning of the step, and consider that $\lambda_{\mathrm{T}}^{(\mathrm{h})}(E)$ remains essentially constant along the step. The energy loss per step can be limited by re-defining the hard mean free path. Thus, if we wish to tolerate average fractional energy losses $\Delta E/E$ along a step of the order of C_2 (a small value, say, 0.01), we simply take

$$\lambda_{\mathrm{el}}^{(\mathrm{h})}(E) = \max\left\{\lambda_{\mathrm{el}}(E), \min\left[C_1\lambda_1(E), C_2\frac{E}{S(E)}\right]\right\}. \tag{16}$$

This effectively limits the average energy loss per step at the expense of increasing the frequency of hard elastic events. The parameters C_1 and C_2 determine the computer time needed to simulate each track. Ideally, they should not have any influence on the accuracy of the simulation results. This happens only when their values are sufficiently small.

In the PENELOPE manual [141], several suggestions for the 'safe' simulation parameters are made: C_1=0.001, C_2=0.01, $W_{\mathrm{CC}} = W_{\mathrm{RC}} = 0.01E_0$ (E_0 is the initial energy of the primary particle, electron or positron). The following values have been recommended when using PENELOPE for microdosimetry applications: $0 \leq C_1 \leq 0.02$, $0 < C_2 \leq 0.02$, 100 eV$\leq W_{\mathrm{CC}} \leq$ 500 eV, 100 eV$\leq W_{\mathrm{RC}} \leq$ 500 eV [148].

For a more detailed description of PENELOPE, including code structure, physical model description and use, the reader is directed to the references mentioned above.

3 Theoretical Models for the Generation of Interaction Cross Sections

In this chapter, electron and positron interactions with neutral atoms are presented in terms of DCSs per solid angle for all interactions that can produce both the deflection of the projectile and its energy loss, i.e. bremsstrahlung emission (known to be particularly important at high energies), as also elastic and inelastic scattering processes. For the analytical description of these interactions, various theoretical models are currently used. Each one of these analytical models has its specific limitations and range of applicability. Following short introductions, the more important theories available at present for the calculation of the DCSs are briefly described, with a certain emphasis on the approximations valid in the low-energy region. Thereby, the theoretical models implemented in the code PSICRO (see Chapter 2) for the calculation of bremsstrahlung, elastic scattering and ionisation cross sections are presented. Finally, a new model is developed for the calculation of electron and positron cross sections for excitation from the ground state of atoms, in the medium to low energy range.

3.1 Bremsstrahlung Emission

In the classical picture of a bremsstrahlung process (Fig. 8), the acceleration of the electron (or positron) with kinetic energy T_1, caused by the interaction with the electric field of an atom, gives rise to the emission of a photon of energy W which takes values in a continuous energy spectrum spanning between 0 to T_1. The interaction with the atomic field involves both the electric field of the atomic nucleus (electron-nucleus bremsstrahlung) and that of the atomic electrons (electron-electron bremsstrahlung). Bremsstrahlung cross sections are differential in the energy W and the direction of the emitted photon (the polar angle θ[11]), as also in the final direction Φ of the projectile. In addition, summation over the directions of the electron spin and photon polarization vectors is assumed.

In comparison with other energy-loss mechanisms such as ionisation or excitation, bremsstrahlung emission is dominant at ultra-relativistic energies, while in the keV region, despite its negligible stopping effect, the process still remains particularly important, because it is the source of continuum background X-ray spectra [149]. The accurate knowledge of these spectra is important for electron probe microanalysis (EPMA) and analytical electron microscopy, for the characterization of medical and analytical X-ray sources, for the dosimetry of high-energy electron beams and, in particular, for studies in radiation transport and the precise MC simulation of low-energy electron distributions.

3.1.1 Introduction

Detailed descriptions of the calculation of DCSs and related data for bremsstrahlung emission in the field of the atomic nucleus, as a result of electron and positron collisions with isolated

---

[11] If a spherically symmetric electrostatic field of the atom is considered, the angular distribution of the emitted photon is independent of the azimuthal emission angle which, for simulation purposes, is taken as uniformly distributed in the interval (0 to 2π).

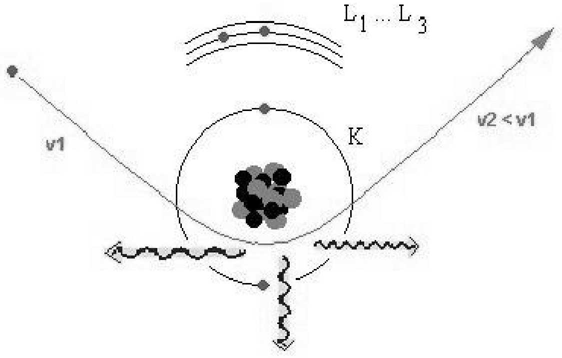

Figure 8: Bremsstrahlung emission *(http://microanalyst.mikroanalytik.de/info1.phtml).*

atoms, have been previously given in several general review papers, e.g. by Koch and Motz [150], Tsai [151] and by Pratt and Feng [152]. They provide the theoretical formulas (along with their specific limitations) in a form convenient for practical calculations, estimates of their accuracy when compared with experimental results, appropriate correction factors, as also considerations related to thick target bremsstrahlung.

We consider here a single bremsstrahlung emission process of a photon with energy W and momentum $\mathbf{k}$ due to the collision between an electron and an atom of atomic number Z represented by a fixed central potential $V(r)$. The initial and final total energies of the electron in the collision are given by $\epsilon_1 = T_1/\mathrm{m_e}c^2 + 1$ and $\epsilon_2 = T_2/\mathrm{m_e}c^2 + 1$ (in $\mathrm{m_e}c^2$ units) and the corresponding initial and final momentum of the electron in a collision by $p_1 = \sqrt{\epsilon_1^2 - 1}$ and $p_2 = \sqrt{\epsilon_2^2 - 1}$ (in $\mathrm{m_e}c$ units), respectively. The DCS (in units of cm^2) for the emission of a photon with energy between W and $W + \mathrm{d}W$, into an element of solid angle $\mathrm{d}\Omega_\mathrm{k}$, and for the outgoing electron scattered into an element of solid angle $\mathrm{d}\Omega_\mathrm{p}$, can be expressed by [150]

$$\mathrm{d}\sigma = \frac{(2\pi/\hbar)\rho_\mathrm{f}|H_\mathrm{if}|^2}{(p_1 c/\epsilon_1)}\left(\frac{\hbar}{\mathrm{m_e}c}\right)^3 L^3, \tag{17}$$

where the electron rest mass $\mathrm{m_e} = 9.109382616 \cdot 10^{-28}\mathrm{g}$, the velocity of light in vacuum $c = 2.99792458 \cdot 10^{10}\mathrm{cm/s}$, L is the side of the cubic volume considered for emission of the photon, $\rho_\mathrm{f} = (p_2\epsilon_2 W^2 \mathrm{d}W \mathrm{d}\Omega_\mathrm{k} \mathrm{d}\Omega_\mathrm{p} L^6)/(2\pi)^2/(\mathrm{m_e}c^2)$ represents the density of final states, Ω_k is the element of solid angle in the direction of $\mathbf{k}$, Ω_p is the element of solid angle in the direction of $\mathbf{p}$, and H_if is the transition matrix element of the system, given by

$$|H_\mathrm{if}|^2 = \left(\frac{2\pi}{k}\frac{e^2}{\hbar c}\right)(\mathrm{m_e}c^2)^2 \left|\int \Psi_\mathrm{f}^*(\lambda^* \cdot \alpha)e^{-i\mathbf{k}\cdot\mathbf{r}}\Psi_\mathrm{i}\mathrm{d}\tau\right|^2 L^{-9}, \tag{18}$$

where λ is the unit polarization vector of the photon, α represents the Dirac matrices, $\mathrm{d}\tau$ is the volume element, and Ψ_i and Ψ_f are the Dirac wave functions for the initial and final electron states, which describe the electron in a screened, nuclear Coulomb field.

Depending on which form of the Hamiltonian (Schrödinger or Dirac) is used for the electron and field system, nonrelativistic or relativistic calculations of the matrix element wave functions can be performed. In order to solve the Dirac wave equation, either approximate analytical solutions or numerical methods have been used. Cross section calculations have been carried out, so far, only for a gas of free atoms, considering

- nonrelativistic Coulomb wave functions for an unscreened Coulomb potential as used in Sommerfeld's theory [153]. This theory is expected to break down when the initial electron energy is greater than a few keV. Moreover, it disregards screening effects, which are important for very low energies and for targets with high atomic numbers.

- free-particle wave functions perturbed to first order in Z (Born-approximation theory of Bethe and Heitler [154-156]. In spite of the fact that this theory becomes less reliable when (a) the atomic number of the target increases, (b) the initial electron energy decreases, and (c) the photon energy approaches the high-frequency limit, the accuracy of the cross section is reasonably good and, in the worst cases, at least a correct order of magnitude can be obtained.

- relativistic Coulomb wave functions (Davies-Bethe-Maximon-Olsen DBMO model [157-159]) valid to first order in $(Z/137)^2/\ell$, where ℓ is the angular momentum quantum number. This theory includes the screening corrections to the Bethe-Heitler Born-approximation results [154] derived with the help of Furry-Sommerfeld-Maue relativistic Coulomb wave functions [160, 161]. It is valid only in the extreme-relativistic region (above 50MeV) when the energies of the electron, both before and after the collision, are large compared with the electron rest energy, but it fails in the high-frequency limit of photon emission (i.e. $W \rightarrow T_1$, the region where the incoming electron is brought to rest so that all its initial kinetic energy is completely converted into radiation).

With the currently increasing computer capabilities, more accurate results from first-principle calculations (numerical partial-wave analysis) have been made available by Pratt *et al.* [162, 163] and by Kissel *et al.* [164] for selected elements and projectile energies below 2 MeV. Given the multitude of methods mentioned above, it has been a common practice in MC simulations to use either the theory of Bethe-Heitler with empirical correction factors as recommended by Koch and Motz [150] for energies below 50 MeV [165], or that of Pratt *et al.* below 2 MeV with appropriate interpolation schemes between 2 MeV and 50 MeV, while for energies above 50 MeV, the DBMO theory with Coulomb correction has been employed. As mentioned above, coherence effects have not been taken into account until now. Such effects have been shown to usually have a very small influence [166] (except at energies below ∼1keV) but they become significant in crystals [167, 168].

Regarding bremsstrahlung in the field of atomic electrons, this has very often been treated in a very approximative manner due to the lack of reliable electron-electron bremsstrahlung cross section data. Thus, the angular distribution of emitted photons has been assumed to be identical to that of electron-nucleus bremsstrahlung. This assumption is not correct as (a) the screening of the field of atomic electrons is different from that of the nucleus, (b) the electron-electron cross section goes to zero in the high-frequency limit because of the Coulomb repulsion between the electrons, (c) there is a component in the electron-electron interaction of soft bremsstrahlung produced by the recoiling target electron, (d) there is a kinematic upper limit on the photon energy that can be emitted in electron-electron interactions, (e) the electron-electron cross section tends to vanish at low energies as a consequence of the lack of a dipole moment for the electron-electron system. Seltzer and Berger [169] have calculated bremsstrahlung cross sections in the field of atomic electrons by using the theory of Haug

[170], which applies in the case of an unscreened free target electron and considers both the recoil of the target electron and exchange effects. In addition, the same authors have employed screening corrections derived from the theory of Wheeler and Lamb [171].

3.1.2 Analytical bremsstrahlung differential cross sections

In this section, two theoretical models commonly used for the generation of bremsstrahlung DCSs for electrons in the field of the atomic nucleus are described in detail. It is assumed that integration over the angular deflection of the projectile Φ has been done, so that the angular distribution of the emitted photon only depends on the photon energy W and the polar angle of emission θ, relative to the direction of the projectile.

A: Kirkpatrick-Wiedmann-Statham (KWS) double differential cross section

A parameterization method has been proposed by Kirkpatrick and Wiedmann [172] for the nonrelativistic bremsstrahlung double DCS in both photon energy and photon angle, obtained from the Sommerfeld's theory for the unscreened Coulomb field. Their analytical formula, further refined by Statham [173], is expressed by:

$$\frac{\mathrm{d}^2\sigma_{\mathrm{KWS}}}{\mathrm{d}W\mathrm{d}\Omega} = \frac{\sigma_{\mathrm{x}}(1-\cos^2\theta)+\sigma_{\mathrm{y}}(1-\cos^2\theta)}{(1-\beta\cos\theta)^2}, \tag{19}$$

where $\beta = v/c$ is the velocity of the projectile (in units of speed of light c), σ_{x} and σ_{y} are factors that depend on the electron incident energy T_1, the energy of the emitted photon W, and the atomic number Z of the target (for which formulas take complicated analytical expressions). The modifications introduced later by Statham regarding the form of these coefficients were deduced such that they produce a better fit to the theoretical data at low electron energies. Although not very accurate, Eq. (19) has been widely used in the MC simulation of X-ray emission, especially in the field of electron probe microanalysis.

B: Bethe-Heitler energy-loss differential cross section

The Bethe-Heitler formula for bremsstrahlung cross sections differential only in photon energy, obtained within the Born-approximation for the case of the unscreened nucleus (no high-energy approximation included), is quite approximate, but it represents a good starting point for developing better analytical models:

$$\begin{aligned}\frac{\mathrm{d}\sigma_{\mathrm{Born}}^{\mathrm{unscreened}}}{\mathrm{d}W} &= \frac{Z^2 r_0^2}{137W}\frac{p_2}{p_1}\left\{\frac{4}{3} - 2\epsilon_1\epsilon_2\left(\frac{p_1^2+p_2^2}{p_1^2p_2^2}\right) + \frac{L_1\epsilon_2}{p_1^3} + \frac{L_2\epsilon_1}{p_2^3} - \frac{L_2L_1}{p_1p_2} + \mathcal{L}\left[\frac{8}{3}\frac{\epsilon_1\epsilon_2}{p_1p_2}\right.\right. \\ &\left.\left. + \frac{W^2(\epsilon_1^2\epsilon_2^2+p_1^2p_2^2)}{p_1^3p_2^3} + \frac{W}{2p_1p_2}\left(\left(\frac{\epsilon_1\epsilon_2+p_1^2}{p_1^3}\right)L_1 - \left(\frac{\epsilon_1\epsilon_2+p_2^2}{p_2^3}\right)L_2 + \frac{2W\epsilon_1\epsilon_2}{p_1^2p_2^2}\right)\right]\right\}, \end{aligned} \tag{20}$$

where $r_0 = e^2/\mathrm{m_e}c^2 = 2.81794 \cdot 10^{-13}$cm is the classical electron radius, $L_1 = 2\ln(\epsilon_1 + p_1)$, $L_2 = 2\ln(\epsilon_2 + p_2)$, $\mathcal{L} = 2\ln((\epsilon_1\epsilon_2 + p_1p_2 - 1)/W)$, ϵ_1 and ϵ_2 are the total energies (in units of the electron rest energy) of the incoming and outgoing electron after the emission of a bremsstrahlung photon with energy W, and p_1 and p_2 are the incoming and outgoing momenta (in units of $\mathrm{m_e}c$), respectively.

This formula has been further modified by Bethe [155] and Olsen and Maximon [159] in order to account for the screening of the nuclear charge by the atomic electrons and for the departure from the Born-approximation results, respectively. The screening corrections, $\mathrm{d}\sigma_{\mathrm{screen}}/\mathrm{d}W$, most important for extreme-relativistic and for nonrelativistic electron kinetic energies, are defined by integrals which depend on the atomic form factors such as the Thomas-Fermi or the Hartree-Fock form factor. The latter approximation is most often expressed in terms of Coulomb corrections, $\mathrm{d}\sigma_{\mathrm{Coulomb}}/\mathrm{d}W$, that account for the distortion effect of the projectile wave function on the unscreened field of the nucleus. In this case, different approximations can be employed according to their region of applicability. It has also been hence shown by the same authors that at high energies, these corrections are nearly independent and additive, so that the electron-nucleus bremsstrahlung cross section can be expressed as:

$$\frac{\mathrm{d}\sigma_{\mathrm{DBMO}}}{\mathrm{d}W}=\frac{\mathrm{d}\sigma_{\mathrm{Born}}^{\mathrm{unscreened}}}{\mathrm{d}W}+\frac{\mathrm{d}\sigma_{\mathrm{screen}}}{\mathrm{d}W}+\frac{\mathrm{d}\sigma_{\mathrm{Coulomb}}}{\mathrm{d}W}. \tag{21}$$

The total electron-nucleus radiative energy-loss cross section, the integral over the three variables, photon energy and the photon and electron emission angles, was introduced by Heitler [156], and is sometimes also called the cross section for the energy lost by the radiation,

$$\Phi_{\mathrm{br}}^{(\mathrm{n})}(T_1)=\mathcal{N}\int_0^{T_1} W\frac{\mathrm{d}\sigma_{\mathrm{DBMO}}}{\mathrm{d}W}\mathrm{d}W. \tag{22}$$

where $\mathcal{N}=N_{\mathrm{a}}\rho/A$ is the number of atoms per unit volume, $N_{\mathrm{a}}=6.022141510\cdot 10^{23}$ atoms (or molecules) per mole, denotes Avogadro's number, and A is the atomic weight of the element.

The radiative energy-loss cross section is especially used in the calculation of the (mass) radiative stopping power, the average rate at which the charged particles lose energy at any point along their tracks,

$$-\frac{1}{\rho}\left(\frac{\mathrm{d}E}{\mathrm{d}x}\right)_{\mathrm{rad}}^{\mathrm{n}}=\frac{N_{\mathrm{a}}}{A}\int_0^{T_1} W\frac{\mathrm{d}\sigma_{\mathrm{n}}}{\mathrm{d}W}\mathrm{d}W\sim Z^2\Phi_{\mathrm{br}}^{(\mathrm{n})}(T_1), \tag{23}$$

where ρ is the target density. Tabulated radiative stopping power data for electrons and positrons due to the emission of bremsstrahlung calculated within the framework of Bethe theory have been included in the ICRU Report 37 [174].

The Bethe-Heitler DCS for bremsstrahlung emission by electrons in the field of the Wentzel atom (i.e. an exponentially screened Coulomb potential) [175] has been calculated by Salvat and Fernández-Varea [165] considering the high-energy Coulomb corrections by Davies *et al.* [158] and an empirical low-energy correction:

$$\frac{\mathrm{d}\sigma^{(\mathrm{BH})}}{\mathrm{d}W}=r_{\mathrm{e}}^2\alpha Z^2\frac{1}{W}[\epsilon^2\varphi_1(b)+4/3(1-\epsilon\varphi_2(b))], \tag{24}$$

where $\alpha=1/137.036$ is the fine-structure constant, $\epsilon=W/(T_0+\mathrm{m_e}c^2)=W/(\gamma\mathrm{m_e}c^2)$, $b=R\epsilon\mathrm{m_e}c/(1-\epsilon)/(2\hbar\gamma)$ ($R\sim Z^{-1/3}a_0$ is the screening radius and a_0 is the Bohr radius), and $\varphi_1(b)$ and $\varphi_2(b)$ are two parameters given by the following analytical expressions

$$\begin{aligned}\varphi_1(b) &= 4\ln(R\mathrm{m_e}c/\hbar)+2-2\ln(1+b^2)-4b\tan^{-1}(b^{-1})\\ \varphi_2(b) &= 4\ln(R\mathrm{m_e}c/\hbar)+\frac{7}{3}-2\ln(1+b^2)-6b\,tan^{-1}(b^{-1})\\ &- b^2[4-4b\tan^{-1}(b^{-1})-3\ln(1+b^{-2})].\end{aligned} \tag{25}$$

Equations 24 and 25 were used in the initial version of the PENELOPE code [140] and emphasize both the proportionality with respect to Z^2 of the energy-loss DCS, and its divergent behaviour as W^{-1} for $W \to 0$. This divergence justifies the introduction of the scaled bremsstrahlung DCS described below.

3.1.3 Numerical representation of bremsstrahlung differential cross sections

The bremsstrahlung emission cross section, differential in the photon energy and the emission solid angle, can be conveniently expressed as:

$$\begin{aligned}\frac{\mathrm{d}^2\sigma_{\mathrm{br}}}{\mathrm{d}W\mathrm{d}\Omega} &= \frac{\mathrm{d}\sigma_{\mathrm{br}}}{\mathrm{d}W}p(Z,T_1,\kappa;\cos\theta) \\ &= \frac{Z^2}{\beta^2}\frac{1}{W}\chi(Z,T_1,\kappa)p(Z,T_1,\kappa;\cos\theta), \qquad (26)\end{aligned}$$

where $\kappa \equiv W/T_1$ is the reduced energy of the photon (takes values between 0 and 1), $\mathrm{d}\sigma_{\mathrm{br}}/\mathrm{d}W$ is the energy-loss DCS (differential only in the emitted photon energy W), $p(Z,T_1,\kappa;\cos\theta)$ is the probability distribution function of $\cos\theta$ (normalized to unity), for given values of T_1 and κ, known also as the shape function, and $\chi(Z,T_1,\kappa)$ is the scaled bremsstrahlung energy spectrum, given by

$$\chi(Z,T_1,\kappa) = \frac{\beta^2}{Z^2}W\frac{\mathrm{d}\sigma_{\mathrm{br}}}{\mathrm{d}W}, \qquad (27)$$

also known as the scaled energy-loss DCS. Due to its smooth variation with κ and T_1, this function has proven to be quite suitable for numerical tabulation and interpolation of bremsstrahlung energy spectra.

Numerical DCSs given in a tabular form for both electron-nucleus and electron-electron interactions, as well as the total (electron-nucleus + electron-electron) scaled bremsstrahlung DCSs, have been published by Seltzer and Berger [169, 176] considering all the atomic elements (Z=1-92) and incident electron energies T_1 from 1 keV to 10 GeV. These tables represent the most reliable theoretical representation of bremsstrahlung energy spectra available at present and provide the source of data for the simulation done with most of the currently used MC codes (ETRAN [30], ITS3 [139], EGSnrc [27], PENELOPE [34], GEANT4 [33] and GEANT-PSI [28]).

A: Electron-nucleus bremsstrahlung emission cross sections

The electron-nucleus bremsstrahlung DCSs were calculated by Pratt *et al.* [162] by combining high-energy theories, such as the DBMO model, with numerical results from the distorted-wave Born approximation for bremsstrahlung emission in the screened atomic field and energies below 2MeV. The latter method is particularly important because it represents the basis of the current development for the generation of accurate low-energy bremsstrahlung cross section data.

For energies below 2 MeV, numerical relativistic partial-wave calculations of the electron-nucleus bremsstrahlung DCS were reported first by Brysk [177] and later by Tseng and Pratt [163]. Due to the oscillatory nature of the radial wave function integrand and the large number of partial-wave contributions required, numerical tables for bremsstrahlung energy spectra $\chi(Z, T_1, \kappa)$ as given by Eq. (27) have been initially obtained only for selected values of Z and W, in the energy range from 5keV to 500 keV [163]. A comprehensive set of data for $2 \leq Z \leq 92$, for $0 \leq \kappa \leq 1$, and for 1 keV$\leq T_1 \leq 2$ MeV was eventually obtained by employing various interpolation schemes such as least-squares, cubic-spline curve fits of the ratios of the results to the predictions of the analytical Born-approximation theory with screening and Coulomb corrections [162]. These numerical data have been completed with the results of Seltzer and Berger [169] for Z =1 and Z =93 to 100, results obtained by using the linear extrapolation of the original data. Examples of scaled numerical DCSs $\chi(Z, T_1, \kappa)$, as given by these authors, for bremsstrahlung emission by electrons of the indicated incident energies T_1, are displayed in Fig. 9 for carbon and lead atoms.

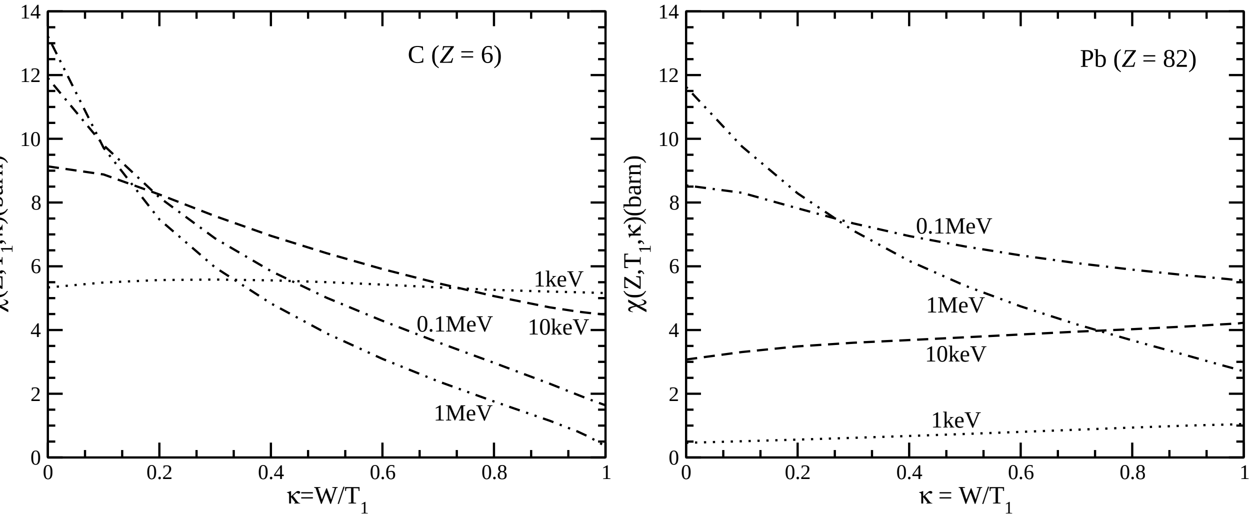

Figure 9: Total scaled DCSs for bremsstrahlung emission by electrons in the field of carbon and lead atoms as a function of the reduced photon energy $\kappa = W/T_1$. The curves correspond to the $\chi(Z, T_1, \kappa)$ functions tabulated by Seltzer and Berger [176] for the indicated electron energies.

Similar partial-wave calculations were carried out by Kissel *et al.* [164] for the shape function $p(Z, T_1, \kappa; \cos\theta)$ for atomic-field bremsstrahlung production from neutral atoms, considered as a single-electron transition in a relativistic self-consistent screened potential [178]. Benchmark calculations for 144 cases were initially performed for elements with atomic number ranging from 1 to 92 [Z=2,8,13,47,79,92], for six incident electron energies [T_1=1,5,10,50,100,500 keV] and for 12 values of the fraction of energy radiated between 0 and 1 [κ=0,0.1,0.2,0.3,0.4, 0.5,0.6,0.7,0.8,0.9,0.95,1.0]. A fitting procedure of these data to the results of the angular distributions obtained from the first Born approximation was eventually applied in order to extend the numerical tabulation to the whole range of elements, Z, and fraction of energy radiated, κ,

$$p(Z, T_1, \kappa; \cos\theta) = \frac{A}{4\pi(1 - \beta\cos\theta)^m} \sum_{\mathrm{i}=0}^{\mathrm{N}} B_{\mathrm{i}} P_{\mathrm{i}}(\cos\theta), \tag{28}$$

where $B_0 = 1$, $N = 5$, $m = 4.5$, β is the velocity of the incident electron (in units of the speed of light), and $P_{\mathrm{i}}(\cos\theta)$ are the Legendre polynomials. Fig. 10 displays the shape functions $p(Z, T_1, \kappa; \cos\theta)$ for bremsstrahlung emission by 1 keV electrons of indicated reduced emission photon energies $\kappa = W/T_1$, as calculated by these authors, for carbon and lead atoms.

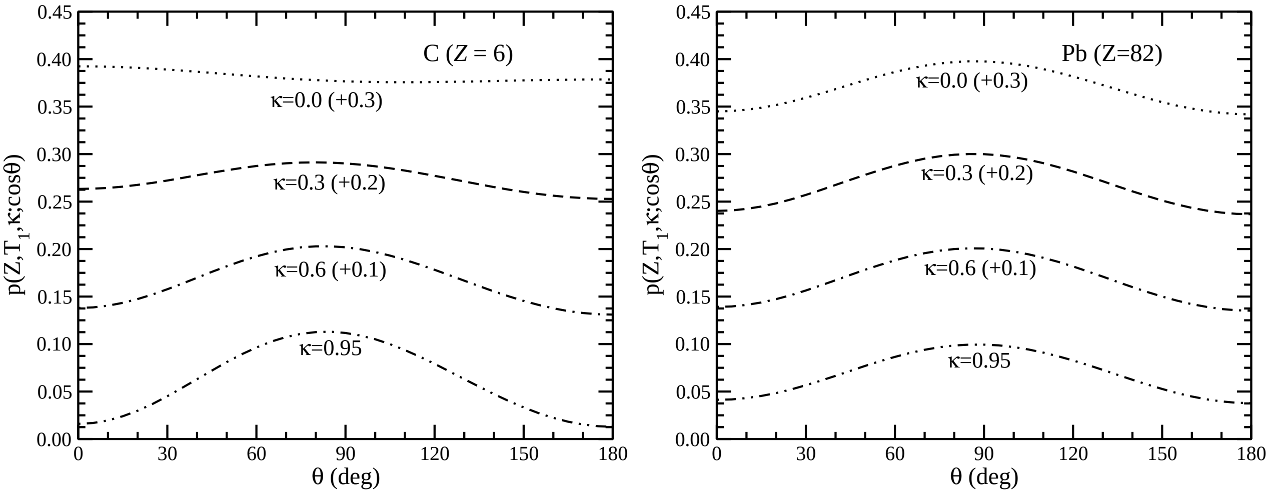

Figure 10: Shape functions for bremsstrahlung emission by 1 keV electrons in the field of carbon and lead. The curves correspond to the functions $p(Z, T_1, \kappa; \cos\theta)$ tabulated by Kissel [164] for the indicated fraction of energy radiated $\kappa = W/T_1$.

Results for the electron-nucleus bremsstrahlung production cross sections as given by the three theoretical models presented above (the Kirkpatrick-Wiedmann-Statham parameterization method [173], the Bethe-Heitler theory [155] and the numerical tabulations from the partial-wave calculations by Seltzer and Berger [176]) are also compared. Thus, Fig. 11 displays together data from the models described above for the scaled energy-loss DCSs $\chi(Z, T_1, \kappa)$ for carbon and silver at 50 keV incident electron energy (in the case of carbon, the results overlap rather closely with the results at lower energies and are thus shown with a vertical displacement specified in parenthesis). Comparisons of the two latter models for lower incident energies are included (T_1=1 keV and T_1=10 keV), but the results for the KWS formula have been left out here. It is seen that the Bethe-Heitler DCSs are in relatively good agreement

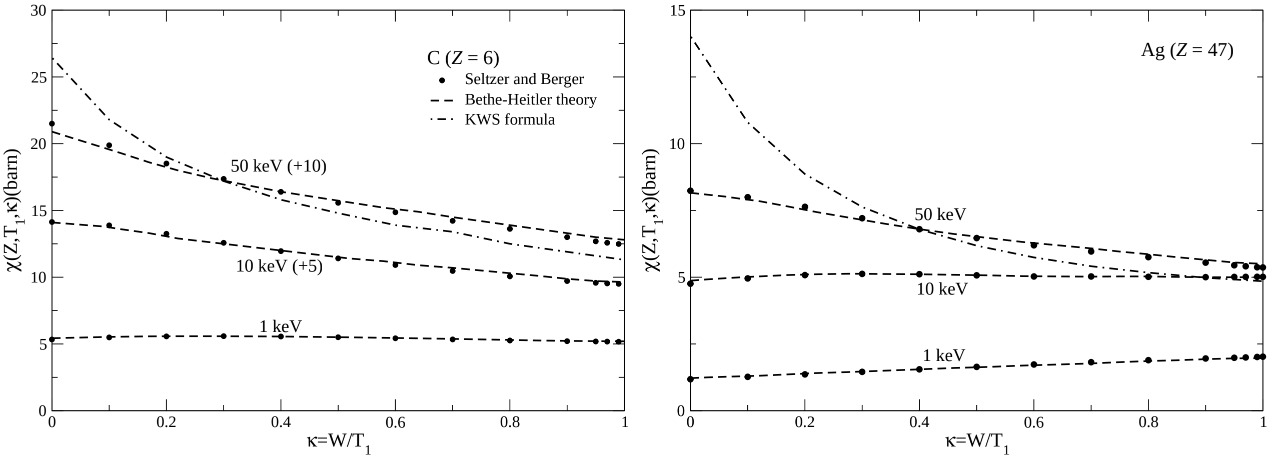

Figure 11: Scaled bremsstrahlung cross sections for carbon and silver, as a function of the reduced photon energy $\kappa = W/T_1$ for the indicated incident electron energies. The symbols correspond to the functions $\chi(Z, T_1, \kappa)$ tabulated by Seltzer and Berger [176], dashed lines are results from Bethe-Heitler theory and dot-dashed lines are results from KWS formulas.

with the partial-wave data, whereas the results given by the KWS formula span a wider range of energy-loss DCS values.

B: Electron-electron bremsstrahlung emission cross sections

As stated in the introduction, bremsstrahlung is also produced by the interaction with atomic electrons, the so-called electron-electron bremsstrahlung emission. The atomic electron absorbs the recoil momentum and is thus ejected. Experimentally, by using the electron-photon coincidence technique, one can differentiate exactly between the electron-electron and the electron-nucleus bremsstrahlung emission processes. However, no experimental results are available for non-relativistic energies for comparison with theoretical models.

For reasons already explained, the cross section for bremsstrahlung in the field of an atomic electron can not always be approximated by the electron-nucleus cross section described above. Triply DCSs for electron-electron bremsstrahlung were first calculated by Hodes [179] in the lowest order quantum electrodynamics. With the progress in computing, Mack and Mitter [180] performed complicated calculations using Feynman diagrams. Later, Seltzer and Berger [169] calculated the electron-electron cross section by considering, in addition to the unscreened cross section given by Haug [170] for bremsstrahlung in the field of a free electron at rest, a screening correction that takes into account the effects of electron binding [171]. At low incident electron energies, this approximation, derived in the context of high-energy considerations, is expected to break down.

The contribution of electron-electron bremsstrahlung to the total (electron-electron + electron-nucleus) cross section is calculated in terms of the ratios $\eta(Z, T_1, \kappa)$,

$$\eta(Z, T_1, \kappa) = \frac{1}{Z^2} \frac{\mathrm{d}\sigma_{\mathrm{e}}/\mathrm{d}W}{\mathrm{d}\sigma_{\mathrm{n}}/\mathrm{d}W}, \tag{29}$$

where $\mathrm{d}\sigma_{\mathrm{e}}/\mathrm{d}W$ is the electron-electron bremsstrahlung DCS and $\mathrm{d}\sigma_{\mathrm{n}}/\mathrm{d}W$ is the electron-nucleus DCS. In Fig. 12, the $\eta(Z, T_1, \kappa)$ ratios are shown at two different incident electron energies 1 MeV (*left*) and 10 MeV (*right*). It is seen that, for initial electron energy T_1=10 MeV, η is of the order of unity for a wide range of energy spectra of the emitted photon, whereas for lower incident electron energies (T_1=1 MeV), the approximation of considering the electron-electron bremsstrahlung cross sections as being equal to the electron-nucleus bremsstrahlung cross sections is no longer valid.

Figure 13 displays the same $\eta(Z, T_1, \kappa)$ ratios for 1 keV (*left*) and 10 keV (*right*) incident electron energies. It is seen that, at low energies, the electron-electron bremsstrahlung cross section is significantly reduced with respect to the electron-nucleus bremsstrahlung cross section. Hence, the possible error introduced by considering the screening correction introduced by Seltzer and Berger [169] (developed in the high-energy limit), although large at low energies, will have a small effect on the total bremsstrahlung cross section.

3.1.4 Theoretical models implemented in PSICRO for total bremsstrahlung data

The bremsstrahlung cross section data included in the EEDL file [146] and also originally implemented in PSICRO, for the scattering of electrons by neutral atoms, differential in terms of

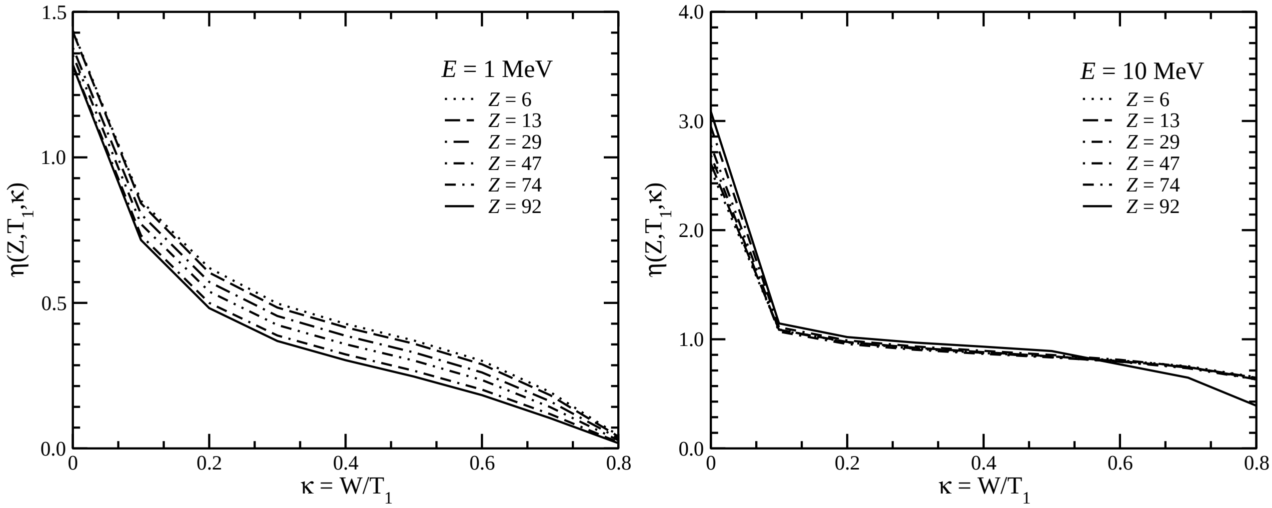

Figure 12: Ratios of electron-electron to electron-nucleus bremsstrahlung cross sections as a function of the reduced photon energy κ for an incident electron energy T_1 =1 MeV (*left*) and T_1 =10 MeV (*right*) in the field of various atoms. The curves correspond to the $\eta(Z, T_1, \kappa)$ functions as obtained from the numerical tabulations by Seltzer and Berger [169] for the indicated electron energies. The apparent discontinuity of the slopes in the figures is due to the limited number of points available for the interpolation.

emitted photon energy W, were derived by using the Seltzer and Berger numerical tabulations [169, 176] generated for different incident electron energies (see earlier section). The total (electron-nucleus + electron-electron) bremsstrahlung emission cross sections were calculated by extending the photon yield spectra down to a certain photon energy cutoff to avoid the $1/W$ singularity for $W \to 0$. The cutoff energy chosen was 0.1 eV, so as to be consistent with the accuracy to which the extrapolated data were calculated. Thus, the original data in the energy range 1 keV to 10 GeV were extrapolated to lower, as well as to higher, energies by cubic spline fits so as to cover the energy range of interest, i.e. 10 eV to 100 GeV. The integrated cross section, $\sigma_{\mathrm{br}}(T_1)$, for an incident electron with energy T_1 was obtained by integrating the DCS over the entire range of emitted photon energies W, i.e. from 0.1 eV to T_1,

$$\sigma_{\mathrm{br}}(T_1) = \int_{0.1}^{T_1} \frac{\mathrm{d}\sigma_{\mathrm{br}}(W, T_1)}{\mathrm{d}W} \mathrm{d}W. \tag{30}$$

As shown in the previous sections, the currently applied procedure goes beyond the results of the Bethe-Heitler theory reviewed by Koch and Motz [150], due to the various correction methods implemented according to the energy range of interest.

During the current thesis work, the electron cross section data for bremsstrahlung emission available in the energy range from 10 eV to 100 GeV, have been extended down to 1 eV incident electron energy by using the Lagrange extrapolation method[12]. More specifically, the data for bremsstrahlung emission by electrons are extracted from the EEDL file (see Section 2.4.1.) and then extended by Lagrange extrapolation down to 1 eV. Several subroutines have

---

[12] performs curve fitting on a given set of $N + 1$ sample points by using a polynomial of degree N; see Appendix B for details

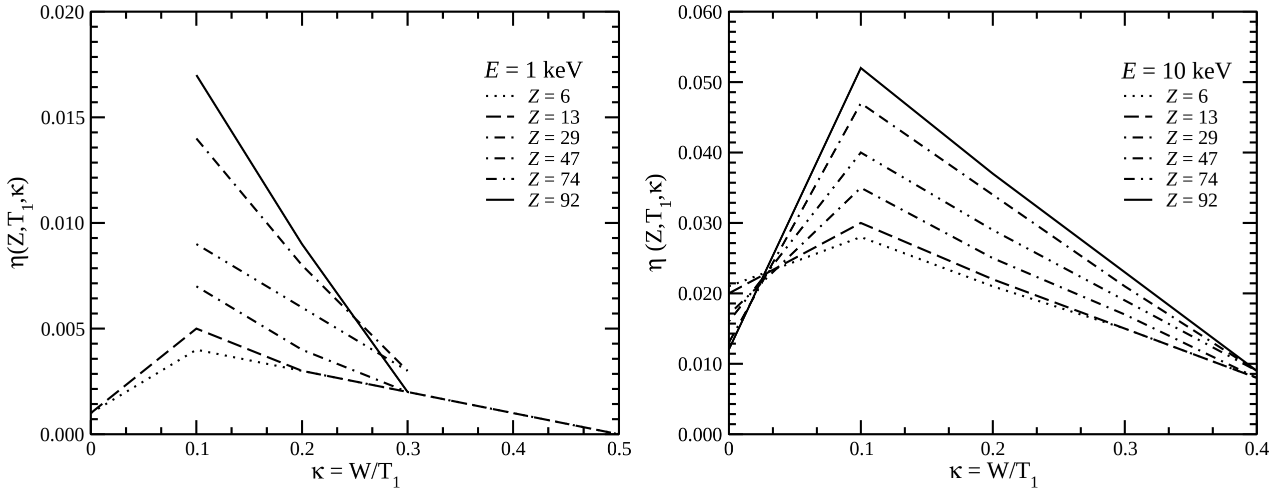

Figure 13: Idem to Fig. 12 for T_1=1 keV (*left*) and T_1=10 keV (*right*) incident electron energy.

been developed and integrated into the code PSICRO to allow the generation of the total bremsstrahlung cross section for incident electrons, as also for the calculation of the spectra and average energy of recoil photons for electron bremsstrahlung emission (e.g. subroutines EXTEN1 and EXTEN2, shown in Fig. 14 which displays the flowchart diagram for the calculation of bremsstrahlung emission cross sections).

Regarding the current bremsstrahlung data generation for positrons, this is based on the observations of several authors [181, 182]. Thus, it has been shown that the stopping power for bremsstrahlung emission due to positron scattering can be obtained with good accuracy by scaling the electron radiative stopping power using a function depending only of the quantity T_1/Z^2,

$$\eta = \frac{\Phi^+_{\rm rad}(Z,T_1)}{\Phi^-_{\rm rad}(Z,T_1)} = \eta\left(\frac{T_1}{Z^2}\right) \tag{31}$$

where T_1 denotes the kinetic energy of the incident particle (in units of MeV) and $\Phi^\pm_{\rm rad}(Z,T_1)$ are the positron/electron cross sections for the energy lost by radiation defined in a similar manner to that given by Eq. (22). For each incident energy T_1, the ratio $\Phi^+_{\rm rad}/\Phi^-_{\rm rad}$ is taken as the ratio of the average probability of interaction for positrons and electrons, integrated over the entire spectrum of secondary photon energy. By fitting the tabulated values available from the relativistic partial-wave multipole-expansion calculations [182], the scaling function η has been evaluated by Urbán [33] as having the following form:

$$\eta(x) = \begin{cases} 0 & \text{if } x \leq -8 \\ 1/2 + 1/\pi \arctan(0.415x + 0.0021x^3 + 0.00054x^5) & \text{if } -8 < x < 9 \\ 1 & \text{if } x \geq 9, \end{cases}$$

where $x = \ln(7522.1 T_1/Z^2)$. The scaling holds for the ratio of the total radiative energy losses, and, in the case of the point Coulomb potential, both in the classical bremsstrahlung formula and the nonrelativistic dipole Sommerfeld formula, also for the radiation energy spectrum.

An analogous approach has been followed for the calculation of the bremsstrahlung cross section for positrons, keeping the average photon energies as well as the photon spectra un-changed and considering that the stopping power is given by $W^{\mathrm{av}}(T_1)\sigma_{\mathrm{br,p}}(T_1)$, where $W^{\mathrm{av}}(T_1)$ is the average photon energy due to bremsstrahlung by positrons/electrons and $\sigma_{\mathrm{br,p}}(T_1)$ is the integrated bremsstrahlung cross section for positrons of incident energy T_1. Also shown in the flowchart diagram of Fig. 14 are the calls to the subroutines that perform the bremsstrahlung emission cross section calculation for positrons.

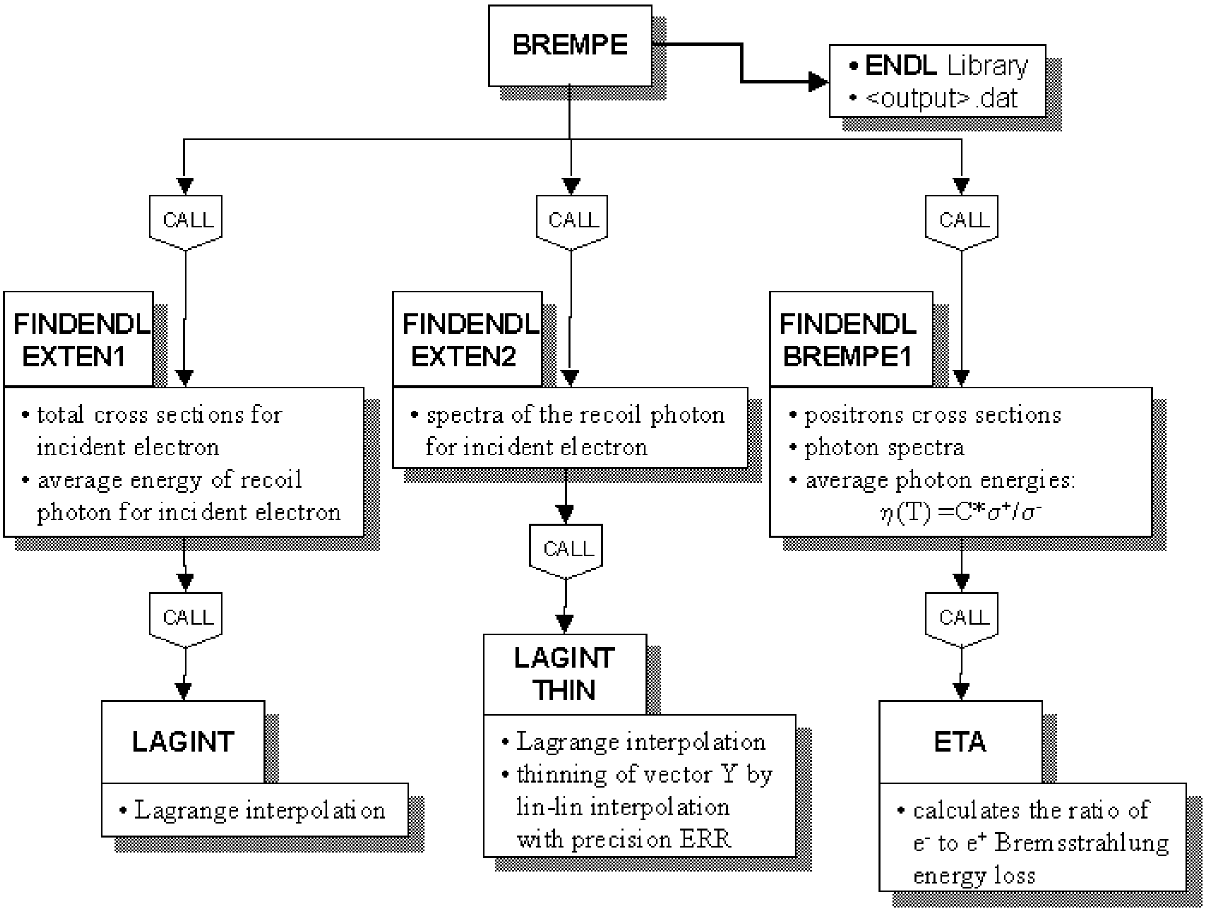

Figure 14: Flowchart of the bremsstrahlung emission cross section calculation with the code PSICRO.

3.2 Elastic Scattering of Charged Particles

In general, a perfect elastic collision of particles is defined as one in which there is no loss of kinetic energy in the collision, the particles involved suffering only a deflection. Due to the relatively large difference between the mass of an electron or positron and that of an atom, the scattering of these charged particles by the nuclear Coulomb field of neutral atoms resulting in a negligible energy loss can also be regarded as elastic scattering. Figure 15 schematically shows the elastic scattering process for a repulsive potential. The elastic scattering of charged particles in the Coulomb field of atomic nuclei is described in terms of DCSs by using various theoretical approaches ranging from simple analytical approximations to detailed state-of-the-art theories.

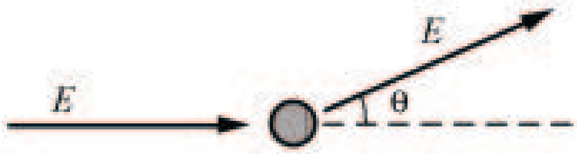

Figure 15: Elastic scattering process.

3.2.1 Introduction

Despite the availability of computer codes that provide accurate elastic scattering DCSs for relatively wide ranges of energy [183, 184], the use of numerical tabulations which contain a limited amount of information [185-191] still represents common practice. Two elastic scattering cross section databases generated by Berger and Seltzer [192] and by Jablonski *et al.* [193] have been recently issued by the U.S. National Institute of Standards and Technology (NIST) for energies from 1 keV to 100 MeV, and from 50 eV to 300 keV, respectively. The former is intended for MC simulations of high-energy electron and positron transport, while the latter is designed for surface electron spectroscopy and electron-probe microanalysis studies. These databases provide information such as DCSs, total (integrated) cross sections and momentum transfer cross sections based on specific scattering models that are known to be of limited validity and applicable only to certain energy ranges. Moreover, neither database contains information on scattering amplitudes and spin polarization necessary for a complete description of the elastic scattering process at arbitrary angle.

The accurate calculation of electron and positron elastic scattering DCSs from first principles [194] has become possible nowadays, thanks to increased computer capabilities. Potentially, the most accurate elastic scattering cross sections are those obtained from a partial-wave analysis solution of the Dirac equation in the nuclear field screened by atomic electrons. Being especially important at medium to low energies, this method will be described in detail in the next section, along with various other theoretical models still in use.

For energies above ~5 MeV, the finite size of the nucleus affects the elastic DCSs, and partial-wave calculations become extremely slow. Therefore, approximative, but more efficient, factorization methods of relativistic Rutherford and screened DCSs must be used [195]. These methods allow the generation of electron and positron elastic DCSs for energies up to 100 GeV [146]. Further refinements concerning the screening factor, which eventually prevent the divergence of the Rutherford DCSs at small angles, have been made [196], thus yielding finite calculated DCSs with an estimated numerical uncertainty of ~0.1%[13]. Finally, nuclear-size corrections which affect the elastic DCSs at relatively large angles have also been introduced

---

[13] Uncertainties throughout the thesis are given at the 1σ level

by expressing the Rutherford DCSs as a product of the DCSs for a point nucleus (which is more accurate than in the Born approximation) and the nuclear form factor, which tries to account for the atom deformation shape. All these methods and corrections have especially improved the elastic scattering DCSs for low-Z elements.

The following section presents the analytical models employed in the context of the partial-wave analysis method, for describing single elastic interactions of an electron or positron, of rest mass $m = m_e$, charge $Z_0 e$ ($Z_0 = -1$ for electrons and $Z_0 = 1$ for positrons) and kinetic energy E, with a neutral atom of atomic number Z placed at the origin of the coordinate system. In these models, the charge distribution of the target atom is considered as spherically symmetric, which may require averaging over degenerate states in the case of electronic configurations with open shells.

3.2.2 Partial-wave analysis method

For intermediate and low energies, the conventional partial-wave analysis method has been implemented in various computer codes such as PWASCH (Partial Wave Analysis SCHrodinger) and PWADIR (Partial Wave Analysis DIRac) [197], in order to address in detail the problem of the elastic scattering of charged particles in the central electrostatic field V(r) of the target atom (i.e. 'the static-field approximation' [194, 198]), which satisfies the condition $rV(r) \rightarrow 0$. This method has been subjected to further developments since its initial implementation by including additional numerical algorithms, which allow relativistic partial-wave based calculations to be performed for energies up to ~20 MeV [196], as well as by carrying out certain model improvements over the entire range of energies [119]. In the latter context, the original analytical built-in scattering field used in 'the static-field approximation' to describe the Dirac-Hartree-Fock-Slater atomic field [199] has been modelled by accounting for additional effective interactions which become particularly important at low and intermediate energies.

Thus, for moderately high energies, the effective interaction between a particle (charge ±e) located at $\mathbf{r}$ and a neutral target at rest can be modelled to a good approximation as an instantaneous Coulomb interaction. Effectively, the atom is modelled as a frozen charge distribution $\rho(r)$ (i.e. it maintains its charge state throughout the interaction process) [198], so that the electrostatic scalar potential can be written as:

$$\varphi(r) = \frac{Z_0 e}{r} - e\left(\frac{1}{r}\int_0^r \rho\left(r'\right) 4\pi r'^2 dr' + \int_r^\infty \rho\left(r'\right) 4\pi r'^2 dr'\right). \tag{32}$$

where $Z_0 e/r$ is the electrostatic potential of the bare (point) nucleus and $\rho\left(r'\right)$ is the atomic electron density, obtained from $\varphi(r)$ by using the well known Poisson equation, $\nabla^2\varphi = -4\pi\rho$.

In more detail, considering the target charge distribution as contributions from both the nucleus $\rho_\mathrm{n}(r)$ and electron cloud surrounding it $\rho_\mathrm{e}(r)$,

$$\begin{aligned} \varphi_\mathrm{n}(r) &= e\left(\frac{1}{r}\int_0^r \rho_\mathrm{n}(r')\, 4\pi r'^2 \mathrm{d}r' + \int_r^\infty \rho_\mathrm{n}(r')\, 4\pi r' \mathrm{d}r'\right) \\ \varphi_\mathrm{e}(r) &= -e\left(\frac{1}{r}\int_0^r \rho_\mathrm{e}(r')\, 4\pi r'^2 \mathrm{d}r' + \int_r^\infty \rho_\mathrm{e}(r')\, 4\pi r' \mathrm{d}r'\right), \end{aligned} \tag{33}$$

the scattering field V_st between the projectile and the target (i.e. the interaction energy as a function of the distance to the atomic nucleus) is given by:

$$V_{\mathrm{st}}\left(r\right) = Z_0 e \varphi(r) = Z_0 e \left[\varphi_{\mathrm{n}}(r) + \varphi_{\mathrm{e}}(r)\right]. \tag{34}$$

Results considering various analytical descriptions of the static potential, given in the equation above, have already been published [119], as also have details of the numerical implementation in the FORTRAN77 code ELSEPA [120].

The atomic nuclear charge distribution, described by the first term of Eq. (34), can be calculated by using several models such as the Point nucleus (P), the Uniform distribution (U), the Fermi distribution (F) [200] or the Helm's uniform-uniform distribution (Uu) [201]. The last-mentioned model is particularly important for modelling the atomic nuclear charge distribution in the case of a very high-energy projectile ($E > 200 MeV$) due to its finite "skin thickness" (i.e. the thickness of the layer of neutrons which is assumed to cover the nucleus of an atom) and the fact that it admits an analytical expression for the nuclear form factor.

The ground-state atomic electron density, given in the second term of Eq. (34), can be obtained from simple analytical models such as the Thomas-Fermi-Moliere density (TFM) [202], the Thomas-Fermi-Dirac density (TFD) [203], and the Dirac-Hartree-Fock-Slater density (DHFS) [204, 199], or are more accurately available in numerical format such as, for example, the Dirac-Fock densities (DF) obtained for free atoms from self-consistent relativistic calculations [205].

For electrons, exchange effects (i.e. the occurrence of rearrangement collisions, when the projectile electron exchanges place with an atomic electron) must also be accounted for in the model by adding an approximate local-exchange interaction term V_{exch} [206] to the electrostatic potential in Eq. (34). Various models such as the Thomas-Fermi exchange potential (TF) [207, 208], the Furness-McCarthy exchange potential (FM) [209] and the Riley-Truhlar exchange potential (RT) [208], are computationally more convenient to use as they eventually reduce to a local term, unlike the expression obtained using the Hartree-Fock method for the bound-electron states which leads to a non-local exchange term much more difficult to handle.

Low energy corrections to 'the static-field approximation' have to be introduced when the energy of the projectile becomes of the order of a few keV or lower, in order to account for the influence brought in by the polarization of the target [199, 210]. These corrections correspond to what is also called 'the adiabatic approximation'. The effect of charge polarization can be described by means of the polarization potential V_{pol}, modelled by using the Buckingham potential [207] or, in a more elaborate manner, the correlation-polarization potential [119], which combines a long-range polarization potential with the correlation[14] potential obtained from the local density approximation (LDA) [211] (i.e. the true exchange-correlation energy of the system is approximated locally by the exchange-correlation energy associated with a homogeneous electron gas of the same density ρ).

For energies above the first excitation threshold, up to about 1 MeV or even higher, there is a loss of particles from the elastic channel to inelastic channels. This effect, extremely important at low energies, causes a reduction of the elastic DCS at intermediate and large angles, and it

---

[14] When the projectile is an electron, its charge is dramatically screened by the atomic electrons so that a "Coulomb hole" surrounding the projectile is formed, an effect which is usually refered to as "correlation".

can be modelled by adding a negative imaginary term $-\mathrm{i}W_{\mathrm{abs}}(r)$ in Eq. (34), defined as

$$W_{\mathrm{abs}}^{(\mathrm{nr})} = A_{\mathrm{abs}} \frac{\hbar}{2} \left[v_{\mathrm{L}}^{(\mathrm{nr})} \rho_{\mathrm{e}}\, \sigma_{\mathrm{bc}}(E_{\mathrm{L}}, \rho_{\mathrm{e}}, \Delta) \right], \tag{35}$$

where A_{abs} is an empirical parameter that takes values of the order of unity, ρ_{e} is the electron density, and $v_{\mathrm{L}}^{(\mathrm{nr})}$ is the projectile velocity, $v_{\mathrm{L}} = (2E_{\mathrm{L}}/\mathrm{m_e})^{1/2}$, inside the homogeneous electron gas which corresponds to the local kinetic energy E_{L}. The cross section $\sigma_{\mathrm{bc}}(E_{\mathrm{L}}, \rho_{\mathrm{e}}, \Delta)$ for binary collisions of the projectile with the local free-electron gas, for an energy transfer larger than a gap Δ, is calculated using the non-relativistic Born approximation, with the Ochkur exchange correction [212] included in the case of electrons as incident particles [119].

The effective interaction potential $V(r)$ between the projectile particle and the atom, according to the optical-model described above, can be written in the following form:

$$\begin{aligned} V(r) &= V_{\mathrm{st}}(r) + V_{\mathrm{pol}}(r) + V_{\mathrm{exch}}(r) - iW_{\mathrm{abs}}(r) && \text{for electrons} \\ V(r) &= V_{\mathrm{st}}(r) + V_{\mathrm{pol}}(r) - iW_{\mathrm{abs}}(r) && \text{for positrons} \end{aligned} \tag{36}$$

The interaction field given by Eq. (36) is used in conjunction with either the relativistic Dirac [213], or with the lower energy (non-relativistic) Schrödinger [214], partial wave analysis method described below. Details of the models used to describe the various potentials that enter in Eq. (36) will be given in the next section.

A: Dirac equation

The Dirac equation is usually applied for incident particles with relativistic kinetic energies (below 10 MeV) and spin 1/2, as well as for low energies (few eV), when the target is a heavy atom and relativistic effects must be accounted for. Due to its complexity with respect to the non-relativistic case, the relativistic calculations consider scattering of the incident particle by an atomic central field, in which the electrostatic potential must be described appropriately. It has been shown that the elastic DCSs per unit solid angle about the direction (θ, ϕ), $\mathrm{d}\sigma/\mathrm{d}\Omega$, are fully described by both the direct $f(\theta)$, and spin-flip $g(\theta)$, scattering amplitudes [194, 198]:

$$\frac{\mathrm{d}\sigma}{\mathrm{d}\Omega} = |f(\theta)|^2 + |g(\theta)|^2. \tag{37}$$

The scattering amplitudes are complex functions of the polar scattering angle θ determined by the large-r behaviour of the Dirac distorted plane-waves (i.e. the solutions of the Dirac equation for the central field $V(r)$ that behaves asymptotically as a plane wave plus an outgoing spherical wave [215]), viz.

$$\begin{aligned} f(\theta) &= \sum_{\ell=0}^{\infty} F_\ell P_\ell(\cos\theta) = \sum_{\ell=0}^{\infty} \frac{1}{2ik} \{(\ell+1)\left[\exp\left(2i\delta_{\ell+}\right) - 1\right] + \ell\left[\exp\left(-2i\delta_{\ell-}\right) - 1\right]\} P_\ell\left(\cos\theta\right) \\ g(\theta) &= \sum_{\ell=0}^{\infty} G_\ell P_\ell^1(\cos\theta) = \sum_{\ell=0}^{\infty} \frac{1}{2ik} \{\exp\left(2i\delta_{\ell-}\right) - \exp\left(-2i\delta_{\ell+}\right)\} P_\ell^1(\cos\theta) \end{aligned} \tag{38}$$

where F_ℓ and G_ℓ are the coefficients of the partial-wave expansions, $k = p/\hbar = \sqrt{E\left(E + 2\mathrm{m_e}c^2\right)}/c$ is the relativistic wave number of the projectile, $P_\ell\left(\cos\theta\right)$ and $P_\ell^1(\cos\theta)$ are the Legendre polynomials and their associated Legendre functions (see Appendix C), respectively. The scattering phase shifts of order ℓ, $\delta_{\ell\pm}$, are obtained from a solution of the coupled pair of differential equations for the two minor, P_κ, and major, Q_κ, scattering wave-function components [197] (with E in the relativistic range),

$$\begin{aligned}\frac{\mathrm{d}P_\kappa}{\mathrm{d}r} &= -\frac{\kappa}{r}P_\kappa - \frac{E - V(r) + 2\mathrm{m_e}c^2}{c\hbar}Q_\kappa \\ \frac{\mathrm{d}Q_\kappa}{\mathrm{d}r} &= \frac{\kappa}{r}Q_\kappa + \frac{E - V(r)}{c\hbar}P_\kappa,\end{aligned} \tag{39}$$

with the boundary conditions $P_\kappa(0) = Q_\kappa(0) = 0$ and where $\kappa \equiv (\ell - j)(2j + 1)$ represents the relativistic angular momentum quantum number (j and ℓ are the total and the orbital angular momentum quantum numbers, respectively). The phase shifts are calculated from the asymptotic behaviour of the radial function $P_\kappa(r)$ in the limit $r \to \infty$

$$P_\kappa(r) \sim \sin\left(kr - \ell\frac{\pi}{2} + \delta_\kappa\right). \tag{40}$$

The total, σ, and the transport, σ_{tr}, elastic cross sections are, respectively, defined by:

$$\sigma \equiv 2\pi\int_0^\pi \frac{\mathrm{d}\sigma}{\mathrm{d}\Omega}\sin\theta\mathrm{d}\theta, \tag{41}$$

and

$$\sigma_{\mathrm{tr}} \equiv 2\pi\int_0^\pi (1 - \cos\theta)\frac{\mathrm{d}\sigma}{\mathrm{d}\Omega}\sin\theta\mathrm{d}\theta. \tag{42}$$

Considering the definition of the DCSs given by Eq. (37) and the orthogonality property of the Legendre polynomials, σ and σ_{tr} are finally given by the following series:

$$\sigma = 4\pi\sum_{\ell=0}^{\infty}\frac{1}{2\ell+1}\left(|F_\ell|^2 + \ell(\ell+1)|G_\ell|^2\right), \tag{43}$$

$$\sigma_{\mathrm{tr}} = \sigma + 4\pi\sum_{\ell=0}^{\infty}\left\{\frac{\ell+1}{(2\ell+1)(2\ell+31)}\left[F_\ell^*F_{\ell+1} + F_\ell F_{\ell-1}^* + \ell(\ell+2)\left(G_\ell^*G_{\ell+1} + G_\ell G_{\ell-1}^*\right)\right]\right\} \tag{44}$$

where F_ℓ^* and G_ℓ^* are, respectively, the complex conjugates of the coefficients F_ℓ and G_ℓ, given in Eq. (38) for the partial-wave expansions of the spin-flip scattering amplitudes $f(\theta)$ and $g(\theta)$.

B: Schrödinger equation

Elastic DCS for incident particles with non-relativistic kinetic energies (up to a few keV[15]) are described by the direct scattering amplitude, $f(\theta)$ [198]:

$$\frac{\mathrm{d}\sigma}{\mathrm{d}\Omega} = |f(\theta)|^2, \tag{45}$$

---

[15] The energies at which non-relativistic expressions for mechanical quantities of electrons and protons are in error by 1% is a reasonable threshold for relativistic treatments. The 1% threshold is then 5.11 keV for electrons and 9.38 MeV for protons.

which can be written using a partial-wave expansion in the following form

$$f(\theta) = \sum_{\ell=0}^{\infty} F_\ell P_\ell(\cos\theta) = \sum_{\ell=0}^{\infty} \frac{1}{2ik}(2\ell+1)\left[\exp(2i\delta_\ell) - 1\right] P_\ell(\cos\theta), \tag{46}$$

where F_ℓ are the coefficients of the partial-wave expansion, $k = (2E)^{1/2}$ is the non-relativistic wave number of the projectile and δ_ℓ is the Schrödinger phase shift of order ℓ obtained from a solution of the upper radial equation (39) [197] (with E in the non-relativistic range).

Equations (43) and (44) can now be rewritten for the non-relativistic case in the form of the series:

$$\sigma = 4\pi \sum_{\ell=0}^{\infty} \frac{1}{2\ell+1} |F_\ell|^2, \tag{47}$$

$$\sigma_{\text{tr}} = \sigma + 4\pi \sum_{\ell=0}^{\infty} \left(\frac{1}{(2\ell+1)(2\ell+3)} \left(F_\ell^* F_{\ell+1} + F_\ell F_{\ell-1}^* \right) \right). \tag{48}$$

where F_ℓ^* are the complex conjugates of the coefficients given in Eq. (46) for the partial-wave expansion of the direct scattering amplitude $f(\theta)$.

To summarize, the differences between the results from relativistic and non-relativistic calculations arise from the way the interaction potential is modelled, as also from the difference in the wave number k, which, in the second case, does not include the mass-energy term. At low energies, these differences (i) increase with increasing atomic number, and (ii) decrease with increasing incident particle energy.

3.2.3 Theoretical models implemented in PSICRO for the generation of elastic scattering data

The elastic scattering cross sections included in the EEDL file [146], and also originally implemented in PSICRO, were generated by LLNL in the energy range from 10 eV to 100 GeV, for atoms ranging from $Z = 1$ to 100, by employing several different scattering models. Thus, in the energy range from 10 eV to 1 keV, the cross sections are obtained via log-log extrapolation of the DCSs calculated between 1 and 256 keV using a fitting procedure with an analytical expression of the results provided by a phase-shift analysis of the Dirac equation [188]. At energies higher than 10 MeV, factorization cross sections in which screening is treated separately from relativistic and spin effects have proven to be satisfactory. The Molière screening parameter [202] has been used, with Seltzer's modification [30] included for better representation at low energies. The Mott-to-Rutherford cross section ratios, as well as convergence parameters [216, 74], are calculated using Wilderman's procedure [217]. The data in between the two ranges for the theoretical models, i.e. from 256 keV to 10 MeV incident electron energy, are obtained by using a cubic spline smoothing algorithm.

The partial wave method described in the previous section has currently been employed [116] for solving the relativistic Dirac and non-relativistic Schrödinger [Eqs. (37), (38), (39), (45) and (46)] for bound electron states, in the energy range from 1 eV to 1 MeV. Two FORTRAN 77 codes, PSIATO and PSICRO, have been used for the generation of both electron and positron elastic scattering cross sections. The code PSIATO is a relativistic atomic-structure program based on the theory of Shadwick and Norman [218] for calculating the variationally optimized static $V_{\rm st}^{\rm opt}(r)$ and exchange potentials $V_{\rm ex}^{\rm b,opt}(r)$ for bound electrons considering atoms in the ground state. The problem is solved self-consistently by starting with an initial approximate potential and solving for the single-particle orbitals and energies, then constructing the kernel and inhomogeneous term in the Voltera type integral equation of the first kind and solving this integral equation numerically. The code PSICRO, on the other hand, calculates the integrated cross sections and the angular spectra for electrons and positrons by using a model based on the relativistic partial wave method of Salvat and Mayol [184] which has been further developed [116]. A detailed flowchart diagram of the code PSICRO which describes the various calls to the subroutines that perform elastic scattering cross section data generation is shown in Fig. 16.

For the region of valence shells electrons, it has been shown by Talman and Shadwick [219] for the total energy, and by Stepanek [116] directly for the local exchange potential, that the variationally optimized method is a better solution than using the well known $X\alpha$-exchange potential developed by Slater [220]

$$V_{\rm ex}(r) = -\frac{3\alpha}{2\pi}k_{\rm F}(r) \tag{49}$$

where $k_{\rm F}(r) = (3\pi^2\rho(r))^{1/3}$ is "the local Fermi momentum" and α is a free adjustable parameter. The variationally optimized method leads to a more realistic dependence at large radii,

$$V_{\rm ex}^{\rm b,opt}(r) = -1/r \tag{50}$$

The exchange effects with the bound state electron can be described with the help of the Furness and McCarthy potential [209], given by

$$V_{\rm ex}(r) = \frac{1}{2}\left[(E - V_{\rm st})\sqrt{(E - V_{\rm st}) + 4\pi\rho(r)}\right] \tag{51}$$

where E is the kinetic energy of the incident electron (in Hartree), $V_{\rm st}$ is the electrostatic potential given by the Eq. (34) and $\rho(r)$ is the electron density of the atom, has been used by many authors. It has also been shown [116], moreover, that this form of the exchange potential is less repulsive and thus it reproduces well the shell dependence at small radii only for high-Z elements.

For the case of electrons, the code PSICRO uses, therefore, the variationally optimized static $V_{\rm st}^{\rm opt}(r)$ and exchange potentials $V_{\rm ex}^{\rm b,opt}(r)$ obtained with PSIATO and adds the O'Hara's exchange potential for free-state electrons [221] (modified to obtain consistency with the optimized exchange potential), which has the form

$$V_{\rm ex}(r,k) = 1/4[(k^2 - 2V_{\rm s}(r)) - \sqrt{(k^2 - 2V_{\rm s}(r))^2 + 16\pi\rho(r)}], \tag{52}$$

as well as the short-range correlation-polarization potential of O'Connell and Lane [222], obtained by using the LDA and assuming that the projectile is slow,

$$V_{\rm pol}^{\rm e}(r) = \begin{cases} -0.096 - 0.02r_{\rm s} + (0.0622 + 0.018r_{\rm s})\ln(r_{\rm s}), & r_{\rm s} \le 0.7, \\ -0.1231 + 0.03796\ln(r_{\rm s}), & 0.7 < r_{\rm s} \le 10, \\ -0.87r_{\rm s}^{-1} + 2.65r_{\rm s}^{-3/2} - 2.8r_{\rm s}^{-2} - 0.8r_{\rm s}^{-5/2}, & r_{\rm s} > 10, \end{cases}$$

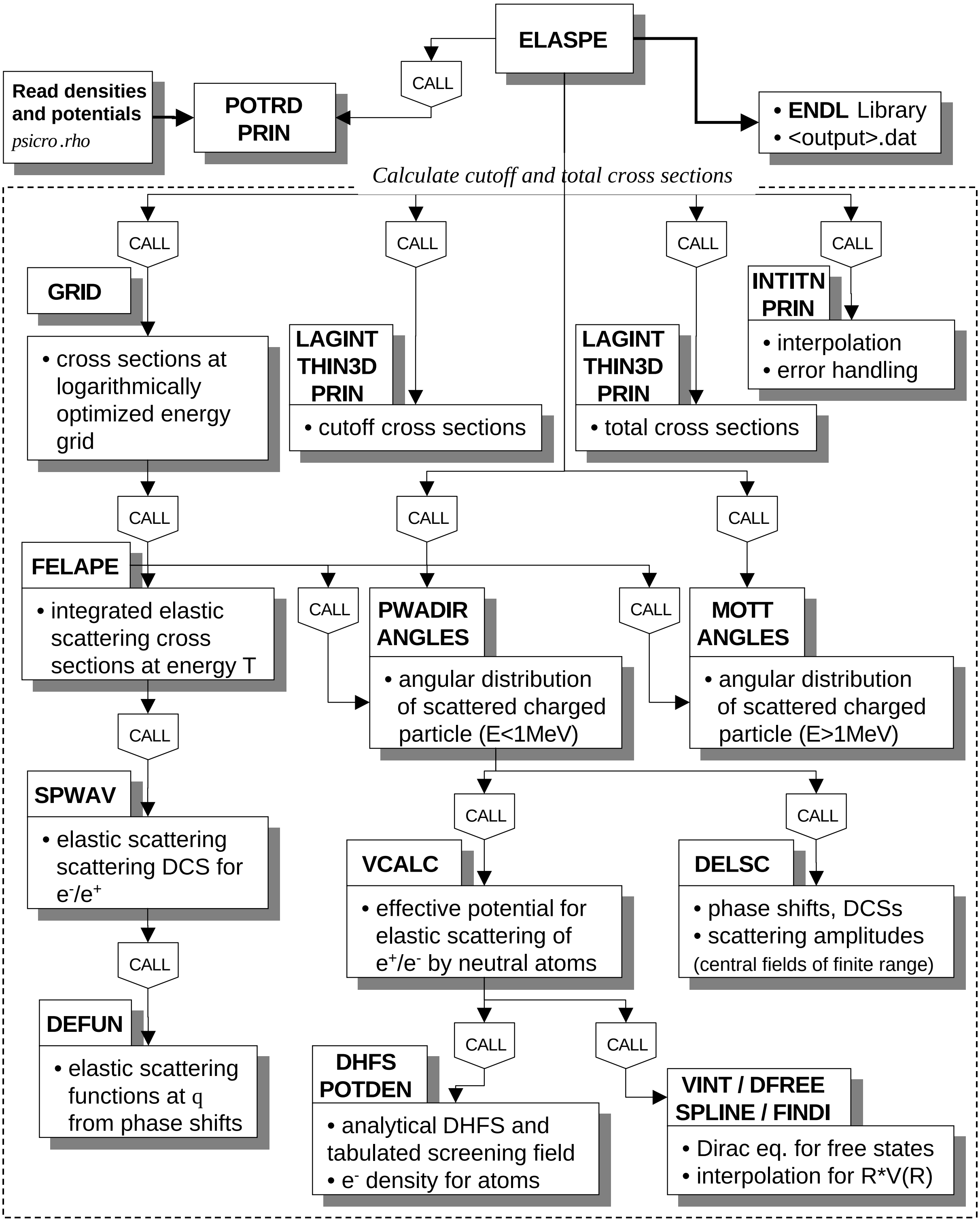

Figure 16: Flowchart of the elastic scattering cross section calculation with the code PSICRO.

with the corrections introduced by Padial and Norcross [223], that calculates the correlation-polarization potential as the functional derivarive of the free-electron-gas correlation energy with respect to the density ρ,

$$V_{\mathrm{pol}}^{\mathrm{e}}(r) = \begin{cases} -0.0584 - 0.015 r_{\mathrm{s}} + (0.0311 + 0.006 r_{\mathrm{s}}) \ln(r_{\mathrm{s}}), & r_{\mathrm{s}} \leq 0.7, \\ -0.07356 + 0.02224 \ln(r_{\mathrm{s}}), & 0.7 < r_{\mathrm{s}} \leq 10, \\ -0.584 r_{\mathrm{s}}^{-1} + 1.988 r_{\mathrm{s}}^{-3/2} - 2.45 r_{\mathrm{s}}^{-2} - 0.733 r_{\mathrm{s}}^{-5/2}, & r_{\mathrm{s}} > 10, \end{cases}$$

where k is the momentum of the electron and $r_{\mathrm{s}} \equiv 1/a_0 (3/4\pi\rho(r))^{1/3}$ is the radius of the sphere that contains (on average) one electron of the gas, in units of the Bohr radius a_0. Then, for each incident electron energy, the required phase shifts are calculated by solving the free-state Dirac equations (39). For positron elastic scattering, the only difference with respect to the theory for electrons is that, in the free-state Dirac equation, the sign of the static potential is changed and only the correlation-polarization potential for positrons based on the free-parameter model of Jain [224]

$$V_{\mathrm{pol}}^{\mathrm{p}}(r) = \begin{cases} -\frac{0.091}{r_{\mathrm{s}}^{1/2}} + (0.0255 r_{\mathrm{s}} - 0.0575) \ln(r_{\mathrm{s}}) + 0.5835, & r_{\mathrm{s}} \leq 0.302, \\ -0.461525 - 0.04549/r_{\mathrm{s}}^{2}, & 0.302 < r_{\mathrm{s}} \leq 0.56, \\ -\frac{4.3837 r_{\mathrm{s}}}{(r_{\mathrm{s}}+2.5)^3} + \frac{(-6.5755 + 0.4776 r_{\mathrm{s}})}{(r_{\mathrm{s}}+2.5)^2} + \frac{1.43275}{(r_{\mathrm{s}}+2.5)} - 0.3149, & r_{\mathrm{s}} > 0.56, \end{cases}$$

is added. As developed at present, the code PSICRO does not include any description of the absorption potential which enters in the formulation of the interaction potential given by Eq. (36).

3.3 Inelastic Scattering of Charged Particles

In general terms, inelastic scattering refers to a process in which a primary particle, such as an electron or a positron, loses a non-negligible amount of energy in the Coulomb field of an atom. Essentially, these processes are: (a) ionisation, the process of ejection of an inner-shell electron[16] (a K-shell or 1s electron), or of an outer-shell electron[17] (a L-shell, a 2s or 2p electron), and (b) the excitation process, which can consist in either the excitation of one or more phonons (quanta of lattice vibration[18]), particle-hole excitation (the interaction with a single electron in the valence band or more inner shell), or the excitation of a plasmon (a collective oscillation of the valence electrons). Figure 17 depicts the process of inelastic scattering schematically. In this section, following a short introduction, the models used to describe the inelastic scattering of electrons and positrons by neutral atoms are introduced for both processes, ionisation in Sections 3.3.2 and 3.3.3., and excitation in Sections 3.3.4. and 3.3.5, with emphasis on the development of algorithms valid for low energies.

---

[16] a localised electron; the term is usually used to refer to K-shell electrons in light atoms or K or L-shell electrons in larger atoms.

[17] a localised electron, but which is not in one of the lowest energy shells; in a small atom such as aluminium the L-shell would be considered to be an outer shell, whereas in a larger atom such as gold the outer shells would be O and P.

[18] the particle-type manifestation of thermal energy waves in solids

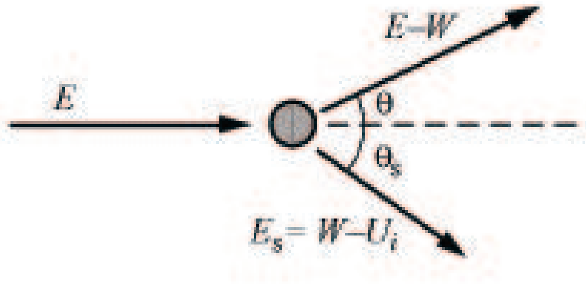

Figure 17: Ionisation process (E, the incident particle kinetic energy; W, the transferred energy, U_i the binding energy, and E, the ejected electron kinetic energy).

3.3.1 Introduction

Despite the theoretical developments achieved in recent years for the description of inelastic collisions, information about the energy-loss and angular dependence of the inelastic DCS for most materials is either scarce or is evaluated from oversimplified analytical models. As for elastic scattering, several databases are available for inelastic scattering, but they only provide information about electron and positron stopping powers above 10 keV [225, 226] and inelastic mean-free paths for low-energy electrons (from ~100 eV to a few keV) [227]. The EEDL database [146], for example, contains ionisation and excitation cross sections which have been calculated using a partly analytical formalism. More accurate calculations for inelastic scattering DCSs based on a semi-empirical optical-data model in the context of the first Born approximation have been performed for electron and positron energies between a few hundred eV and ~1 GeV [228, 229]. Using the same model, additional quantities of interest such as the total cross section, stopping power, straggling parameter and restricted inelastic transport cross sections have also been calculated.

3.3.2 Analytical models for ionisation cross sections

Electron impact inner-shell ionisation cross sections are important from both theoretical and practical points of view. Theoretically, they help to elucidate up to which extent the analytical models developed so far in the energy range from the threshold to several tens of keV are reliable, and so, a much better understanding of the electron-atom collision can be gained. Practically, data of this type are required in many fields, e.g. electron probe microanalysis, Auger electron spectroscopy and electron-energy-loss spectroscopy, as well as for the diagnosis of plasmas in both inertial and magnetic confinement fusion reactors, where considerable energy is lost in the ignition process due to X-ray production from highly stripped ions or inner-shell excitations.

This section describes the status of the theoretical description of ionisation cross sections for the removal of inner-shell or core electrons by electron and positron impact, referring exclusively to the production of single vacancies in a particular neutral atom. The main objective of the next section is to perform a detailed analysis of the existing calculated, semi-empirical and measured cross section data for the ionisation of inner-shell electrons of relatively low binding energies (less than 1500 eV) by incident electrons and positrons of low energy (less than 100 keV), considering the latest theoretical and experimental developments. Emphasis will be put on the assessment, with respect to other existing analytical models, of the degree of accuracy of the Weizsäcker-Williams method [230, 231], which has presently been used for the generation of electron and positron ionisation cross section data [117].

The theoretical developments made so far for the calculation of inner-shell ionisation cross sections have different regions of validity, no single analytical model as yet being completely successful in describing the process over a wide range of atomic numbers, atomic shells and impact energies. A systematic method for the calculation of ionisation cross sections from first-principles, particularly for energies near the ionization threshold, still remains to be formulated. However, various theoretical treatments have proven suitable for either nonrelativistic or for relativistic energies, and for low- or high-Z materials. For example, the Bethe theory provides a simple, convenient and physically sound basis for calculating inner-shell ionisation cross sections at higher energies ($U_\mathrm{i} \gg 1$, $U_\mathrm{i} = E/E_\mathrm{i}$, i.e. the ratio between the incident electron energy E and the i^{th} subshell ionisation threshold energy E_i of the target atoms, $i = K$, L_1, L_2, L_3) which ensure the validity of the first Born approximation [232, 233]. For low energies near the threshold region ($1 \leq U_\mathrm{i} \leq 4$), better agreement is achieved when using the Rudge and Schwartz formulas [234], which are based on the second Born and Born-exchange approximations. In addition, a number of semi-empirical modifications of the plane-wave Born approximation have been proposed to account for the distortion of the incident and emerging waves caused by the atomic field, and for exchange scattering (e.g. Mayol and Salvat [235], Hippler [236]). A more appropriate approach is to use the distorted-wave Born approximation [237], in which the initial and the final projectile wavefunctions include the distortion caused by the atomic field. In the following, the theories used for comparison of the DCS data will be presented in more detail.

A: The Bethe theory of inner-shell ionisation

The i^{th}-shell ionisation cross section, as derived by Bethe [238] using the first-Born approximation, is given by the following expression:

$$\sigma_\mathrm{i}(E) = \frac{2\pi e^4}{\mathrm{m_e} v^2 E_\mathrm{i}} Z_\mathrm{i} b_\mathrm{i} \ln\left[\frac{2\mathrm{m_e} v^2}{B_\mathrm{i}}\right] = \frac{6.51 \cdot 10^{-14}}{E E_\mathrm{i}} Z_\mathrm{i} b_\mathrm{i} \ln\left[\frac{c_\mathrm{i} E}{E_\mathrm{i}}\right] \tag{53}$$

where $E = (1/2)\mathrm{m_e}v^2$ is the incident electron beam energy and E_i is the binding energy of electrons in the atomic i^{th}-shell, both expressed in electron volts, Z_i is the number of electrons in that shell, b_i and B_i are the so-called Bethe parameters, and $c_\mathrm{i} = 4E_\mathrm{i}/B_\mathrm{i}$. The Bethe formula is expected to be valid when the incident electron energy, E, is much greater than the binding energy, E_i, and when the transfer energy in the ionizing collision is much less than E [239, 240]. The two parameters which appear in Bethe's formula are conveniently obtained from a linear least-squares fit to the following equation (a Fano plot [241]):

$$\frac{\sigma_\mathrm{i} E_\mathrm{i}^2 U_\mathrm{i}}{6.51 \cdot 10^{-14} Z_\mathrm{i}} = b_\mathrm{i} \ln U_\mathrm{i} + A_\mathrm{i} \tag{54}$$

where $U_\mathrm{i} = E/E_\mathrm{i}$ is also called the reduced energy and $A_\mathrm{i} = b_\mathrm{i} \ln c_\mathrm{i}$.

In order to compare cross sections for different elements, the Bethe formula (Eq. (53)) is rewritten in the following form:

$$\sigma_{\mathrm{i}} E_{\mathrm{i}}^{2} = 6.51 \cdot 10^{-14} Z_{\mathrm{i}} b_{\mathrm{i}} \ln \left[c_{\mathrm{i}} U_{\mathrm{i}} \right] / U_{\mathrm{i}}. \tag{55}$$

B: The Gryzinski binary encounter approximation

A relatively simple and widely used expression was deduced within the classical theory of inelastic atomic collisions, for both ionisation and excitation, by Gryzinski [242], on the basis of the relations for binary and Coulomb collisions derived in the laboratory system of coordinates:

$$\sigma_{\mathrm{i}}(E) = Z_{\mathrm{i}} (\sigma_0 / E_{\mathrm{i}})^2 g_{\mathrm{i}}(U_{\mathrm{i}}), \tag{56}$$

with

$$g_{\mathrm{i}}(U_{\mathrm{i}}) = \frac{1}{U_{\mathrm{i}}} \left(\frac{U_{\mathrm{i}} - 1}{U_{\mathrm{i}} + 1} \right)^{3/2} \left[1 + \frac{2}{3} \left(1 - \frac{1}{2U_{\mathrm{i}}} \right) \ln \left[2.7 + (U_{\mathrm{i}} - 1)^{1/2} \right] \right] \tag{57}$$

where Z_{i} is the number of electrons in the i^{th} subshell ($i = K$, L_1, L_2, L_3), and σ_0 a constant, the value of which for an elementary charge is $6.56 \cdot 10^{-14}$ $\mathrm{eV}^2\mathrm{cm}^2$.

This classical scaling law seems to predict the same value of σ_{i} at the same E/E_{i} for all subshells, but it fails to describe well the experimental data close to threshold (i.e. for energies less than 4 times the binding energy).

C: The McGuire neoclassical scaling law

The aplicability of the classical scaling law introduced above to subshells different than the K-shell was often questionable. Another theoretical calculation for the ionisation of atomic subshells by electrons using the partial-wave Born approximation, was proposed by McGuire [243] as expressed by the following scaled form

$$\sigma_{\mathrm{i}}(E_{\mathrm{i}})^{\alpha} = f(E/E_{\mathrm{i}}), \tag{58}$$

where $f(E/E_{\mathrm{i}})$ is obtained by plotting $\sigma_{\mathrm{i}}^{\max}(E_{\mathrm{i}})^{\alpha}$ against E_{i}, and $\alpha \neq 2$ unless E_{i} is sufficiently large. Unlike the case of K-shell ionisation, in which a simple scaling law ($\alpha = 2$) is adapted for all elements in the nonrelativistic limit, this neoclassical[19] scaling law for L-shell ionisation predicts consistent $f(E/E_{\mathrm{i}})$ features only for subshells having the same angular momentum, such as $2p_{1/2}$ and $2p_{3/2}$.

3.3.3 Theoretical models implemented in PSICRO for the generation of ionisation cross section data

The electron impact ionisation cross sections included in the EEDL library [146], as calculated originally by the code PSICRO, are obtained based on the Weizsäcker-Williams theory of virtual quanta which applies to processes involving electromagnetic interactions of relativistic particles

---

[19] does not vary inversely with the square of the ionisation potential

[230, 231]. This method exploits the similarities between the fields of rapidly moving charged particles and the fields of pulsed radiation, correlating the corresponding effects. Thus, for an incident particle of mass $\mathrm{m_e}$, charge q and velocity $v \simeq c$, the method is useful for an impact parameter $b_{\mathrm{min}} = \hbar/Q_{\mathrm{max}} \simeq \hbar/(2m_{\mathrm{e}}v)$ chosen such that, for $b > b_{\mathrm{min}}$, the effects of the incident particle's field can be accurately represented by the effects of equivalent pulses of radiation and, for $b < b_{\mathrm{min}}$, the effects of the particle's field can be neglected or taken into account by other means.

The Weizsäcker-Williams method, as implemented in the code PSICRO, has currently been used for the generation and validation of the electron impact ionisation cross section data presented in the next chapter, for each atomic shell in the energy range from electron shell binding energy, E_{i}, to 100 GeV. The total electron and positron ionisation cross sections are obtained by summing the contributions of all atomic shells. Following this method and using the improved methodology of Seltzer [244], which applies the binary encounter method to each atomic subshell, the cross sections for i^{th} orbital, differential in kinetic energy transfer W, have been calculated as a sum of two contributions arising from close and distant collisions, respectively:

$$\frac{\mathrm{d}\sigma^{\mathrm{i}}(E,W)}{\mathrm{d}W} = \frac{\mathrm{d}\sigma^{\mathrm{i}}_{\mathrm{c}}(E,W)}{\mathrm{d}W} + \frac{\mathrm{d}\sigma^{\mathrm{i}}_{\mathrm{d}}(E,W)}{\mathrm{d}W}, \tag{59}$$

where E is the kinetic energy of the incident electron/positron. The cross section for close collisions is described in terms of a collision between two electrons using the Møller's [245] formula refined by Seltzer [244],

$$\begin{aligned}\frac{\mathrm{d}\sigma^{\mathrm{i}}_{\mathrm{c}}(E,W)}{\mathrm{d}W} &= \frac{2\pi r_0^2 \mathrm{m_e} c^2}{\beta^2} Z_{\mathrm{i}} P_{\mathrm{i}} \left[\frac{1}{(W+E_{\mathrm{i}})^2} + \frac{1}{(E-W)^2} + \frac{1}{E^2}\left(\frac{\tau}{\tau+1}\right)^2 \right.\\ &\left. \qquad - \frac{2\tau+1}{(\tau+1)^2}\frac{1}{(W+E_{\mathrm{i}})(E-W)} + G_{\mathrm{i}}\right],\end{aligned} \tag{60}$$

or that of a collision between a positron and a bound electron using the Bhabha's [246] formula which was further refined by Stepanek [23, 117],

$$\begin{aligned}\frac{\mathrm{d}\sigma^{\mathrm{i}}_{\mathrm{c}}(E,W)}{\mathrm{d}W} &= \frac{2\pi r_0^2 \mathrm{m_e} c^2}{\beta^2} Z_{\mathrm{i}} P_{\mathrm{i}} \left[\frac{1}{(W+E_{\mathrm{i}})^2} + \frac{\beta^2}{E^2}\left(-B_1\frac{E}{W+E_{\mathrm{i}}} + B_2 \right.\right.\\ &\left.\left. \qquad - B_3\frac{W+E_{\mathrm{i}}}{E} + B_4\frac{(W+E_{\mathrm{i}})}{E^2}\right)^2 + G_{\mathrm{i}}\right],\end{aligned} \tag{61}$$

where Z_{i} is the number of electrons in the i^{th} orbital, E_{i} is the orbital binding energy, $\mathrm{m_e}c^2$ is the electron rest mass, τ is the kinetic energy of the incident electron/positron in units of the electron rest energy ($\tau = E/\mathrm{m_e}c^2$), r_0 is the classical electron radius, and $\beta = E(E + 2\mathrm{m_e}c^2)/(E+\mathrm{m_e}c^2)^2$. $P_{\mathrm{i}} = E/(E + E_{\mathrm{i}} + S_{\mathrm{i}})$ is the focusing term with S_{i} as the mean kinetic energy of the target electron in the i^{th} orbital. The factor G_{i} results from averaging over an isotropic distribution of orbital electron velocities and is defined as

$$G_{\mathrm{i}} = \frac{8U_{\mathrm{i}}}{3\pi}\left[\frac{1}{(W+E_{\mathrm{i}})^3} + \frac{1}{(E-W)^3}\right]\left[\arctan\sqrt{y} + \frac{\sqrt{y}(y-1)}{(y+1)^2}\right], \tag{62}$$

where $y = W/U_{\mathrm{i}}$.

The cross section for distant collisions, described in terms of the interaction of the equivalent radiation field (virtual photons) with the orbital electrons and corrected due to the density effect caused by the polarisability of the medium, can be written in the form

$$\frac{\mathrm{d}\sigma_{\mathrm{d}}^{\mathrm{i}}(E,W)}{\mathrm{d}W} = Z_{\mathrm{i}} I(W+E_{\mathrm{i}})\sigma_{\mathrm{pi}}^{\mathrm{i}}(W+E_{\mathrm{i}}), \tag{63}$$

where $\sigma_{\mathrm{pi}}^{\mathrm{i}}(E,W)$ is the photo-ionisation cross section for the i^{th} orbital per single orbital electron and for an incident photon energy $E = W + E_{\mathrm{i}}$. For the virtual-photon spectrum $I(W+E_{\mathrm{i}})$, the latest photo-ionisation cross sections distributed by LLNL in the form of a EPDL [145] file were used. The correction due to the density effects arising from the polarizability of the medium was applied, based on the Scofield's relativistic HartreeSlater method [247], which treated the medium as composed of free electrons,.

The total ionisation cross section for the i^{th} orbital is given by

$$\sigma^{\mathrm{i}}(E) = \int_0^{\mathrm{W_{max}}} \frac{\mathrm{d}\sigma^{\mathrm{i}}(E,W)}{\mathrm{d}W}\mathrm{d}W, \tag{64}$$

with W_{max} the maximum energy loss kinematically allowed (E for positrons, and $(E+U_{\mathrm{i}})/2$ for electrons).

The total ionisation cross section data thus generated are known to describe, in a satisfactory manner, experimental values in the entire energy range of interest. Somewhat larger disagreements exist between the calculated and the experimental inner-shell ionisation cross sections, especially in the threshold region. The corresponding data for positrons are calculated in a similar fashion.

3.3.4 Analytical models for excitation cross sections

Electron impact excitation for atoms has been a subject of continuing interest for gaining insight into fundamental physical processes, e.g. spin-dependent interactions in electron-atom collisions, as well as for practical applications in the fields of astrophysical plasmas, lighting technologies, gas-discharge lasers, etc. In the field of radiobiology, new requirements have been identified for micro- and nanodosimetric assessments in various applications. Consequently, there is a growing need for accurate low-energy (down to 1 eV) range cross section data for MC codes to enable the reliable modelling of the different relevant processes involved in the interaction of ionizing radiation with matter at DNA level.

Theoretical calculations of excitation cross sections have been performed earlier using the first-Born approximation [248], the relativistic distorted-wave approximation [249], close coupling [250] and R-matrix methods [251], or a simpler scaling procedure based on the plane-wave Born approximation [252]. Despite the relative simplicity compared to many other collision processes, large disagreements still exist for the prediction of excitation cross sections, not only in magnitude, but also in reproducing the cross section shape as a function of energy. The excitation cross section data included in the EEDL library [146] have been calculated, using a relatively simplistic model, assuming that all excitations arise through distant collisions from the outermost shell. More recently, calculations for liquid water shell-excitation cross sections have been performed based on the first-Born approximation, with the energy-loss spectrum modelled by employing the derivative Drude dielectric response function fitted to the available experimental data for liquid water [253]. A comparison of various optical-data models for constructing inelastic cross sections for low-energy electron transport in liquid water has been carried out [254]. This has shown the strong dependence of the shape and peak position of the total and DCSs on the dispersion algorithm adopted for incorporating momentum-transfer dependence.

The following section describes the details of a new model which has been developed for the calculation of cross section data for excitation from the ground state of neutral atoms with Z=1-100, following electron and positron scattering by conduction electrons, over a wide energy range. The aim has been to improve upon the distant collisions based algorithm, while also providing additional information characteristic of the low-energy range of interaction and of high-density systems. The model is based on the many-body field theory (MBT) and allows us to calculate new, comprehensive integrated cross sections, as well as energy and angular distribution data. In addition, the newly developed model can also be used for the generation and validation of water cross section data needed for comparison with previously developed models within the low-density approximation. The current theoretical model has been implemented in the PSICRO code and, in conjunction with the previously described models for the other interaction types (bremsstrahlung, elastic scattering, ionisation), has made it possible to provide a comprehensive calculational tool for the generation of the cross sections, down to 1 eV, necessary for MC simulations.

3.3.5 Theoretical models implemented in PSICRO for the generation of excitation cross section data

The propagation of a single charged particle, electron or positron, in a condensed medium, is considered further. In solid state physics, the medium can be described using the free-electron gas (FEG) approximation. The FEG is a model for conduction, i.e. delocalized electrons that form a uniform "free electron gas" unperturbed by the ion cores. Thus, the electrons are assumed to move unperturbed on a positive ion core neutralizing background (as for a classical gas, no interaction exist in between except collisions). The incident particle with kinetic energy E and momentum $\mathbf{p}$, just before an inelastic collision[20], interacts with the N-electron system by purely Coulomb interactions. After the collision, the particle is assumed to have the momentum $\mathbf{p}'$, the kinetic energy $E' = E - W$, and the scattering direction defined by the polar angle $\theta \equiv \arccos(\mathbf{p}, \mathbf{p}')$, with W being the energy loss and $\mathbf{q} \equiv \mathbf{p} - \mathbf{p}'$ the momentum transfer. Instead of the scattering angle, the recoil energy, $Q = \sqrt{(cq)^2 + \mathrm{m}_\mathrm{e}^2 c^4} - \mathrm{m}_\mathrm{e} c^2$ [255], is most often used.

In such many-fermion systems, the screening of a particle is generally changing due to many-body effects and, thus, the behaviour of strongly interacting real particles is commonly described with the help of the quasiparticle approximation, i.e. the positive screening charge and the bare electrons form a "Coulomb cloud" with finite lifetime, the quasiparticle, that weakly interacts with another quasiparticle. The residual interaction between quasiparticles leads to complex energies such as the proper quasiparticle self-energy, $\Sigma_\mathrm{I}(\mathbf{p})$, i.e. the energy difference between the bare and the screened particle. The imaginary part of the self-energy is assumed

---

[20] These quantities are measured in the reference frame where the stopping medium is at rest.

to be proportional to the total transition rate of the particle in the given medium, $\dot{n}(\mathbf{p})$,

$$\Sigma_{\mathrm{I}}\left(\mathbf{p}\right) = \int f\left(\mathbf{p},\mathbf{p}'\right)\mathrm{d}^3p' \approx \dot{n}\left(\mathbf{p}\right), \tag{65}$$

with $\dot{n}(\mathbf{p}) = \int \sigma(\mathbf{p},\mathbf{p}')\mathrm{d}^3p'$, so that one obtains the bulk differential transition probability from the momentum state $\mathbf{p}$ to $\mathbf{p}'$ per unit time, $\sigma(\mathbf{p},\mathbf{p}')$, as [256]

$$\sigma\left(\mathbf{p},\mathbf{p}'\right) = 2\left|f\left(\mathbf{p},\mathbf{p}'\right)\right|. \tag{66}$$

where $f\left(\mathbf{p},\mathbf{p}'\right)$ is the integrand of the imaginary part of the quasiparticle self-energy, $\Sigma_{\mathrm{I}}(\mathbf{p})$, the expression for which will be deduced further.

With $\sigma(\mathbf{p},\mathbf{p}')$ defined above, additional data such as the mean free path between collisions, $\lambda(\mathbf{p})$, the mean energy change per collision, $\mathrm{d}E(\mathbf{p})/\mathrm{d}n$, and the mean angular deflection per collision, $\mathrm{d}\theta(\mathbf{p})/\mathrm{d}n$, can be calculated using the following equations:

$$\begin{aligned}
\lambda\left(\mathbf{p}\right) &= \frac{\left[2\mathrm{m_e}E\left(\mathbf{p}\right)\right]^{1/2}}{\int\sigma\left(\mathbf{p},\mathbf{p}'\right)\mathrm{d}^3p'},\\
\dot{E}(\mathbf{p}) &= \frac{\mathrm{d}E\left(\mathbf{p}\right)}{\mathrm{d}n} = \frac{\int\sigma\left(\mathbf{p},\mathbf{p}'\right)\left[E\left(\mathbf{p}'\right)-E\left(\mathbf{p}\right)\right]\mathrm{d}^3p'}{\int\sigma\left(\mathbf{p},\mathbf{p}'\right)\mathrm{d}^3p'},\\
\dot{\theta}(\mathbf{p}) &= \frac{\mathrm{d}\theta\left(\mathbf{p}\right)}{\mathrm{d}n} = \frac{\int\sigma\left(\mathbf{p},\mathbf{p}'\right)\theta\left(\mathbf{p}'\right)\mathrm{d}^3p'}{\int\sigma\left(\mathbf{p},\mathbf{p}'\right)\mathrm{d}^3p'},
\end{aligned} \tag{67}$$

where the angle of deflection θ is measured about the direction of $\mathbf{p}$ and $E(\mathbf{p}) = p^2/2\mathrm{m_e}$.

Considering the interaction Hamiltonian in the Schrödinger picture, $\hat{H} = \hat{H}_0 + \hat{H}_{\mathrm{int}}$, as a weak disturbance to the system, the propagation of a particle (hole) added to the N-electron system has been evaluated with the help of Green's functions by using perturbation theory. Thus, the self-energy of a quasiparticle has been calculated by means of the Feynman-Dyson perturbation expansion (i.e. summing over the amplitudes of all possible intermediate states) using the free-electron[21] Green's functions, $G_0\left(\mathbf{k},\omega\right)$, expressed mathematically by:

$$G\left(\mathbf{k},\omega\right) = G_0\left(\mathbf{k},\omega\right) + G\left(\mathbf{k},\omega\right)\Sigma\left(\mathbf{k},\omega\right)G_0\left(\mathbf{k},\omega\right). \tag{68}$$

where $\mathbf{k}$ is the wave number, ω is the angular frequency, and $G\left(\mathbf{k},\omega\right) = 1/(\omega - E(\mathbf{k}) - \Sigma_{\mathrm{I}}(\mathbf{k},\omega))$ describes the particle propagation for a fully interacting system, which involves the electron/positron proper self-energy $\Sigma_{\mathrm{I}}(\mathbf{k},\omega)$.

By using the random phase approximation (RPA) [257], valid in the high-density electron gas limit such as in metals, the singularities occurring within the more widely used Hartree-Fock approximation (i.e. the wavefunction is the "Slater" determinant, which is an antisymmetrized determinantal product of one-electron orbitals) are removed, accounting at the same time for the correlations between the particles. Thus, the proper quasiparticle self-energy can be calculated as

$$\begin{aligned}
\Sigma_{\mathrm{I}}\left(\mathbf{p}\right) \equiv \Sigma_{\mathrm{RPA}}\left(\mathbf{p},\omega\right) &= \frac{i}{\left(2\pi\right)^4}\int \mathrm{d}^3k\mathrm{d}\omega' G_0\left(\mathbf{p}-\mathbf{k},\omega-\omega'\right)v_{\mathrm{eff}}^{\mathrm{P}}\left(k,\omega'\right)\\
&= \frac{1}{\left(2\pi\right)^3}\mathrm{Im}\int_{0<E(\mathbf{p}-\mathbf{k})<\omega}\mathrm{d}^3k\frac{v\left(k\right)}{\varepsilon_{\mathrm{RPA}}\left(k,\omega-E\left(\mathbf{p}-\mathbf{k}\right)+i\eta\right)},
\end{aligned} \tag{69}$$

---

[21] for a non-interacting system, i.e. when the interaction of the particle with the electron gas is set equal to zero

where the effective potential of the particle propagated through the electron gas, $v_{\text{eff}}^{\text{p}}(k,\omega)$, corresponds to an effective (screened) interaction that exponentially drops off for $r \gg 1/\lambda$, in contrast to the long range Coulomb interaction. The effective potential has been expressed with the help of the Lindhard dielectric energy-loss function [258], $\epsilon_{\text{RPA}}(k,\omega)$, which depends on the angular frequency ϵ and the wave number k. These quantities are related to the energy transfer and the recoil energy by $W = \hbar\omega$ and $Q = (\hbar k)^2/2\text{m}_\text{e} = E - W - 2\sqrt{E(E-W)}\cos\theta$, respectively. The Lindhard dielectric response function can be calculated analytically. Thus, the real, $\epsilon_\text{r}(k,\omega)$, and imaginary, $\epsilon_\text{i}(k,\omega)$, parts of this function are defined, according to certain general constrains (viz. the Bethe sum rule [238] and the Kramers-Kronig relation), by the following expressions:

$$\begin{aligned}\varepsilon_\text{r}\ (k,\omega) = 1 + \frac{2\text{m}_\text{e}e^2p_0}{\pi k^2}\{1- \\ \frac{p_0}{2k}\left[1-\left(\frac{\text{m}_\text{e}\omega}{p_0k}-\frac{k}{2p_0}\right)^2\right]\ln\left|\left[1+\left(\frac{\text{m}_\text{e}\omega}{p_0k}-\frac{k}{2p_0}\right)^2\right]/\left[1-\left(\frac{\text{m}_\text{e}\omega}{p_0k}-\frac{k}{2p_0}\right)^2\right]\right|+ \\ \frac{p_0}{2k}\left[1-\left(\frac{\text{m}_\text{e}\omega}{p_0k}+\frac{k}{2p_0}\right)^2\right]\ln\left|\left[1+\left(\frac{\text{m}_\text{e}\omega}{p_0k}+\frac{k}{2p_0}\right)^2\right]/\left[1-\left(\frac{\text{m}_\text{e}\omega}{p_0k}+\frac{k}{2p_0}\right)^2\right]\right|\Bigg\},\end{aligned} \tag{70}$$

$$\varepsilon_\text{i}\,(k,\omega) = \begin{cases} \varepsilon_{\text{i}1} = \frac{\text{m}_\text{e}e^2p_0^2}{k^3}\left[1-\left(\frac{\text{m}_\text{e}\omega}{p_0k}-\frac{k}{2p_0}\right)\right], & \frac{k}{p_0}+\frac{1}{2}\left(\frac{k}{p_0}\right)^2 \geq \frac{\text{m}_\text{e}\omega}{p_0^2} \geq \left|\frac{k}{p_0}-\frac{1}{2}\left(\frac{k}{p_0}\right)^2\right| \\ \varepsilon_{\text{i}2} = \frac{2\text{m}_\text{e}^2e^2\omega}{k^3}, & \frac{k}{p_0} \leq 2, \qquad 0 \leq \frac{\text{m}_\text{e}\omega}{p_0^2} \leq \frac{k}{p_0}-\frac{1}{2}\left(\frac{k}{p_0}\right)^2. \end{cases} \tag{71}$$

where p_0 is the Fermi momentum and e is free particle electrical charge.

Thus, knowledge of the dielectric function allows the calculation of the double DCS per electron in the FEG, as following

$$\frac{\text{d}^2\sigma_{\text{FEG}}}{\text{d}k\text{d}\omega} = \frac{2\pi e^4}{\hbar E}\frac{1}{k\omega}\frac{\text{d}f_\text{L}(k,\omega)}{\text{d}\omega} \tag{72}$$

where the quantity

$$\frac{\text{d}f_\text{L}(k,\omega)}{\text{d}\omega} = \frac{4\text{m}_\text{e}}{\pi\omega_0^2}\frac{\omega}{k^2}\text{Im}\left(\frac{-1}{\varepsilon_{\text{RPA}}(k,\omega)}\right) = \frac{4\text{m}_\text{e}}{\pi\omega_0^2}\frac{\omega}{k^2}\frac{\varepsilon_\text{i}(k,\omega)}{\varepsilon_\text{r}^2(k,\omega)+\varepsilon_\text{i}^2(k,\omega)} \tag{73}$$

represents the generalized oscillator strength (GOS) per electron in the FEG, expressed in terms of the complex dielectric function, and $\omega_0 = \sqrt{3r_\text{s}^{-3}\text{m}_\text{e}e^4/\hbar^3}$ is the plasma frequency of the FEG, an intrinsic characteristic of each material.

Due to the properties of ϵ in the ω-k plane (Fig. 18), three different contributions to the imaginary part of proper self-energy, expressed in Eq. (69), can be identified. For consistency with the solid-state models from which they have been derived, the three components are termed "phonon", $\Sigma_{\text{I}_{\text{pho}}}(\mathbf{p})$, "particle-hole", $\Sigma_{\text{I}_{\text{ph}}}(\mathbf{p})$, and "plasmon", $\Sigma_{\text{I}_{\text{pl}}}(\mathbf{p})$, excitation:

$$\Sigma_{\text{RPA}}\,(\mathbf{p}) = \Sigma_{\text{I}_{\text{pho}}}\,(\mathbf{p}) + \Sigma_{\text{I}_{\text{ph}}}\,(\mathbf{p}) + \Sigma_{\text{I}_{\text{pl}}}\,(\mathbf{p}) \tag{74}$$

The FEG approximation is first used to calculate the three contributions given above, and, in a second step, the particle-hole excitation part is generalized to describe discrete excitations of atomic electrons bound in individual electronic shells.

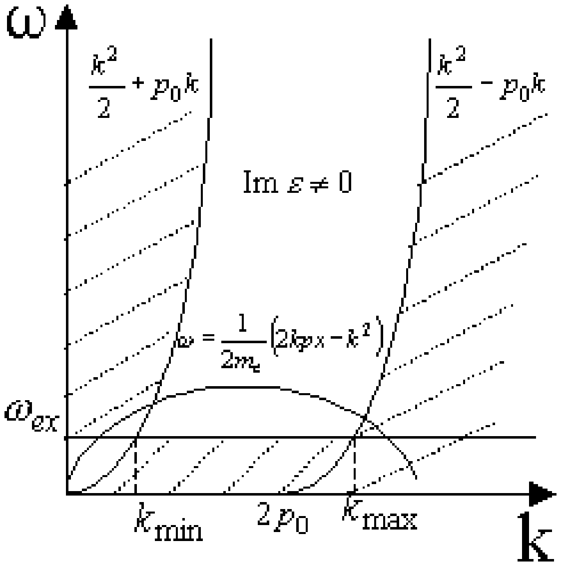

Figure 18: The excitation region of the free-electron gas in space (the Lindhard continuum).

A: Phonon excitation cross sections

Temperature-dependent phonon excitation data have been evaluated by Perkins and Carbote [259] within the Debye model (i.e. approximating the phonon density of states as a constant up to a cutoff frequency) using Migdal's approximation (i.e. retaining only the lowest-order self-energy corrections due to particle-phonon interaction) and including finite temperature effects. In order to calculate the phonon component of the proper self-energy defined by Eqs. (69), (70) and (71), the Lindhard dielectric function has been approximated by its high energy and low momentum transfer limit (here neglecting the dispersion),

$$\varepsilon\left(k,\omega\right) \approx 1 - \omega_0^2/\omega^2, \tag{75}$$

Thus, the phonon contribution, $\Sigma_{\mathrm{I_{pho}}}(\mathbf{p})$, is given by:

$$\begin{aligned}\Sigma_{\mathrm{I_{pho}}}\left(\mathbf{p},\mathbf{p}-\mathbf{k}\right) = {} & \frac{\gamma^2}{4\pi^2}k\left\{\left[\eta\left(k\right)+1\right]\delta\left(E\left(p\right)-v_{\mathrm{s}}k-E\left(\mathbf{p}-\mathbf{k}\right)\right)\Theta\left(\omega_{\mathrm{D}}-\omega\left(k\right)\right)+\right.\\ & \left.\eta\left(k\right)\delta\left(E\left(p\right)+v_{\mathrm{s}}k-E\left(\mathbf{p}-\mathbf{k}\right)\right)\Theta\left(\omega_{\mathrm{D}}-\omega\left(k\right)\right)\right\}, \qquad (76)\end{aligned}$$

where $\omega(k) = v_{\mathrm{s}}k$ is the phonon energy with v_{s} the speed of sound, $\omega_{\mathrm{D}} = v_{\mathrm{s}}k_{\mathrm{D}}$ is the Debye frequency, $\eta(k) = [\exp(v_{\mathrm{s}}k/k_{\mathrm{B}}T)]^{-1}$ is the Bose-Einstein distribution function, and $\gamma^2 = (Z^2\pi^2e^4/\lambda_{\mathrm{TF}}^4)(8N/Mv_{\mathrm{s}})$ is the square of the positron-photon coupling constant, Z is the valence, N is the ion density, $M$is the ion mass, $\lambda_{\mathrm{TF}}^2 = 6\pi ZN/\epsilon_{\mathrm{F}}$ is the Thomas-Fermi screening length for the electrons and $\epsilon_{\mathrm{F}} = 1/2(9\pi/4)^{2/3}r_{\mathrm{s}}^{-2}me^4/\hbar^2$ is the Fermi energy.

The total inelastic electron and positron-phonon scattering rate, $\dot{n}(\mathbf{p})$, given by Eq. (65), the energy loss rate, $\dot{E}(\mathbf{p})$, and the mean rate of angular deflections from phonon collisions, $\dot{\theta}(\mathbf{p})$, given in Eq. (67), have been obtained by integration of the above relations over all momentum transfer, $\mathbf{k}$, multiplied with an weighting factor, $\alpha(\mathbf{k})$, defined by

$$\alpha(\mathbf{k}) = \begin{cases} 1, & \text{for total transition rate} \\ \pm v_{\mathrm{s}} k, & \text{for the mean energy loss rate} \\ \alpha(\mathbf{k},\mathbf{x}) = \sin^{-1}\left(\frac{k(1-x^2)^{(1/2)}}{(p^2+k^2-2pkx)^{(1/2)}}\right), & \text{for mean rate of angular deflection.} \end{cases} \tag{77}$$

B: Particle-hole excitation cross sections

The free-electron particle-hole contribution to the single particle proper self-energy, $\Sigma_{\mathrm{I_{ph}}}(\mathbf{p})$, arises, as shown in Eqs. (69), (70) and (71), from finite $\epsilon_{\mathrm{i}}(k,\omega)$ (Fig. 18) and is given by [256]:

$$\Sigma_{\mathrm{I_{ph}}}(p) = \frac{1}{(2\pi)^3}\mathrm{Im}\int_{0<E(\mathbf{p}-\mathbf{k})<\omega_{\max}(p)} \mathrm{d}^3k \frac{v(k)}{\varepsilon\left(k, E(p) - E(\mathbf{p}-\mathbf{k}) + i\eta\right)}, \tag{78}$$

where the maximum energy loss $\omega_{\max}$ is equal to $E(\mathbf{p})$ and $[E(\mathbf{p}) - E_{\mathrm{F}}]/2$ for positrons and electrons, respectively. Also, only for electrons, in addition to the Pauli's exclusion principle which forbids transitions that would place the projectile into a filled Fermi sphere, the effect of exchange interaction has been considered by means of the Born-Ochkur approximation [212]:

$$F_{\mathrm{ex}}(k,\omega) = 1 - \frac{4k^2}{p - 2\mathrm{m_e}\omega} + \frac{16k^4}{(p - 2\mathrm{m_e}\omega)^2}. \tag{79}$$

For particles with incident energies below the Fermi level, the above integral in $\mathbf{k}$ momentum space consists of only one branch, while for higher energies a second contribution, given by points in the region bounded by the two limits of the $\varepsilon_{\mathrm{i2}}(k,\omega)$ (Fig. 18), is added:

$$\begin{aligned} \Sigma_{\mathrm{I_{ph}}}(p) &= \frac{e^2}{\pi}\mathrm{Im}\int_0^1 \mathrm{d}x \int_0^{2px} \mathrm{d}k \frac{1}{\varepsilon_{\mathrm{r}}(k,\omega) + i\varepsilon_{\mathrm{i_2}}(k,\omega)} F_{\mathrm{ex}}(k,\omega) \qquad , \text{for } p \le p_0 \\ &= \frac{e^2}{\pi}\mathrm{Im}\left(\int_0^{p_0/p} \mathrm{d}x \cdot \int_0^{2px} \mathrm{d}k \frac{1}{\varepsilon_{\mathrm{r}}(k,\omega) + i\varepsilon_{\mathrm{i_2}}(k,\omega)} + \right. \\ &\qquad \left. \int_{p_0/p}^1 \mathrm{d}x \cdot \int_{px-p_0}^{px+p_0} dk \frac{1}{\varepsilon_{\mathrm{r}}(k,\omega) + i\varepsilon_{\mathrm{i_1}}(k,\omega)}\right) F_{\mathrm{ex}}(k,\omega) \qquad , \text{for } p > p_0 \end{aligned} \tag{80}$$

It is in particular the above equation, describing the free-electron excitation model, which has currently been modified in order to treat the excitation process by electrons bound in atomic subshells. For the bound-electron case, an additional parameter has been taken into account - the excitation energy, ω_{ex} - which forbids transitions for incident electrons and positrons with energy below this cutoff:

$$\Sigma_{\mathrm{I_{ph}}}(p) = \frac{1}{(2\pi)^3}\mathrm{Im}\int_{\omega_{\mathrm{ex}}<E(\mathbf{p}-\mathbf{k})<\omega_{\max}(p)} \mathrm{d}^3k \frac{v(k)}{\varepsilon\left(k, E(p) - E(\mathbf{p}-\mathbf{k}) + i\eta\right)} \tag{81}$$

In order to preserve the delta behaviour of the proper self-energy at the excitation momentum transfer, k_{ex}, we assume $\omega_{\mathrm{ex}} = 1/(2\mathrm{m_e})(2pk_{\mathrm{ex}}x - k_{\mathrm{ex}}^2)$ so that the new contributions to the imaginary part of the proper self-energy are given by:

$$\begin{aligned}\Sigma_{\mathrm{I_{ph}}}(p) &= \frac{e^2}{\pi}\mathrm{Im}\int_0^1 \mathrm{d}x\int_{k_{\mathrm{ex}}}^{2px-k_{\mathrm{ex}}}\mathrm{d}k\frac{1}{\varepsilon'_{\mathrm{r}}(k,\omega)+i\varepsilon'_{\mathrm{i}_2}(k,\omega)}F'_{\mathrm{ex}}(k,\omega) \qquad , \text{ for } p\le p_0\\ &= \frac{e^2}{\pi}\mathrm{Im}\left(\int_0^{\frac{\sqrt{p_0^2+2\mathrm{m_e}\omega_{\mathrm{ex}}}}{p}}\mathrm{d}x\cdot\int_{k_{\mathrm{ex}}}^{2px-k_{\mathrm{ex}}}\mathrm{d}k\frac{1}{\varepsilon'_{\mathrm{r}}(k,\omega)+i\varepsilon'_{\mathrm{i}_2}(k,\omega)}+\right.\\ &\qquad \left.\int_{\frac{\sqrt{p_0^2+2\mathrm{m_e}\omega_{\mathrm{ex}}}}{p}}^{1}\mathrm{d}x\cdot\int_{px-p_0}^{px+p_0}\mathrm{d}k\frac{1}{\varepsilon'_{\mathrm{r}}(k,\omega)+i\varepsilon'_{\mathrm{i}_1}(k,\omega)}\right)F'_{\mathrm{ex}}(k,\omega),\ \text{ for } p>p_0\end{aligned} \tag{82}$$

where the new real, $\varepsilon'_{\mathrm{r}}(k,\omega)$, and imaginary, $\varepsilon'_{\mathrm{i}}(k,\omega)$, parts of the Lindhard dielectric function, that correspond to the case of excitation of an electron bound in an electronic shell, are defined by:

$$\begin{aligned}\varepsilon'_{\mathrm{r}}(k,\omega) &= 1+\frac{2\mathrm{m_e}e^2p_0}{\pi(k-k_{\mathrm{ex}})^2}\{1-\\ &\frac{p_0}{2(k-k_{\mathrm{ex}})}\left[1-\left(\frac{px-k}{p_0}\right)^2\right]\ln\left|\left[1+\left(\frac{px-k}{p_0}\right)\right]/\left[1-\left(\frac{px-k}{p_0}\right)\right]\right|+\\ &\frac{p_0}{2(k-k_{\mathrm{ex}})}\left[1-\left(\frac{px-k_{\mathrm{ex}}}{p_0}\right)^2\right]\ln\left|\left[1+\left(\frac{px-k_{\mathrm{ex}}}{p_0}\right)\right]/\left[1-\left(\frac{px-k_{\mathrm{ex}}}{p_0}\right)\right]\right|\Bigg\}\end{aligned} \tag{83}$$

$$\varepsilon'_{\mathrm{i}}(k,\omega)=\begin{cases}\varepsilon'_{\mathrm{i1}}=\frac{\mathrm{m_e}e^2p_0^2}{(k-k_{\mathrm{ex}})^3}\left[1-\left(\frac{px-k}{p_0}\right)^2\right], & \frac{k}{p_0}+\frac{1}{2}\left(\frac{k}{p_0}\right)^2\ge\frac{\mathrm{m_e}\omega}{p_0^2}\ge\left|\frac{k}{p_0}-\frac{1}{2}\left(\frac{k}{p_0}\right)^2\right|\\ \varepsilon'_{\mathrm{i2}}=\frac{2\mathrm{m_e}e^2p_0}{(k-k_{\mathrm{ex}})^2}\left(\frac{px}{p_0}-\frac{k+k_{\mathrm{ex}}}{2p_0}\right), & \frac{k}{p_0}\le 2,\qquad 0\le\frac{\mathrm{m_e}\omega}{p_0^2}\le\frac{k}{p_0}-\frac{1}{2}\left(\frac{k}{p_0}\right)^2\end{cases} \tag{84}$$

and which, for any momentum transfer, satisfy the Bethe sum rule [238]:

$$\int_0^\infty \omega\varepsilon'_i(k,\omega)\,\mathrm{d}\omega=\frac{\pi}{2}\omega_0. \tag{85}$$

C: Plasmon excitation cross sections

The plasmon contribution to the imaginary part of the proper self-energy, defined by Eqs. (69), (70) and (71), $\Sigma_{\mathrm{I_{pl}}}(\mathbf{p})$, arises from the poles of $\varepsilon^{-1}(k, E(p)-E(\mathbf{p}-\mathbf{k})+i\eta)$ which fall within the domain of the integration:

$$\Sigma_{\mathrm{I_{pl}}}(p)=\frac{1}{(2\pi)^3}\int_{\mathrm{oval}}\mathrm{d}^3k\mathrm{Im}\frac{\upsilon(k)}{\varepsilon(k,E(p)-E(\mathbf{p}-\mathbf{k})+i\eta)},\qquad p>p_{\mathrm{th}} \tag{86}$$

For this interaction, as for the phonon excitation case, the Lindhard dielectric function, $\varepsilon(k,\omega)$, has been approximated by its high energy, low wave vector form, as expressed by Eq. (75). It has been shown that both the positron and electron threshold momenta are equal, as also are the corresponding self-energy contributions [256]:

$$\Sigma_{\mathrm{I_{pl}}}(p)=\frac{\mathrm{m_e}e^2\omega_0}{2p}\ln\left(\frac{\left(p_0^2+2\mathrm{m_e}\omega_0\right)^{1/2}-p_0}{p-\left(p^2+2\mathrm{m_e}\omega_0\right)^{1/2}}\right),\qquad p>p_{\mathrm{th}} \tag{87}$$

3.4 Summary

In this chapter, theoretical models used for the calculation of bremsstrahlung emission, as also the elastic and inelastic scattering of electrons and positrons by neutral atoms, in particular in the medium to low-energy range, have been described. For each interaction type, the models implemented in the code PSICRO have been presented together with similar models available in the literature. A critical comparison of the various theoretical models will be performed in the next chapter. In conjunction with experimental comparisons, this will help ensure that reliable cross section data have been made available for MC simulations.

For bremsstrahlung emission, analytical models based on Bethe-Heitler theory and the partial-wave analysis method have been presented. Special emphasis has been put on the description of the approximations used for the generation of state-of-the-art low-energy numerical cross sections for bremsstrahlung emission that are needed for the detailed and accurate simulation of particle transport in different materials.

The partial wave analysis method, used currently to describe the elastic scattering of charged particles by neutral atoms, together with its implementation into the currently upgraded version of the code PSICRO, has also been presented. The model is relatively simple and somewhat "incomplete" because it does not account for the loss of flux from the elastic to the inelastic channels above the excitation threshold.

The Weizsäcker-Williams method is currently used with the code PSICRO for the calculation of K-shell and L-shell ionisation cross section data in the energy range from the ionisation threshold to 100 GeV. This method is known not to predict good results near the threshold. In this chapter, the basic equations of this formalism have been introduced together with similar theoretical models developed more recently.

The proposed MBT model implemented in the code PSICRO provides a detailed description of the excitation process from the ground state of neutral atoms (Z=1 to 100) in the energy range from 1 eV to 1 MeV. In the high-energy range, the original LLNL formalism for excitation cross section data, that considers distant ('resonance') collisions, is retained. The program calculates integrated cross sections, energy loss, and average angular distributions of the incident particle and the emitted photon, for phonon, particle-hole and plasmon excitation for incident electrons and positrons for the free-electron case. In addition, a model for the construction of bound-electron particle-hole excitation cross sections, based on the free-electron Lindhard dielectric energy-loss function, has been proposed.

4 Interaction Cross Section Data Generated with PSICRO and Their Validation

This chapter presents calculations of bremsstrahlung, elastic and inelastic (ionisation and excitation) cross sections of electrons and positrons by neutral atoms, using the theoretical models implemented in PSICRO. For validation purposes, comparisons have been made with other theoretical results and/or experimental data. The resulting assessment of the implemented models for generating cross sections down to 1 eV electron energy ensures that a reliable set of data is made available for the accurate MC simulation of low-enegy secondary electron distributions. As mentioned in Section 1.1.3, this work has been performed in order to meet the requirements of the 5^{th} EU-FWP on Low Dose Risk Models, i.e. the provision of electron and positron cross section data libraries down to 1 eV.

4.1 Bremsstrahlung Emission

In the course of the present thesis work, the electron cross section data for bremsstrahlung emission included in the original EEDL library [146] have been first extended down to 1 eV incident electron energy. To achieve this, the Lagrange extrapolation method, integrated into the code PSICRO, has been used for the calculation of the bremsstrahlung cross section data down to 1 eV incident electron energy (see Section 3.1.4.). Thus, a new electron data library has currently been generated in the ENDL *(Evaluated Nuclear Data Library)* format which includes cross section data, normalized angular distributions, normalized energy spectra and energy deposition terms.

In Fig. 19 (*left*), macroscopic bremsstrahlung emission cross sections (or the inverse mean free path[22]) down to 1 eV, as a function of incident electron energy T_1, are shown for various materials from hydrogen (^{1}H) to lead (^{82}Pb). The greater importance of high-Z absorbers, relative to low-Z materials, as regards the radiative energy loss, is clearly seen.

In a second step, the calculation and generation of bremsstrahlung emission cross section data for positrons has also been considered based on the algorithm described by Eqs. (31) and (32). Figure 19 (*right*) displays, for comparison, bremsstrahlung emission cross sections for electrons and positrons in the field of several selected atoms: beryllium (^{4}Be), copper (^{29}Cu), silver (^{47}Ag) and lead (^{82}Pb). It can be seen that the differences between the two sets of cross-section data (corresponding to the two different type of particles) increase with increasing atomic number and for lower incident energies. The results for bremsstrahlung emission by positrons have been included in an additional cross section data library which has been generated in ENDL format, similarly to the original EEDL library [117, 118].

---

[22] The macroscopic cross section, which is the product of the microscopic cross section and the number of particles per unit volume, has units of inverse length. Macroscopic entities are used in the simulation of particle propagation in macroscopic media.

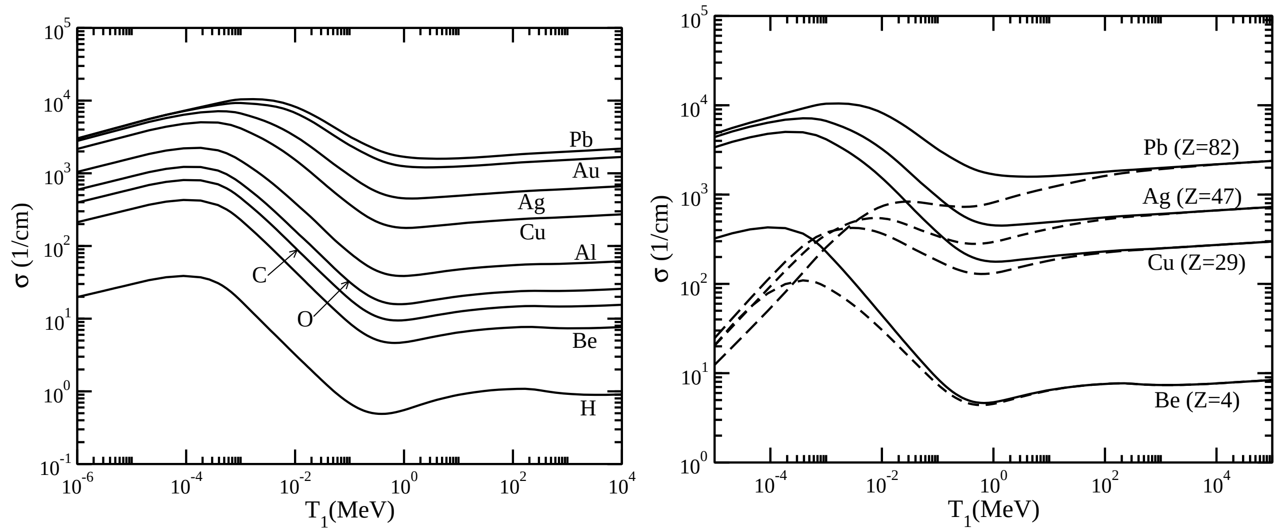

Figure 19: Bremsstrahlung emission cross sections $\sigma_{\rm br}$ as a function of the incident electron energy T_1 in the field of hydrogen, beryllium, carbon, oxygen, aluminium, copper, silver, gold and lead atoms (*left*). Bremsstrahlung emission cross sections by electrons (*continuous line*) and positrons (*dashed line*) for beryllium, copper, silver and lead (*right*).

4.2 Elastic scattering

The comparison of calculated partial-wave DCSs for the elastic scattering of electrons and positrons by various elements, in particular by rare-gases, with experimental data from the literature has been performed previously by several authors [119, 116], considering various elastic scattering models, and especially for intermediate incident particle energies ($\sim 100-500$ eV). In this section, for the same range of energies, further comparison between the results obtained with PSICRO and other theoretical models described in Section 3.2.2, as well as with experimental data, is done for electron elastic scattering by several neutral metal atoms such as sodium (^{11}Na), potassium (^{19}K), copper (^{29}Cu) and gold (^{49}Au) [117]. In addition, the study of electron scattering in rare-gases has been extended to energies below 10 eV, for which an extensive comparison of calculated and experimental data is shown. Differential cross section data for positron elastic scattering have been analysed and reported previously [117].

For the generation of elastic DCSs with PSICRO, the scattering model described in Section 3.2.3 has been used. Thus, the effective interaction potential $V(r)$, given by Eq. (36), consists of the variationally optimized static potential $V_{\rm st}^{\rm opt}(r)$, and exchange potential $V_{\rm ex}^{\rm b,opt}(r)$ for the description of the bound-electron states [219], O'Hara's exchange potential $V_{\rm exch}(r)$, given by Eq. (52), for the description of free-electron states [221], and the correlation-polarization potential of O'Connell and Lane $V_{\rm pol}(r)$, given by Eq. (53) [222, 223], and introduced at lower energies in order to take into account the influence brought in by polarization of the target by the incident particle. For positrons, the exchange potential has been excluded from the description of the effective interaction potential as shown in Eq. (36), the sign of the static potential is changed, and, for the correlation-polarization potential, the free-parameter model of Jain [224] given by Eq. (53) is used. The theoretical DCS results generated with PSICRO by using this method are shown as a continuous line in Figs. 17-26.

Additional theoretical calculations have been considered in the present study for comparison. Thus, the electron elastic DCSs generated with PSICRO are displayed together with results of two additional models obtained by combining the different elastic scattering models options offered by the code ELSEPA [119, 120]. As mentioned in Chapter 2, this code can accurately handle various elastic scattering interactions, in particular at medium to low energies (up to few hundred eV), providing a detailed description of the interaction potential (Eq. (36)), necessary for solving the Dirac equation. Thereby, the nuclear target charge distribution model $\varphi_{\mathrm{n}}(r)$, given by Eq. (33) and considered in the description of the static scattering potential V_{st} between the projectile and the target, has employed a Fermi distribution [200]. Similarly, the ground-state atomic electron density $\varphi_{\mathrm{e}}(r)$, has been obtained from a Dirac-Hartree-Fock density distribution [204, 199]. The exchange effects for electrons have presently been described considering two different models for additional comparison purposes: the Thomas-Fermi exchange potential V_{TF} [207, 208], and the Furness-McCarthy exchange potential V_{FM} [209]. The polarization potential V_{pol}, has been modelled [119] by using a long-range polarization potential combined with the correlation potential obtained from the LDA [211]. Moreover, the code ELSEPA uses an absorption potential $W_{\mathrm{abs}}^{(\mathrm{nr})}$, first introduced by Salvat [119], in order to describe an extremely important effect at low energies, caused by the loss of particles from the elastic channel to inelastic channels. The results corresponding to the two different elastic scattering models (refered to further in this thesis as the "Thomas-Fermi" and "Furness-McCarthy" models) are shown in Figs. 20-30 as dashed and dashed-dot lines, respectively.

4.2.1 Data generation and validation for energies above 10 eV

- Sodium (Z=11): Electron-sodium scattering experiments and calculations at intermediate impact energies have been extensively performed over the past decade due to their practical as well as theoretical importance. In practice, DCSs are important in sodium plasma modelling, while from a theoretical point of view, certain similarities are expected with the hydrogen atom due to the resemblance of the electronic configurations (i.e. an inert core with a single valence electron in the outer shell). Electron elastic scattering by sodium has been measured by Gehenn and Reichert [260] for an energy range between the first excitation threshold to 20 eV and over the angular range from 25° to 150°, by Teubner *et al.* [261] for 54.4-150 keV energies and an angular range between 12° and 140°, by Srivastava and Vuskovic [262] for 10 to 54.4 eV incident electron energies and 10° to 120° angular range, by Allen *et al.* [263] for 54.4 eV and angles from 10° to 140°, by Marinkovic *et al.* [264] for 10, 20 and 54.4 eV and for angles between 6° and 150°, and by Lorentz and Miller [265]. Theoretical calculations of the elastic DCSs using the two-states close coupling method have been made by Carse [266] from 20 to 200 eV and Issa [267] and using the coupled-chanel optical theory by McCarthy *et al.* [268] at 54.4 eV and Mitroy *et al.* [269] for energies between 10 and 150 eV. Additional calculations have been done by Balashov *et al.* [270] from 20 to 100 eV using the distorted wave approximation with a phenomenological optical potential and by Madison *et al.* [271] from 10 to 150 eV incident electron energy using the second-order distorted wave approximation with electron exchange included. However, due to the large discrepancies existing between different sets of experimental data, as well as when compared with various theoretical approaches, the DCSs are not yet known with the desired accuracy, the need for further studies being stressed in this context [269].

The results of the elastic DCSs of electrons scattered by sodium obtained with the partial-wave method described in Chapter 3 are shown in Fig. 20 for four energies between 10 and 100 eV. Experimental values by Teubner *et al.* [261], Srivastava and Vuskovic [262], Marinkovic *et al.* [264], Lorentz and Miller [265] are also included for comparison. At 10 and 20 eV, where the differences between the three theoretical calculations seem to increase, the angular distribution exhibits two minima, the first one prominent, whereas the second becomes exceedingly dominant with increasing energy. The position of these minima, as well as their magnitude seem to be well described by the partial-wave calculations obtained with PSICRO at all energies and, overall, a very good agreement is obtained with the experimental data (10% [262] to maximum 30% [265] differences, while errors of maximum 30% were reported experimentally), even though this model does not account for the absorption interaction. At lower energies, PSICRO gives results which have the same peak position as the model which considers the exchange effects described by the Thomas-Fermi potential, while at higher energies, its results practically coincide with those given by the Furness-McCarthy exchange potential. In particular for lower energies, the agreement of the experimental data of Srivastava and Vuskovic [262] with the results of the current theoretical models, in the forward angle domain, is very good (about 5%). This shows that these models properly account for the exchange and, in particular, for the strong absorption and polarization effects known to be present in the sodium atom, largely due to the loosely bound valence electron.

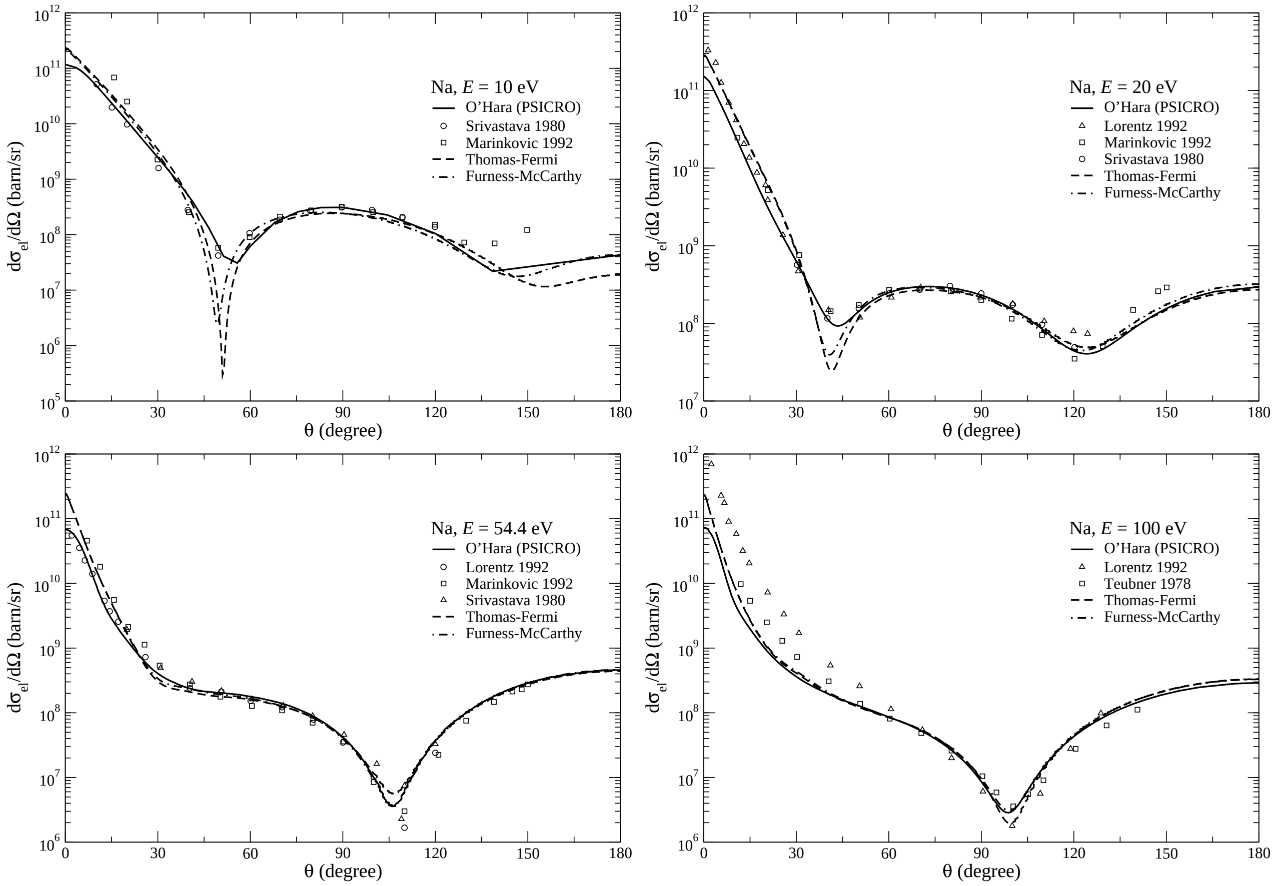

Figure 20: Comparison of partial-wave differential cross sections (*lines*) with experimental data (*symbols*) for electron elastic scattering by sodium at four impact energies.

- Potassium (Z=19): As with other alkali atoms, potassium has received particular attention from both theoretical and experimental point of views: it represents an ideal testing ground for general scattering theories and, in spite of its high chemical activity, it is preferred to hydrogen because it is easier to produce. Among the experimental work performed on potassium, relative measurements have been reported by McMillan [272] for 25° to 160° angular range and 5 to 150 eV incident energies, by Gehenn and Wilmers [273] for angles between 25° to 150° and impact energies between 0.9 to 15 eV, by Eyb [274] from 2 to 3.2 eV and 20°-140° scattering angles, and by Rao [275] in the energy range from 150 to 500 eV and angular range from 30° to 120°, while normalized DCSs have been reported by Williams and Trajmar [276] for 6.7 to 60 eV, Buckman *et al.* [277] in the energy range 54.4 to 217.7 eV, and Vuskovic and Srivastava [278] from 7 to 100 eV incident energy. Theoretical non-relativistic calculations have been performed by Buckman *et al.* [277], whereas relativistic partial wave theory for scattering for an effective potential has been applied by Gregory and Fink [279]. First-order distorted-wave polarized orbital results have been published by Kennedy *et al.* [280], close coupling calculations by McCarthy *et al.* [268] and Bray *et al.* [281, 282], and second-order distorted wave calculations by Madison *et al.* [283]. The principal reason for the divergence between the various sets of cross section data arises from the normalization method employed in order to obtain the absolute values. As yet, no satisfactory experimental method exists for determining the absolute values of metal vapour cross sections. Therefore, a reliable set of theoretical calculations is always necessary in order to perform normalization of the experimental data for low-energy electron scattering.

Figure 21 shows the comparison of calculated and experimental elastic DCSs of electrons scattered by potassium at various energies in the range between 7 and 400 eV. The theoretical calculations have been performed using the partial-wave method described in Sections 3.2.2 and 3.2.3. A large set of experimental data, such as those of Gehenn and Wilmers [273], Williams and Trajmar [276], Buckman *et al.* [277], Vuskovic and Srivastava [278], and Rao [275], has been included for the comparison. As in the case of sodium, the angular distributions exhibits two minima at lower energies (below 100 eV) and only one single minimum is seen in the backward scattering direction (>90°) for higher energies. The results obtained with PSICRO agree very well with those given by the Furness-McCarthy model at energies above 20 eV, and they seem to agree better with those given by the Thomas-Fermi model at lower energies. A very good agreement between all calculated sets of data and the experimental values is obtained in the whole range of energies considered, in particular for energies below 50 eV, a region for which earlier theoretical work reported differences of the order of at least 50%.

- Copper (Z=29): As in the case of other metal vapours, studies of electron-copper scattering have been carried out in the past mainly due to the interest in the development of high-power lasers. Experimental elastic DCSs have been reported by Trajmar *et al.* [284] in the energy range between 6 and 100 eV and the angular range between 0° and 180°, and by Madison *et al.* [285] for 40 to 100 eV electron incident energy and 14° and 130° scattering angle. The absolute values were obtained in both experiments by normalizing the experimental results at 100 eV and 40° to theoretical calculations based on the static-exchange method [286] which is known to neglect polarization effects. Fink and Ingram [186] performed relativistic non-exchange approximation calculations using Hartree-Fock-Slater bound-state atomic wavefunctions, whereas theoretical four-state close-coupling method calculations were made by Msezane and Henry [287] in the energy range of 6-100 eV. First and second order distor-

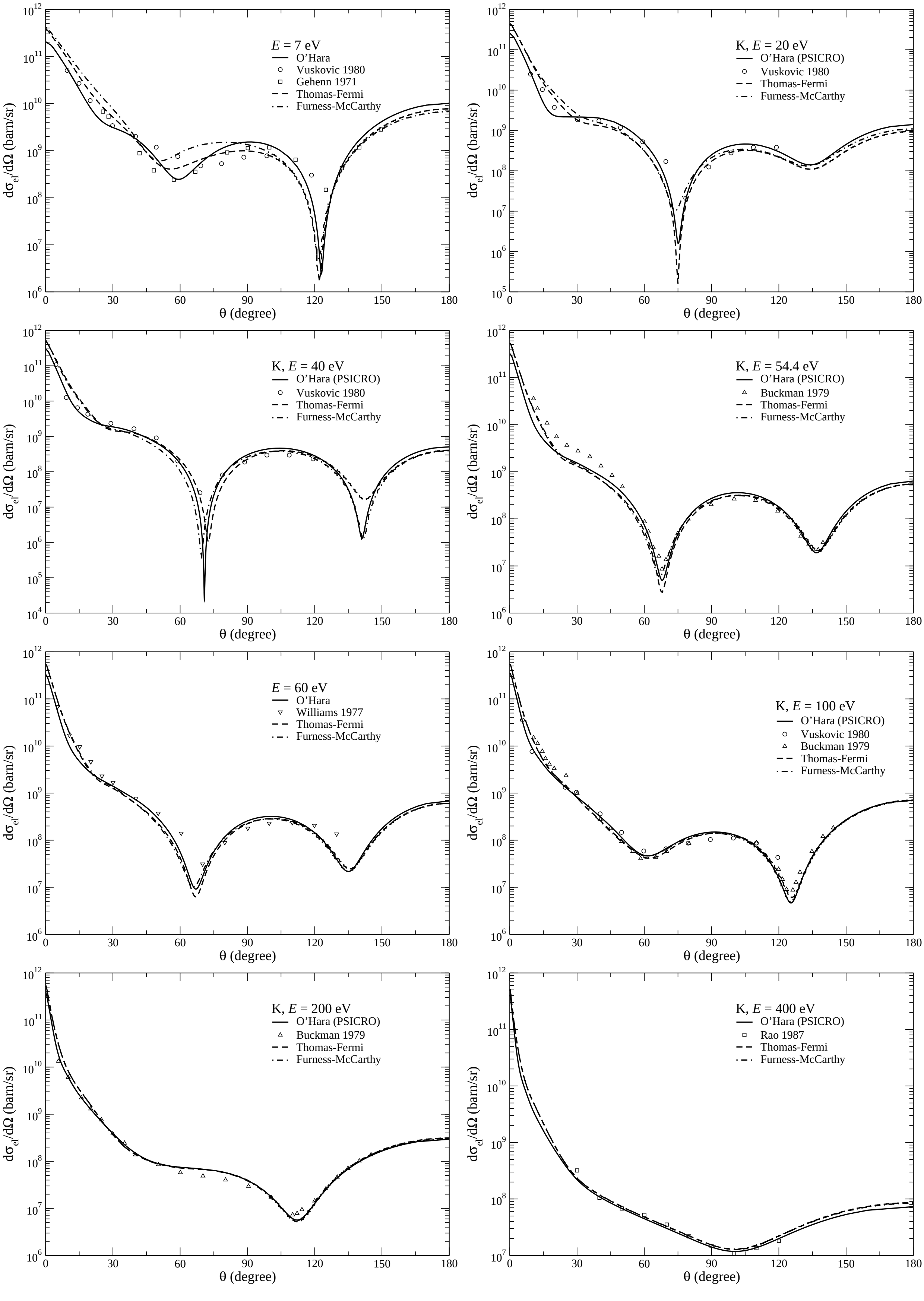

Figure 21: Comparison of partial-wave differential cross sections (*lines*) with experimental data (*symbols*) for electron elastic scattering by potassium at various impact energies.

ted-wave Born approximation and potential scattering DCS calculations have also been presented by Madison *et al.* [285]. A good agreement between the two sets of experimental data, as well as between experiment and the second order distorted-wave Born approximation calculation, has been obtained for 100 eV electron incident energy, but large differences, both in magnitude and shape of the angular distribution, have been observed at lower energies.

Figure 22 shows a comparison of the results obtained with the present partial-wave analysis method and the experimental measurements of Trajmar *et al.* [284] and of Madison *et al.* [285] for the elastic DCSs of electrons scattered by copper at four incident energies. The experimental data cover a restricted angular range in order to avoid saturation effects in the detector. The complex shape of the angular dependence of the DCSs consists of three minima which are present at all energies in a manner similar to the experimental data. It is seen that the results of the calculations obtained with PSICRO are in good qualitative and quantitative agreement with the other two theoretical models considered for comparison, as well as with the measured values, for all energies and scattering angles, indicating the fact that exchange, polarization and absorption are significant effects that have to be accounted for, especially at low energies.

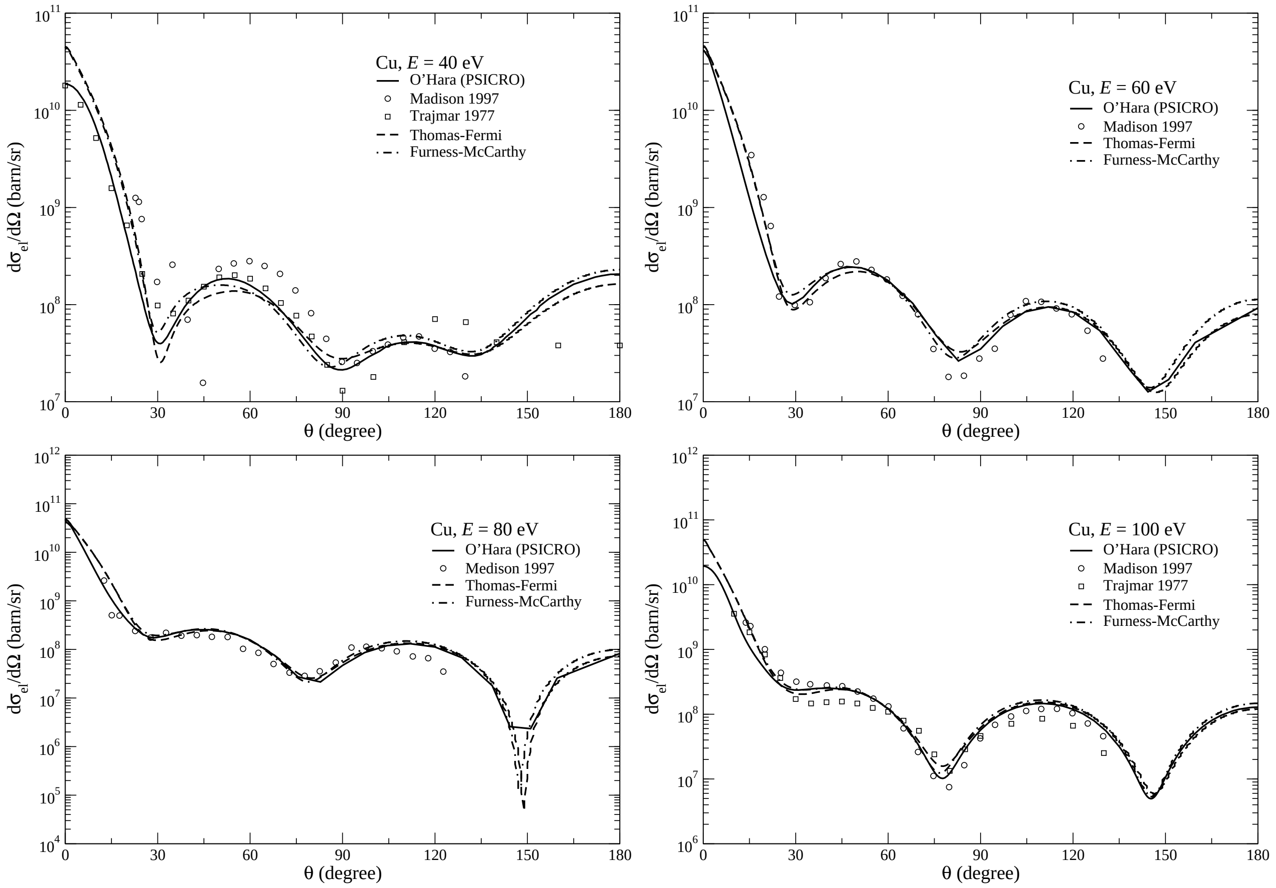

Figure 22: Comparison of partial-wave differential cross sections (*lines*) with experimental data (*symbols*) for electron elastic scattering by copper at four impact energies.

• Gold (Z=79): Experiments on high atomic number elements are relevant for checking the relativistic effects which have to be accounted for at low incident electron energy (less than 100 eV), not only in the calculation and description of the target states, but also in the description of the continuum electron. Relative DCS for electron elastic scattering of gold atoms have been measured by Reichert [288] for 150 to 1900 eV electron incident energy, while absolute data have been reported by Holst *et al.* [289] in the energy range from 30 to 200 eV and scattering angles from 5° to 140°. In the latter case, the absolute values were derived by normalization against argon and copper cross-sections. Theoretical elastic DCSs for gold atoms have also been calculated by Holzwarth and Meister [290] for energies between 0.2 and 290 keV and by Schonfelder [291] between 0.1 and 2 keV, both using the partial-wave method with a relativistic Hartree approximation, by Fink and Yates [185] between 0.1 and 1.5 keV using relativistic Hartree-Fock-Slater scattering potentials, and by Reimer and Lödding [189] between 1 and 100 keV.

The DCS results of the partial-wave calculations currently performed with the code PSICRO for electrons elastically scattered by gold are shown in Fig. 23 in comparison with the experimental data of Holst *et al.* [289] and of Reichert [288] at four incident energies. In addition, Furness-McCarthy and Thomas-Fermi exchange potential results have also been displayed. Despite the complex shape with alternating dominant minima, it is seen that the angular dependence of the calculated DCSs agree very well with the experimental values at all energies considered. Unlike previous theoretical calculations, a good agreement is obtained as well for energies

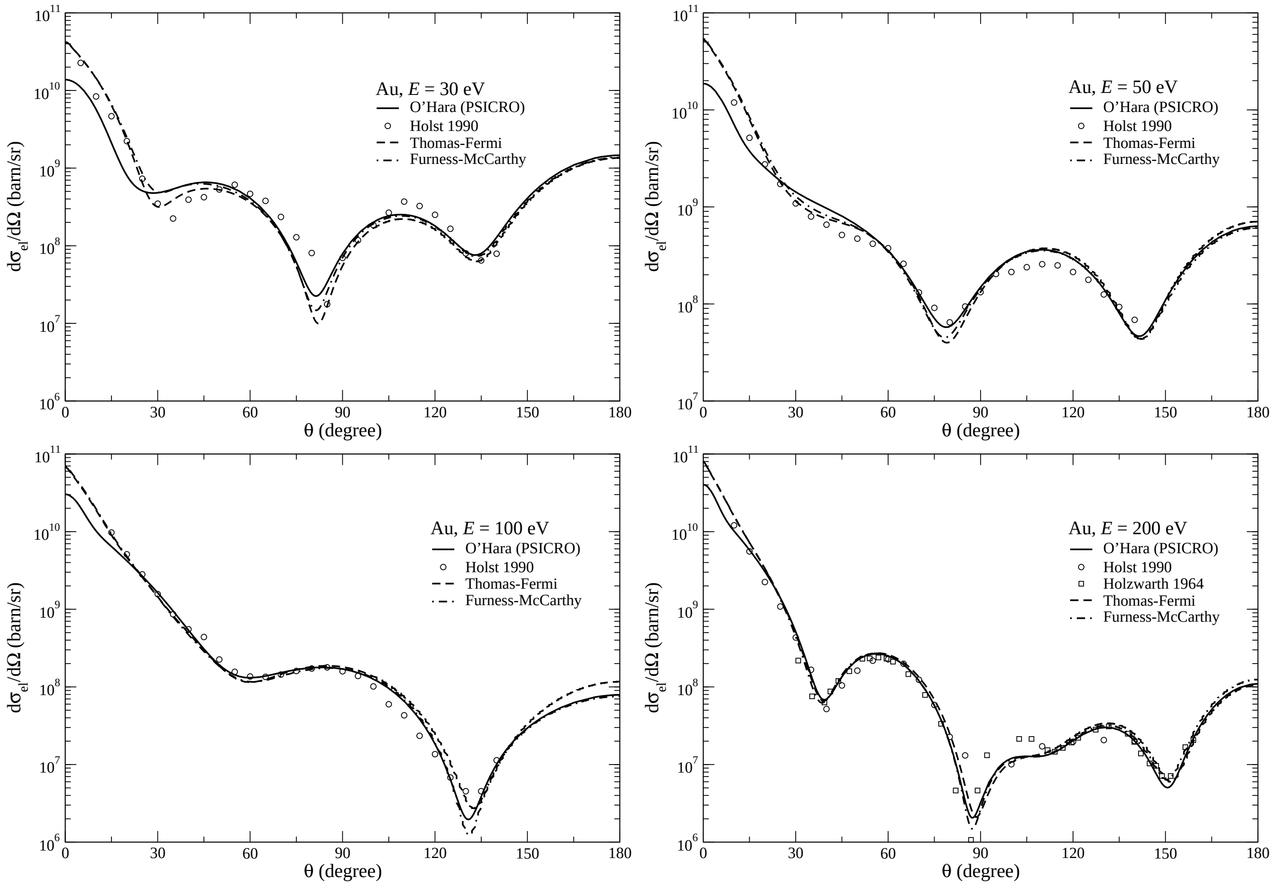

Figure 23: Comparison of partial-wave differential cross sections (*lines*) with experimental data (*symbols*) for electron elastic scattering by gold at four impact energies.

below 100 eV, thus showing that electron exchange and polarization effects have been properly addressed by the present model. For these energies, however, it is seen that the differences between the PSICRO results and the other theoretical models are somewhat increased for electron scattering in the forward direction ($\theta < 60°$). This indicates that, for heavy targets, the absorption potential can play a significant role and should, therefore, be accounted for.

To summarize, Fig. 24 shows the forward angle region of the partial-wave DCSs, with and without absorption taken into account, for electron elastic scattering by sodium, potassium, copper and gold for different incident energies. In each case, the two sets of data are results obtained with the code ELSEPA considering both the (Thomas-Fermi) exchange and the polarization potentials modelled using the local density approximation. It is well known that the effect of the absorption interaction decreases with increasing energy, but as observed in the above study, this effect plays a larger role for high-Z elements and must be considered in the calculation at very low energies.

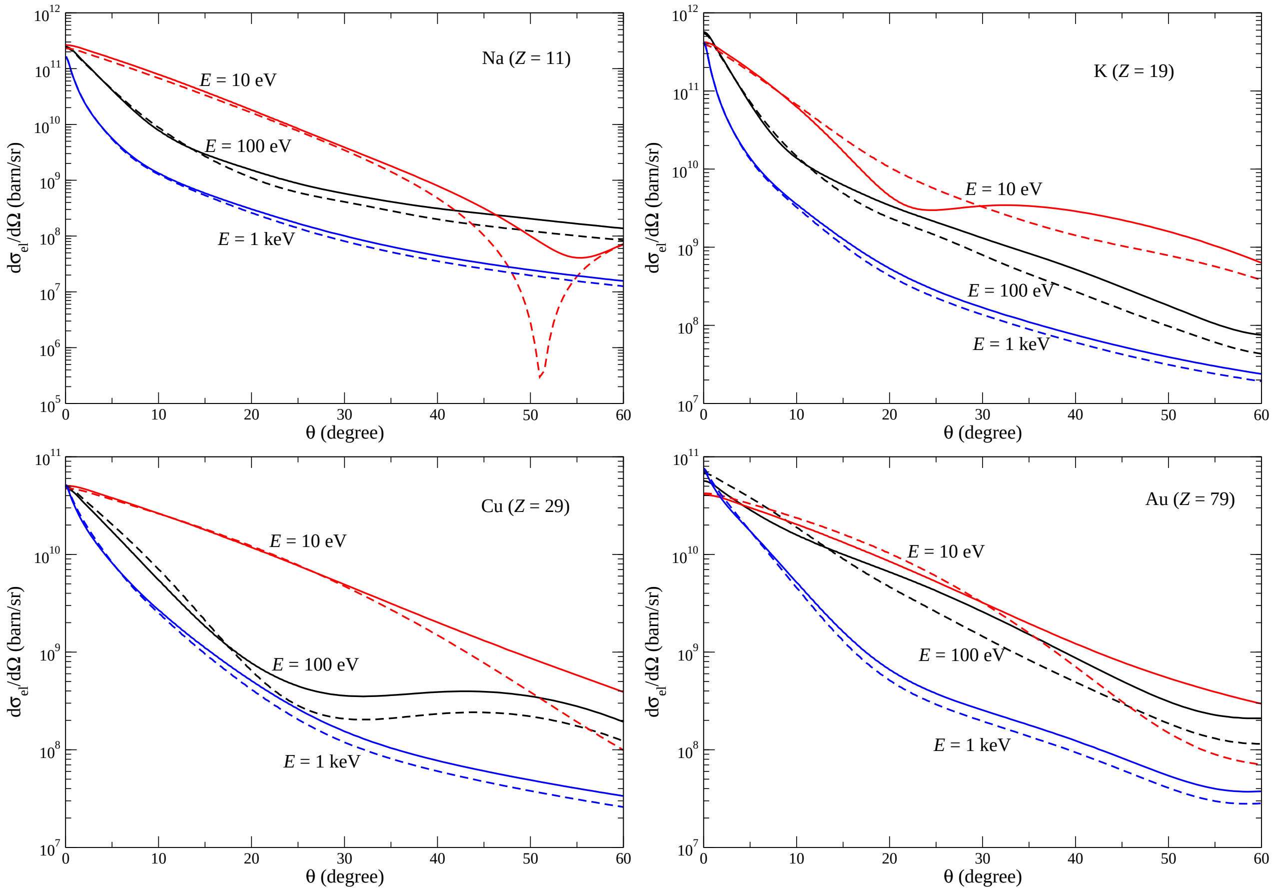

Figure 24: Comparison of partial-wave differential cross sections with (*solid lines*) and without (*dashed lines*) absorption taken into account, for electron elastic scattering by sodium, potassium, copper and gold at three different impact energies.

4.2.2 Data generation and validation for energies between 1 and 10 eV

Calculations of electron and positron elastic scattering DCSs by neutral atoms in the static field approximation using the partial-wave analysis method as described above can also be performed with high accuracy for incident electron/positron energies in the range from 1 to 10 eV. In addition to medical applications described in the introduction, low-energy electron scattering from atoms and molecules has also received particular interest in the field of atomic collisions, for providing data needed for both the testing of theoretical calculations and for modelling an increasing number of processes which are based on low-temperature discharges or plasmas. In the present section, a comparative study of the three theoretical models described above is presented for low-energy electrons incident on hydrogen and the rare-gases which, because they are inert and readily available, represent standard targets in electron scattering experiments. Since the discovery of the Ramsauer effect [75, 292-294], rare-gas based electron-collision experiments have helped to gain an understanding of the scattering process, thus leading to the development of quantum mechanical computational methods, as well as to the development of rare-gas halide high-power lasers. Review articles on experimental DCSs of electron scattering by different rare-gas atoms have been authored among others by Zecca *et al.* [295]. The present section represents an extension of the work previously performed for the intermediate energy range [116, 119] to energies below 10 eV. As the examples considered refer in particular to energies which are below the first excitation threshold for each element, the absorption interaction does not play any role, the Furness-McCarthy and the Thomas-Fermi models describing explicitly the effects of the exchange and correlation-polarization potentials only.

- Hydrogen (Z=1): For sufficiently low energies such that inelastic scattering and resonance processes may be neglected, the accuracy of the theoretical description of elastic scattering of electrons and positrons by ground-state hydrogen atoms depends on the approximation methods used to solve the Schrödinger equation describing such a three-body system. Due to the difficulty to produce a high-density hydrogen beam source and well collimated low-energy electron beams, as also to measure absolute angular DCSs, the experimental study of elastic scattering by hydrogen has received less attention than corresponding theoretical work. Absolute results have been obtained by Williams [296, 297] from relative data by means of phase shift analysis for incident energies between 0.5-8.7 eV and 20-680 eV and for scattering angles between 10° and 150°, and by Shyn and Cho [298] and Shyn and Grafe [299] for the energy ranges 5-30 eV and 40-200 eV, and for the angular interval from 12° to 156°; in all experiments, the modulated crossed-beam method was used. At low energies, the experimental data agree very well over the entire angular range. Relative elastic angular distributions have been measured by Gilbody *et al.* [300] at 3.8, 5.7, 7.1 and 9.4 eV and by Teubner *et al.* [301] for energies above 9.4eV. Both groups normalized their atomic data to the molecular cross sections reported by other authors. Theoretical calculations of DCSs for hydrogen scattering have been performed by Burke *et al.* [302] and Callaway and Oza [303] in the energy range from 11.0 to 54.4 eV and from 12 to 27 eV, both using the close-coupling method, and by Klingston and Walters [304] for energies between 30 to 680 eV by using the distorted-wave second-order Born approximation, while at very low energies (below 9 eV) Temkin and Lamkin [305] used the method of polarized orbitals. The agreement with experimental values has been found to be within the experimental accuracy of ±6% for those methods which use antisymmetrized wavefunctions and that properly account for the full ground-state polarizability of the atom.

Figure 25 shows the present calculated DCS data at four impact energies, along with the experimental values of Williams [296], Gilbody *et al.* [300] and Teubner *et al.* [301] and with the calculational results obtained with the Furness-McCarthy and Thomas-Fermi models described in the Section above. At 4.889 and 6.691 eV incident electron energies, the experimental results of Shyn and Cho [298] measured for, respectively, 5 and 7 eV have also been included. It is seen that the cross section values at lower energies are reduced in the forward direction due to the *p*-, *d*- and *s*-wave phase-shift interference. Thus, for 3.009 eV, the angular distribution exhibits a broad angular minimum around 60° which is due to the interference between the *s*-, *p*- and the increasing *d*-waves, while at 9.4 eV the behaviour of the distribution is forward peaked because of the increasing effect of the higher partial waves. Comparison between the shapes of the angular distributions for 6.691 and 9.4 eV shows that the forward peaking increases with increasing energy, whereas the angular width of the peak decreases with increasing energy. It is seen that the present results are in excellent agreement with the experimental data, i.e. within the experimental uncertainty which in the case of the Williams results [296] was about 6%. The other two scattering models considered in the present comparison seem to be less succesful in describing the experimental data. It is seen, however, that the Thomas-Fermi model is a better approximation for the exchange effects at such low energies than the Furness-McCarthy model.

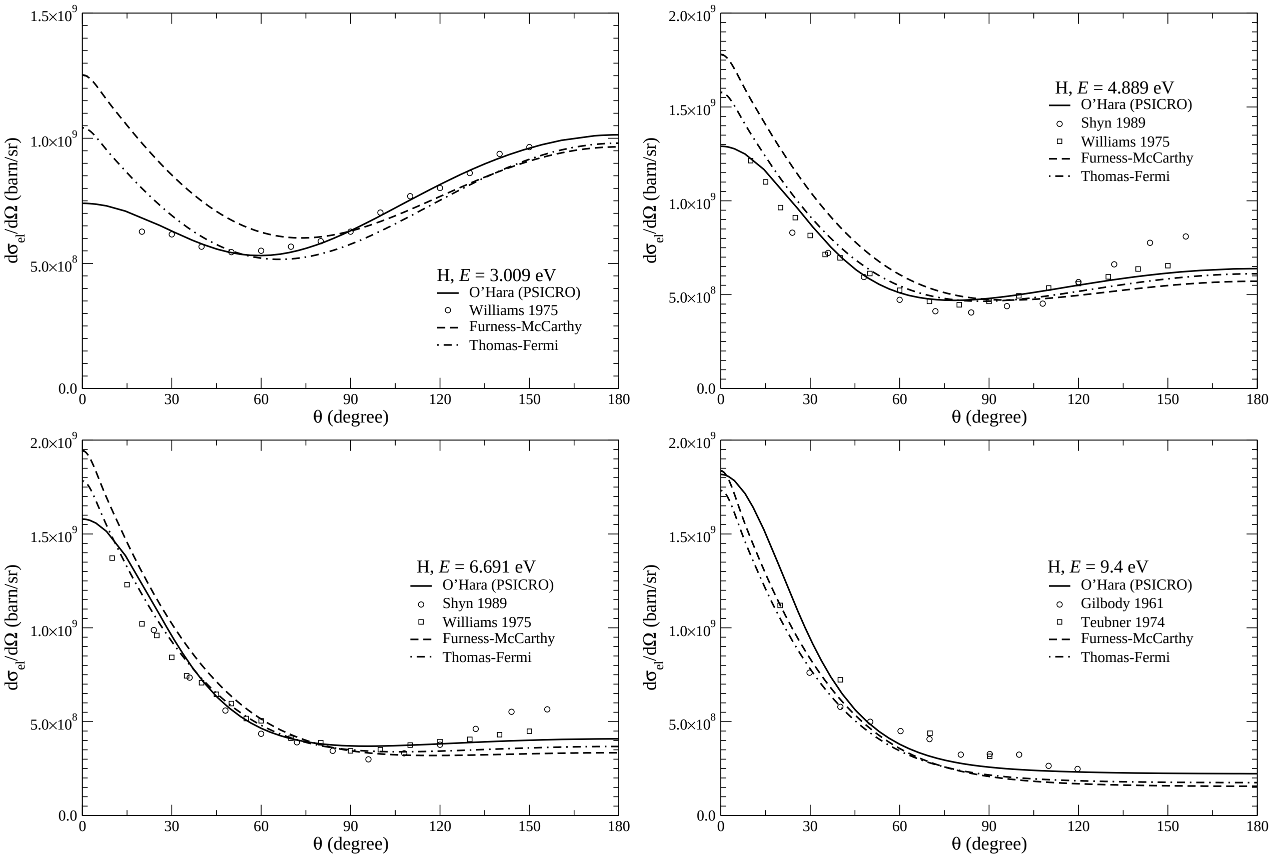

Figure 25: Comparison of partial-wave differential cross sections (*lines*) with experimental data (*symbols*) for electron elastic scattering by hydrogen at four impact energies.

- Helium (Z=2): Due to the fact that helium is an element easily amenable to experimental studies and, more important, because theoretical and experimental investigations on electron-helium scattering process have generally been in very good agreement, the elastic DCSs for helium have often been chosen as standard data for the calibration of scattering intensities and the calculation of absolute values. Many measurements of DCSs for the elastic scattering of electrons by helium have been done since the early 1930's, e.g. those by Bullard and Massey [306] in the energy and angular ranges from 4 to 50 eV and from 20° to 120°, respectively, Gibson and Dolder [307] from 3.1 to 19.1 eV incident energy and from 25° to 145°, Andrick and Bitsch [308] for energies between 2 and 19 eV and angles between 15° and 145°, McConkey and Preston [309] for 1.5-100 eV electron energy and 20°-90°, Srivastava and Trajmar [310] for energies from 5.0 to 75 eV and scattering angles from 60° to 135°, Shyn [311] for 2-400 eV incident energy and 6°-156° scattering angles, and by Brunger *et al.* [312] for incident energies between 1.5 and 50 eV and an angular range between 10° and 125°, the last two sets of experiments involving application of the crossed electron-atomic beam technique. Theoretically, Mott [313] and Kim and Inokuti [314] have calculated the scattering cross sections using the Born approximation which is expected to be valid for energies above say 20 eV. At lower energies, variational calculations carried out by Nesbet [315], La Bahn and Callaway [316] have used the extended polarization potential method for energies 1-500 eV and Brunger *et al.* [312] have performed coupled channel optical model calculations for incident energies between 1.5 and 50 eV. The agreement between calculated and experimental data for energies below the 2^3S inelastic threshold is in general good except for large angles, say above 140°.

In Fig. 26, the calculated angular distribution results of the presently applied partial-wave method and the Furness-McCarthy and the Thomas-Fermi exchange models are compared with experimental measurements by Gibson and Dolder [307], Andrick and Bitsch [308], McConkey and Preston [309], Shyn [311] and Brunger *et al.* [312] at four energies. At energies below 5 eV, the DCS has a pronounced backward scattering trend. As the energy increases, forward scattering becomes stronger and the backward scattering reduces, the minimum point in the angular distribution moving towards larger angles. It is seen that the level of agreement with the experimental results, in particular with those obtained by Andrick and Bitsch [308] and Brunger *et al.* [312], is very good at small as well as at large scattering angles. As in the case of hydrogen, the Thomas-Fermi and the Furness-McCarthy exchange potentials fail to describe the experimental data at all energies considered; at energies as low as 1.5 eV, the Thomas-Fermi model is, however, a somewhat closer representation than the Furness-McCarthy exchange potential.

- Neon (Z=10): Due to the numerous experimental and theoretical studies on electron scattering by neon which are generally in excellent agreement (±5% in the energy range below 10 eV), it has been proposed [317] that this element could be used for normalization purposes as a secondary standard for low-energy electron scattering. However, at energies below about 5 eV, differences of the order of 10-30% are observed between different sets of experimental data. Elastic scattering cross sections for neon have been measured in the low energy range by Williams [318], by Brewer *et al.* [319] at 7.5-20 eV, by Register and Trajmar [320] from 5 to 100 eV impact energy and scattering angles ranging from 10° to 145°, by Shi and Burrow [317] at 0.25-7 eV energy and 30° to 120° scattering angle, and by Gulley *et al.* [321] from 0.75-7 eV and over the angular range 10°-130°. Theoretical *ab initio* calculations have been done by Saha [322] for the impact-energy range from 0.136 to 70 eV, while O'Malley and Crompton [323]

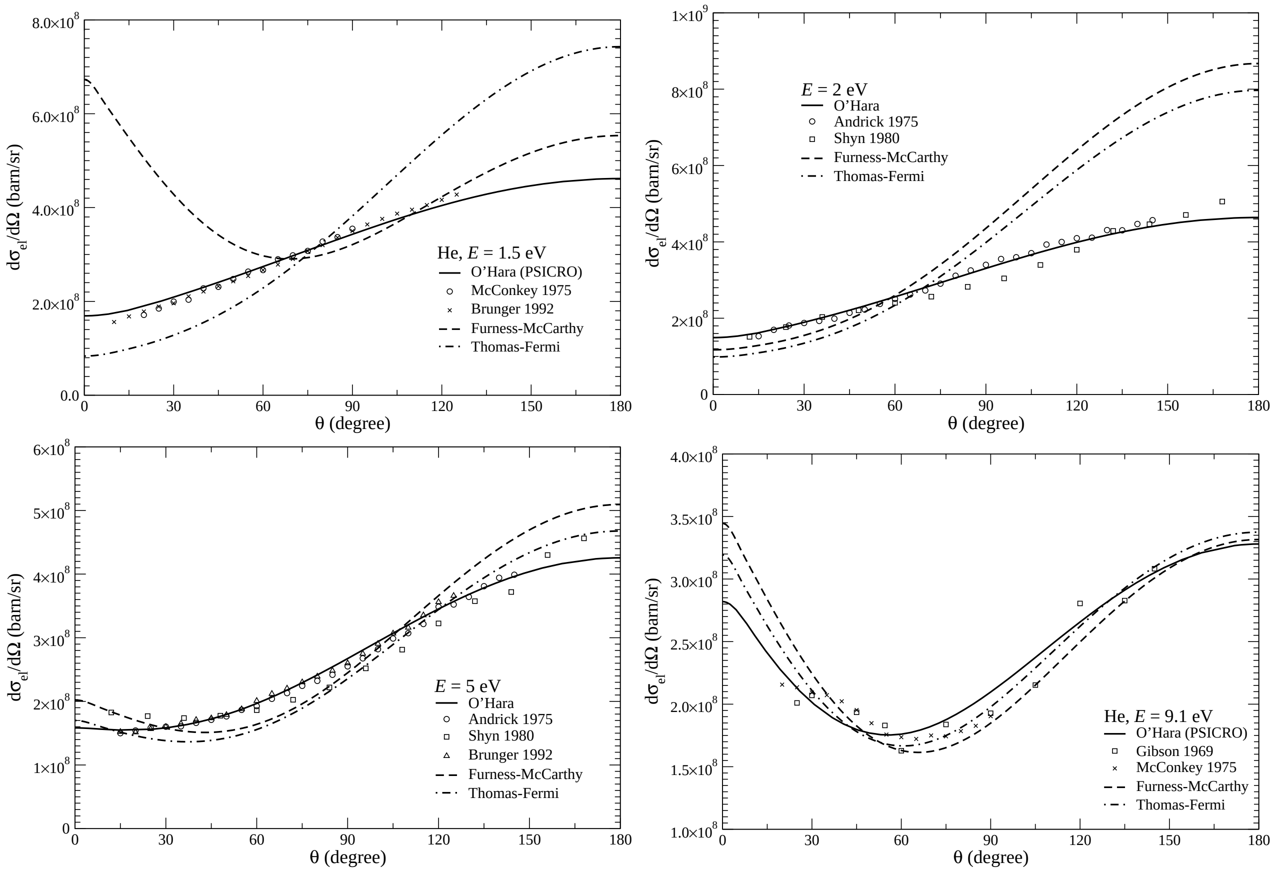

Figure 26: Comparison of partial-wave differential cross sections (*lines*) with experimental data (*symbols*) for electron elastic scattering by helium at four impact energies.

have deduced the phase-shift data from electron drift velocity measurements[23], deriving the DCS data at energies from 0.136-2.18 eV. It has been seen [317] that the agreement between these data is of the order of 1% or better, but they overestimate the reported experimental data of Williams [318] by 20% at angles between 100° and 180°.

Comparison between the present partial-wave calculations for electron elastic DCSs of neon obtained with the code PSICRO, the theoretical results given by the Furness-McCarthy and the Thomas-Fermi exchange potential models, and the experimental data measured by Register and Trajmar [320], Shi and Burrow [317] and Gulley *et al.* [321] are shown in Fig. 27 at four impact energies. An excellent agreement between the present calculations and the experimental data is obtained for energies above 5 eV. For lower energies, differences in the peak position, as well as in the magnitude of the DCSs of the order of 5-10%, are observed at small as well as at large angles for all theoretical models considered. In this very low energy range, the theoretical model based on the Furness-McCarthy exchange potential seems to provide better results than that based on the Thomas-Fermi exchange potential, unlike the previous cases.

- Argon (Z=18): Electron elastic DCS for argon have been measured by Bromberg [324] from 200 to 700 eV, Lewis *et al.* [325] from 15 to 200 eV, DuBois and Rudd [326] from 20 to 800

---

[23] the average velocity that a particle, such as an electron, attains due to an electric field

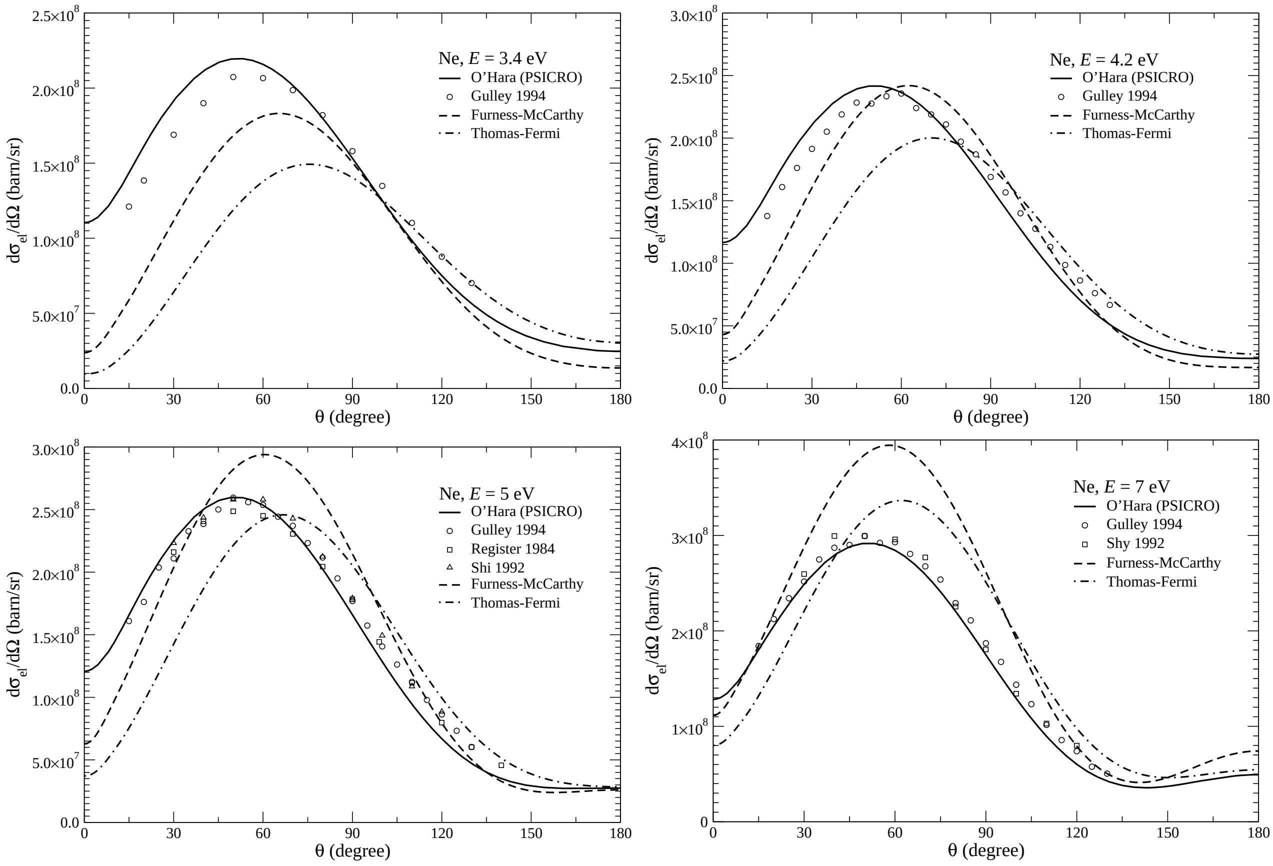

Figure 27: Comparison of partial-wave differential cross sections (*lines*) with experimental data (*symbols*) for electron elastic scattering by neon at four impact energies.

eV, Jansen *et al.* [327] from 100 to 3000 eV, Vuskovic and Kurepa [328] from 60 to 150 eV, Andrick and Langhans [329] from 5 to 16 eV, Williams [318] from 0.6 to 20 eV, Srivastava *et al.* [330] from 3 to 100 eV, Wagenaar *et al.* [331] from 20 to 100 eV, Iga *et al.* [332] from 400 to 1000 eV, Weyhreter *et al.* [333] from 0.05 to 2 eV, and Furst *et al.* [334] from 3 to 20 eV. Srivastava *et al.* [330] have normalized their relative DCSs both to the phase-shifts fit and via the relative-flow technique to helium data. In the low energy range, the first normalization method yields DCSs which are known to be in excellent agreement with Andrick and Langhans [329] and agree very well (within 10% on average) with the results of Furst [334] and Williams [318]. When normalized to helium data, they turn out to be underestimated for energies above 20 eV.

Figure 28 presents results of the calculations performed with the code PSICRO and ELSEPA for electron elastic scattering cross sections by argon neutral atoms at four incident energies. Experimental values obtained by Srivastava *et al.* [330] are included for comparison. At all energies considered, two minima are observed for scattering angles between 20° and 130°. A good overall agreement between the data obtained with PSICRO and the experimental values is obtained in the entire angular range. Unlike previous calculations, such as those of Walker [335], which took into consideration exchange and polarization effects by using the polarized orbital method, the present results based on the partial-wave method agree relatively well with the experimental data also for angles lower than 70°. For 3 and 5 eV electron energy, however, the minima and maxima seem to be slightly (2-3°) shifted to the right for scattering angles in the forward direction. For these energies, the best theoretical approximation seems to be the model based on the Thomas-Fermi exchange potential.

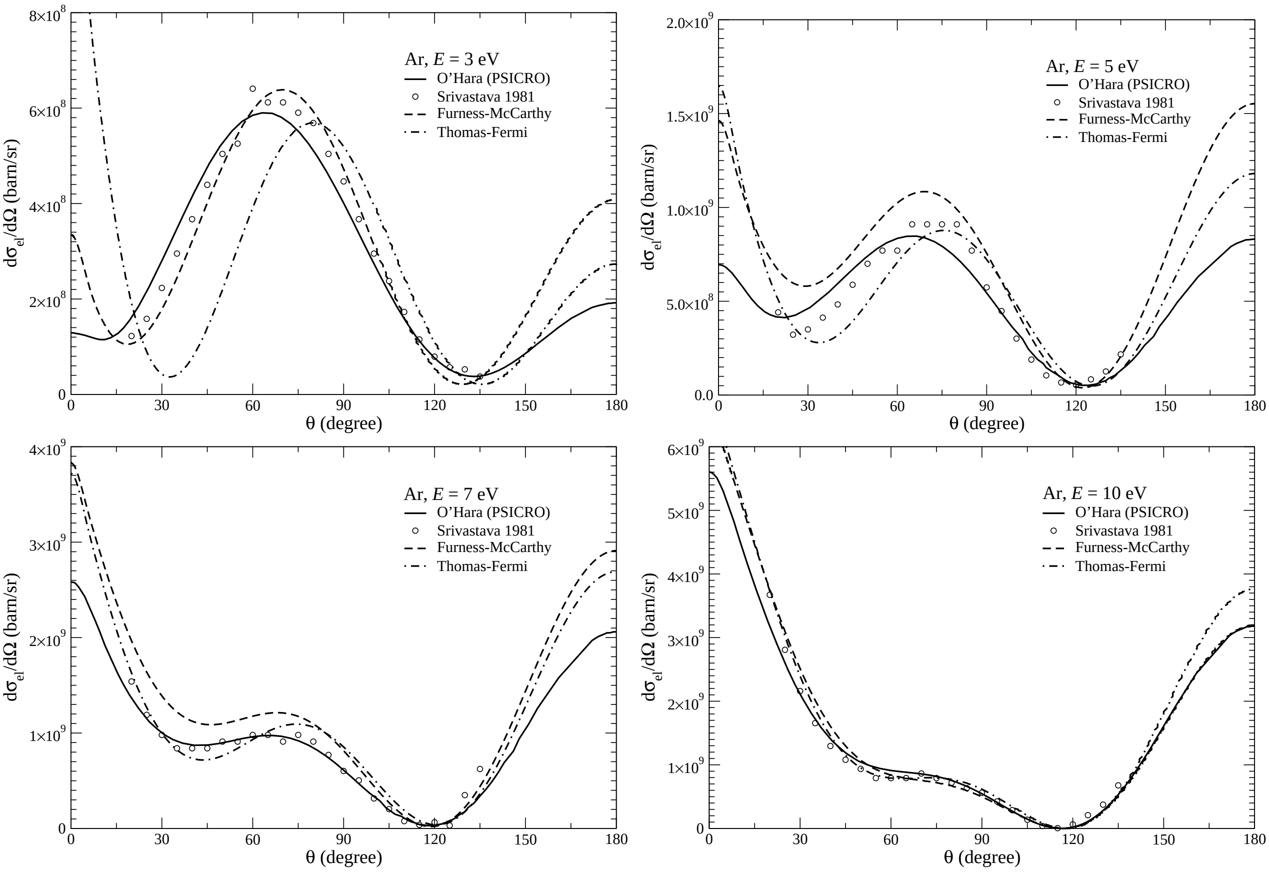

Figure 28: Comparison of partial-wave differential cross sections (*lines*) with experimental data (*symbols*) for electron elastic scattering by argon at four impact energies.

- Krypton (Z=36): Electron elastic DCS for krypton have been measured by Bromberg [324] from 30 to 200 eV, Lewis *et al.* [336] from 20 to 400 eV, Williams and Crowe [337] from 200 to 700 eV, Heidörff *et al.* [338] from 3 to 10.5 eV, Jansen and de Heer [339] from 100 to 3000 eV, Srivastava *et al.* [330] from 3 to 100 eV, Wagenaar *et al.* [331] from 20 to 100 eV, Weyhreter *et al.* [333] from 0.05 to 2 eV, and Danjo [340] from 15 to 100 eV. The DCS data of Srivastava *et al.* [330] are known to agree well (within the limits of normalization uncertainties) with other experimental results such as those of Danjo [340], when the results using the relative-flow technique for normalization are considered. At large angles, the experimental results of Srivastava *et al.* were found to be shifted towards values for smaller angles in comparison with the measurements of Heidörff *et al.* [338].

Using the code PSICRO with the presently applied partial-wave method, DCSs for electron elastic scattering by krypton neutral atoms have been calculated for 3, 5, 7.5 and 10 eV. Comparisons of calculated angular distributions, obtained considering the three theoretical models introduced above, with the experimental measurements of Srivastava *et al.* [330] are shown in Fig. 29. It is found that the shape of the present theoretical DCS curves agrees very well with the experimental measurements at all energies considered, the discrepancies being much lower than the error limit of the measurements (20%). As shown previously for gold, it is seen, however, that the maxima and minima of the angular DCS curves, are slightly shifted to the right. Unlike the case of gold, for which comparison has been done for energies larger than 10 eV, it is seen that the shift is larger with decreasing energy. Unlike the case of lower-Z elements, at energies as low as 3 eV, the best theoretical approximation appears to be the Furness-McCarthy model for the exchange potential.

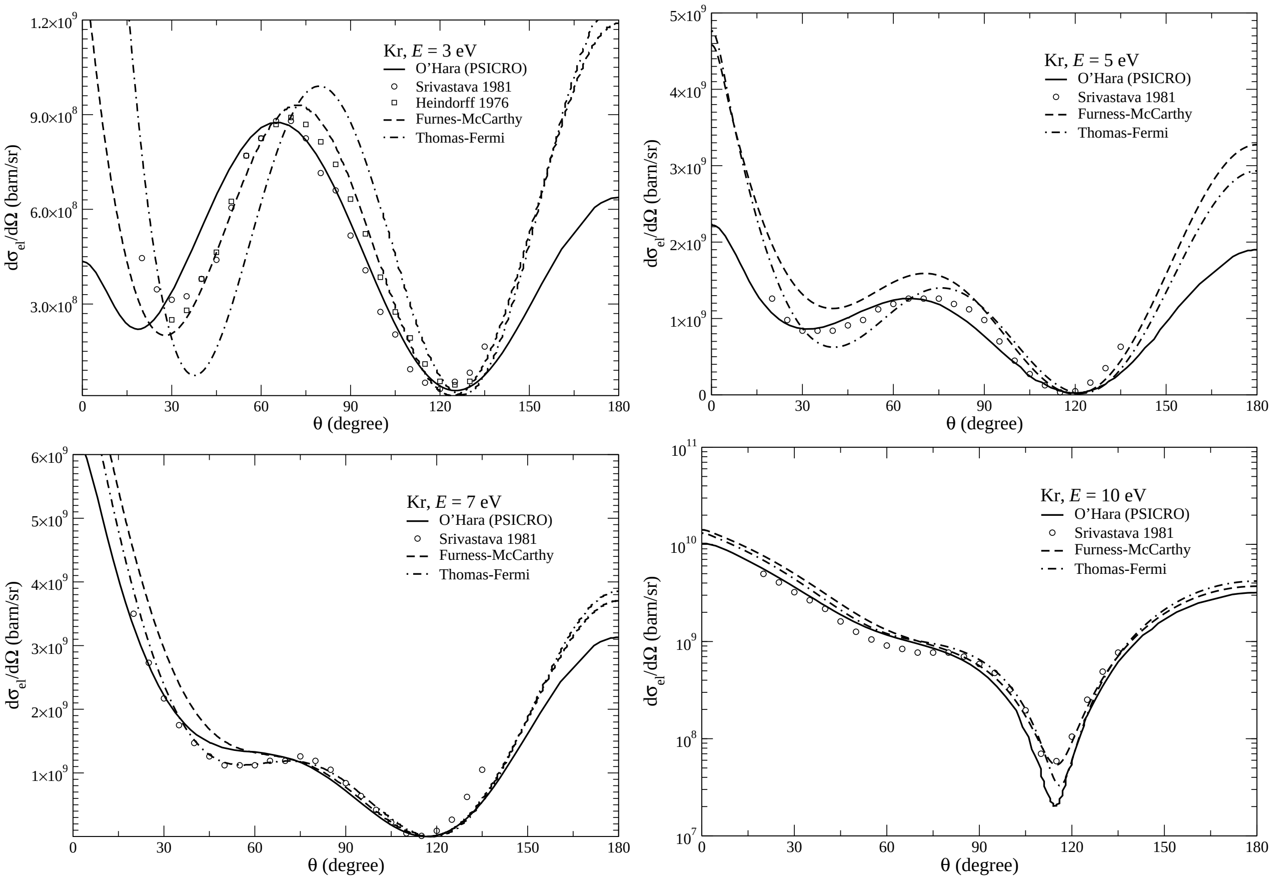

Figure 29: Comparison of partial-wave differential cross sections (*lines*) with experimental data (*symbols*) for electron elastic scattering by krypton at four impact energies.

- Xenon (Z=54): Electron scattering by xenon atoms represents both an experimental and a theoretical challenge. From the experimental point of view, the problems arise from the large polarizability of this atom, as well as from the complicated dependence on the energy and the scattering angle of the DCSs. Xenon is used in lighting technologies and in excimer lasers[24]. Theoretically, difficulties have appeared in the accurate modelling of such many-electrons system. Absolute DCSs of electrons elastically scattered from xenon at low collision energies have been measured by Williams and Crowe [337], Register *et al.* [341], Weyhreter *et al.* [342], Holtkamp and Jost [343], and by Register [344] in the angle range 15°-145° and

---

[24] An excimer is an energized molecule with two identical components or excited dimer; the excimer laser produces an ultraviolet beam of light which is emitted in pulses; it is used in the microprocessor industry since 1971 and in refractive surgery to remove corneal tissue since 1983.

at energies from 1 to 100 eV. Relative DCSs have also been given by Mehr [345] for 50-1000 eV and scattering angle from 20° to 155°, from 20 to 400 eV by Lewis *et al.* [336], for 3-7.5 eV energy and 30°-120° scattering angle by Heindorff *et al.* [346], and for 2-300 eV energy and 30°-120° scattering angles by Klewer *et al.* [347]. Comparison between various sets of experimental measurements for the electron elastic DCSs of xenon has shown significant discrepancies in both the shape and the magnitude of the angular distributions at energies below the inelastic threshold [344]. Theoretical calculations have been carried out by using an optical potential model by McCarthy *et al.* [348] for 20-3000 eV, by employing the local exchange approximation for energies from 5.5 to 10 eV by Berg [349], by making use of an adiabatic exchange method with includes also the dipole part of the polarization potential by McEachran and Stauffer [350] for 2.75-50 eV, and by applying the relativistic non-local two-channel theory of Kemper *et al.* [351] for energies up to 30 eV.

In Fig. 30, comparison of the present calculations for the electron elastic scattering DCSs of xenon with the results of the Furness-McCarthy and Thomas-Fermi theoretical models considered, and with the experimental data of Register [344], is shown at four energies below the inelastic threshold energy. The shape of the angular distributions corresponding to the three sets of data seems to agree well with experimental data, the theoretical calculations providing a good description of the experimentally obtained minima as well as of their magnitude.

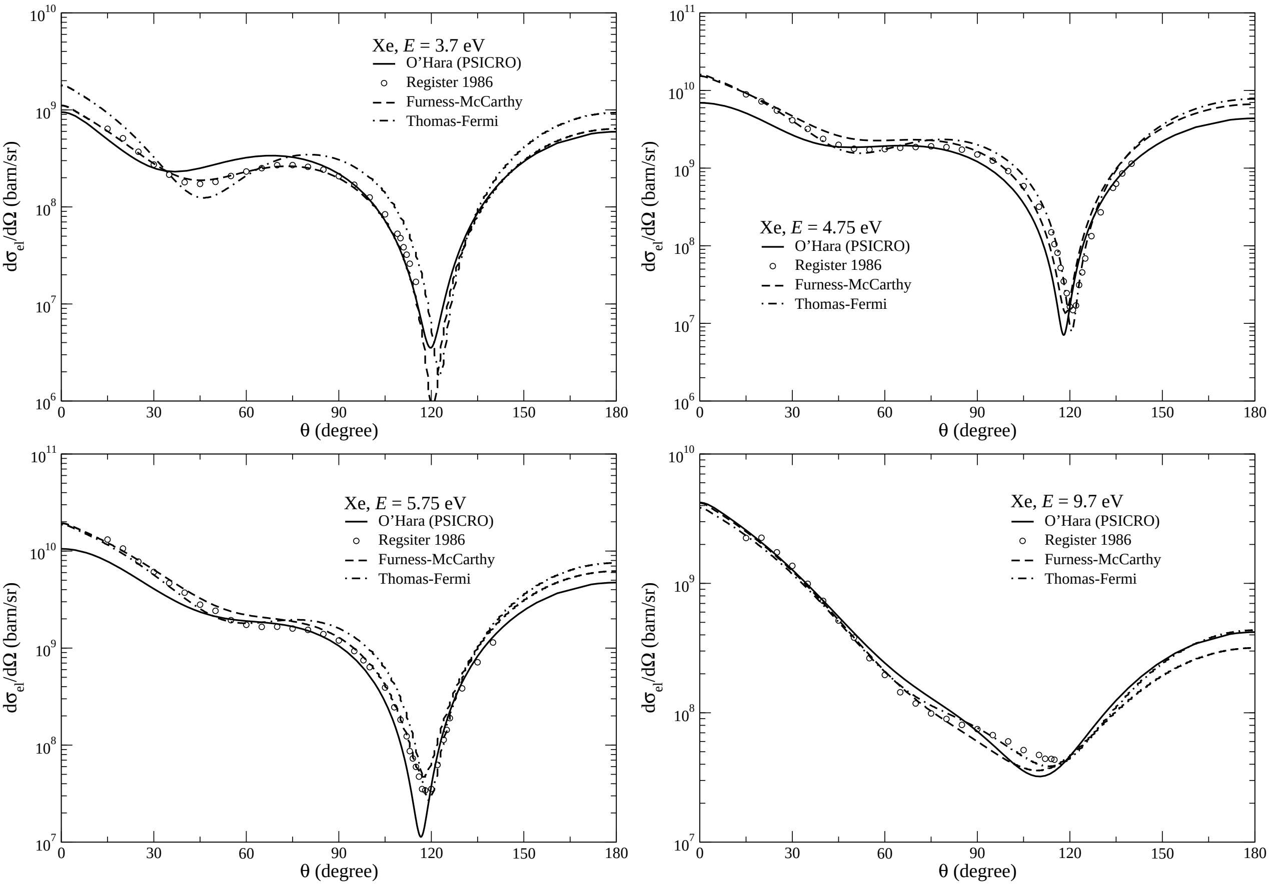

Figure 30: Comparison of partial-wave differential cross sections (*lines*) with experimental data (*symbols*) for electron elastic scattering by xenon at four impact energies.

However, for 5.75 eV incident energy and lower, differences between the three sets of calculations are observed for forward scattering directions ($\theta < 60°$), these differences increasing with decreasing incident electron energy. For such low energies and angles, in particular for 3.7 eV, the best thoretical fit of the experimental data is seen to be the model based on the Furness-McCarthy exchange potential.

4.3 Inelastic scattering

4.3.1 Ionisation cross section generation and validation

Recently, developments have been made, both experimentally and theoretically, in the study of ionisation cross sections of atomic inner shells by electron impact. Such cross sections for the removal of atomic inner-shell electrons are needed, over a wide energy region, in many branches of physics, e.g. radiation physics, plasma physics, atmospheric physics, astrophysics and electron-matter interactions, as well as for quantitative microanalysis by electron probe (EPMA) or Auger electron spectroscopy (AES). It is thus quite important to determine the acuracy of the theoretical models currently used to generate ionisation cross sections for MC simulations. In this section, the Weizsäcker-Williams method [230, 231], which has currently been used for the calculation of electron K- and L-shell ionisation cross sections of neutral atoms, is assessed by performing an extensive comparison with the most recent experimental results as well as with various other theoretical calculations. A preliminary such comparison for total electron and positron ionisation cross sections (done in the same context of data generation and validation for the 5^{th} EU-FWP "Low Dose Risk Models") was reported earlier [117].

Figure 31 shows a plot of $\sigma_{\mathrm{i}}E_{\mathrm{i}}^2$ versus reduced energy U_{i}, as given by Eq. (55) for the Weizsäcker-Williams electron ionisation cross sections of various elements. Further investigations considering the Bethe theory of inner-shell ionisation [238] are, however, not recommended at low energies as the validity of Eqs. (53)-(55) becomes questionable. Accordingly, for an appropriate assessment of the energy dependence of σ_{i} at low U_{i} values, a more detailed analysis, considering in paricular the K- and the L-shell ionisation cross sections, has been carried out.

Experimentally, three techniques have been mostly used to measure inner-shell ionisation cross sections for both gaseous and solid targets. In one technique, electron energy-loss spectra associated with the excitation of the electrons from a particular shell are measured. In the other two techniques, the decay products, either characteristic X-rays or Auger electrons, are measured. Due to the difficulty in directly measuring subshell ionisation cross sections (σ_{L_1}, σ_{L_2}, σ_{L_3}), the X-ray production cross sections have been considered. The X-ray production cross sections $\sigma_{\mathrm{i}}^{\mathrm{x}}$ ($i = K_\alpha$, L_α, L_β, L_γ) are related to the observed X-ray counts $N_{\mathrm{i}}^{\mathrm{x}}$ ($i = K_\alpha$, L_α, L_β, L_γ) by the formula

$$\sigma_{\mathrm{i}}^{\mathrm{x}} = \frac{4\pi N_{\mathrm{i}}^{\mathrm{x}} \cos\theta}{N_{\mathrm{e}} d n \eta \Omega} \tag{88}$$

where n (atoms/cm^3) and d (cm) are the atomic density and thickness of the target, respectively, N_{e} is the number of electrons hitting the target, $\eta\Omega/4\pi$ refers to the total detection

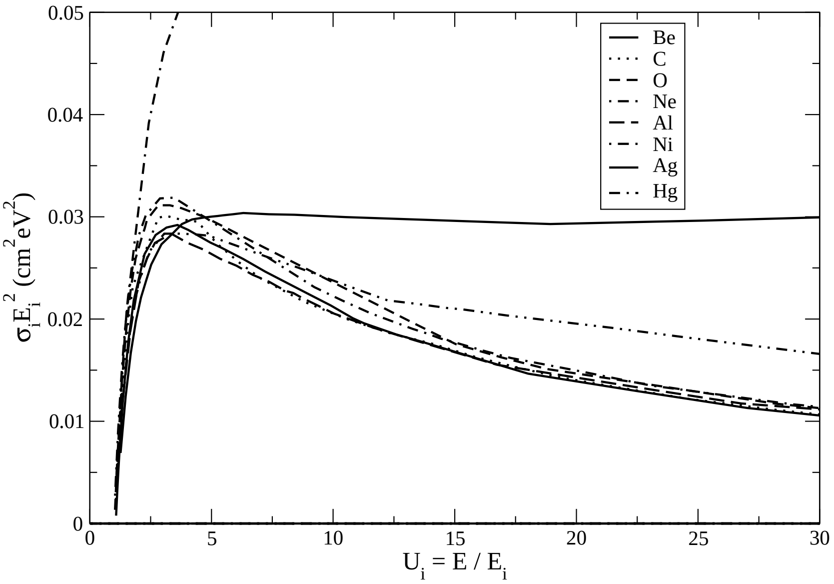

Figure 31: Electron K-shell ionisation cross sections for various elements calculated within the Bethe theory [Eq. (55)].

efficiency for characteristic X-rays, and θ denotes the angle between the incident electron beam and the normal at the target surface.

One problem difficult to overcome is the preparation of thin uniform self-supporting element targets with a small thickness. It has been shown, for the K-shell, that this difficulty can be surmounted by using thin element targets deposited on a thick substrate [352] which can be easily prepared by vacuum-coating techniques. In this case one has, instead, the need to correct for the additional influence of electrons reflected by the substrate [353, 354], as well as for the effect of multi-scattering processes in the target layer, an effect which becomes significant for low-energy electrons (near the threshold) and high-Z materials (e.g. Hf, W, Au). This technique has been further employed for measurements of absolute X-ray production cross-sections for L-shell ionisation [355]. The resulting formula is

$$\sigma_{\mathrm{i}}^{\mathrm{x}} = \frac{4\pi N_{\mathrm{i}}^{\mathrm{x}} \cos\theta}{N_{\mathrm{e}} d n P \eta \Omega} - \cos\theta \int_{\mathrm{E_i}}^{\mathrm{E}} \Phi_{\mathrm{ref}}(E') \sigma_{\mathrm{i}}(E') \mathrm{d}E', \tag{89}$$

where P denotes the mean path length of electrons that undergo the effect of multiple-scattering, E_{i} is the i^{th}-shell binding energy, $\Phi_{\mathrm{ref}}(E)$ is the energy spectrum of the electrons reflected by the substrate which can be obtained by using the so-called "bipartition model" for the electron transport [353] or any MC code, and $\sigma_{\mathrm{i}}(E)$ represents the ionisation cross sections induced by electrons with energy E. The corrected ionisation cross sections, $\sigma_{\mathrm{i}}^{\mathrm{x}}$ can be obtained from Eq. (89) through an iteration procedure.

The mean ionisation cross section, $\overline{\sigma}_{\mathrm{L}}$, of the L-shell can be written as

$$\overline{\sigma}_{\mathrm{L}} = \frac{\sigma_{\mathrm{L}}^{\mathrm{x}}}{\overline{\omega}_{\mathrm{L}}} = \frac{\sigma_{\mathrm{L}_\alpha}^{\mathrm{x}} + \sigma_{\mathrm{L}_\beta}^{\mathrm{x}} + \sigma_{\mathrm{L}_\gamma}^{\mathrm{x}}}{\overline{\omega}_{\mathrm{L}}}, \tag{90}$$

where $\sigma_{\mathrm{L}}^{\mathrm{x}}$ is the total production cross section and $\overline{\omega}_{\mathrm{L}}$ is the mean fluorescence yield of the

L-shell (i.e. the mean number of x-rays emitted per vacancy produced), which is defined by

$$\overline{\omega}_{\rm L} = \frac{\omega_1^{\rm eff}/I_1 + \omega_2^{\rm eff}/I_2 + \omega_3^{\rm eff}/I_3}{1/I_1 + 1/I_2 + 1/I_3}. \tag{91}$$

In the relation above, $I_{\rm i}$ is the ionisation energy of the $i^{\rm th}$ subshell, and $\omega_{\rm i}^{\rm eff}$ the Coster-Kronig-corrected subshell effective fluorescence yields, which are evaluated using the following relations:

$$\begin{aligned} \omega_1^{\rm eff} &= \omega_1 + f_{12}\omega_2 + (f_{13} + f_{12}f_{23})\omega_3 \\ \omega_2^{\rm eff} &= \omega_2 + f_{23}\omega_3 \\ \omega_3^{\rm eff} &= \omega_3, \end{aligned} \tag{92}$$

where $\omega_{\rm i}$ is the fluorescence yield for the $i^{\rm th}$ subshell and $f_{\rm ij}$ is the Coster-Kronig transition probability between the $i^{\rm th}$ and $j^{\rm th}$ subshells.

A: K-shell ionisation cross sections for electrons and positrons

According to the compilations of Long *et al.* [356] and Joy [357], until about ten years ago the experimental K-shell ionisation cross sections by electron impact were scarce, especially in the low-energy region (i.e. energies less than 4 times the binding energies) and with large discrepancies among data from different measurements.

Measurements for K-shell ionisation cross sections of free atoms by electron impact have been carried out for ^{4}Be [358], ^{5}B [358], ^{19}K [359], ^{20}Ca [359], ^{21}Sc [360], ^{22}Ti [361, 362], ^{23}V [360], ^{24}Cr [354,362-364], ^{25}Mn [365-368], ^{26}Fe [366, 368], ^{27}Co [369], ^{28}Ni [354,361-364,370], ^{29}Cu [362,363,369,371-373], ^{30}Zn [367], ^{31}Ga [373, 374], ^{32}Ge [372, 374, 375], ^{34}Sc [376], ^{37}Rb [359], ^{38}Sr [359], ^{39}Y [376], ^{40}Zr [374], ^{41}Nb [377], ^{42}Mo [378], ^{47}Ag [379], ^{50}Sn [379], and ^{79}Au [379]. For most experiments, the technique of using crossed beams of electrons and neutral atoms has been applied.

Unlike the situation for electrons, there are almost no experimental data available for positrons in the threshold energy regime [380]. The reason is the major difficulty which arises from the large background in the registered X-ray spectra due to bremsstrahlung and, in particular at lower positron impact energies, by the $\gamma - \gamma$ annihilation (E_γ = 511 keV) [381]. This process may occur in flight through the target, and hence even when using target thicknesses comparable or smaller than the meanfree path of the incident positrons.

Regarding the comparison with other theoretical models, the results provided by Gryzinski's [242] and the Rudge and Schwartz [234] formulas, as well as by Mayol and Salvat [235] and Hippler [236] models, have been also considered in this study for several atoms. The Hippler model uses a Coulomb correction to take into account the distortion effect of the incident electron wavefunctions by the atomic field, and incorporates the exchange effects by the Ochkur approximation [212]. The generalized oscillator strength is calculated by using the hydrogenic wavefunctions. The Mayol-Salvat model is based upon a representation of the generalized oscillator strength obtained from the dipole cross sections for the photoelectric absorption of photons. This model considers also the exchange effects and the empirical Coulomb corrections.

An extensive comparison for the K-shell ionisation cross sections from near-threshold up to about 60 keV electron impact energies, obtained by using the Weizsäcker-Williams method [230, 231], with other experimental and theoretical results is shown in Fig. 32 for beryllium, boron, potassium, scandium, vanadium, chromium, manganese and nickel, and in Fig. 33 for zinc, germanium, selenium, strontium, rubidium, niobium, silver and gold. Included in the comparison are experimental cross-sections as obtained from thin element targets deposited on a thick substrate. They correspond to values provided by Eq. (89) and have been corrected for the additional contributions from the substrate. It is seen that, for the elements with only one set of experimental data available, the present results provided by the Weizsäcker-Williams method are, generally, in good agreement with the measured data within the absolute uncertainties of the experiments. For instance, in the case of potassium and scandium, the Weizsäcker-Williams cross sections seem to lie somewhat above the experimental results, whereas for zinc and selenium the presently calculated cross sections are slightly lower than the measurements. For the other elements, beryllium, boron, vanadium, strontium, rubidium, and niobium, the Weizsäcker-Williams cross section curves intersect the experimental results at some point. Excellent agreement is obtained in particular with the results of Luo *et al.* [358] for ^{4}B, An *et al.* [360] for ^{21}Sc and ^{23}V, An *et al.* [364] for ^{24}Cr and ^{28}Ni, Tang *et al.* [367] for ^{25}Mn and ^{30}Zn, Luo *et al.* [376] for ^{34}Sc and Peng *et al.* [377] for ^{41}Nb. A very good description of the ionisation threshold is observed for various elements (^{19}K - ^{79}Au).

Because of the substantial disagreement between data from different sources (which is incoherently larger than the uncertainties claimed by the authors), it is more difficult to draw a conclusion for the elements for which more than one set of experimental data is available such as for chromium, manganese, nickel, and germanium. For example, in the case of ^{24}Cr, the Weizsäcker-Williams model is in very good agreement (about 5%) with the measurements of An *et al.* [364], while the results lie systematically above the measurements of He *et al.* [362] and below those of Luo *et al.* [366] and Llovet *et al.* [363]. In the case of ^{25}Mn, the Weizsäcker-Williams model seems to reproduce reasonably well the experiments by Tang *et al.* [367], Shima [365] and Luo *et al.* [366], i.e. within the experimental error of maximum 15%, while the predictions are about 30% lower than the data of Llovet *et al.* [368]. For ^{28}Ni, a good agreement is obtained with the measurements of An *et al.* [364], but the results lie systematically above the measurements of He *et al.* [362] and Pockman *et al.* [370], while being below the data of Llovet *et al.* [363], Luo *et al.* [354] and Jessenberger *et al.* [361].

Among the theoretical calculations considered for comparison and shown in Fig. 32 for ^{24}Cr, and ^{28}Ni, and in Fig. 33 for ^{41}Nb, the formula of Gryzinski [242] gives results which lie systematically below the other calculations as well as below the experimental results, whereas the shape of the cross section curve obtained by using the Rudge and Schwartz [234] formula is different from both Weizsäcker-Williams calculations and experimental measurements at low and at high energies. The Weizsäcker-Williams results seem to be in better agreement with the predictions of the Mayol-Salvat model [235] than with those of Hippler [236], the overall agreement with experimental work also being better. It has been actually demonstrated that the Mayol-Salvat model is formally equivalent to the Weizsäcker-Williams method of virtual quanta [235] and that, apart from low-energy corrections, both models should yield essentially the same results.

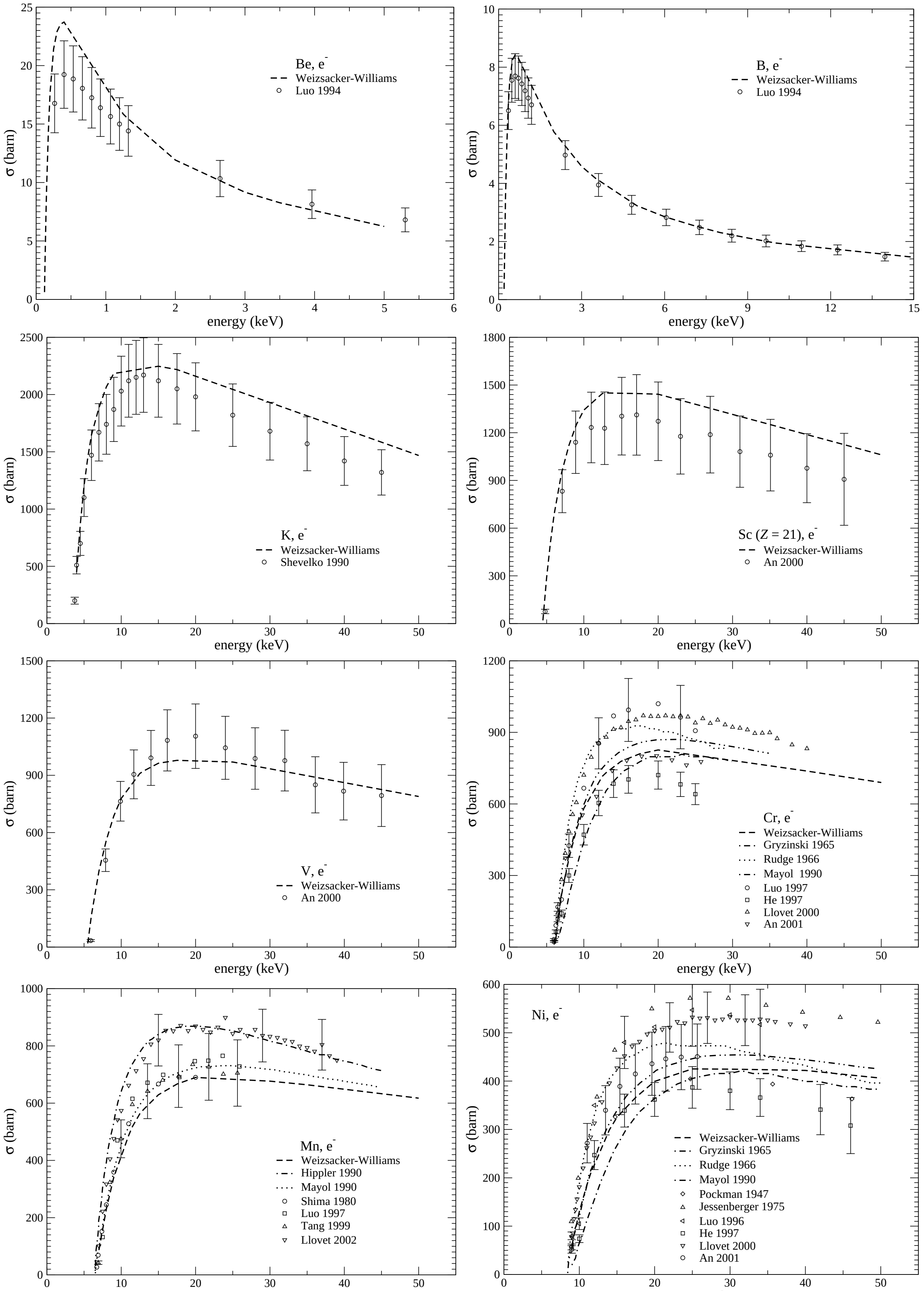

Figure 32: Comparison of theoretical and experimental electron K-shell ionisation cross sections for beryllium, boron, potassium, scandium, vanadium, chromium, manganese and nickel.

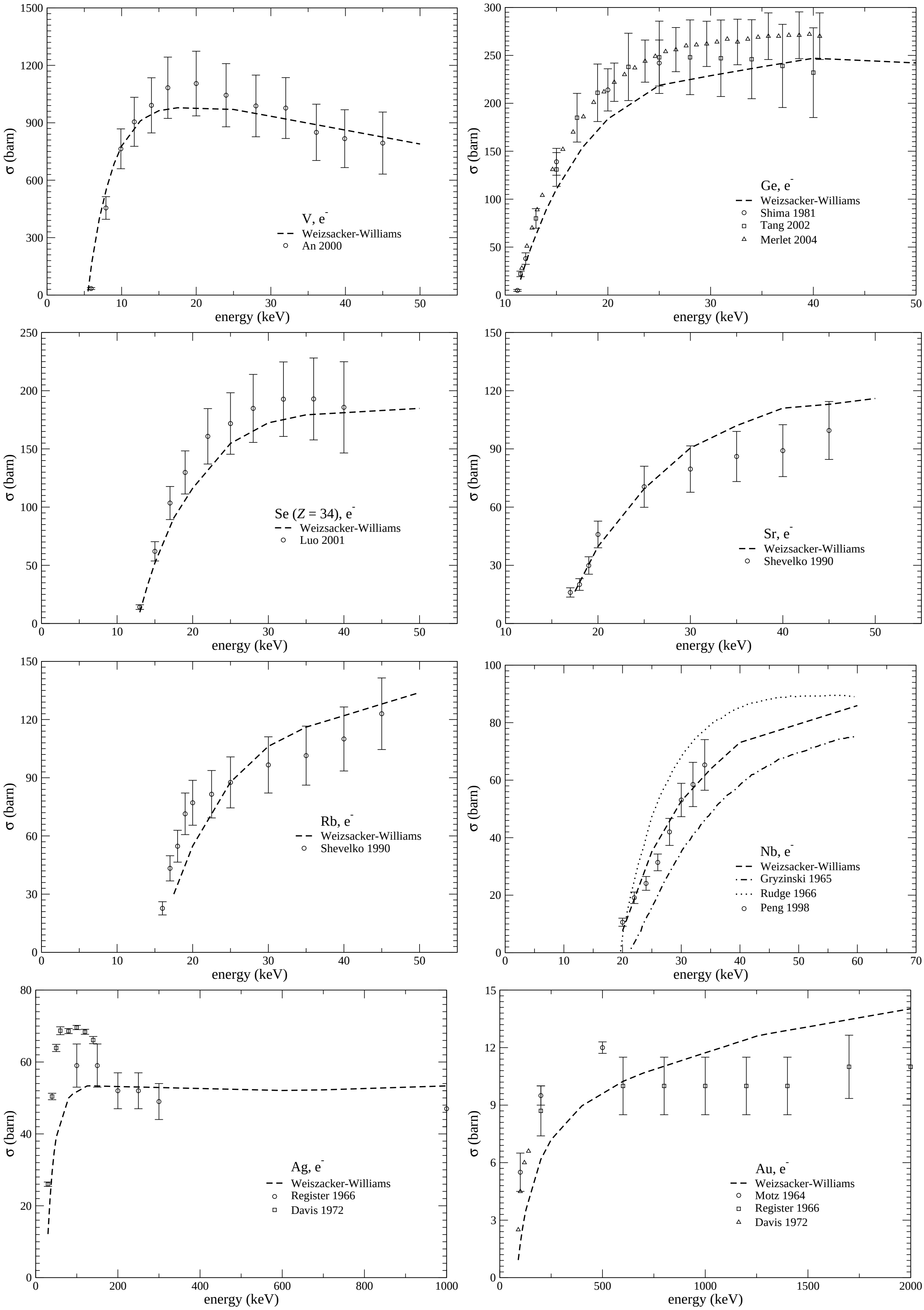

Figure 33: Comparison of theoretical and experimental electron K-shell ionisation cross sections for zinc, germanium, selenium, strontium, rubidium, niobium, silver and gold.

Similar comparisons are shown in Fig. 34 for K-shell ionisation by positron impact. The Weizsäcker-Williams cross section results are displayed together with the experimental data of Nagashima *et al.* [382] for ^{29}Cu and of Schneider *et al.* [380] and of Hansen and Flammersfeld [383] for ^{47}Ag. Theoretical calculations for ionisation process by positrons differ from those for electrons in two respects: the absence of the exchange interaction and the Coulomb effect caused by the projectile-target nucleus interaction which results in a slowing down (for positrons) or acceleration (for electrons) of the incident projectile. Thus, Fig. 34 includes calculations using the binary encounter formalism of Gryzinski and Kowalski [384] and the plane-wave Born approximation with Coulomb and exchange effects acounted for [236], respectively. For both elements, reasonable agreement (within the experimental errors of 25%) is observed between the calculated cross sections provided by the Weizsäcker-Williams method and the experimental data.

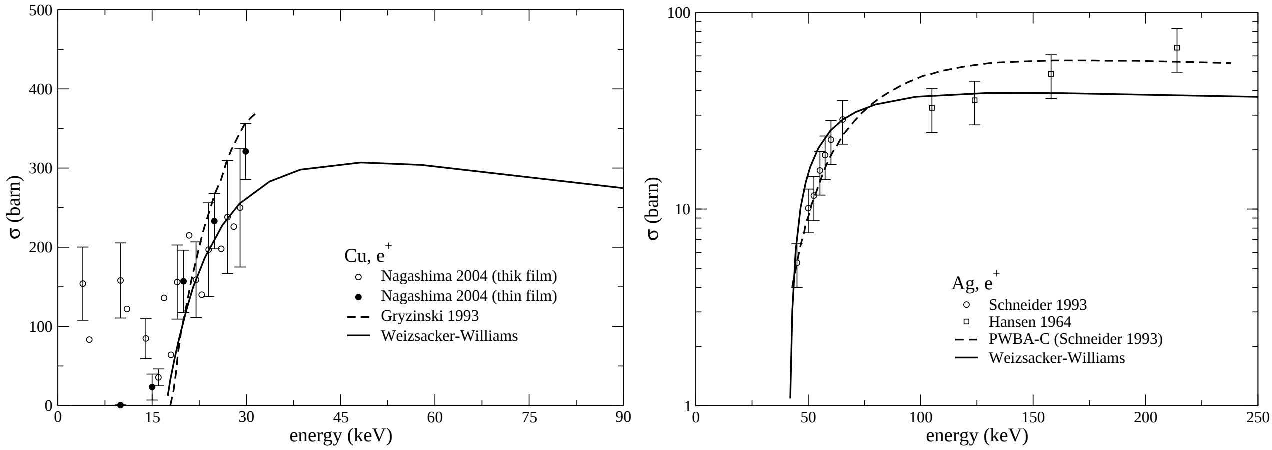

Figure 34: Comparison of theoretical (*lines*) and experimental (*symbols*) positron K-shell ionisation cross sections for copper (*left*) and silver (*right*).

B: L-shell ionisation cross sections for electrons and positrons

Despite the growing interest during the past years and, also, the considerable amount of work reported essentially for K-shell ionisation [358-379], measured data for L- and M-shells at lower energies are scarce and, in most cases, there are no data available at present. In addition to the problems related to preparation of thin uniform self-supporting element targets, the increasing complexity of multiple decay channels following L- and higher-shell ionisation is also responsible for the generally poorer knowledge of these cross sections as compared with K-shell data.

Table 2 summarizes the main experimental work on electron L-shell ionisation cross sections. In the threshold energy region, absolute electron X-ray production cross sections, $\sigma^{\mathrm{x}}_{\mathrm{L}_\alpha}$, $\sigma^{\mathrm{x}}_{\mathrm{L}_\beta}$, $\sigma^{\mathrm{x}}_{\mathrm{L}_\gamma}$, due to electron impact have been measured by Peng *et al.* [385] for ^{41}Nb in the energy range from 3 to 40 keV, by Tang *et al.* [386] for ^{49}In, ^{50}Sn, and ^{75}Re from 5 to 40 eV, by Luo *et al.* [387] for ^{72}Hf from 10 to 36 keV, by Peng *et al.* [388] for ^{74}W from 11 to 36 keV, by Yang *et al.* [389] for ^{72}Hf and ^{74}W for energies from 10 to 36 keV, and by Wu *et al.* [390] for ^{77}Ir and ^{79}Au between 10 and 40 keV, the last four sets of authors directly counting the number of characteristic X-rays generated from the L-shell, and providing as well the calculated total production, $\sigma^{\mathrm{x}}_{\mathrm{L}} = \sigma^{\mathrm{x}}_{\mathrm{L}_\alpha} + \sigma^{\mathrm{x}}_{\mathrm{L}_\beta} + \sigma^{\mathrm{x}}_{\mathrm{L}_\gamma}$, and mean ionisation, $\overline{\sigma}_{\mathrm{L}}$, cross sections. In addition, for ^{82}W, four papers with measured L-shell ionisation cross section data have been found: the L-shell ionisation cross section ratios, $\sigma_{\mathrm{L}_3}/\sigma_{\mathrm{L}_2}$ and $\sigma_{\mathrm{L}_2}/\sigma_{\mathrm{L}_1}$ reported by Carvalho *et al.* [391] in the range of energy from 12.5 to 40 keV, $\sigma_{\mathrm{L}_3}/\sigma_{\mathrm{L}_2}$ and by Salgueiro *et al.* [392] from 11.6 to 12.0 keV, the relative cross sections, σ_{L_1}, σ_{L_2}, σ_{L_3}, being determined by Huizinga [393], and by Chang [394] between 11 and 40 keV from X-ray production cross sections which have been scaled to the corresponding values calculated using the McGuire scaling method [243]. Only the L_α-shell X-ray production cross sections have been measured by Merlet *et al.* [375] for ^{32}Ge, and by Campos *et al.* [395] for ^{82}W, ^{78}Pt and ^{79}Au. McCue [396], Llovet *et al.* [397] and Salem [398] have measured the relative cross sections for ^{47}Ag, for ^{53}Te, ^{79}Au, and ^{83}Bi, and for ^{79}Au, respectively. At higher energies, absolute partial production cross sections have been measured by Park *et al.* [399] for 14 elements from ^{56}Ba to ^{83}Bi and for a range of energy from 1.04 to 1.76 MeV, and by Middleman *et al.* [400] for ^{69}Tm, ^{73}Ta, ^{79}Au and ^{83}Bi between 150 and 900 MeV.

Table 2: Experimental work on electron L-shell ionisation cross sections.

Element	Quantity measured	Energy range (keV)	Reference
^{32}Ge	$\sigma^{\mathrm{x}}_{\mathrm{L}_\alpha}$	1.6 - 40.6	[375]
^{41}Nb	$\sigma^{\mathrm{x}}_{\mathrm{L}_\alpha}$, $\sigma^{\mathrm{x}}_{\mathrm{L}_\beta}$, $\sigma^{\mathrm{x}}_{\mathrm{L}_\gamma}$	3 - 40	[385]
^{47}Ag	σ_{L_3}	-	[396]
^{49}In, ^{50}Sn, ^{75}Re	$\sigma^{\mathrm{x}}_{\mathrm{L}_\alpha}$, $\sigma^{\mathrm{x}}_{\mathrm{L}_\beta}$, $\sigma^{\mathrm{x}}_{\mathrm{L}_\gamma}$	5 - 40	[386]
^{53}Te, ^{79}Au, ^{83}Bi	σ_{L_1}, σ_{L_2}, σ_{L_3}		[397]
^{72}Hf	$\sigma^{\mathrm{x}}_{\mathrm{L}_\alpha}$, $\sigma^{\mathrm{x}}_{\mathrm{L}_\beta}$, $\sigma^{\mathrm{x}}_{\mathrm{L}_\gamma}$, $\sigma^{\mathrm{x}}_{\mathrm{L}}$, $\overline{\sigma}_{\mathrm{L}}$	10 - 36	[387]
^{72}Hf, ^{74}W	$\sigma^{\mathrm{x}}_{\mathrm{L}_\alpha}$, $\sigma^{\mathrm{x}}_{\mathrm{L}_\beta}$, $\sigma^{\mathrm{x}}_{\mathrm{L}_\gamma}$, $\sigma^{\mathrm{x}}_{\mathrm{L}}$, $\overline{\sigma}_{\mathrm{L}}$	10 - 36	[389]
^{74}W	$\sigma_{\mathrm{L}_3}/\sigma_{\mathrm{L}_2}$, $\sigma_{\mathrm{L}_2}/\sigma_{\mathrm{L}_1}$	12.5-40	[391]
^{74}W	$\sigma_{\mathrm{L}_2}/\sigma_{\mathrm{L}_1}$	11.59 - 11.98	[392]
^{74}W	σ_{L_1}, σ_{L_2}, σ_{L_3}	11 - 40	[393, 394]
^{74}W	$\sigma^{\mathrm{x}}_{\mathrm{L}_\alpha}$, $\sigma^{\mathrm{x}}_{\mathrm{L}_\beta}$, $\sigma^{\mathrm{x}}_{\mathrm{L}_\gamma}$, $\sigma^{\mathrm{x}}_{\mathrm{L}}$, $\overline{\sigma}_{\mathrm{L}}$	11 - 36	[388]
^{74}W, ^{78}Pt, ^{79}Au	$\sigma^{\mathrm{x}}_{\mathrm{L}_\alpha}$	10 - 30	[395]
^{77}Ir, ^{79}Au	$\sigma^{\mathrm{x}}_{\mathrm{L}_\alpha}$, $\sigma^{\mathrm{x}}_{\mathrm{L}_\beta}$, $\sigma^{\mathrm{x}}_{\mathrm{L}_\gamma}$, $\sigma^{\mathrm{x}}_{\mathrm{L}}$, $\overline{\sigma}_{\mathrm{L}}$	10 - 40	[390]
^{79}Au	σ_{L_2}, σ_{L_3}	-	[398]
^{56}Ba to ^{83}Bi	$\sigma^{\mathrm{x}}_{\mathrm{L}_\alpha}$, $\sigma^{\mathrm{x}}_{\mathrm{L}_\beta}$, $\sigma^{\mathrm{x}}_{\mathrm{L}_\gamma}$	1040 - 1760	[399]
^{69}Tm, ^{73}Ta, ^{79}Au, ^{83}Bi	$\sigma^{\mathrm{x}}_{\mathrm{L}_\alpha}$, $\sigma^{\mathrm{x}}_{\mathrm{L}_\beta}$, $\sigma^{\mathrm{x}}_{\mathrm{L}_\gamma}$	150000 - 900000	[400]

Concerning the theoretical calculation of L-shell ionisation cross-sections, the binary encounter approximation (BEA) proposed by Gryzinski [242] and the neoclassical scaling law proposed by McGuire [243] (described earlier in Section 3.3.2) are used most often for comparison. In the high-energy range, the plane-wave first-Born approximation with exchange, Coulomb and relativistic corrections has been successfuly applied [401, 402], including also the transverse interaction of virtual photons with atoms. In order to perform comparisons with measured experimental data, the L-shell ionisation cross sections (σ_{L_1}, σ_{L_2}, and σ_{L_3}) obtained from theoretical calculations must be converted into X-ray production cross sections ($\sigma^{\mathrm{x}}_{\mathrm{L}_\alpha}$, $\sigma^{\mathrm{x}}_{\mathrm{L}_\beta}$ and $\sigma^{\mathrm{x}}_{\mathrm{L}_\gamma}$). Despite the straightforward procedure, the conversion involves a set of atomic parameters such as the fluorescent and Coster-Kronig yields [403-405] and the X-ray emission rates [406] which presently have quite high errors (5-20%) [403]. Previous comparisons of theoretical calculations with experimental data have shown that, in general, the measurements do not follow the trends expected from the theory with some exceptions in the case of Gryzinski theory for high-Z elements in the high energy region [385-387].

In Figs. 35, 36 and 37, the Weizsäcker-Williams calculated L-shell production cross sections for indium, tin and rhenium, versus incident electron energy, are displayed in comparison with the experimental data of Tang *et al.* [386]. In the conversion calculations, the fluorescence and Coster-Kronig yields given by Krause [403] and the X-ray emission rates of Scofield [406] have been used. The contribution of L-shell vacancies created by filling K-shell vacancies by L-shell electrons has been considered negligible. It can be seen that for $\sigma^{\mathrm{x}}_{\mathrm{L}_\alpha}$ and $\sigma^{\mathrm{x}}_{\mathrm{L}_\beta}$ in the case of indium and tin (Fig. 35), and tin (Fig. 36), and for $\sigma^{\mathrm{x}}_{\mathrm{L}_\alpha}$, $\sigma^{\mathrm{x}}_{\mathrm{L}_\beta}$ and $\sigma^{\mathrm{x}}_{\mathrm{L}_\gamma}$ in the case of rhenium (Fig. 37), the agreement achieved between the calculational and the experimental results is generally good, i.e. within the uncertainty of the experimental measurements, estimated to be in all cases less than 15%.

Fig. 38 shows absolute ionisation cross sections by positron impact. The Weizsäcker-Williams results are compared with the experimental data of Nagashima *et al.* [382] for the L-shell ionisation of ^{47}Ag and of Schneider *et al.* [380] for the $L3$-shell ionisation of ^{79}Au. Theoretical calculations obtained from the binary encounter formalism of Gryzinski and Kowalski [384], and from the partial-wave Born approximation with Coulomb and exchange effects acouted for, are also displayed. For both elements, the present results agree relatively well with the experimental values (within the 25% errors of the measurements). In addition, the Weizsäcker-Williams analytical approximation is seen not to lose accuracy with increasing target atomic number, a trend previously observed for the binary encounter approximation by several authors [380, 386].

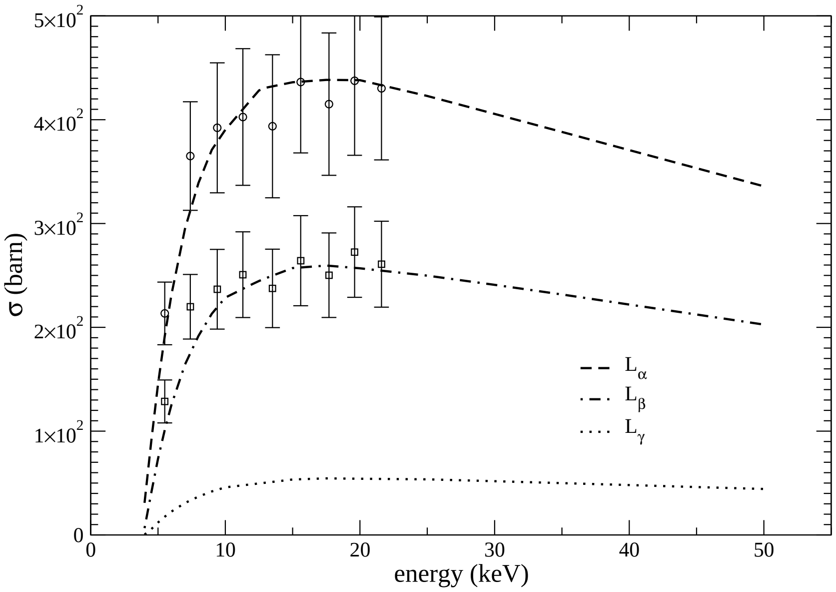

Figure 35: Comparison of the Weizsäcker-Williams results (*lines*) with experimental data [386] (*symbols*) for X-ray production cross sections for L-shell ionisation of indium by electrons.

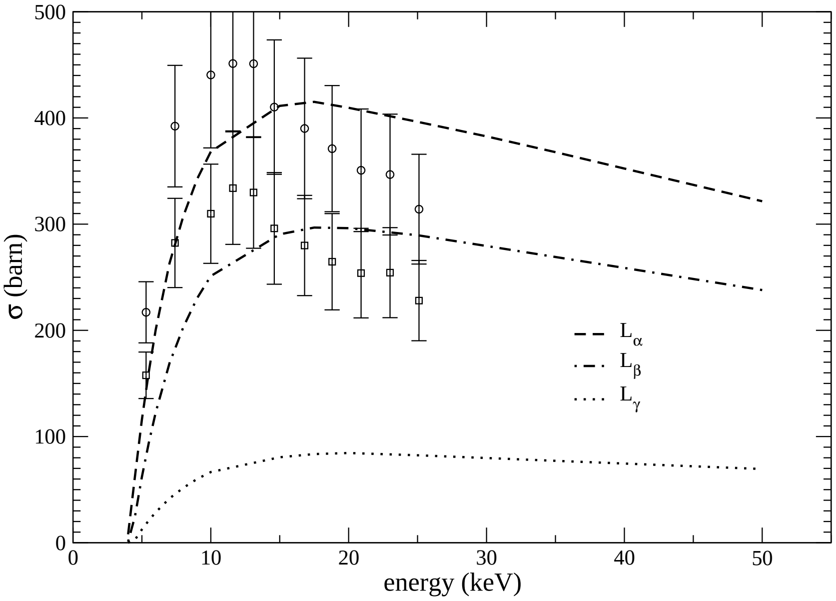

Figure 36: Comparison of the Weizsäcker-Williams results (*lines*) with experimental data [386] (*symbols*) for X-ray production cross sections for L-shell ionisation of tin by electrons.

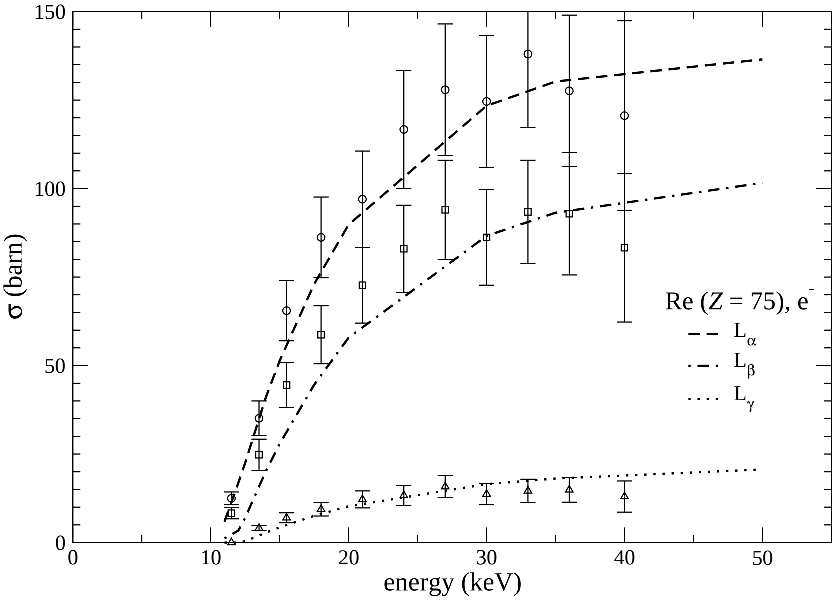

Figure 37: Comparison of the Weizsäcker-Williams results (*lines*) with experimental data [386] (*symbols*) for X-ray production cross sections for L-shell ionisation of rhenium by electrons.

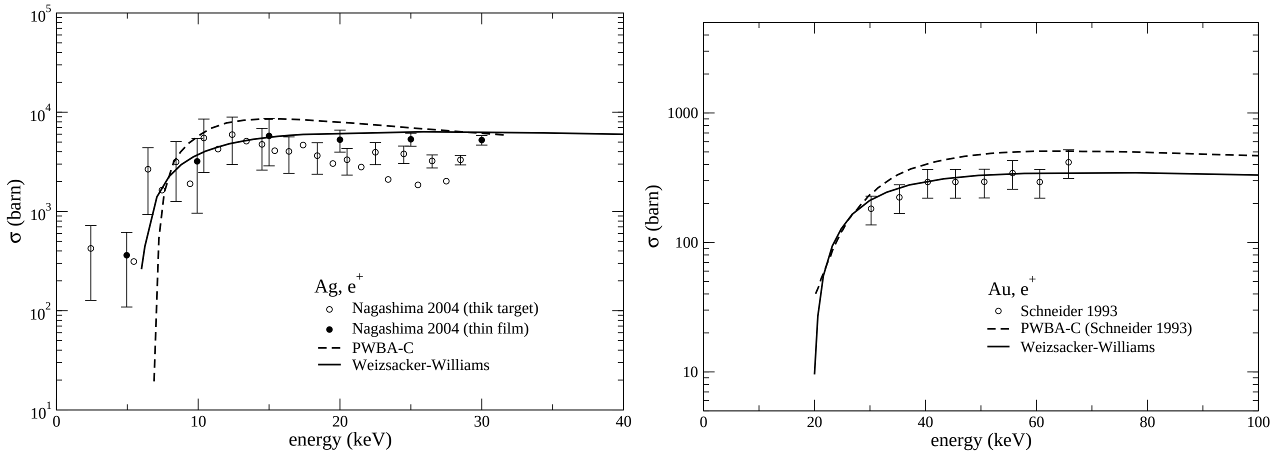

Figure 38: Comparison of the Weizsäcker-Williams results (*lines*) for positron L-shell ionisation cross sections with experimental data (*symbols*) for silver (*left*) and gold (*right*).

In order to draw definite conclusions about the reliability of a given theoretical model over a consistent set of elements, shells and incident electron energies, it is however necessary that more accurate experimental measurements of ionisation cross sections, in particular for positrons, are performed. Meanwhile, we conclude that the Weizsäcker-Williams model describes reasonably well a substantial body of the experimental data available. It can thus be safely used in a general-purpose MC code for medical applications.

4.3.2 Excitation cross section generation and validation

This section describes the excitation cross section results obtained using the code PSICRO and based on the MBT model developed in the previous chapter (Section 3.4.1). Calculated cross sections for the three contributions corresponding to the phonon (Eq. (76)), free-electron particle-hole (Eq. (80)) and plasmon (Eq. (87)) excitation, are shown in Fig. 39 (*left*) for positrons scattered by hydrogen in the low and medium energy range. The phonon excitation data are displayed at three different temperatures (T_1 =100K, T_2 =200K, T_3 =300K) . At energies lower than the Fermi energy, the rates of energy loss due to the phonon excitation mechanism dominate over other types of inelastic scattering processes while, for higher energies, particle-hole pair excitation and plasmon excitation become more important. Further, excitation cross sections for electrons bound in individual electronic shells have been calculated as given by Eq. (81). Thus, discrete particle-hole excitation data for two particular transitions in hydrogen (1s-2p and 1s-3p, having the excitation energy, ω_{ex}, equal to 10.2 eV and 12.1 eV, respectively) due to positron scattering are also displayed in Fig. 39 (*left*).

In addition to the free-electron particle-hole excitation cross-sections shown for positron scattering by hydrogen, Fig. 39 (*right*) includes as well excitation data for electrons, in order to illustrate the difference in the behaviour of the two types of particles as given by Pauli's exclusion principle. Also, the total cross sections are compared with experimental data obtained by Trajmar [407], indicating a satisfactory overall agreement.

Figure 40 displays calculated cross sections for plasmon excitation, as well as for free- and bound-electron excitation, as function of the incident energy for the scattering of positrons

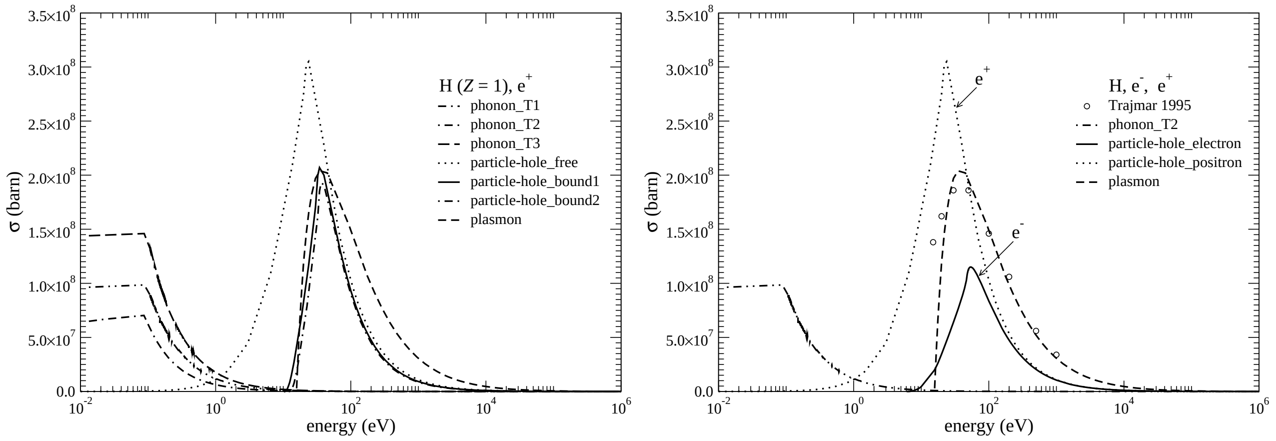

Figure 39: Temperature-dependent phonon, free and bound particle-hole, and plasmon excitation cross sections for positrons scattered by hydrogen (*left*). Phonon, free particle-hole and plasmon excitation cross sections for electrons scattered by hydrogen (*right*). Free-electron particle-hole calculations for positrons are also displayed, together with the experimental data of Trajmar [407].

by helium. Excitations of weakly bound atomic electrons by positrons are possible for any incident energy. Results of calculations for bound-state excitation cross-sections are also shown for an excitation energy of 21.22 eV, a comparison being made with the experimental results obtained by Mori (1994) [408] using a time-of-flight method. A good agreement is obtained in this case, as also a very good theoretical description of the excitation threshold.

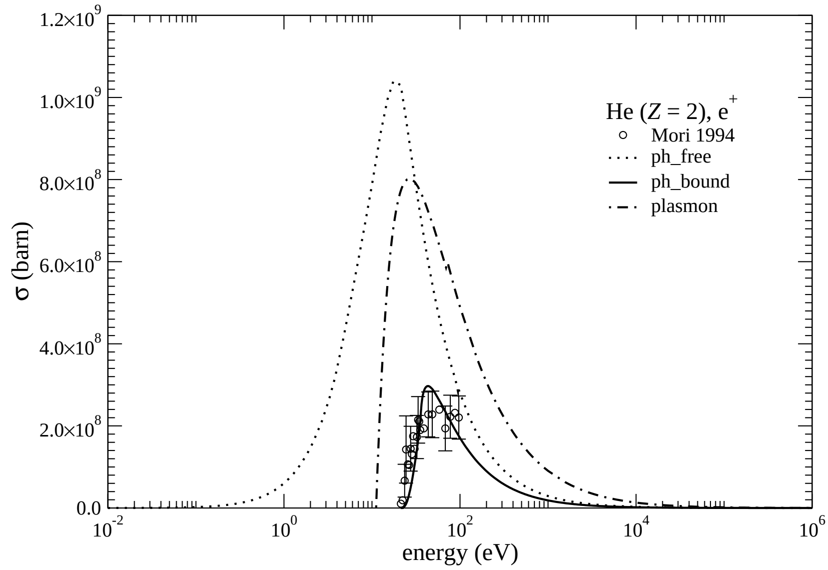

Figure 40: Positron excitation cross sections for helium (ω_{ex}=21.22 eV).

Similar calculations for positron excitation cross sections have been done for other rare-gas atoms, e.g. for neon and argon for which results are displayed in Fig. 41. The excitation energies considered for the calculation of inner-shell data are 17.7 eV for neon and 11.8 eV in the case of argon. A very good agreement between the theoretical results for bound-electron

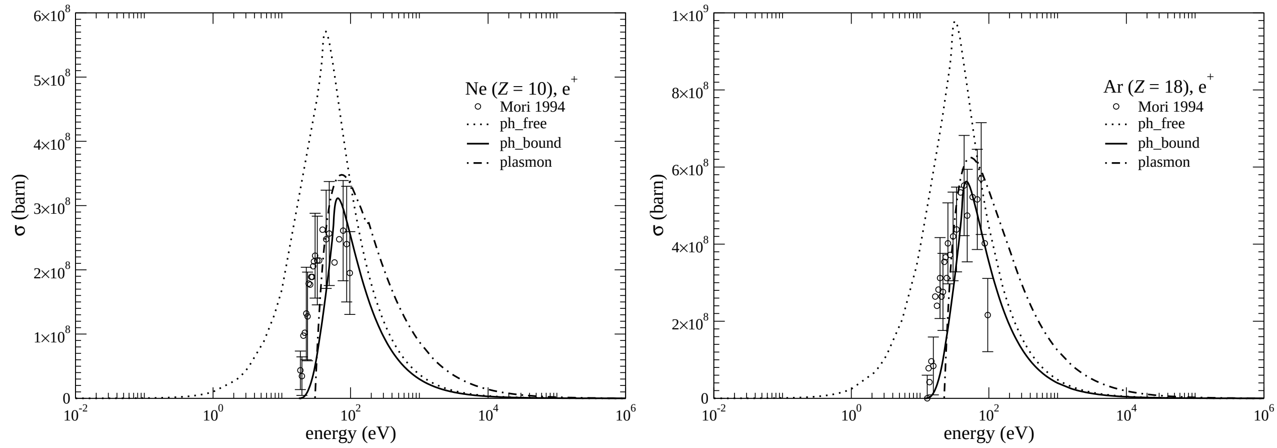

Figure 41: Positron excitation cross sections for neon ($\omega_{\rm ex}$=17.7 eV) and argon ($\omega_{\rm ex}$=11.8 eV).

excitation cross sections and the experimental measurements performed by Mori (1994) [408] can be noted in the case of argon. Although the relative difference between the plasmon and the discrete particle-hole excitation cross sections is lowered due to the increase in the number of electrons in the last occupied shell, for both neon and argon, plasmon excitation remains the dominant interaction at energies higher than the Fermi energy.

For electron scattering by neutral atoms, calculations have been performed for both the free-electron and the discrete excitation models. In Fig. 42, phonon, plasmon, free- and bound-electron particle-hole, together with total excitation cross sections, are displayed for argon. The theoretical results for discrete excitation have been compared with LLNL data, because in both cases only the contribution of large momentum transfer (small energy-loss) type of collisions has been taken into account. It is seen, as expected, that there is very good agreement in the peak position, as well as in the magnitude, of the bound-electron particle-hole excitation.

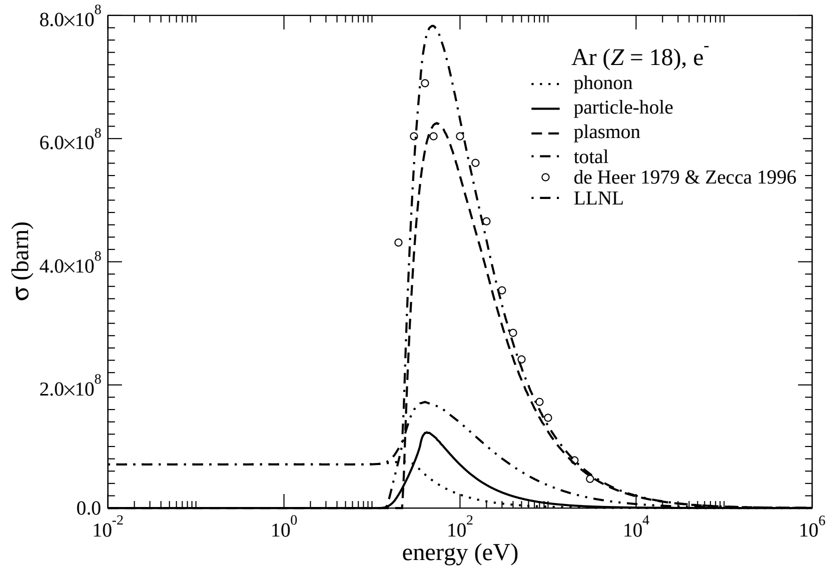

Figure 42: Electron excitation cross sections for argon.

This indicates that the particle-hole contribution to the total excitation cross section best represents the excitation component that arises from the distant collision type of interaction. If the plasmon excitation is also considered, the agreement of the total excitation cross sections with the experimental measurements [408, 409] is found to be significantly better. Thus, the description of the excitation mechanism can be considered as improved upon by including not only the phonon interaction which, as shown, is the dominant part at low energies, but also the close interaction type of mechanism (i.e. small momentum transfer or large energy-loss), the contribution of which becomes significant at higher energies.

Additional examples are given in Fig. 43 for electron excitation cross sections, the data shown being for krypton and xenon, respectively. In both cases, the theoretical calculations for bound-electron particle-hole excitation have been compared with LLNL data, and similar conclusions as for the argon case can be drawn. Comparisons with experimental results for total excitation cross sections [408-410] have also been done for both atoms, and the agreement is found to be very good. As seen earlier, accounting for phonon and plasmon excitation, as calculated with the optical model considered in the present development results in more accurate total excitation cross sections.

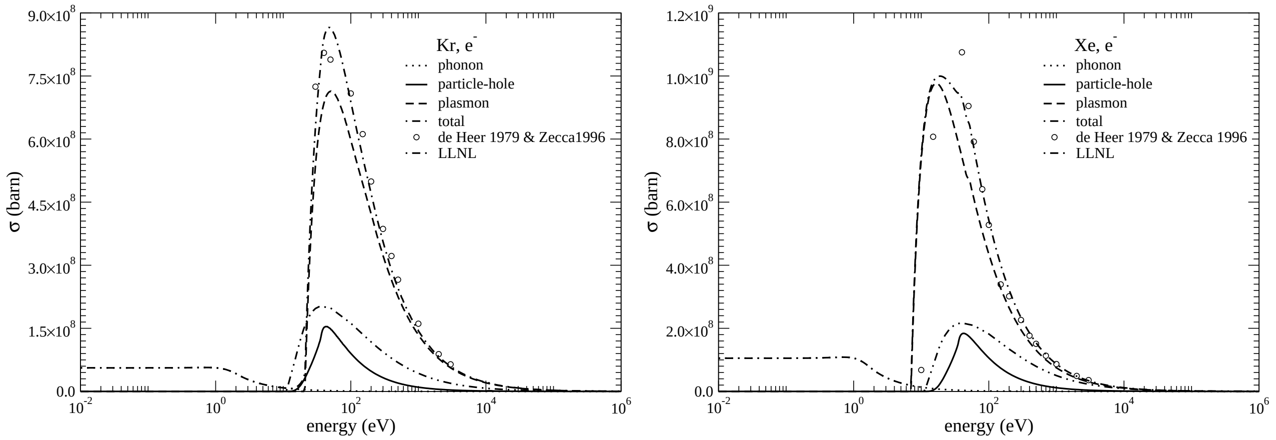

Figure 43: Electron excitation cross sections for krypton and xenon.

4.4 Summary

In this chapter, representative results have been presented of the calculations performed for the generation of bremsstrahlung, elastic and inelastic (ionisation and excitation) cross sections for the scattering, by neutral atoms, of electrons and positrons of energies down to 1 eV. Special emphasis has been put on the analyses of the low-energy numerical cross sections that are needed for the accurate simulation of particle transport in different materials. The various results have been included in two newly generated electron and positron data libraries [117], generated in a similar manner as the original LLNL library for electrons [146].

For bremsstrahlung emission, the results consist of two sets of cross section data and emitted photon energy spectra, viz. for electrons and positrons interacting with neutral atoms of atomic numbers Z=1-100 and for incident energies between 1 eV and 100 GeV.

The elastic scattering of electrons and positrons by neutral atoms, in particular in the medium to very low energy range of the incident particle, has been addressed in detail in terms of angular DCSs. The results of the partial-wave method, as presently implemented into the currently upgraded version of the code PSICRO, described in the previous chapter, have been assessed against the most recently developed theoretical models and experimental data available. Such validation of the electron and positron elastic DCSs has been carried out for a significant number of high as well as low-Z elements and for medium down to 1 eV incident energy. It has been observed that, despite the apparent incompleteness of the theoretical model used currently to describe the scattering potential of charged particles by neutral atoms, which does not account for the loss of flux from the elastic to the inelastic chanels above the excitation threshold, a very good agreement of the theoretical and experimental DCS data has been obtained for all energies considered, in particular for low-Z elements. For high-Z elements, small differences have been observed for scattering in the forward direction ($\theta < 60°$), with respect to the other theoretical models included in this study. These are believed to be due to the absorption interaction which is not accounted for by the present model of the scattering potential. For the high-Z case, the Thomas-Fermi model of the exchange potential for energies above 10 eV, and the Furness-McCarthy model for energies below 10 eV, are better theoretical approximations for reproducing experimental data. Thus, the elastic scattering DCSs generated using the code PSICRO, with the presently implemented partial-wave method, have been shown to well describe the elastic scattering process of charged particles by neutral atoms for energies above 10 eV and for low-Z materials for energies as low as 1 eV.

Regarding validation of the results for ionisation, a comprehensive study has been done for the Weizsäcker-Williams K-shell and L-shell ionisation cross sections for electrons, taking into account a variety of theoretical and experimental data available. For the entire range of incident energies over which experiments have been done, the Weizsäcker-Williams method shows excellent agreement with measured values for a wide range of atoms. Moreover, this method is also found to predict results in good agreement with data based on other theoretical models recently developed.

Representative results of the MBT model proposed for the description of the excitation process from the ground state of neutral atoms (Z=1 to 100), implemented in the code PSICRO during the present thesis work, have also been presented. Comparison of calculated discrete and total excitation cross sections with experimental results available in the literature has been performed for electron and positron scattering by rare-gas atoms, at medium to low energies of the incident particle. For all cases, a general good agreement has been observed. The present model, as used to generate discrete excitation cross sections, has been found to provide an adequate description of the excitation process, accounting for the close collision part of the interaction. The latter is increasingly important at lower energies of the incident particle, and was disregarded in the calculation of the excitation data originally included in the LLNL library [146].

In summary, the present results for elastic, ionisation and excitation, corresponding to the models described in the previous chapter, ensure the generation of reliable electron and positron cross sections for a large number of materials at low and medium energies. The present development and validation efforts have thus rendered the newly generated electron and positron numerical cross section libraries an adequate source for accurate modelling of electron and positron transport, particularly in the cellular and sub-cellular ranges.

5 PENELAST - Extension of the PENELOPE Code System

5.1 Introduction

The transport of electrons and positrons through matter is equivalent to considering a repetitive scattering process, both elastic and inelastic, of the projectile into a new direction of motion together with a permanent degradation of its energy. Owing to the random nature of the particle track in a medium, the generation of its spatial and angular displacements after a given interaction process is amenable to MC simulations (as briefly discussed in the introduction, Section 1.2).

The present as well as the next chapter address the problem of electron/positron transport in materials, especially when the number of interaction events per particle track is so large that the "detailed" simulation of every interaction along the particle track is computationally very expensive or even unfeasible, viz. for medium to high energy incident particles and for thick geometries. Unlike Class II "mixed" MC simulation algorithms, for which the elastic and inelastic events above a given threshold are simulated in detail, Class I algorithms solve the transport problem in a "condensed" manner. Thus, the latter simulate the global effect of a large number of small-mean-free-path and small-scattering-angle collisions using a considerably smaller number of artificial large-mean-free-path and large-angle-of-scattering collisions by applying an appropriate multiple-scattering theory. As such, Class I simulation represents a powerful means for developing fast MC codes for charged particle transport.

In order to meet the current goal of speeding up simulation algorithms effectively, it is clearly necessary to examine the limitations of the existing multiple-scattering models (e.g. Goudsmit-Saunderson [29], Lewis [49] or Wentzel-Molière [32]) that have been implemented in various MC codes. This aspect will be addressed in detail in the next chapter via comparisons between calculated angular multiple-scattering probability distribution functions (PDFs) with detailed MC simulations and/or with available experimental values.

The other factor determining the accuracy of condensed stochastic calculations is represented by the DCS data used to model the different interaction mechanisms. Thus, as a complementary goal to that of the previous two chapters, a principal aim of the present chapter is to ensure that reliable and, in particular, the same numerical cross section input data (elastic, inelastic, bremsstrahlung, stopping power, etc.) are implemented in codes that are being compared with each other for benchmarking purposes. To achieve this, an extension of the PENELOPE code system has currently been undertaken to incorporate the numerical elastic DCSs obtained from the relativistic (Dirac) partial-wave expansion method, in tabular form, as a function of the incident particle energy and scattering angle. For the other interaction mechanisms, the newly written code, named PENELAST, uses the options existing in PENELOPE (version 2001). PENELAST can thus be used for simulating the angular, spatial and energy PDFs of electrons that have traveled a certain path length. These results can then be compared with calculations provided by Goudsmit-Saunderson, Lewis or Wentzel-Molière formalisms that use the same numerically tabulated elastic DCS data (see next chapter).

Section 5.2 gives details of the elastic and inelastic DCSs and stopping power data as implemented in the code PENELAST. These data are first generated in the form of numerical tabulations for specific grids of angular deflections and incident particle energy, as required for a given application. The development of subroutines that are able to read these numerical cross section data and generate values needed for arbitrary energies and angles using various interpolation methods (while considering the requirements of both high accuracy and computational speed) is described in Section 5.3. Comparisons of the results for the angular and energy distributions of charged particles obtained with the original version of PENELOPE and the newly developed code are presented in Section 5.4. Several mixed and detailed simulation examples are given in the present chapter to demonstrate the extension which has currently been achieved for studies of radiation transport down to very low energies and particle ranges, particularly to the DNA range. In the next chapter, the code PENELAST will be used more systematically to provide comparisons with direct calculations performed, using other multiple-scattering models, for angular distributions of high-energy charged particles that have travelled a given path-length.

In the present chapter, equations are expressed in cgs Gaussian units; occasionally, energies are given in eV. In the computer programs, however, unless otherwise stated, all the internal calculations are performed in Hartree atomic units, in which the absolute magnitude of the electron charge e, the electron rest mass $\mathrm{m_e}$ and the reduced Planck constant $\hbar$ have unit values ($\hbar = \mathrm{m_e} = e = 4\pi\epsilon_0 = 1$). The atomic units of energy and length are the Hartree ($E_\mathrm{h} = 27.21138$ eV) and the Bohr radius ($a_0 = 5.291772 \times 10^{-9}$ cm), respectively.

5.2 Numerical Cross Section Data Tabulations

As seen earlier in Chapters 3 and 4, various theoretical approaches are used to describe, in terms of DCSs, the elastic and inelastic scattering of charged particles in the Coulomb field of atomic nuclei. These theoretical models range from simple analytical approximations to detailed state-of-the-art theories. Moreover, complex computer codes such as PWASCH, PWADIR and, in particular, PSICRO, ELSEPA [119, 120] and RODM [228, 229], have been developed to account for the details of the interactions down to very low incident particle energies. The limitations of the presently available models (see Chapters 3 and 4) have been pointed out following a validation procedure of the elastic and inelastic calculated cross section data by comparison with a large set of experimental results in the low to medium energy range. For instance, it has been shown that, in the representation of the interaction potential used to describe the elastic scattering process, the code PSICRO does not account for the absorption potential, so that the DCSs calculated with this code appear to be underestimated (especially at forward angles) and the peaks shifted to lower angles. Similarly, for the inelastic scattering process, the model implemented in PSICRO to describe the generalized oscillator strength, although it leads to fairly realistic description of the integrated cross sections, is relatively simple and does not entirely reproduce the global features of the Bethe surface. Thus, more accurate theoretical models will be further used for the generation of up-to-date cross section input to be used in MC calculations.

In the following sections, the theoretical models presently employed for the generation of purely numerical elastic [119, 184, 197] and inelastic [228, 229] scattering DCSs of electrons/positrons by neutral atoms for kinetic energies in the range from 50 eV up to about 1 GeV are described. For instance, to describe the elastic scattering interactions, numerical DCSs are generated in tabulated form by using the relativistic (Dirac) partial-wave expansion method already described in Chapter 3. For energies above 1 keV, these cross sections are the same[25] as those implemented in the standard PENELOPE system (version 2001). In order to account for angular deflections due to inelastic collisions, analytical inelastic DCSs derived from the Lijlequist-Sternheimer generalized oscillator strength (GOS) model are generated for the same scattering angle and energy grids as those for which the elastic scattering data are available. The stopping powers calculated from this model coincide with the values recommended by Berger and Seltzer [225] for energies above 10 keV, and they are expected to remain accurate for energies down to a few hundred eV. Details of the numerical implementation of these cross section and stopping power data are also given below.

5.2.1 ELSEP - Numerical elastic scattering differential and integrated cross section tabulations

The following addresses the generation of a set of numerical elastic DCSs for MC simulation of electron/positron transport in various materials (atomic numbers Z=1-100). The procedures applied to obtain tabulated cross section data, differential in energy and scattering angle, are presented. These data will then be used in Section 5.4 and Section 6.5 (the next chapter) to compute the multiple-scattering angular and energy probability distribution functions of charged particles after travelling a given path length. In the range from about 10 MeV down to very low incident energies, the PWA method described earlier in Chapter 3 and implemented in the Fortran 77 code ELSEPA [119, 120] allows us to carry out accurate calculations of elastic DCSs for electrons/positrons scattered in a static screened Coulomb potential of neutral atoms at rest. Thereby, the effective screening potential between the projectile and the target atom, given by Eq. (36), can be modelled by combining the different options offered in the code ELSEPA, for each particular interaction potential, exchange, correlation-polarization and absorption, as well as for both electronic and nuclear charge distributions. Effectively, an analytical model is chosen among the various implemented ones such that the set of calculated DCSs best describes the experimental data available for a given projectile kinetic energy. In specific terms, the DCS input data used in this work have been generated by selecting the following options for each case:

- The models employed for the calculation of *the nuclear charge distribution* $\rho_{\mathrm{n}}(r)$, which enters the definition of the effective interaction potential are known to affect the calculated elastic DCSs only for projectiles with kinetic energies larger than about 10MeV, in particular at large angles. At low energies, the four models considered agree very closely, the differences in the DCSs being no larger than about 0.5%. For this reason, it is a good approximation to consider the nucleus as a point charge, with a purely Coulombian electrostatic potential,

$$\varphi_{\mathrm{n}}(r) = \frac{Ze}{r}, \qquad \rho_{\mathrm{n}}(r) = Z\delta(\mathbf{r}). \tag{93}$$

However, during the present work, the Helm's uniform-uniform distribution model [201] is used as default to model the nuclear charge distribution, as the DCSs calculated in this manner join smoothly with the results from the high-energy factorization model. In this model, the nuclear charge distribution is expressed as a convolution of two uniform convolutions,

$$\rho_{\mathrm{n}}(r) = Z\int \rho_1(\mathbf{r}')\rho_2(\mathbf{r}-\mathbf{r}')\mathrm{d}\mathbf{r}' \tag{94}$$

---

[25] The total and two first transport cross sections calculated from the partial-wave method are reproduced.

where ρ_1 and ρ_2 are normalized to unity.

• By default, *the atomic electron densities* $\rho_e(r)$, are handled numerically as they are available in data files for neutral atoms of elements hydrogen to lawrencium ($Z = 1$-103), obtained from multiconfiguration Dirac-Fock self-consistent atomic calculations [205]. Several approximative analytical models are also available. The Thomas-Fermi-Molière model is the simplest theoretical method in which the electron cloud is considered as a locally homogeneous electron gas bound by the screened Coulomb field of the nucleus that is taken as a point charge.

$$\rho_{\mathrm{e}} = \frac{Z}{4\pi r}\sum_{\mathrm{i}=1}^{3} A_{\mathrm{i}} a_{\mathrm{i}}^{2} exp(-a_{\mathrm{i}} r). \tag{95}$$

where

$$\begin{aligned} A_1 &= 0.10 \qquad A_2 = 0.55 \qquad A_3 = 0.35 \\ a_1 &= 6/b \qquad a_2 = 1.2/b \qquad a_3 = 0.3/b \end{aligned}$$

and b is the Thomas-Fermi scale parameter which gives the $Z^{-1/3}$ scaling property to the Thomas-Fermi model, and a_0 is the Bohr radius. If an electron exchange correction is taken into account, one obtains the Thomas-Fermi-Dirac model. In this case the screening function needs to be calculated for each particular atom or ion. The code ELSEPA also includes an electron density which has been obtained by fitting the Dirac-Hartree-Fock-Slater electron densities of neutral atoms [199]. The differences in the calculated DCSs obtained by these models are larger than in the case of the nuclear charge distribution. At high energies the differences are confined to the region of low scattering angles (Fig. 44), while at low energies they become significant at larger angles as well due to the complex shape of the DCSs (with multiple maxima and minima).

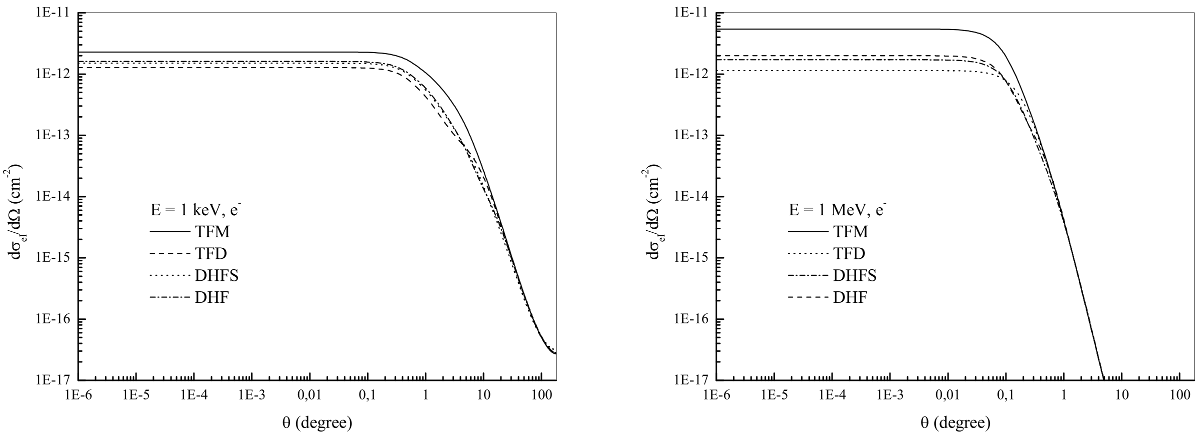

Figure 44: Elastic DCSs for 1 keV and 1 MeV energy electrons scattered by sodium, obtained considering various atomic electron density models.

• When the projectile is an electron, one has to take into account the effect of *exchange* collisions in which the projectile exchanges place with an atomic electron. The default ELSEPA exchange potential for electron scattering is the Furness-McCarthy potential [209],

$$V_{\mathrm{ex}}(r) = \frac{1}{2}[E - V_{\mathrm{st}}(r)] - \frac{1}{2}\{[E - V_{\mathrm{st}}(r)]^2 + 4\pi a_0 e^4 \rho_{\mathrm{e}}(r)\}^{1/2} \tag{96}$$

although, as indicated earlier, the three models available yield, for energies above 10 eV, essentially the same results. The potential is derived form a non-local exchange interaction by using the Wentzel-Kramers-Brillouin (WKB)-like approximation[26] for the wave functions. Other analytical models are based on the Thomas-Fermi approximation [207], as a generalization of the Slater's potential,

$$V_{\mathrm{ex}}(r) = -\frac{e^2}{\pi k_{\mathrm{L}}}\left[k_{\mathrm{L}} k_{\mathrm{F}} - \frac{1}{2}(k_{\mathrm{L}}^2 - k_{\mathrm{F}}^2)\ln\left|\frac{k_{\mathrm{L}} + k_{\mathrm{F}}}{k_{\mathrm{L}} - k_{\mathrm{F}}}\right|\right], \tag{97}$$

or the Riley-Truhlar exchange potential [208], valid in the high energy limit,

$$V_{\mathrm{ex}}(r) = -\pi a_0 e^4 \rho_{\mathrm{e}}(r)\left[\frac{\hbar^2}{2m}k^2 + e\varphi(r)\right]^{-1} \tag{98}$$

where $k_{\mathrm{F}}(r) = [3\pi^2 \rho_{\mathrm{e}}(r)]^{1/3}$ is the local Fermi wave number of the atomic electron cloud, and $k_{\mathrm{L}}(r) = \sqrt{k^2 + k_{\mathrm{F}}^2}$ is the local wave number of the projectile electron.

In Chapter 4, a detailed study of these theoretical exchange models has been done for elastic scattering of electrons of medium to very low energy by various neutral atoms. Comparisons of experimental and calculated DCSs have been displayed in Figs. 25-30 for electrons elastically scattered by hydrogen, helium, neon, argon, krypton and xenon. The results of the partial-wave calculations, provided by the detailed models which consider the Furness-McCarthy exchange potential as given by Eq. (96) [209] and the Thomas-Fermi exchange potential described by Eq. (97) [207], have been included in these comparisons, along with the results generated with PSICRO, i.e. as obtained by considering simply the O'Connell-Lane polarization potential [Eq. (53)] [223] and the O'Hara exchange potential [Eq. (52)] [221]. In these cases, the models based on the Furness-McCarthy and the Thomas-Fermi exchange potentials do not take into account the absorption potential because they refer to energies below the first excitation threshold for each element. A shift of the first minimum of the DCS data to higher energies is observed, in particular for high-Z elements such as argon, krypton and xenon. Moreover, for energies around 10 eV, the Thomas-Fermi model has been shown to provide resuls in excellent agreement with the experimental data for all these elements. For energies significantly lower than 10 eV, it has been observed that the local density approximation model does not provide a satisfactory description of the experimental DCSs. In this lower energy range, the second model based on the Furness-McCarthy exchange potential is seen to give results which are in better agreement with the measurements. However, for low atomic numbers, such as helium and neon (shown in Fig. 26), the most accurate theoretical model seems to remain the one implemented in PSICRO, i.e. that based on the O'Hara exchange potential for the whole energy range of interest and, in particular, for energies significantly below 10 eV.

• *The correlation-polarization* and *the absorption* potentials cannot be calculated easily from first principles; the options offered in ELSEPA are based on models that combine empirical

---

[26] The WKB method asymptotically approximates the solutions to linear ODEs which exhibit high frequency oscillations.

information (static polarizability, lowest excitation energy, etc.) with the local-density approximation [119]. The model used to account for the absorption of particles from elastic to inelastic channels for energies above the first excitation threshold was described previously in Chapter 3. Regarding the polarization of the charge cloud of the target atom, the Buckingham polarization potential [207] given by

$$V_{\mathrm{cp,B}}(r) = -\frac{\alpha_{\mathrm{d}} e^2}{2(r^2 + d^2)^2}, \tag{99}$$

represents a long-range approximation that quantifies the effect produced by the electric field of the induced diplole moment. In the above relation, α_{d} is the dipole polarizability of the target atom, and $d = \sqrt[4]{1/2\alpha_{\mathrm{d}} a_0 Z^{1/3} b_{\mathrm{pol}}^2}$ is a phenomenological cut-off parameter which prevents the polarization potential from diverging at $r = 0$. The default ELSEPA correlation-polarization potential is the LDA potential [119], is calculated as

$$V_{\mathrm{cp}}^{\pm}(r) \equiv \begin{cases} \max\{V_{\mathrm{co}}^{\pm}(r), V_{\mathrm{cp,B}}(r)\}, & \text{if} \quad r < r_{\mathrm{cp}}, \\ V_{\mathrm{cp,B}}(r), & \text{if} \quad r \geq r_{\mathrm{cp}}, \end{cases}$$

where $V_{\mathrm{co}}^{\pm}(r)$ is the LDA correlation potential, $V_{\mathrm{cp,B}}(r)$ is the long-range Buckingham polarization potential, and r_{cp} is the outer radius at which $V_{\mathrm{co}}^{\pm}(r)$ and $V_{\mathrm{cp,B}}(r)$ cross. The LDA correlation potential for electrons $V_{\mathrm{co}}^{-}(r)$ is given by [411],

$$V_{\mathrm{co}}^{-}(r) = \begin{cases} -\frac{e^2}{a_0}(0.0311 \ln r_{\mathrm{s}} - 0.0584 + 0.00133 r_{\mathrm{s}} \ln r_{\mathrm{s}} - 0.0084 r_{\mathrm{s}}, & r_{\mathrm{s}} < 1, \\ -\frac{e^2}{a_0}\beta_0 \frac{1+(7/6)\beta_1 r_{\mathrm{s}}^{1/2}+(4/3)\beta_2 r_{\mathrm{s}}}{(1+\beta_1 r_{\mathrm{s}}^{1/2}+\beta_2 r_{\mathrm{s}})^2}, & r_{\mathrm{s}} \geq 1, \end{cases}$$

where $\beta_0 = 0.1423$, $\beta_1 = 1.0529$, and $\beta_2 = 0.3334$, and for positrons $V_{\mathrm{co}}^{+}(r)$ is given by [224]

$$V_{\mathrm{cp}}^{\pm}(r) \equiv \begin{cases} \frac{e^2}{a_0}\left\{0.5835 + 0.91 r_{\mathrm{s}}^{-1/2} + [0.00255 \ln(r_{\mathrm{s}}) - 0.0575] \ln(r_{\mathrm{s}})\right\}, & \text{if} \quad r_{\mathrm{s}} < 0.302, \\ \frac{e^2}{a_0}\left[0.461525 - 0.04549 r_{\mathrm{s}}^{-2}\right], & \text{if} \quad 0.302 \leq r_{\mathrm{s}} < 0.56, \\ \frac{e^2}{a_0}\left[-\frac{4.3637}{(r_{\mathrm{s}}+2.5)^3} + \frac{-6.5755+0.4776 r_{\mathrm{s}}}{(r_{\mathrm{s}}+2.5)^2} + \frac{1.43275}{r_{\mathrm{s}}+2.5} - 0.3149\right], & \text{if} \quad 0.56 \leq r_{\mathrm{s}} < 8, \\ \frac{e^2}{a_0} - 15375.8679 r_{\mathrm{s}}^{-6} + 44.5047 r_{\mathrm{s}}^{-3} - 0.262, & \text{if} \quad r_{\mathrm{s}} \geq 8. \end{cases}$$

where $r_{\mathrm{s}} \equiv 1/a_0[3/(4\pi\rho_{\mathrm{e}}(r)]^{1/3}$ is the density parameter.

Figs. 20-23, displayed in Chapter 4, show the comparison between experimental and calculated results of DCSs for electron elastic scattering by sodium, potassium, copper and gold, at energies which account for the absorption interaction. In the present analysis, the theoretical partial-wave calculations generated with PSICRO, i.e. as obtained by considering only the O'Connell-Lane polarization potential [Eq. (53)] [223] and the O'Hara exchange potential [Eq. (52)] [221], have been, in additon to the experimental measurements, compared with detailed calculations of the electron DCSs. These were obtained by taking into account the absorption potential, as given by Eq. (35) [119], as well as the local density approximation exchange potential (also called the Thomas-Fermi potential) described by Eq. (97) [207], and the Furness-McCarthy exchange potential given by Eq. (96) [209]. It has been seen that, in particular for high-Z elements such as potassium and gold, the inclusion of the absorption potential in the description of the interaction between the projectile and the target changes the shape of the calculated DCS data over the entire angular range but especially at forward angles.

In addition, the first minimum is shifted to higher angles, the models including absorption providing, in general, a better description of the experimental data.

With the effective interaction potential defined as described above, the algorithm used to integrate the radial equations (39) is as follows. The function $rV(r)$ is replaced by the natural cubic spline that interpolates the values of this function for a given grid of atomic radii, densely spaced to ensure that interpolation errors have a negligible effect on the computed radial functions. The integration of the radial equations is started at $r = 0$, with the boundary conditions $P_{E\kappa}(0) = Q_{E\kappa}(0) = 0$, and extended outwards up to a distance r_{m} beyond the effective range of the interaction potential (or such that the function $rV(r)$ has reached its asymptotic value). Between consecutive grid points, the radial wave functions and the phase shifts are calculated by using Buhring's [412] power-series method (38) with terms being summed up until a desired accuracy is reached (viz. 10^{-15} with double precision arithmetic). In the case of a too large grid interval, the convergence of the series is accelerated by splitting the radii grid interval into smaller subintervals. With this method, truncation errors are avoided, the calculated radial functions and phase shifts being affected only by unavoidable round-off errors.

In the case of the scattering of particles by finite-range fields, the phase shifts in Eq. (38) are obtained by matching the outward computed radial wave function with the free-particle wave function (i.e. a combination of spherical Bessel and Neumann functions). For electron and positron scattering by a pure Coulomb field or a modified Coulomb field (such that it contains a short-range real or complex potential which vanishes for $r > r_{\mathrm{c}}$), the phase shifts are computed with the help of a Dirac-Coulomb spherical wave and Dirac spherical wave solution, respectively [119].

In order to select the lowest energy cutoff for the generation of the DCS input data, several examples were given in Section 4.2. In this way, the validity region of the various models, which can be used for the theoretical description of the interaction potential that models the elastic scattering interaction by neutral atoms at medium to very low energies, could be understood relatively well. It has been seen thereby that the validity of each model depends significantly on the incident energy and the atomic number of the element. Accordingly, in order to ensure the generation of an accurate set of elastic DCS data (for all elements, Z=1-100) that can be used in conjunction with the MC simulation of charged particle transport in matter, it is recommended that an energy cutoff of 10 eV be chosen at present.

5.2.2 Differential and integrated inelastic scattering cross sections based on the optical data model.

This section presents the details of an optical-data model, originally implemented in PENELOPE, for the generation of up-to-date inelastic DCSs, and which is presently employed in the code PENELAST for the simulation of the angular distributions and energy spectra of charged particles after a given path length. In this model, the ionization of each atomic electron shell is described by a single δ-oscillator, whose "resonance energy" is set in such a way that the mean ionization energy tabulated by Seltzer and Berger is reproduced. The δ-oscillator model has recently been generalized to a N-oscillator [229] which provides improved stopping power and inelastic cross sections in the low-energy region.

As indicated in Chapter 3, the quantum mechanical approach to the inelastic collision theory of charged particles with individual atoms and molecules was first introduced by Bethe [238, 413] based on the first-order plane-wave Born approximation. For condensed matter, the theory of inelastic collisions had been described by Fano [255]. Similar results are obtained using classical dielectric theory [258, 414] which expresses the stopping power wielded by a given medium on the charged particle when subject to polarization due to the induced monochromatic electromagnetic field of wavevector $\mathbf{k}$ and frequency ω.

In the following, the inelastic collisions of electrons/positrons of rest mass $m = m_e$ and charge $Z_0 e$ moving in a homogeneous amorphous medium with $\mathcal{N}$ randomly oriented atoms or molecules, Z electrons per atom or molecule, and ρ its mass density, is considered:

$$\mathcal{N} = N_\mathrm{a}\, \rho / A_\mathrm{w}, \tag{100}$$

where N_a denotes the Avogadro constant and A_w is the atomic weight of the medium.

As in the case of elastic scattering, due to the random orientation of the target atom or molecule, the inelastic DCSs are assumed to be independent of the azimuthal angle, ϕ. Therefore, the effect of individual inelastic collisions on the projectile is completely described by the energy loss W and the polar scattering angle, θ. However, instead of $\theta \equiv \arccos(\mathbf{p} \cdot \mathbf{p}')$, it is more convenient to use the recoil energy Q [255],

$$Q(Q + 2\mathrm{m_e}c^2) = (cq)^2 = c^2(p^2 - p'^2 - 2\mathbf{p}\mathbf{p}' \cos\theta). \tag{101}$$

where q is the momentum transfer, $\mathbf{q} \equiv \mathbf{p} - \mathbf{p}'$, given by the linear momenta of the projectile just before ($\mathbf{p}$) and after ($\mathbf{p}'$) the collision.

The DCSs per atom for collisions with energy loss W and recoil energy Q obtained from the first Born approximation can be written as [255]

$$\frac{\mathrm{d}^2\sigma_\mathrm{in}}{\mathrm{d}W\,\mathrm{d}Q} = \frac{\mathrm{d}^2\sigma_\mathrm{L}}{\mathrm{d}W\,\mathrm{d}Q} + \frac{\mathrm{d}^2\sigma_\mathrm{T}}{\mathrm{d}W\,\mathrm{d}Q}, \tag{102}$$

which corresponds to two contributions from longitudinal and transverse interactions, induced by the instantaneous Coulomb field and by the exchange of virtual photons, respectively. Using their detailed expressions, the inelastic DCSs are expressed as:

$$\frac{\mathrm{d}^2\sigma_\mathrm{in}}{\mathrm{d}W\,\mathrm{d}Q} = \frac{2\pi z_0^2 e^4}{\mathrm{m_e}v^2} \left(\frac{2\mathrm{m_e}c^2}{WQ(Q + 2\mathrm{m_e}c^2)} + \frac{\beta^2 \sin^2\theta_\mathrm{r} W 2\mathrm{m_e}c^2}{[Q(Q + 2\mathrm{m_e}c^2) - W^2]^2} \right) \frac{\mathrm{d}f(Q,W)}{\mathrm{d}W}, \tag{103}$$

where $v = \beta c$ is the velocity of the projectile, θ_r is the angle between the initial momentum of the projectile and the momentum transfer, given by

$$\cos^2\theta_\mathrm{r} = \frac{W^2/\beta^2}{Q(Q + 2\mathrm{m_e}c^2)} \left(1 + \frac{Q(Q + 2\mathrm{m_e}c^2) - W^2}{2W(E + \mathrm{m_e}c^2)} \right)^2. \tag{104}$$

and $\mathrm{d}f(Q,W)/\mathrm{d}W$ is the atomic generalized oscillator strenght (GOS), which has the form of a surface over the (Q,W) plane, called the Bethe surface [239, 415].

The inelastic DCSs obtained from dielectric theory reduce to those based on the quantum mechanical one in the low-density approximation where the GOS can be defined as:

$$\frac{\mathrm{d}f(Q,W)}{\mathrm{d}W} \equiv W \frac{Q+\mathrm{m_e}c^2}{\mathrm{m_e}c^2} \frac{2Z}{\pi\Omega_\mathrm{p}^2} \operatorname{Im}\left(\frac{-1}{\epsilon(Q,W)}\right), \tag{105}$$

where $\Omega_\mathrm{p}^2 = 4\pi\mathcal{N}Z\hbar^2e^2/\mathrm{m_e}$ is the plasma energy of a free-electron gas and $\epsilon(Q,W) = \epsilon_1(Q,W)+i\epsilon_2(Q,W)$ is the complex dielectric function which characterizes the medium in the semiclasical treatment (in the low-density approximation $\epsilon_1 \sim 1$ and $\epsilon_2 \ll 1$).

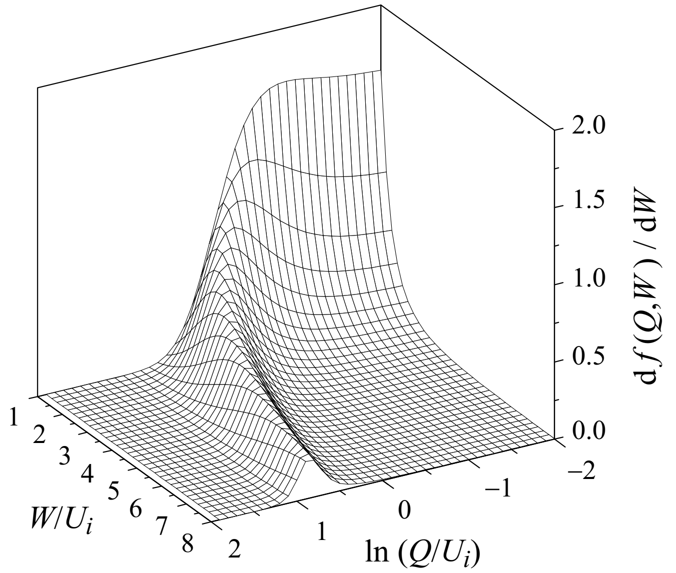

Figure 45: The GOS for ionization of the hydrogen atom ($Z = 1$) in the ground state. All energies are in units of the ionization energy $U_i = 13.6$ eV. The GOS for ionization of (non-relativistic) hydrogenic ions is independent of Z if energies are expressed in units of the ionization energy.

Figure 45 shows the Bethe surface for ionization of the hydrogen atom. For large recoil energies, the target electrons behave as if they were free and at rest, and the GOS reduces to the Bethe ridge [239] along the line $W = Q$. In the limit $Q \rightarrow 0$, the GOS reduces to the optical oscillator strength (OOS),

$$\frac{\mathrm{d}f(W)}{\mathrm{d}W} \equiv \frac{\mathrm{d}f(Q=0,W)}{\mathrm{d}W}. \tag{106}$$

The atomic DCSs for inelastic interactions in a dense medium are given by

$$\frac{\mathrm{d}^2\sigma_\mathrm{in}}{\mathrm{d}W\,\mathrm{d}Q} = \frac{2\pi z_0^2e^4}{\mathrm{m_e}v^2}\frac{\mathrm{d}f(Q,W)}{\mathrm{d}W}\left(\frac{2\mathrm{m_e}c^2}{WQ(Q+2\mathrm{m_e}c^2)}\right.$$
$$\left. + \left\{\frac{\beta^2\sin^2\theta_\mathrm{r}W2\mathrm{m_e}c^2}{[Q(Q+2\mathrm{m_e}c^2)-W^2]^2} - \mathcal{D}(Q,W)\right\}\right), \tag{107}$$

where the term $\mathcal{D}(Q,W)$ accounts for the density-effect correction [416] in Eq. (103) and has its origin in the polarizability of the medium which screens the transverse interaction, thus reducing the stopping power.

The GOS satisfies the Bethe sum rule [239]

$$\int_0^\infty \frac{\mathrm{d}f(Q,W)}{\mathrm{d}W}\,\mathrm{d}W = Z \qquad \text{for any } Q. \tag{108}$$

and leads to the interpretation of the GOS as the effective number of electrons per unit energy transfer for interactions with a given recoil energy Q. Another quantity of interest is the mean excitation energy I, defined as [255, 239]

$$Z \ln I = \int_0^\infty \ln W \,\frac{\mathrm{d}f(W)}{\mathrm{d}W}\,\mathrm{d}W, \tag{109}$$

which is important in defining the Bethe stopping power of a given medium.

In order to allow fast random sampling of W and Q during the MC simulations (such as in PENELOPE [34]), the GOS model is split into contributions arising from different atomic shells, each shell being characterized by the number Z_k of electrons and the ionization energy U_k. Observations based on well known systems (such as the hydrogen atom, the free-electron gas or the inner-shell for heavy atoms) have shown certain universal macroscopic features for the GOS. Thus, the GOS of each atomic electronic shell can be modelled as a simple δ-oscillator [417], as follows

$$F(W_k;Q,W) = \delta(W-W_k)\Theta(W_k-Q) + \delta(W-Q)\Theta(Q-W_k), \tag{110}$$

where $\delta(x)$ is the Dirac delta function, and Θ is the unit step function. The first term of the expression (110) corresponds to low-Q (distant) collisions described by a single resonance at the discrete resonant energy W_k, while the second term accounts for large-Q (close) interactions which relate to the target electrons reacting as if they were free and at rest ($W = Q$). In this way, the δ-oscillator corresponds to one electron in the target,

$$\int_0^\infty F(W_k;Q,W)\,\mathrm{d}W = Z \qquad \text{for any } Q. \tag{111}$$

Consequently, the GOS model for the whole atom becomes [417]

$$\frac{\mathrm{d}f(Q,W)}{\mathrm{d}W} = \sum_k f_k\left[\delta(W-W_k)\Theta(W_k-Q) + \delta(W-Q)\Theta(Q-W_k)\right]. \tag{112}$$

where the summation in k extends over all bound electron shells (and the conduction band for conductors) and the partial oscillator strenght f_k is identified with the number of electrons in the k-th shell, $f_k = Z_k$.

The inelastic DCSs obtained from the GOS model described above can be split into three contributions from distant longitudinal, distant transversal and close interactions,

$$\frac{\mathrm{d}^2\sigma_{\mathrm{in}}}{\mathrm{d}W\,\mathrm{d}Q} = \frac{\mathrm{d}^2\sigma_{\mathrm{dis,l}}}{\mathrm{d}W\,\mathrm{d}Q} + \frac{\mathrm{d}^2\sigma_{\mathrm{dis,t}}}{\mathrm{d}W\,\mathrm{d}Q} + \frac{\mathrm{d}^2\sigma_{\mathrm{clo}}}{\mathrm{d}W\,\mathrm{d}Q}. \tag{113}$$

each term being described by an appropriate expression, viz.

$$\frac{\mathrm{d}^2\sigma_{\mathrm{dis,l}}}{\mathrm{d}W\,\mathrm{d}Q} = \frac{2\pi e^4}{\mathrm{m_e} v^2}\sum_k f_k \frac{1}{W}\frac{2\mathrm{m_e}c^2}{Q(Q+2\mathrm{m_e}c^2)}\delta(W-W_k)\,\Theta(W_k-Q), \tag{114}$$

$$
\begin{aligned}
\frac{\mathrm{d}^2\sigma_{\mathrm{dis,t}}}{\mathrm{d}W\,\mathrm{d}Q} &= \frac{2\pi e^4}{\mathrm{m_e}v^2}\sum_k f_k \frac{1}{W}\left\{\ln\left(\frac{1}{1-\beta^2}\right) - \beta^2 - \delta_{\mathrm{F}}\right\} \\
&\quad \times \delta(W-W_k)\,\Theta(W_k-Q)\,\delta(Q-Q_-),
\end{aligned}
\tag{115}
$$

$$
\frac{\mathrm{d}^2\sigma_{\mathrm{clo}}}{\mathrm{d}W\,\mathrm{d}Q} = \frac{2\pi e^4}{\mathrm{m_e}v^2}\sum_k f_k \frac{1}{W^2}\left(1 + \frac{\beta^2(E-W)W - EW}{E(W+2\mathrm{m_e}c^2)}\right)\delta(W-Q)\,\Theta(W-W_k) \tag{116}
$$

where Q_- is the minimum recoil energy for the energy transfer W, and δ_f is the Fermi density effect correction on the stopping power [255, 416], which in the high-energy limit ($\beta \to 1$) is defined by the mean excitation energy, I, as follows

$$
\delta_{\mathrm{F}} \simeq \ln\left(\frac{\Omega_{\mathrm{p}}^2}{(1-\beta^2)I^2}\right) - 1. \tag{117}
$$

5.2.3 Stopping power

As introduced in Chapter 2 [Eq. (1)], the slowing-down process of a particle is completely characterized by the stopping power of the penetrated medium $S(E)$, i.e. the average energy loss per unit path length:

$$
S(E) = S_{\mathrm{in}}(E) + S_{\mathrm{br}}(E) = \frac{\Delta E}{\Delta s} \tag{118}
$$

where $S(E)$ is the total (collisional, $S_{\mathrm{in}}(E)$, and radiative, $S_{\mathrm{br}}(E)$) stopping power.

The collisional stopping power is evaluated for high energy projectiles, for which $E \gg U_{\mathrm{k}}$ ($U_{\mathrm{k}} \ll 2\mathrm{m_e}c^2$ in the most unfavourable case of the K-shell of heavy elements), as two contributions that arise from close and distant collisions,

$$
S_{\mathrm{in}}(E) \equiv N\left(\sigma^{(1)}_{\mathrm{dis}}(E) + \sigma^{(1)}_{\mathrm{clo}}(E)\right) \tag{119}
$$

The contribution from distant (longitudinal and transversal) interactions to the stopping cross sections, evaluated by using the δ-oscillator model, is given by

$$
\sigma^{(1)}_{\mathrm{dis}}(E) = \frac{2\pi e^4}{\mathrm{m_e}v^2}\sum_k f_k\left(\ln\left(\frac{2\mathrm{m_e}c^2}{W_k}\right) + \ln\left(\frac{1}{1-\beta^2}\right) - \beta^2 - \delta_F\right) \tag{120}
$$

and the contribution arising from close interactions is calculated through the summation

$$
\sigma^{(1)}_{\mathrm{clo}}(E) = \frac{2\pi e^4}{\mathrm{m_e}v^2}\sum_k f_k \int_{W_k}^{W_{\mathrm{max}}} W^{-1}F(E,W)\,\mathrm{d}W. \tag{121}
$$

Recalling that the GOS from the present optical-data model satisfies the f-sum rule [Eq. (108)] and considering in addition the definition of the main excitation energy I [Eq. (109)], the stopping power is given by the following expression (which is also known as ‘the Bethe stopping power’ formula):

$$S_{\mathrm{in}}(E) = N\frac{2\pi e^4}{\mathrm{m_e}v^2}Z\left(\ln\left(\frac{E^2}{I^2}\frac{\gamma+1}{2}\right) + f^{\pm}(\gamma) - \delta_{\mathrm{F}}\right) \tag{122}$$

where

$$\begin{aligned} f^{(+)} &= 1-\beta^2-\frac{2\gamma-1}{\gamma^2}\ln 2+\frac{1}{8}\left(\frac{\gamma-1}{\gamma}\right)^2 && \text{for electrons} \\ f^{(-)} &= 2\ln 2-\frac{\beta^2}{12}\left(23+\frac{14}{\gamma+1}+\frac{10}{(\gamma+1)^2}+\frac{4}{(\gamma+1)^3}\right) && \text{for positrons.} \end{aligned}$$

The radiative stopping power caused by bremsstrahlung $S_{\mathrm{br}}(E)$ is defined by:

$$S_{\mathrm{br}}(E) \equiv N\int_0^E WF_{\mathrm{p}}(Z,E)\frac{\mathrm{d}\sigma_{\mathrm{br}}}{W}\,\mathrm{d}W = N\frac{Z^2}{\beta^2}E\int_0^1 \chi(Z,E,\kappa)\mathrm{d}\kappa \tag{123}$$

where $F_{\mathrm{p}}(Z,E)$ is a κ-independent factor set equal to the ratio of the radiative stopping powers for positrons and electrons [182] (available in tabulated form with an accuracy of about 0.5%), W is the energy of the emitted photon, κ is the reduced photon energy (defined as $\kappa = W/E$ and taking values between 0 and 1) and $\chi(Z,E,\kappa)$ is the “scaled” bremsstrahlung DCS which, for a given Z, varies smoothly as a function of E and κ. The most reliable theoretically scaled DCSs available at present have been generated in tabular form by Seltzer and Berger [169, 176] for all elements from $Z=1$ to 92 and for electron energies from 1keV to 10GeV.

For high energies, the stopping power calculated from Eqs. (119) and (123) given above coincide with ICRU37 (1984) values. Figure 46 displays the collisional stopping power S_{in}/ρ (a) and the radiative stopping power S_{br}/ρ (b) for electrons in hydrogen, carbon and oxygen as a function of incident particle kinetic energy.

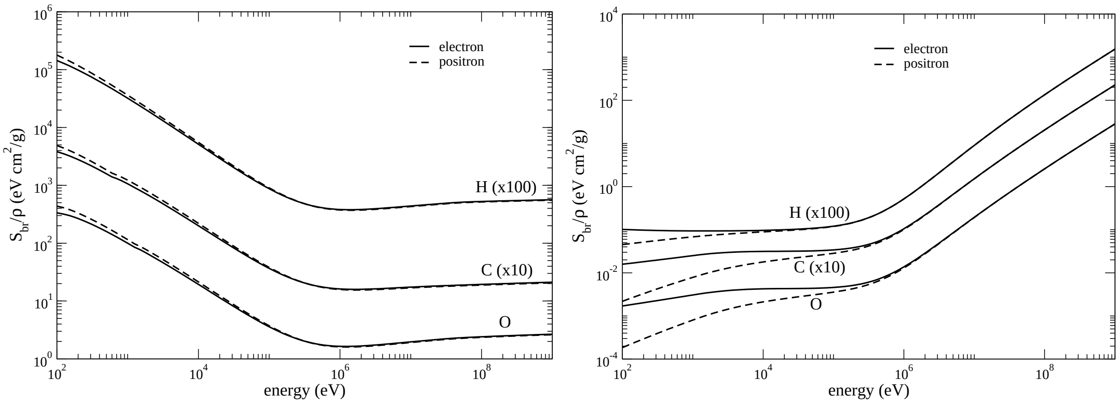

Figure 46: Collision S_{in}/ρ (*left*) and radiative S_{br}/ρ (*right*) stopping power for electrons and positrons in hydrogen (x100), carbon (x10) and oxygen as a function of the kinetic energy.

5.2.4 Angular deflections

As mentioned previously, calculations of inelastic cross sections differential in the polar scattering angle, $\mu = (1 - \cos\theta)/2$, are needed to account for angular deflections due to inelastic collisions. Thereby, in order to describe only the "soft" interactions, the inelastic DCSs are restricted to energy losses less than a chosen cutoff energy loss value W_{cc}, and are calculated through the following expression:

$$\frac{\mathrm{d}\sigma(W_{\mathrm{cc}})}{\mathrm{d}\mu} = \int_0^{W_{\mathrm{cc}}} \frac{\mathrm{d}^2\sigma_{\mathrm{in}}}{\mathrm{d}W\,\mathrm{d}Q}\,\frac{\mathrm{d}Q}{\mathrm{d}\mu}\,\mathrm{d}W, \tag{124}$$

The component coresponding to the distant longitudinal contribution [Eq. (114)] can be expressed in terms of the variable μ as

$$\frac{\mathrm{d}\sigma_{\mathrm{dis,l}}}{\mathrm{d}\mu} = \frac{4\pi e^4}{\mathrm{m_e} v^2} \sum_k f_k \frac{1}{W_k} \frac{\mathrm{m_e}c^2}{4\,cp\,cp_k\mu + (cp - cp_k)^2} \frac{cp\,cp_k}{2(Q + \mathrm{m_e}c^2)}, \qquad 0 < \mu < \mu_k \tag{125}$$

where

$$\mu_k = \mu(Q = W_k) = \frac{W_k(W_k + 2\mathrm{m_e}c^2) - (cp - cp_k)^2}{4\,cp\,cp_k}. \tag{126}$$

The term coresponding to the distant transversal interactions [Eq. (115)] can be written in terms of the variable μ as

$$\frac{\mathrm{d}\sigma_{\mathrm{dis,t}}}{\mathrm{d}\mu} = \frac{4\pi e^4}{\mathrm{m_e} v^2} \sum_k f_k \frac{1}{W_k} \frac{\mathrm{m_e}c^2}{4\,cp\,cp_k\mu + (cp - cp_k)^2} \frac{cp\,cp_k}{2(Q + \mathrm{m_e}c^2)}, \qquad 0 < \mu < \mu_k \tag{127}$$

The DCS per unit oscillator strength for close collisions with the i-th oscillator [Eq. (116)] is given by the Møller formula for electrons, properly accounting for the indistinguishability of the projectile and the target electrons, and by the Bhabha formula for positrons, including also the creation/annihilation mechanism,

$$\frac{\mathrm{d}\sigma_{\mathrm{clo}}}{\mathrm{d}\mu} = \frac{2\pi e^4}{\mathrm{m_e} v^2} \sum_k f_k \frac{1}{W_k} F^{\pm}(E, W) \frac{\mathrm{d}W}{\mathrm{d}\mu}, \qquad \mu_k < \mu < \mu_{\mathrm{cc}} \tag{128}$$

where the factor $F^{\pm}(E, W)$ is expressed by

$$F^{(-)}(E, W) \equiv 1 + \left(\frac{W}{E - W}\right)^2 - \frac{W}{E - W} + a\left(\frac{W}{E - W} + \frac{W^2}{E^2}\right), \qquad \text{for electrons}$$

$$F^{(+)}(E, W) \equiv 1 - b_1 \frac{W}{E} + b_2\left(\frac{W}{E}\right)^2 - b_3\left(\frac{W}{E}\right)^3 + b_4\left(\frac{W}{E}\right)^4, \qquad \text{for positrons}$$

with the coefficients given by

$$a = \left(\frac{E}{E + \mathrm{m_e}c^2}\right)^2 = \left(\frac{\gamma - 1}{\gamma}\right)^2, \qquad \gamma = \frac{E + \mathrm{m_e}c^2}{\mathrm{m_e}c^2}$$

$$b_1 = \left(\frac{\gamma - 1}{\gamma}\right)^2 \frac{2(\gamma + 1)^2 - 1}{\gamma^2 - 1}, \qquad b_2 = \left(\frac{\gamma - 1}{\gamma}\right)^2 \frac{3(\gamma + 1)^2 + 1}{\gamma^2 + 1},$$

$$b_3 = \left(\frac{\gamma - 1}{\gamma}\right)^2 \frac{2\gamma(\gamma - 1)}{(\gamma + 1)^2}, \qquad b_4 = \left(\frac{\gamma - 1}{\gamma}\right)^2 \frac{(\gamma - 1)^2}{(\gamma + 1)^2}.$$

The energy loss differential in the scattering angle μ is defined by

$$\frac{\mathrm{d}W}{\mathrm{d}\mu} = \frac{E(E+2\mathrm{m_e}c^2)\mathrm{m_e}c^2 2(1-2\mu)}{2E(\mu-\mu^2)+\mathrm{m_e}c^2} \tag{129}$$

and the cutoff angle μ_{cc} by

$$\mu_{\mathrm{cc}} = \mu(Q=W_{\mathrm{cc}}) = \frac{W_{\mathrm{cc}}(W_{\mathrm{cc}}+2\mathrm{m_e}c^2)-(cp-cp_{\mathrm{cc}})^2}{4\,cp\,cp_{\mathrm{cc}}}. \tag{130}$$

Regarding the angular deflections caused by bremsstrahlung emission, these are assumed to be taken into account by the elastic scattering. Therefore, the DCS for bremsstrahlung emission depends only on the energy W of the emitted photon and on its direction of emission (the polar angle θ relative to the direction of the projectile) and can be written as

$$\frac{\mathrm{d}^2\sigma}{\mathrm{d}W\,\mathrm{d}(\cos\theta)} = \frac{\mathrm{d}\sigma}{\mathrm{d}W}\,p(Z,E,\kappa;\cos\theta), \tag{131}$$

where $\kappa \equiv W/E$ is the reduced energy of the photon, $\mathrm{d}\sigma/\mathrm{d}W$ is the energy-loss DCS (differential only in the energy of the emitted photon) and $p(Z,E,\kappa;\cos\theta)$ is the shape function, i.e. the probability distribution function (PDF) of $\cos\theta$ for given values of E and κ (normalized to unity).

PENELOPE reads tables of energy-loss scaled DCSs produced by Seltzer and Berger [169, 176]. The energy-loss scaled DCS is defined as $(\beta^2/Z^2)W\mathrm{d}\sigma/\mathrm{d}W$, where $\beta = v/c$ is the velocity of the electron in units of the speed of light. Seltzer and Berger's data base, which covers elements Z =1-92 and electron energies from 1 keV to 10 GeV, is considered to be the most reliable theoretical representation of bremsstrahlung energy spectra available. The numerical data is tabulated for a dense grid of electron energies, which allows accurate (and fast) linear interpolation in the variable $\ln E$. With respect to the angular distibution of emitted photons $p(Z,E,\kappa;\cos\theta)$, PENELOPE uses a statistical mixture of two Lorentz-boosted dipole distributions. The code reads the radiative stopping power for electrons from the input material data file and renormalizes the DCS by multiplying it with a κ-independent factor such that it reproduces the input radiative stopping power.

5.3 PENELAST Code Features

PENELAST effectively represents an extension of the MC code system PENELOPE in that it permits the simulation of electron and positron transport based on numerically calculated external elastic DCS information from the ELSEP database. The code employs a mixed (Class II) simulation algorithm available from the PENELOPE code system itself (see Chapter 2). The main new features are related to the subroutines that read and write the elastic DCS database, viz. `EELdR` and `EELdW`, and the subroutines that calculate the deflection for electron and positron hard elastic events, `EELd` and `PELd`, respectively. In the following, the technical procedures and implementation details are presented.

First, the DCSs are written onto the standard PENELOPE '<material>.mat' file for the elements of interest, immediately after the energy-dependent elastic scattering cross sections and additional transport data. They are in the form of tables of cross sections for e^- and e^+ for an angular grid with 606 intervals from 0 to 2π rad. Each table is headed by a line indicating the type of particle (-1: e^-, +1: e^+), the particle energy, and total angle-integrated, energy-dependant cross sections, which are used for consistency checking of the DCSs. There is a table for each of the 96 energy intervals in a grid spanning the range from 50 eV to 100 MeV. The generation of the '<material>.mat' file by the programs PENELAST and MATERIAL is described schematically in the flowchart diagram given in Fig. 47.

Thus, the DCS information is written in the '<material>.mat' file by the subroutine `EELdW` which is part of PENELAST. This subroutine is called by the subroutine `PEMATW` when PENELAST is compiled together with MATERIAL, in order to generate the program for processing the data from the ELSEP and the standard PENELOPE material database files (465 ascii files):

`pdatconf.tab`	- contains atomic ground state configurations, ionization energies and central values of the one-electron shell Compton profiles for the elements, from hydrogen to uranium (Z=1-92).
`pdbrang.tab`	- contains parameters of the intrinsic angular distribution of bremsstrahlung photons. Determined by fitting the set of benchmark partial-wave shape functions tabulated by Kissel, Quarles and Pratt.
`pdcompos.tab`	- contains composition data and physical parameters for 279 materials, taken from the database of the ESTAR program of Berger (NISTIR 4999, 1992).
`pdeflist.tab`	- list of materials included in the 'pdcompos.tab' file, with their identification numbers.
`pdrelax.tab`	- data on atomic relaxation, extracted from the LLNL Evaluated Atomic Data Library.
`pdebr`ZZ`.tab`	- contain electron bremsstrahlung data. These files were generated from the database of Seltzer and Berger. The same grid of energies is used for all elements.
`pdeel`ZZ`.tab`	- contain electron and positron elastic scattering data. The same grid of energies is used for all elements.
`pdein`ZZ`.tab`	- contain cross sections for ionization of K-shells and L-subshells by electron and positron impact.
`pdgph`ZZ`.tab`	- contain total atomic photoelectric cross sections and partial cross sections for inner (K- and L-) shells, generated from the EPDL97 data library of Cullen et al.
`pdgpp`ZZ`.tab`	- contain cross sections for pair production in the field of neutral atoms (sum of pair and triplet contributions), obtained from the XCOM program of Berger and Hubbell. The same energy grid is used for all elements.

ZZ above represents the atomic number (or identifier in the case of a molecule) of the material of interest. Hence, the energy-dependent elastic scattering information, included in the original PENELOPE `pdeelZZ.tab` files, is complemented in PENELAST by the ELSEP format database, `eeldxZZZ.tab` and `peldxZZZ.tab` files, which contain the DCSs (energy and angular dependency) for e^- and e^+ elastic scattering respectively, for the considered material ZZZ.

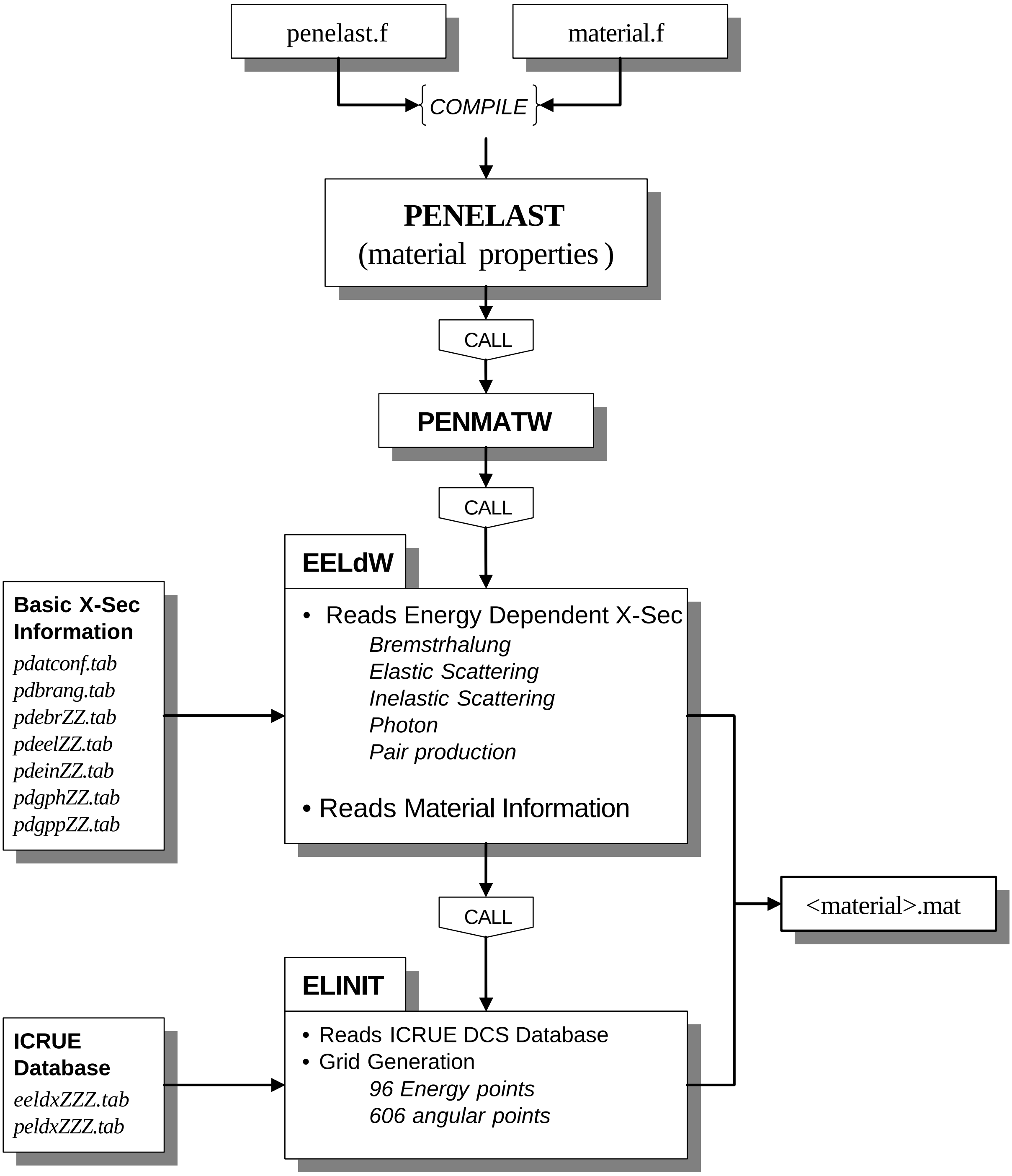

Figure 47: Generation of '<material>.mat' file by the Fortran77 codes PENELAST and MATERIAL.

The files `eeldxZZZ.tab` and `peldxZZZ.tab` are read by subroutine `ELINIT`, which is called by `EELdW` before the '<material>.mat' file is written, in order to input the DCSs for the standard energy and angular grid, and to process them so that DCSs for molecules can be computed as an incoherent sum of the DCSs of individual elements that form it. `ELINIT` also prepares the energy and angle grids corresponding to the 96 energy and 606 angle intervals for which the DCSs are tabulated. The angle variable is represented in terms of the angular deflection, i.e. $\mathtt{RMU} = (1 - \cos(\theta))/2$.

MC calculations with PENELAST are then carried out in the standard manner within PENELOPE, i.e. a main program has to be used that describes the specific problem to be studied and drives the execution of the particle transport simulation by calling the main PENELOPE subroutines. Thus, to solve, for instance, problems in slab geometry, the set of subroutines that form PENELAST (collected in file penelast.f) must be compiled together with the file penslab.f, which gathers all the necessary information to describe the problem and acts as the main simulation driver. In addition, a timing subroutine, timer.f, which writes the execution time in second, is added to complete the package.

Thus, the subroutine `EELdR` is used by PENELAST when the code is applied to the calculation of radiation transport, in order to read the DCSs for elastic scattering in the '<material>.mat' file. The subroutine is called only once during the calculation, viz. during the initialization process started by `PENSLAB` (in the case of a slab type problem). The latter calls the main initialization subroutine `PEINIT`. `PEINIT` then calls `PEMATR`, which initializes the information about material properties and cross section data and, in the process, makes use of the new subroutine `EELdR` to retrieve the elastic scattering DCS data from '<material>.mat'. `EELdR` complements the information acquired by `EELR`, an original PENELOPE subroutine used to retrieve elastic cross sections as a function only of energy from the '<material>.mat' file. Fig. 48 schematically shows the new subroutines integrated into PENELOPE in order to perform MC calculations based on numerical elastic scattering DCSs.

Further, subroutine `EELdR` initializes the algorithm for the simulation of e^- and e^+ elastic collisions. The internal databases, containing the DCS information in the form of cumulative probability distributions for the deflection angle after a elastic collision, are created by calls to two new subroutines, `DCSEL0` and `QRND0`, and are included in the common blocks `CEELDB` and `CPELDB`. In addition, the (restricted) moments of the PDF are also obtained in `EELdR` by call to the subroutine `QRNDMS`. The calculation of soft interactions (the mean free path and the cut-off angle for soft elastic collisions) is carried out by using appropriate models already implemented in PENELOPE, but with the information in common block `CEEL00` obtained from the processing of the DCS ELSEP database. PENELAST also includes two subroutines `EELd` and `PELd` to simulate hard elastic scattering collision events for electrons and positrons, respectively, with cross sections from the ELSEP database, which are read by `EELdR` as described above. Fig. 49 depicts the calculation of the internal DCS database information.

To summarize, the various subroutines of PENELAST which have been described in this section and introduced with respect to PENELOPE, serve to:

- read the ELSEP databases during the generation of '<materal>.mat': `ELINIT` and `EELdW`.

- read and process the information in '<materal>.mat', so that DCS information for the elastic scattering of e^- and e^+ is stored in variables accessible by the subroutines that perform

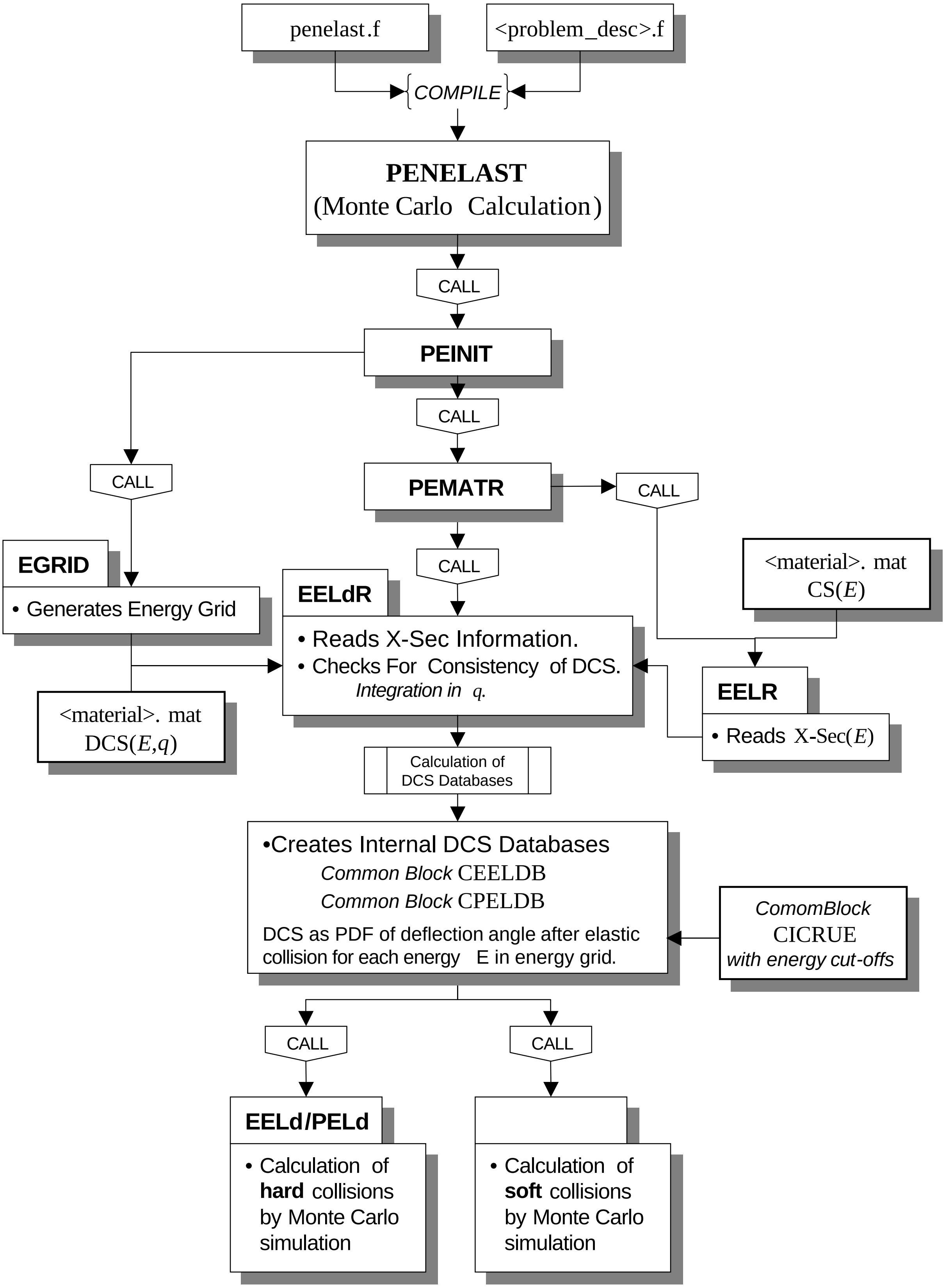

Figure 48: The new subroutines integrated into PENELOPE in order to perform MC calculation based on numerical elastic scattering DCS.

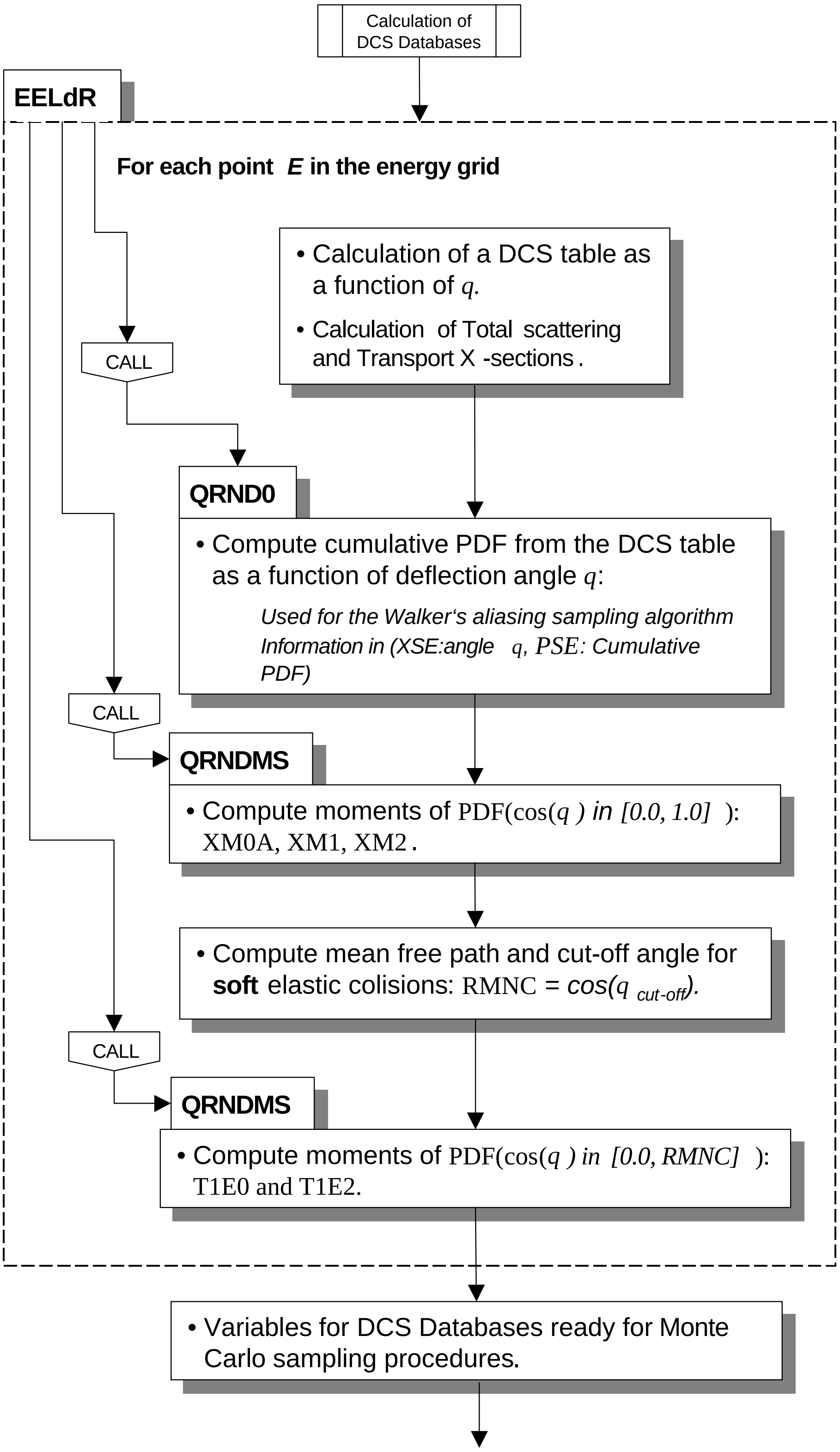

Figure 49: Calculation of the internal DCS database information.

soft and hard collision simulations: `EELdR`, `DCSELO`, `QRNDO` and `QRNDMS`. This information is mapped onto new angular and energy grids that provide accurate log-log linear and spline interpolations for the sampling procedures during the MC simulation.

- compute hard elastic scattering interaction simulations based on the ELSEP DCS databases: `EELd` and `PELd`.

Supplementary detailed information is given in Appendix D.

5.4 Mixed and Detailed Simulation of Angular Distributions and Energy Spectra of Electrons after a Given Path Length

The elastic and inelastic cross section data described in Section 5.2 have been used in conjunction with the PENELAST code to simulate the angular distribution and energy spectra of charged particles after travelling a certain path length in a given material. The energy distribution is a very sensitive test of the simulation of the multiple-scattering process and of the computation of the energy loss (dE/dx and its fluctuation). A comparison of the results given by PENELAST with those obtained using the PENELOPE code system in its original form, as well as with experimental data, is done below in order to validate the implementation of the new numerical cross section data and calculation methodology.

Figure 50 compares the total transmitted electron energy spectra for 1 MeV electrons passing through Al foils with mass thicknesses of 0.1 g/cm^2 (*left*) and 0.22 g/cm^2 (*right*). Mixed

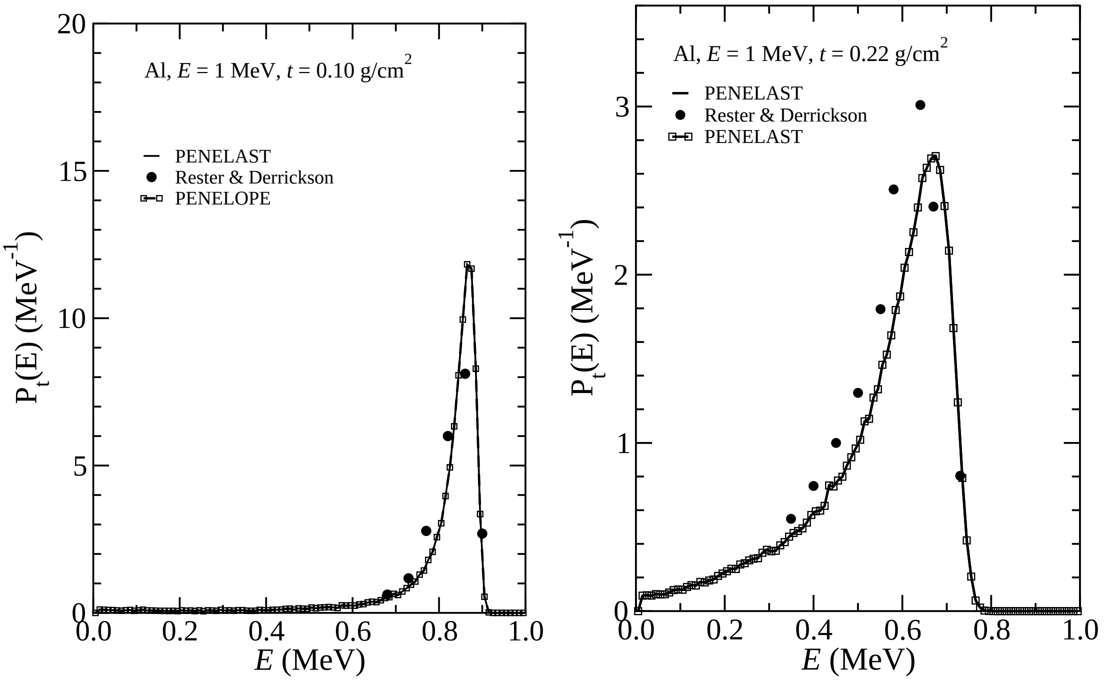

Figure 50: Energy spectra for 1 MeV electrons transmitted through 0.1 g/cm^2 (*left*) and 0.22 g/cm^2 (*right*) Al foils. The simulation results obtained with PENELAST (*solid line*) and PENELOPE (*symbol line*) are compared with experimental data (*black dots*) [418].

algorithm simulation results with PENELAST have been obtained considering a 1 keV energy cutoff as the lowest transport energy value of the calculation done with the original PENELOPE. As expected, no differences are observed in this higher range of energies, between the results obtained with the two codes, there being no differences in the analytical models used for the generation of the elastic and inelastic DCS data. There is, however, useful confirmation that accurate implementation of the numerical DCSs has been achieved in PENELAST. In addition, the agreement obtained with the experimental results of Rester and Derrickson [418] is seen to be very good, especially for 0.1 g/cm^2 mass thickness. The small differences observed between the simulated and experimental spectra could, in principle, be attributed to the experimental errors [418].

Experimental investigations have also been reported for the plural scattering of electrons in different materials, typically for mass-thicknesses corresponding to between 3 and 20 elastic scattering events. Cosslett *et al.* [419] have measured angular distributions of 20 keV electrons scattered in thin films of various materials. The overall experimental accuracy is about 6%. In Fig. 51, detailed simulation results obtained with PENELAST for angular distributions (*left*) and energy spectra (*right*) of electrons are displayed. Comparison with experimental measurements

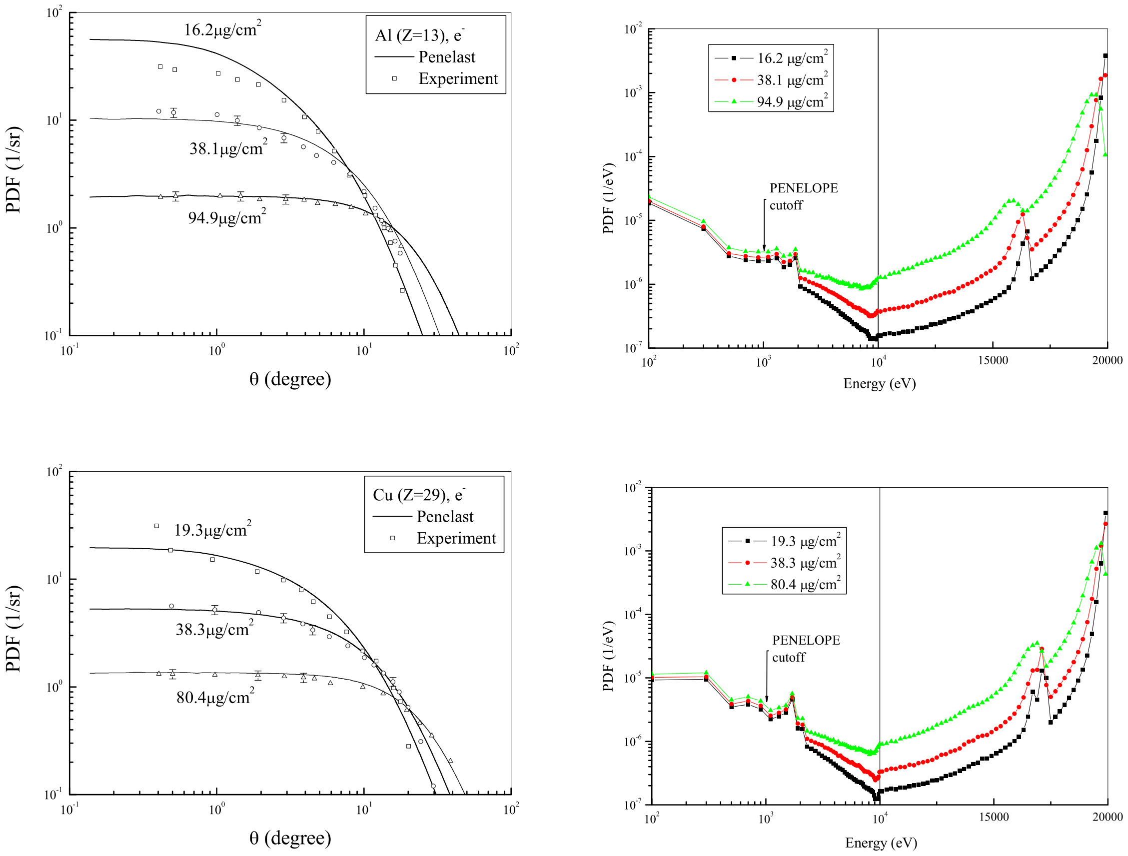

Figure 51: Multiple-scattering angular distributions (*left*) and energy spectra (*right*) of electrons with energy 20 keV after passing through Al (*up*) and Cu (*down*) foils. The lines (both with and without dots) are results simulated with PENELAST and the symbols are experimental data [419].

for the angular distributions obtained by Cosslett *et al.* are done for Al (*upper*) and Cu (*lower*), respectively. Various films with mass-thicknesses of 16.2 μg/cm^2, 38.1 μg/cm^2 and 94.9 μg/cm^2 for Al, and 19.3 μg/cm^2, 38.3 μg/cm^2 and 80.4μg/cm^2 for Cu, have been considered. Excellent agreement between both experimental and PENELAST angular distribution results is obtained for each material, in particular when the number of collisions is large enough to consider multiple-scattering processes. The agreement seems to become poorer when the number of collisions per path length decreases to only a few. Table 3 gives additional information such as the mean electron energy in the foil and the number of collision for each particular case.

Clearly indicated in Fig. 51, for both elements (*right*), is the extension to lower projectile energies which has been achieved by PENELAST with respect to the original cutoff of 1 keV provided by the original PENELOPE. It is thus now possible to obtain the energy and spatial distribution of low-energy electrons which, as discussed in the introduction, are known to be responsible for late biological effects of the interaction of ionizing radiation with matter.

Table 3: Multiple-scattering of 20 keV electrons by Al and Cu.

Material	Target thickness (μg/cm^2)	(nm)	Average energy (keV)	No. of collisions
Al	16.2	60.0245	19.92	3.95
	38.1	141.169	19.81	9.33
	94.9	351.625	19.52	23.54
Cu	19.3	21.5402	19.92	3.86
	38.3	42.7455	19.84	7.69
	80.4	89.7321	19.67	16.25

Experimental data for the angular distribution of charged particles at lower ranges, such as at the nanometer level, are very scarce. Lencinas *et al.* [420] have reported data for the transmission of 1.6 keV and 4.8 keV electrons through thin carbon foils with thickness of 150-1900 Å, which correspond to different subcellular ranges, from the DNA to the chromosome size. They found their results to be in good agreement with the Goudsmit-Saunderson theory for angular distributions and the Landau theory [421] for the energy distributions if the regime of short path-length, several times larger than the mean elastic free path $\lambda_{\text{el}}(E)$, is treated properly within the framework of multiple-scattering expansion of the distribution function. The detailed simulation results currently obtained by running PENELAST have also been compared with the experimental angular distribution data of Lencinas *et al.* [420]. The results are displayed in Fig. 52, and additional quantities of interest are given in Table 4. It is seen that the agreement with the experimental data is good for both incident electron energies, especially for path-lengths above 30 nm. Below this range, the discrepancies between PENELAST and the experimental data become significantly larger. For all cases considered, the energy spectra of the transmitted particles are also displayed for energies down to the numerical cross section energy cutoff for PENELAST.

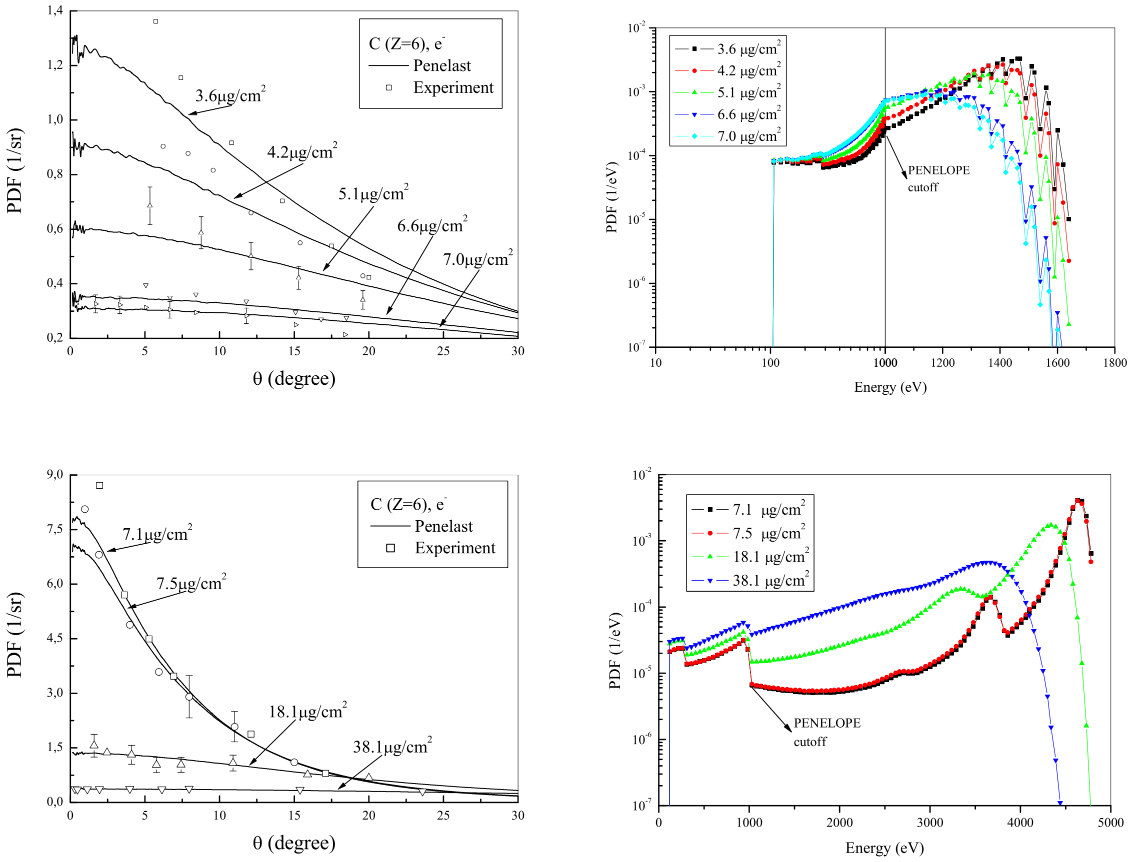

Figure 52: Multiple-scattering angular distributions (*left*) and energy spectra (*right*) of electrons with energy 1.646 keV (*up*) and 4.8 keV (*down*) after passing through C foils. The lines (both with and without dots) are results simulated with PENELAST and the symbols are experimental data [420].

5.5 Summary

In this chapter, the generation of elastic and inelastic numerical cross section data for MC simulation of radiation transport has been done in the energy range from 50 eV to 1 GeV. Extension of the data to lower energies, such as 1 eV, considering one single model, has been seen to encounter various problems arising from the change in the validity range of the individual models used (in terms of particle energy and the atomic number of the target element).

New numerical elastic cross section data have been implemented for use in a mixed algorithm MC code PENELAST, in order to calculate angular distributions and energy spectra of charged particles after passing through various materials. Since, for the high and medium energy range, the algorithms used for the generation of the numerical elastic and inelastic cross sections employ similar analytical models to those in the original PENELOPE, no discrepancies are observed between the latter's results and PENELAST for energies above the original energy cut-off of 1 keV. This comparison provides useful confirmation that the numerical implementation of the tabulated cross sections into the new MC code has been properly achieved. However, more advanced checks will be done in the next chapter. In addition, detailed simulations of the transport of charged particles with energy below 100 keV has enabled extension of computed energy spectra to lower energies well into the eV range, thus providing the possibility for future studies of radiation transport in subcellular size ranges.

Table 4: Multiple-scattering of 1.646 keV and 4.8 keV electrons by C.

Energy (keV)	Target thickness (μg/cm^2)	Target thickness (nm)	Average energy (keV)	No. of collisions
1.646	3.6	18.0	1.49935	6.83
	4.2	21.0	1.47276	8.10
	5.1	25.5	1.43144	10.10
	6.6	33.0	1.35831	13.73
	7.0	35.0	1.33786	14.77
4.800	7.1	35.5	4.67268	4.64
	7.5	37.5	4.66534	4.91
	18.1	90.5	4.46768	12.36
	38.1	190.5	4.03686	28.71

6 A New Multiple-scattering Numerical Algorithm

As discussed previously in the introduction and in Chapter 5, condensed history (Class I) or mixed (Class II) MC simulation algorithms have been developed for medium and high energies, say above 100keV, in order to account in a rather faster way for the large number of elastic scattering interactions that occur durring the passage of a charged particle through matter. For such energies, the detailed tracking (i.e. interaction by interaction) of charged particles is still impractical despite the current advances in computer technology. Assuming identical interaction models, Class II algorithms are, generally, more stable and accurate than Class I. However, the development of even faster MC codes based on Class I simulation algorithms is often demanded by practical applications such as routine clinical therapy planning. This requires improved robust simulation algorithms, able to provide accurate knowledge of the multiple-scattering distributions, both angular and spatial, of particles after travelling a certain path length. In this chapter, the development of a new Class I MC code based on Lewis multiple-scattering theory is reported [422].

Thus, following a short introduction, the theoretical description of various multiple-scattering algorithms are given in Section 6.2, with emphasis on the differences existing with respect to both the analytical formulation for the DCSs as well as the methodology used to compute the multiple-scattering distribution functions. The numerical implementation of the Lewis theory in a FORTRAN 77 computer program is described in detail in Section 6.3. Comparisons of the numerical results obtained for multiple-scattering angular distributions are made with those of simulations based on other theories presented in this chapter, and with experimental data, in Section 6.4 and Section 6.5, respectively. In Section 6.6, straggling effects on the multiple-scattering angular distributions are analysed, whereas effects of inelastic scattering are discussed in Section 6.7.

6.1 Introduction

In Class I MC simulation schemes, the transport of charged particles in matter is simulated by considering (a) finite pre-defined step lengths, usually corresponding to a given average fractional energy loss, and (b) angular deflections that account for the cumulative effect of many interactions along a given track segment with the help of multiple-scattering theories such as those of Molière [26, 425], Goudsmit-Saunderson [29], and Lewis [49], the latter including also the energy loss by means of the continuous slowing-down approximation. Algorithms, based on physical first principles, to account for spatial displacement (which is strongly correlated with the angular deflection) have not yet been developed. Different electron-transport mechanistic algorithms have been proposed to describe it [423, 424].

MC codes such as EGS4 and GEANT3 which use the Molière theory have a rather limited range of applications, due to the various assumptions made in order to obtain a simple final distribution function (in terms of a scaled angular variable) from which angular deflections can be easily sampled. In addition, these codes in general use analytical, approximate functions, such as the screened Rutherford formula or the small angle approximation [32, 426, 427], in order to calculate the elastic DCSs and the transport coefficients required by the multiple-scattering theory. The theories of Goudsmit-Saunderson and Lewis have been implemented in various MC codes, such as ETRAN, MCNP and GEANT4, and allow the exact calculation of the multiple-scattering angular distribution for an arbitrary DCS given in numerical form. However, these two theories are based on the Legendre expansion of the single-scattering angular distribution and face practical difficulties when a large number of Legendre terms is required such as in the case of transport along very small path length. For this reason, various analytical approximations have been employed for the DCSs, enabling the Legendre coefficients to be evaluated by means of recursion relations, but the method becomes unstable due to the accumulation of numerical errors [428].

One additional aspect is that all the multiple-scattering theories mentioned above account for the effect of inelastic scattering on the angular deflections by means of rough approximations (simply multiplying the elastic DCSs by a factor $1 + Z^{-1}$ [425], where Z is the atomic number of the medium). A more elaborate treatment is based on the incoherent-scattering-function approximation, as initially introduced into the Molière theory [241] and later extended to Goudsmit-Saunderson [429].

In this chapter, a complete algorithm for the calculation of multiple-scattering angular distributions of electrons and positrons in matter according to the theories of Goudsmit-Saunderson and of Lewis is described. The aim is to analyze the reliability of the approximations used to model the angular multiple-scattering distribution of charged particles given by the Lewis theory. The latter's range of validity needs to be evaluated in terms of incident electron energies, materials, angles, path-lengths, etc., for both elastic and inelastic types of interactions. For this purpose, up-to-date interaction cross sections, viz. those described in Section 5.2, will be used in the present work to mathematically model both elastic and inelastic scattering. To check the reliability of the Lewis theory by comparison with other multiple-scattering algorithms, the same set of DCSs have also been used in PENELAST (Section 5.3). In addition, calculated Lewis multiple-scattering angular distributions of electrons/positrons, after travelling a given path length, are compared with results from the original Molière theory, as well as with experimental data (whenever possible). Furthermore, a more accurate method to account for the inelastic scattering effect on the multiple-scattering angular deflections is formulated and verified.

A final aspect considered in the present work is to try to correct the multiple-scattering distributions obtained from the Lewis theory so as to reproduce those obtained by MC simulations. Such a correction, if properly implemented, would allow the development of a fast Class I program which can be reliably used in practice. After all, a consistent multiple-scattering theory, with energy straggling accurately included, is the ultimate aim for a general-purpose Class I MC simulation code.

As in Chapter 5, equations are expressed in cgs Gaussian units; occasionally, energies are given in eV. In the programs, however, unless otherwise stated, all the internal calculations are performed in Hartree atomic units, in which the absolute magnitude of the electron charge e, the electron rest mass $\mathrm{m_e}$ and the reduced Planck constant $\hbar$ have unit value ($\hbar = \mathrm{m_e} = e = 4\pi\epsilon_0 = 1$). The atomic units of energy and length are the Hartree ($E_\mathrm{h} = 27.21138$ eV) and the Bohr radius ($a_0 = 5.291772 \times 10^{-9}$ cm), respectively.

6.2 Multiple-scattering Theories

An electron (or positron) with kinetic energy E that starts off at the origin of the reference frame, and moves in the direction of the z-axis in a hypothetical infinite homogeneous medium with $\mathcal{N}$ scattering centres (spherically symmetrical atoms or randomly oriented molecules) per unit volume, is further considered. $f(\mathbf{r}, \hat{\mathbf{d}}; s)$ represents the probability density of finding the particle at the position $\mathbf{r} = (x, y, z)$, moving in the direction given by the unit vector $\hat{\mathbf{d}} \equiv (\theta, \phi)$ after having travelled a path length s. For this problem, the diffusion equation can be written as follows [49]:

$$\frac{\partial f}{\partial s} + \hat{\mathbf{d}} \cdot \nabla f = \mathcal{N} \int \left[f(\mathbf{r}, \hat{\mathbf{d}}'; s) - f(\mathbf{r}, \hat{\mathbf{d}}; s) \right] \frac{\mathrm{d}\sigma(\chi; s)}{\mathrm{d}\Omega} \, \mathrm{d}\Omega, \tag{132}$$

where $\chi \equiv \cos^{-1}(\hat{\mathbf{d}} \cdot \hat{\mathbf{d}}')$ is the scattering angle corresponding to the angular deflection $\hat{\mathbf{d}}' \to \hat{\mathbf{d}}$ and $\mathrm{d}\sigma(\chi; s)/\mathrm{d}\Omega$ is the elastic DCS for an electron with energy $E - W(s)$, $W(s)$ being the path-dependent energy-loss of the particle. This equation has to be solved under the boundary condition $f(\mathbf{r}, \hat{\mathbf{d}}; 0) = (1/\pi)\delta(\mathbf{r})\delta(1 - \cos\theta)$, where θ is the polar angle of the direction $\hat{\mathbf{d}}$.

6.2.1 Goudsmit-Saunderson multiple-scattering distribution

The Goudsmit-Saunderson theory [29] of multiple-scattering provides the exact angular distribution of particles which have travelled a total path length s, disregarding the energy-loss effects of electrons upon the scattering distribution as well as the interference effects resulting from coherent scattering by several centres (e.g. atoms in lattice, molecules, etc.).

The angular distribution, $f_1(\theta)$, after a single elastic scattering event, is given by

$$f_1(\theta) = \frac{1}{\sigma} \frac{\mathrm{d}\sigma(\theta)}{\mathrm{d}\Omega}, \tag{133}$$

where $\mathrm{d}\sigma(\theta)/\mathrm{d}\Omega$ is the elastic DCS that depends only on the polar scattering angle θ, i.e. it is axially symmetric about the direction of incidence, and σ is the total (integrated) elastic cross section,

$$\sigma = \int \frac{\mathrm{d}\sigma(\theta)}{\mathrm{d}\Omega} \mathrm{d}\Omega = \int \frac{\mathrm{d}\sigma(\theta)}{\mathrm{d}\mu} d\mu, \tag{134}$$

where $\mu = (1 - \cos\theta)/2$, variable which varies from 0 (forward scattering) to 1 (backscattering).

The probability of having a polar scattering angle between θ and $\theta + \mathrm{d}\theta$ in a single collision is equal to $2\pi f_1(\theta) \sin\theta \mathrm{d}\theta$. Using the Legendre series expansion, $f_1(\theta)$ can be written in the following form

$$f_1(\theta) = \sum_{\ell=0}^{\infty} \frac{2\ell + 1}{4\pi} F_\ell P_\ell(\cos\theta), \tag{135}$$

where P_ℓ are the Legendre polynomials (see Appendix C for details), and the coefficients F_ℓ are given by

$$F_\ell \equiv 2\pi \int_{-1}^{1} P_\ell(\cos\theta) f_1(\theta) \, \mathrm{d}(\cos\theta) = \langle P_\ell(\cos\theta) \rangle_1, \tag{136}$$

where the subscript "1" indicates average values for a single collision.

Considering the electron moving in the direction (θ, ϕ), after exactly n collisions, the angular distribution is found to be (using Eq. (135) and a folding property of Legendre polynomials, i.e. $\langle P_\ell(\cos\theta)\rangle_1 = \langle P_\ell(\cos\theta)\rangle_1^{\mathrm{n}}$)

$$f_n(\theta) = \sum_{\ell=0}^{\infty} \frac{2\ell+1}{4\pi}(F_\ell)^n P_\ell(\cos\theta), \tag{137}$$

which is independent of the azimuthal angle due to the axial symmetry of the problem. Therefore, the angular distribution after a path length s can be expressed as

$$F_{\mathrm{GS}}(\theta; s) \;=\; \sum_{n=0}^{\infty} P(n) f_n(\theta) = \sum_{\ell=0}^{\infty} \frac{2\ell+1}{4\pi}\left[\exp(-s/\lambda)\sum_{n=0}^{\infty}\frac{(s/\lambda)^n}{n!}(F_\ell)^n\right] P_\ell(\cos\theta),$$

where $P(n) = \exp(-s/\lambda)(s/\lambda)^n/n!$, is the Poisson probability distribution of the number n of collisions after a path length s with the mean $\langle n\rangle = s/\lambda$ and λ is the elastic mean free path.

Considering the coefficients

$$G_\ell \equiv \frac{1-F_\ell}{\lambda} = \mathcal{N}\sigma\, 2\pi \int_{-1}^{1} \left[1 - P_\ell(\cos\theta)\right] f_1(\theta)\, \mathrm{d}(\cos\theta), \tag{138}$$

the Goudsmit-Saunderson multiple-scattering distribution can be finally written as

$$F_{\mathrm{GS}}(\theta; s) = \sum_{\ell=0}^{\infty} \frac{2\ell+1}{4\pi} \exp(-sG_\ell) P_\ell(\cos\theta), \tag{139}$$

and the ℓ-th transport mean free path, λ_ℓ, which completely characterizes the elastic scattering within a given medium, is defined by

$$\lambda_\ell = G_\ell^{-1} = (\mathcal{N}\sigma_\ell)^{-1}, \tag{140}$$

where σ_ℓ is the ℓ-th transport cross section; in particular, the first inverse transport mean free path, λ_1^{-1}, which gives a measure of the average angular deflection per unit path length, also called the "scattering power" [430], is given by,

$$\lambda_1^{-1} = G_1 = \frac{2\pi}{\lambda}\int_{-1}^{1} \left[1 - \cos\theta\right] f_1(\theta)\, \mathrm{d}(\cos\theta) = \frac{\langle 1 - \cos\theta\rangle_1}{\lambda}. \tag{141}$$

In order to improve the convergence of the series given in Eq. (139) for small path lengths, the multiple-scattering distribution $F_{\mathrm{GS}}(\theta; s)$ can be expressed by considering the separate contributions arising from electrons that have had either no collision or exactly one collision [428], as follows:

$$\begin{aligned} F_{\mathrm{GS}}(\theta; s) \;\equiv\; & \exp(-s/\lambda)\frac{\delta(\cos\theta - 1)}{\pi} + \frac{s}{\lambda}\exp(-s/\lambda) f_1(\theta) \\ & + \sum_{\ell=0}^{\infty} \frac{2\ell+1}{4\pi}\left[\exp(-sG_\ell) - \exp(-s/\lambda)(1 + s/\lambda - sG_\ell)\right] P_\ell(\cos\theta), \end{aligned} \tag{142}$$

where the first and second terms on the right-hand side represent unscattered and singly-scattered electrons, respectively.

6.2.2 Molière-Wentzel multiple-scattering distribution

In order to avoid difficulties in calculating multiple-scattering angular distributions while using realistic elastic scattering DCSs, in particular difficulties connected to the numerical calculation of the transport coefficients as defined in Eq. (138) (see [428, 431]), use has sometimes been made of simple analytical models such as the Wentzel model [175] (i.e. an exponential screened Rutherford cross section):

$$\frac{d\sigma^{(\mathrm{W})}(\theta)}{d\Omega} = \frac{1}{\mathcal{N}\lambda^{(\mathrm{W})}} p_{\mathrm{W}}\left(A;\theta\right), \tag{143}$$

where

$$p_{\mathrm{W}}\left(A;\theta\right) = \frac{A\left(1+A\right)}{\pi\left(2A+1-\cos\theta\right)^2}, \tag{144}$$

and

$$\sigma^{(\mathrm{W})} = \frac{1}{\mathcal{N}\lambda^{(\mathrm{W})}} = \frac{\left(zz'e^2\right)^2}{\left(p\beta c\right)^2}\frac{\pi}{A\left(1+A\right)}, \tag{145}$$

The transport coefficients for the Wentzel DCSs are calculated using Legendre functions of the second kind $Q_\ell\left(x\right)$ [184] as follows:

$$\begin{aligned} G_\ell^{(\mathrm{W})} &= \mathcal{N}\sigma^{(\mathrm{W})}\left[1-2A\left(1+A\right)\int_{-1}^{1}\frac{P_\ell\left(\cos\chi\right)}{\left(2A+1-\cos\chi\right)^2}\mathrm{d}\left(\cos\chi\right)\right] \\ &= \mathcal{N}\sigma^{(\mathrm{W})}\{1-\ell\left[Q_{\ell-1}\left(1+2A\right)-\left(1+2A\right)Q_\ell\left(1+2A\right)\right]\}, \end{aligned} \tag{146}$$

where the coefficients $Q_\ell\left(x\right)$ [432] are given by the recurence relation:

$$\left(\ell+1\right)Q_{\ell+1}\left(x\right)-\left(2\ell+1\right)xQ_\ell\left(x\right)+\ell Q_{\ell-1}\left(x\right)=0. \tag{147}$$

Given a realistic DCS $\mathrm{d}\sigma(\theta)/\mathrm{d}\Omega$ with total cross section σ and first transport cross section σ_1, one can determine the screening parameter A by requiring that $G_1^{(\mathrm{W})} = \mathcal{N}\sigma_1$. Using this method, the Wentzel DCS given in Eq. (143) describes an elastic scattering process that has the same mean free path and the same single-scattering average deflection as the real process. For relatively large path-lengths, when the number of interactions is larger than about 20 (multiple-scattering regime), repeated scattering smears out the details of the DCS and the angular distributions obtained from the realistic differential cross section and the Wentzel are practically equal.

An analytical expression that can be easily sampled has been derived by Molière for the multiple-scattering angular distribution currently used with several Class II MC codes (such as GEANT3, EGS4) in which the step length s fluctuates randomly. It has been shown [32] that Molière theory is equivalent to Goudsmit-Saunderson theory for a Wentzel model with specific values for the total cross section $\sigma^{(W)}$ given by

$$\sigma^{(\mathrm{M})} = \frac{(Ze^2)^2}{\beta^2E(E+2m_ec^2)}\frac{\pi}{A^{(\mathrm{M})}(1+A^{(\mathrm{M})})} \tag{148}$$

and the screening parameter A given by,

$$A^{(M)} = \frac{1}{4} \frac{(\hbar c)^2}{E(E + 2m_e c^2)} \frac{1.13 + 3.76 Z^2/(137\beta)^2}{(0.885 Z^{-1/3} a_0)^2}, \tag{149}$$

an analytical expression obtained by considering several additional numerical approximations. Molière obtained these expressions by fitting the elastic DCSs given by the eikonal approximation with a Thomas-Fermi atomic field.

6.2.3 Lewis multiple-scattering distribution

A more advanced theory of multiple-elastic scattering, which considers the angular deflections of particles and, in addition, their space displacements, was formulated by Lewis [49]. This theory accounts for the effect of energy loss on the multiple-scattering process by means of the continuous slowing down approximation, i.e. the projectile is assumed to lose energy continuously along its path, so that the process is characterized by the stopping power $S(E)$ [Eq. (118)].

The CSDA completely neglects energy straggling, i.e. statistical variation in the energy loss due to the discreteness of the energy transfers in inelastic and radiative interactions. In the approximation that the particle follows a straight line trajectory, the CSDA range of an electron with kinetic energy E is given by

$$R(E) = \int_{E_{\rm abs}}^{E} \frac{{\rm d}E'}{S(E')}, \tag{150}$$

where $E_{\rm abs}$ is the "absorption" energy, i.e. the energy at which the electron is assumed to be effectively absorbed in the medium. The energy loss W of an electron with kinetic energy E, after having travelled a path length s, is determined by the equation

$$s = \int_{E-W(s)}^{E} \frac{{\rm d}E'}{S(E')} = R(E) - R(E - W). \tag{151}$$

Hence, the energy loss as a function of the path length, $W(s)$, is calculated using the CSDA range as a function of energy, $R(E)$. The average number of elastic collisions undergone by the electron along the path length s is given by

$$\langle n \rangle = \int_0^s \frac{{\rm d}s'}{\lambda(s')} = \int_{E-W(s)}^{E} \frac{1}{\lambda(E')} \frac{{\rm d}E'}{S(E')}. \tag{152}$$

By expanding the probability $f(\mathbf{r}, \hat{\mathbf{d}}; s)$ given by Eq. (132) in spherical harmonics, Lewis [49] obtained general expressions for the angular distribution and the first moments of the spatial distribution after a given path length s. The angular distribution is given by

$$F_{\rm L}(\theta; s) \equiv \int f(\mathbf{r}, \hat{\mathbf{d}}; s)\, {\rm d}\mathbf{r} = \sum_{\ell=0}^{\infty} \frac{2\ell + 1}{4\pi} \exp[-\mathcal{G}_\ell(s)] P_\ell(\cos\theta), \tag{153}$$

where

$$\mathcal{G}_\ell(s) = \int_0^s G_\ell(s)\, {\rm d}s = \int_{E-W(s)}^{E} \frac{G_\ell(E')}{\rho} \frac{{\rm d}E'}{S(E')/\rho}. \tag{154}$$

In the last expression, G_ℓ and S are considered functions of kinetic energy of the projectile. $(G_\ell/\rho)^{-1} = \rho\lambda_\ell$ is the ℓ-th transport mean free path (see Eq. (140)), in mass thickness units (g/cm^2); $S(E)/\rho$ is the mass stopping power (in eV cm^2/g).

For small path lengths, the Legendre expansion (153) converges very slowly, mainly due to the contribution of unscattered electrons, which is proportional to $\delta(\cos\theta - 1)$. It is thus advantageous to separate the contribution from electrons that have undergone no collisions [138],

$$
\begin{aligned}
F_\mathrm{L}(\theta; s) \equiv\ & \exp(-\langle n\rangle)\frac{\delta(\cos\theta - 1)}{\pi} \\
& + \sum_{\ell=0}^{\infty} \frac{2\ell+1}{4\pi}\left[\exp(-\mathcal{G}_\ell) - \exp(-\langle n\rangle)\right] P_\ell(\cos\theta). \qquad (155)
\end{aligned}
$$

The Lewis theory also yields analytical formulae for the first moments of the spatial distribution as also the correlation function for z, and $\cos\theta$. The results explicitly given in Lewis's paper are

$$
\langle z\rangle_\mathrm{L} \equiv 2\pi \int z f(\mathbf{r}, \hat{\mathbf{d}}; s)\, \mathrm{d}(\cos\theta)\, \mathrm{d}\mathbf{r} = \int_0^s \exp[-\mathcal{G}_1(s')]\, \mathrm{d}s', \qquad (156)
$$

$$
\begin{aligned}
\langle x^2 + y^2\rangle_\mathrm{L} &\equiv 2\pi \int \left(x^2 + y^2\right) f(\mathbf{r}, \hat{\mathbf{d}}; s)\, \mathrm{d}(\cos\theta)\, \mathrm{d}\mathbf{r} \\
&= \frac{4}{3}\int_0^s \mathrm{d}s' \exp[-\mathcal{G}_1(s')] \int_0^{s'} \mathrm{d}s'' \left\{1 - \exp[-\mathcal{G}_2(s'')]\right\} \exp[\mathcal{G}_1(s'')] \qquad (157) \\
\langle z\cos\theta\rangle_\mathrm{L} &\equiv 2\pi \int z\cos\theta f(\mathbf{r}, \hat{\mathbf{d}}; s)\, \mathrm{d}(\cos\theta)\, \mathrm{d}\mathbf{r} \\
&= \exp[-\mathcal{G}_1(s)] \int_0^s \mathrm{d}s' \left\{1 + 2\exp[-\mathcal{G}_2(s')]\right\} \exp[\mathcal{G}_1(s')]. \qquad (158)
\end{aligned}
$$

6.3 Numerical Implementation of Lewis Theory

A FORTRAN 77 computer program LEWIS has been written in order to calculate multiple-scattering angular distributions of electrons and positrons after travelling a given path length by using Lewis theory [49]. The program reads the ELASP input database (described in the previous chapter and generated such as to be usable with the code PENELAST) which contains numerical elastic scattering cross sections available in tabulated form, differential in the scattering angle for a given grid of energies. The energy grid is chosen dense enough such as to allow generation of accurate atomic elastic DCSs by using log-log cubic spline interpolation (see Appendix E for details). The inelastic DCSs are generated for the same grid of energies by using the Sternheimer-Liljequist GOS model, the same as that implemented in the PENELOPE code system, but with the density effect correction included. Similarly, the stopping power as function of energy is obtained by editing a file generated by the PENELOPE program 'material'. The radiative stopping powers are evaluated from the scaled bremsstrahlung cross sections tabulated by Seltzer and Berger [169, 176] used also for the ICRU37 data tables, whereas the collision stopping powers above 10 keV are esentially identical to those in the ICRU37 tables because the mean excitation energy I defined by Eq. (109) is that recomended by the ICRU37 report. For the case of stopping power as well, the energy grid, in the same range as the elastic and inelastic data, is assumed to be dense enough in order to allow accurate log-log cubic spline interpolation.

The program LEWIS first reads the input file 'lewis.in' which contains information about the composition of the material, the stopping powers, the number of oscillators needed for the generation of the inelastic DCS data, and other details of the calculation. Then, it executes the initialization routine 'LEWIS0' which stores the parameters needed for computing the multiple-scattering distributions (MSDs) in a dump file (with the extension '.dmp'). The energy of the incident particle and the path length are introduced by the user from the keyboard, and the Lewis MSDs are calculated and written on a file named 'lewispdf.dat'. For a new execution of the program with the same input file, the transport coefficients are read directly from the dump files, thus avoiding the lengthy initialization.

In order to compute the Lewis multiple-scattering probability distribution function (PDF) for a given single elastic scattering DCS, available as described above in numerical form, the path-dependent transport coefficients G_ℓ have first been evaluated as defined in Eq. (154). The number of terms needed to get convergence of the Legendre series, expressed in Eq. (153), increases as the path length decreases. In the limit of large path lengths, only the term with $\ell = 0$ contributes and the angular distribution becomes isotropic.The single-scattering distribution function $f_1(\theta)$ is considered as a function of the variable $y = \cos\theta$. A partition of the integration interval, $y_1 = -1 < y_2 < ... < y_\mathrm{n} < y_{\mathrm{n}+1} = 1$, is established such that, within each subinterval $(y_\mathrm{j}, y_{\mathrm{j}+1})$ the single-scattering distribution varies by less than a factor of 10. Then,

$$G_\ell = \frac{2\pi}{\lambda}\sum_{\mathrm{j}=1}^{\mathrm{n}}\int_{\mathrm{y_j}}^{\mathrm{y_{j+1}}}\left[1 - P_\ell(y)\right] f_1(y)\mathrm{d}y, \tag{159}$$

and the integrals in the right-hand-side involve only Legendre polynomials and a slowly varying function.

The integrals have been evaluated to very high accuracy by using the N-point Gauss-Legendre quadrature formula [433, 434] with an adaptive bipartition scheme (see Appendix B for details). This method calculates the integral of a function $f(z)$ over the interval $[a, b]$ obtained as a weighted sum of function values at fixed points inside the interval:

$$\int_a^b f(y)\mathrm{d}y = \frac{b-a}{2}\sum_{i=1}^{N} w(x_\mathrm{i}) f(y_\mathrm{i}) + R_\mathrm{N}(f) \tag{160}$$

with y_i given by

$$y_\mathrm{i} = \frac{b-a}{2}x_\mathrm{i} + \frac{b+a}{2}. \tag{161}$$

where the abscissas x_i $(-1 < x_\mathrm{i} < 1)$ are the N zeros of the Legendre orthogonal polynomial $P_\mathrm{N}(x)$ for the same interval and the corresponding weights w_i are defined as follows

$$w_\mathrm{i} = \frac{2}{(1 - x_\mathrm{i}^2)(P'_\mathrm{N}(x_\mathrm{i}))^2}. \tag{162}$$

The remainder $R_\mathrm{N}(f)$ is given by

$$R_\mathrm{N}(f) = \frac{(b-a)(2N+1)(N!)^4}{(2N+1)\left[(2N)\right]^3} f^{(2N)}(\eta) \tag{163}$$

where η is a point inside the interval $[a, b]$. Notice that the formula (160) yields the exact results for polynomials of degree up to $2N - 1$.

The difference between the exact value of the integral and the one obtained with the Gauss-Legendre method is given by

$$\Delta_{20} = \frac{(b-a)^{41}(20!)^4}{41(40!)^3} f^{(40)}(\eta) \tag{164}$$

where η is a point inside the interval $[a, b]$.

The advantage of the above method over other similar integration methods is that it allows selection of the abscissa points (at which the function is to be evaluated) that are not equally spaced, as well as the selection of weighting coefficients so that the integration of higher and higher order can be achieved. In our calculations, we have used an adapted version of the subroutine GAULEG described in [435], which delivers the abscissas and the weights of the N-point Gauss-Legendre formula for an arbitrary N. The number N_{L} of Legendre coefficients that are to be calculated is selected in advance; the maximum number of coefficients that can be obtained with our code is $N_{\mathrm{L}}^{\max} = 15,000$ (although this value can be increased by editing the source program). The number of points N in the quadrature formula is determined as

$$N = \max\{500, \min(N_{\mathrm{L}}/2, N_{\mathrm{L}}^{\max}/2) + 10\}. \tag{165}$$

Assuming that within each subinterval the function $f_1(y)$ can be accurately approximated by a polynomial of degree 20 or less, the integrands for the coefficient G_ℓ of highest order $\ell = N_{\mathrm{L}}$ are polynomials of degree less than $2N$ and, therefore, the Gauss-Legendre formula should yield essentially exact values for all coefficients with $\ell \leq N_{\mathrm{L}}$. Moreover, for the evaluation of these coeficients, only the values of the single-scattering distribution $f_1(y)$ at the points y_{i} corresponding to the abscissa x_{i} are needed. The Legendre polynomials are generated using their recurrence relation,

$$\begin{aligned} P_0(x) &= 1, \qquad P_1(x) = x \\ P_\ell(x) &= \frac{1}{\ell}\left[(2\ell-1)xP_{\ell-1}(x) - (\ell-1)P_{\ell-2}(x)\right] \end{aligned} \tag{166}$$

Thus, all the coefficients $G_\ell(E)$ with $\ell \leq N_{\mathrm{L}}$ can be calculated simultaneously; the algorithm can be coded in a very compact form, as four nested DO loops with a small number of arithmetic operations.

In order to check the accuracy achieved in the calculation of the G_ℓ coefficients, the original elastic DCSs are compared with those "reconstructed" by adding the Legendre expansion and making use of the calculated transport coefficients, $F_\ell = 1 - \lambda G_\ell$,

$$\frac{\mathrm{d}\sigma_{\mathrm{el}}(\theta)}{\mathrm{d}\Omega} = \sigma_{\mathrm{el}} \sum_{\ell=0}^{\infty} \frac{2\ell+1}{4\pi} F_\ell \, P_\ell(\cos\theta), \tag{167}$$

as shown in Fig. 53 for electron and positron scattering by beryllium, oxygen, aluminium and lead. The reconstructed values are obtained by adding about 5,000 terms of the corresponding Legendre expansions, so that to ensure fast calculations. It is seen that, for both electrons and positrons with relatively low energies, the agreement between the original DCSs and the reconstructed ones is highly satisfactory, at small as well as at large angles, with differences less than 0.5%. Differences are in fact only visible at higher energies such as $E = 1$ MeV, where the number of terms seems to be insufficient to reach the convergence of the Legendre series. There are, however, limited to relatively large angles and could be reduced further by simply adding more terms in the Legendre expansion. For beryllium and aluminium, the analytical DCSs obtained from the Wentzel model are also displayed for the lowest and the highest energies in order to highlight the discrepancies existing between different aproaches, diferences that seem to increase with decreasing energy. It is seen that the Wentzel model for the differential cross section cannot reproduce the complex trend of the numerical low-energy elastic DCSs.

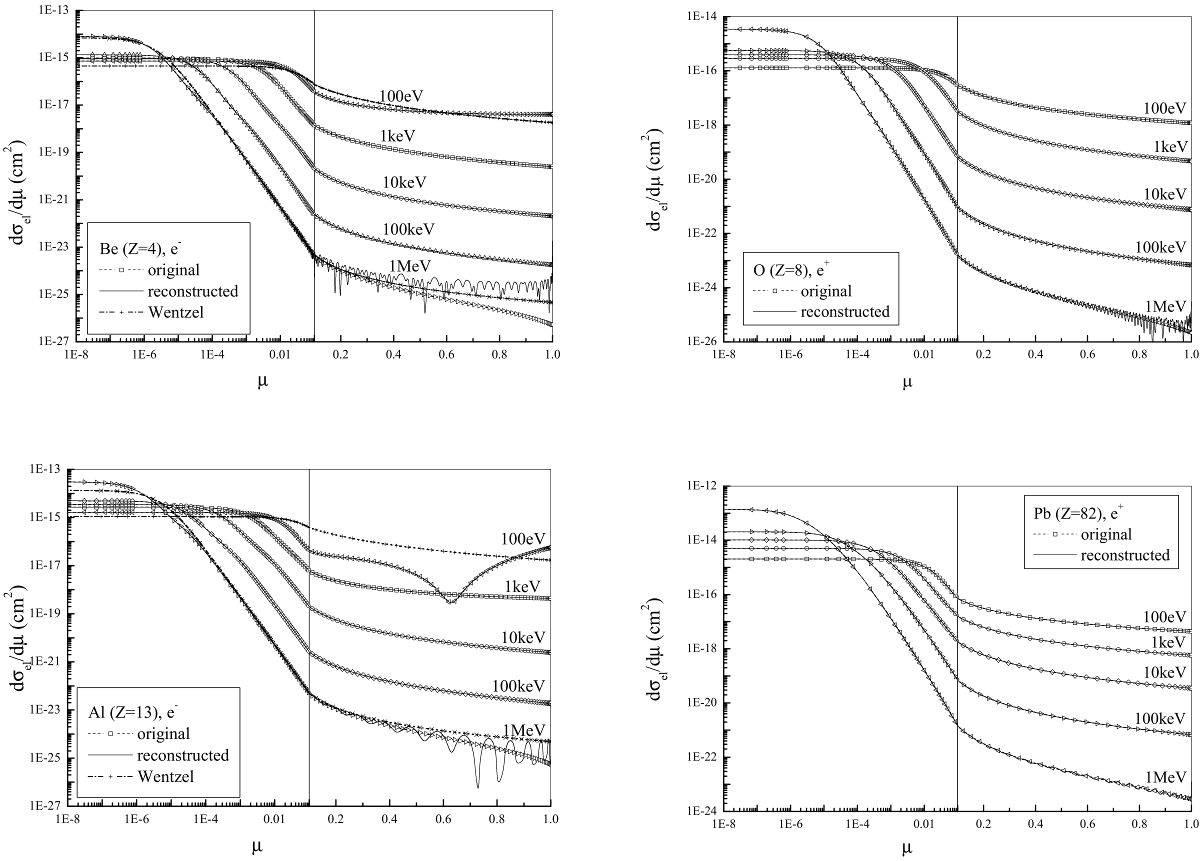

Figure 53: Elastic DCSs for electrons and positrons of the indicated energies scattered as a function of the scattering angle ($\mu = (1 - \cos(\theta))/2$) for beryllium, oxygen, aluminium and lead. The symbols correspond to the original DCSs; the continuous lines (visible only for 1 MeV) are the results "reconstructed" numerically from their Legendre expansion (Eq. (167)) by adding up to 5,000 terms. The dash-dot lines (displayed for beryllium and aluminium for the lowest and the highest energy) are analytical DCSs obtained from the Wentzel model.

6.4 Angular Distribution of Electrons after a Given Path Length: Comparison of Lewis, Wentzel-Molière and PENELAST

Qualitatively, the angular distribution of charged particles after travelling a given path s shows two angular regimes: a forward regime (Gaussian like) dominated by multiple small-angle scatters, and a large-angle regime dominated by single scattering events. In general, different elastic DCS models may lead to differences in the trend of the calculated angular multiple-scattering distribution. Thus, for very short path length (i.e. of the order of a few times the elastic mean free path), the average number of collisions is small (plural scattering) and hence, the multiple-scattering distributions depend strongly on the adopted DCS model. With increasing path length (multiple-scattering), the angular distributions become broader and, at the same time, the details of the multiple-scattering distributions are progressively washed out.

To ilustrate the sensitivity of multiple-scattering angular distributions to the adopted DCSs, various examples have been considered. Thus, Figs. 54 and 55 display multiple-scattering angular distributions for 10 MeV electrons for different path lengths and materials calculated using the Lewis theory with partial-wave (PWA) DCSs from the ELSEP database, the Wentzel-Molière DCS model and PENELAST. For the multiple-scattering calculations, stopping powers were taken from the ICRU37 report [174]. The comparisons are shown for deflection angles smaller than 90 degrees. In general, the distributions obtained with the Lewis theory are in reasonably good agreement with those obtained with PENELAST. In the multiple-scattering regime, say when the average number of collisions is of the order of 20 or larger, the "width" of the angular distribution is determined by the first transport mean free path, $\lambda_1(E)$, which is the same for both simulation procedures. In this case, only the large-angle tail of the distribution is sensitive to details of the DCS model. When the path length increases and approaches the continuous slowing down range, the angular distribution becomes isotropic, i.e. is independent of the adopted DCSs. It is worth bearing in mind that $\lambda_1^{-1}(E)$ represents the "scattering power" (average angular deflection per unit path length) and, therefore, DCSs with smaller first transport mean free path yield wider multiple-scattering distributions. However, it is seen that with increasing path-length, for deflection angles near 90 degrees, simulation results obtained with PENELAST seem to depart increasingly from the Lewis distributions. This trend is studied in the next section.

For low-atomic number elements, the distributions obtained from the Wentzel-Molière DCS model are in reasonable agreement with those obtained with PENELAST and the Lewis theory using the partial-wave analysis model, in spite of the approximative nature of the DCSs (as shown in Fig. 53). This fact explains why MC codes based on Molière theory, such as GEANT3 and EGS4, provide reliable results for electron transport in water and other biological materials. However, for high-atomic number elements like gold, mercury and lead, the Wentzel-Molière DCS yields distributions that are systematically lower, for angles larger than say 15 degrees, to those obtained from PENELAST and the Lewis theory. These differences are seen to increase for increasing deflection angles.

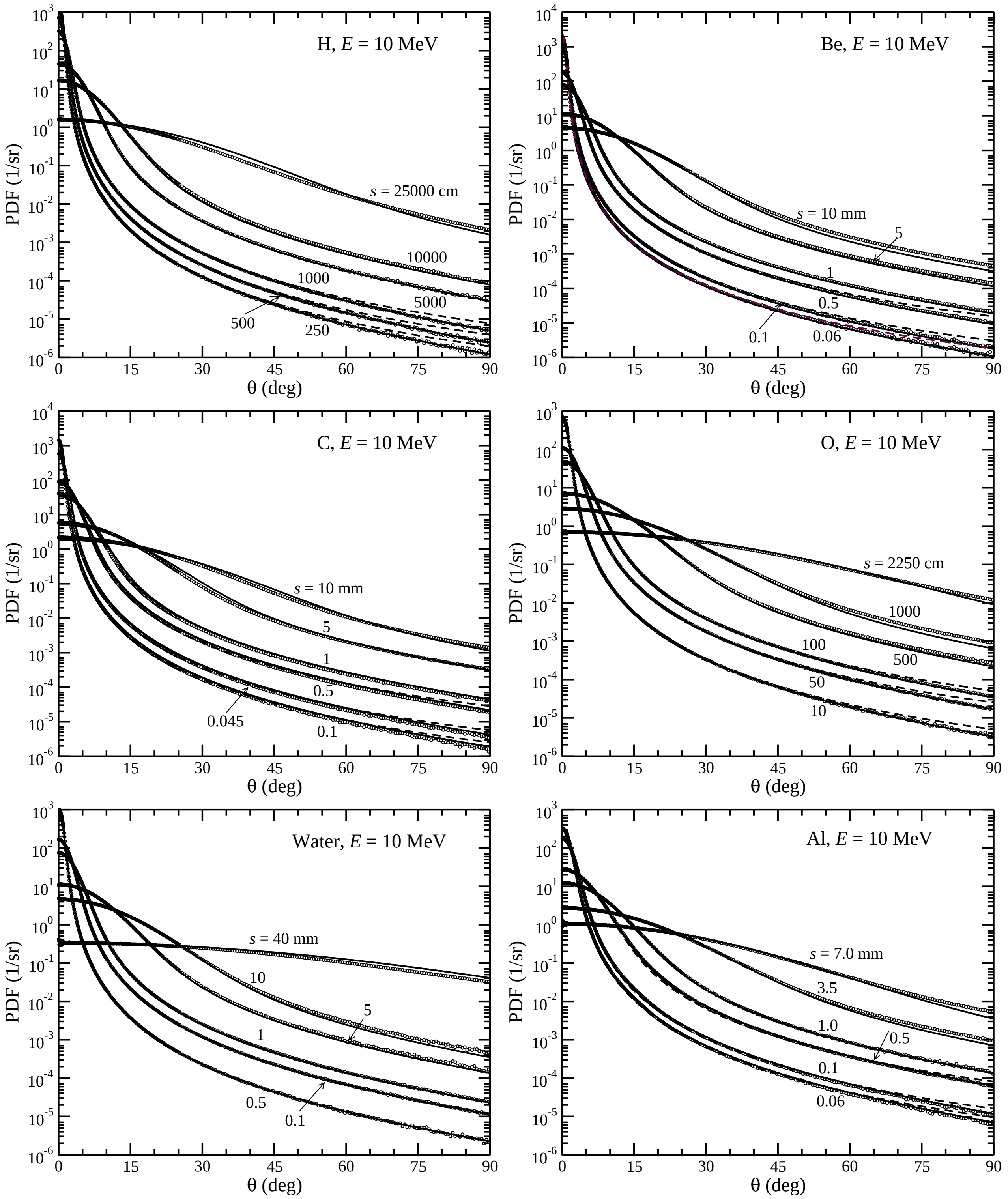

Figure 54: Multiple-scattering angular distributions of 10 MeV electrons after traveling the indicated path lengths in hydrogen, beryllium, carbon, oxygen, water and aluminium. The continuous curves represent distributions calculated from the Lewis expansion, using the partial-wave elastic DCSs. The dashed curves are PDFs obtained from the Wentzel-Molière theory. The symbols are simulation results obtained with PENELAST.

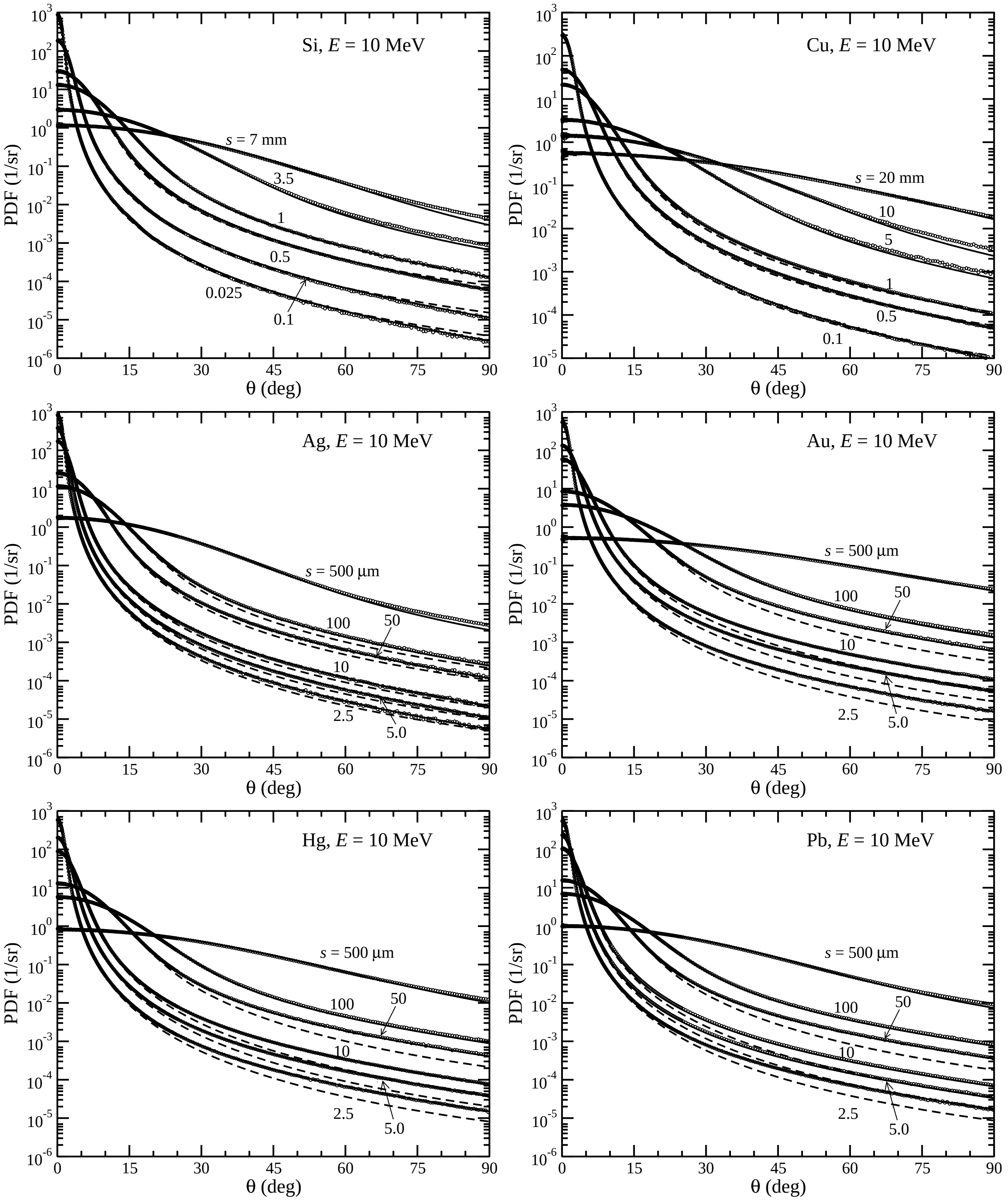

Figure 55: Idem Fig. 54 for silicon, copper, silver, gold, mercury and lead.

The origin of the differences between distributions calculated from the two different DCS models can be understood from a comparison of the corresponding first transport mean free paths $\lambda_1(E)$. Thus, for hydrogen, beryllium, water and gold, Fig. 56 displays elastic mean free path, elastic first transport mean free path, stopping power and continuous slowing down approximation ranges (as function of the kinetic energy), as calculated with the help of the LEWIS code for electrons using the partial-wave cross section model. The additional quantities are helpful for the correct understanding of the ranges of validity for the different simulation algorithms. In addition, the elastic mean free path and elastic first transport mean free path from Wentzel-Molière DCSs are also displayed for comparison. The first transport mean free path obtained from the two DCS models are seen to agree closely for low-atomic number materials, but they differ significantly in the case of gold (and the same is to be expected for other higher-Z elements).

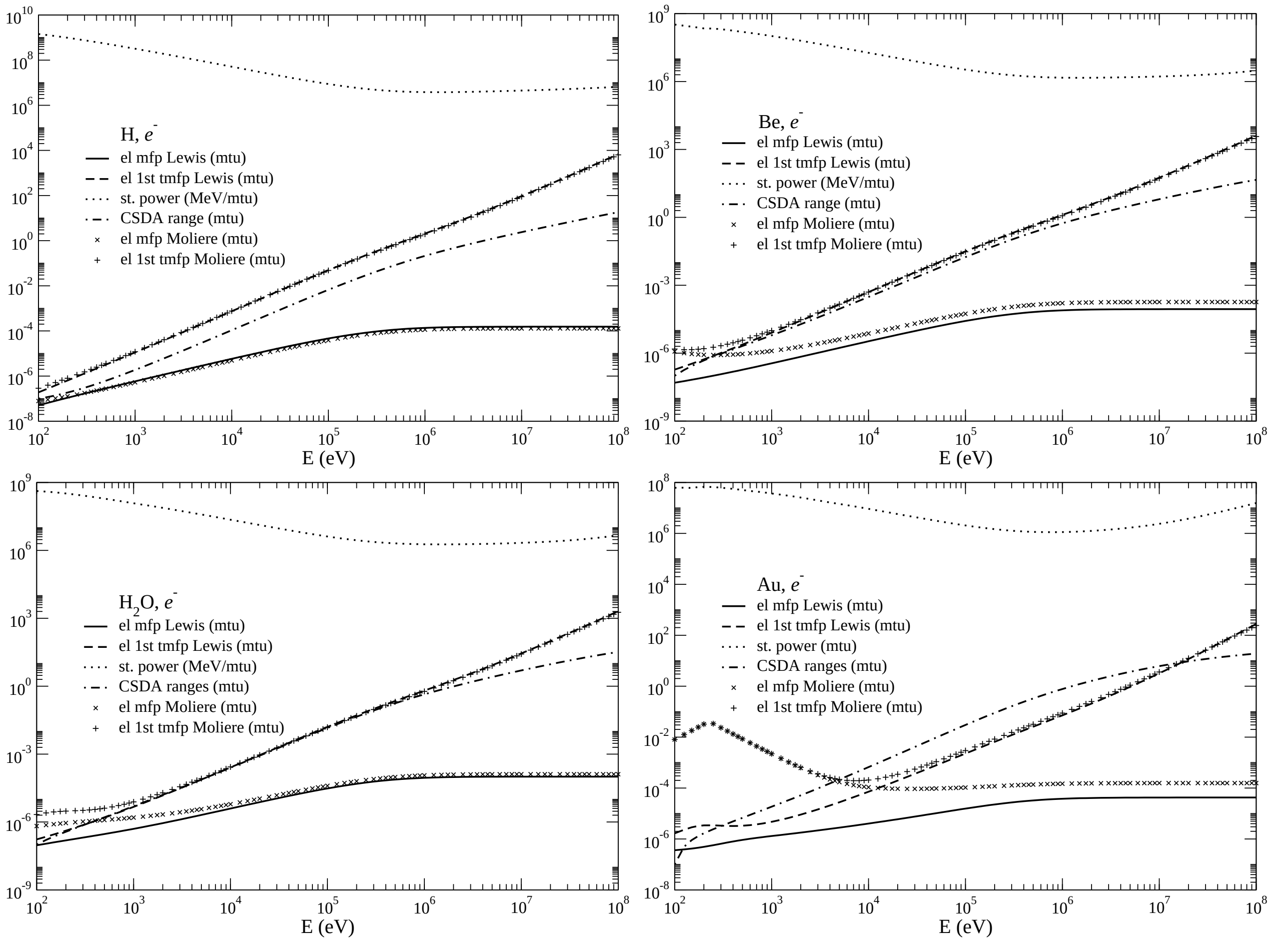

Figure 56: Elastic mean-free-path, elastic 1st transport mean-free-path, stopping power and CSDA ranges from PWA and Wentzel-Molière electron DCSs for hydrogen, beryllium, water and gold.

As indicated above, the average angular deflection $\langle \cos\theta \rangle$ along the path length s is determined by the function $\lambda_1(E)$ and, consequenty, the DCSs that have the same first transport mean free path will yield multiple-scattering angular distributions with the same average deflection. As the Wentzel-Molière DCS for water has a plausible shape and reproduces the first transport mean free path, it correctly predicts the broad features of the multiple-scattering distributions.

Indeed, the partial-wave and the Wentzel-Molière distributions for water (see Fig. 54) are seen to differ only at angles larger than about 60 degrees, where the probability has very small values and the relative differences decrease with s. In the case of lead, the differences between the first transport mean free paths of the two DCSs are larger, and this has a direct effect on the multiple-scattering distributions.

6.5 Angular Distribution of Electrons after a Given Path Length: Comparison of LEWIS with PENELAST and Experimantal Data

There have been a number of experimental investigations of the multiple-scattering of electrons in various materials. A complete series of experiments was carried out by Kulchitsky and Lathyshev [436] for 2.25 MeV electrons scattered in thin foils of ^{13}Al, ^{26}Fe, ^{29}Cu, ^{42}Mo, ^{47}Ag, ^{50}Sn, ^{73}Ta, ^{79}Au and ^{82}Pb. For low-Z elements from ^{13}Al to ^{50}Sn, their results were found to be in very good agreement with the calculational data provided by the Goudsmit-Saunderson theory [29] if the inelastic scattering contribution on the multiple scattering distributions was accounted for through the correction factor $(1+1/Z)^{1/2}$. In all cases, the deviation from the theoretical results was of the order of about 1%. For heavier nuclei such as ^{73}Ta to ^{82}Pb, the measured values of the distributions were 10 to 18% narrower than those predicted by theoretical models.

Figure 57 shows the comparison of multiple-scattering angular distributions of 2.25 MeV electrons given by the Lewis theory [49] with results obtained from the MC simulation with

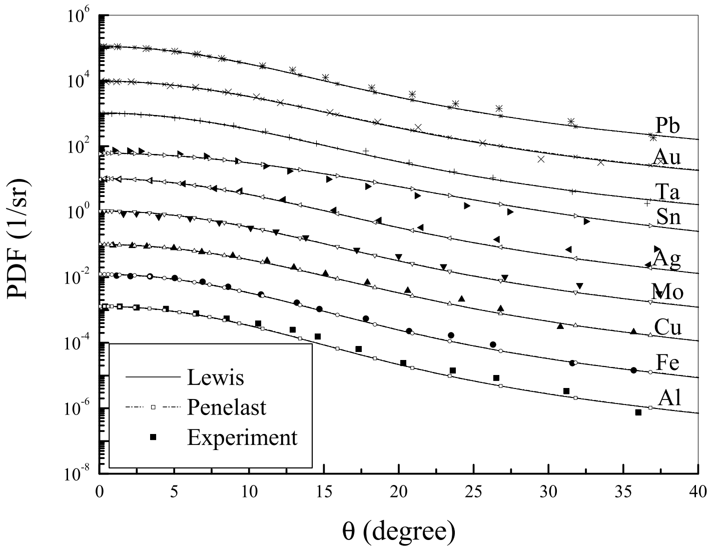

Figure 57: Probability distribution functions of 2.25 MeV electrons after passing through Al(x10^{-4}), Fe(x10^{-3}), Cu(x10^{-2}), Mo(x10^{-1}), Ag, Sn(x10^{1}), Ta(x10^{2}), Au(x10^{3}) and Pb(x10^{4}) foils from calculations with LEWIS (*continuous line*), simulations with PENELAST (*dashed-dot line*) and experiments (*symbols*).

PENELAST and data from the above experiments. The thickness of the scattering foils in the experiments was chosen such that the half-width values of the Gaussian curve corresponding to the multiple-scattering region of the distribution was the same for all the elements studied ($\sim 10°$). Additional quantities of interest calculated from Lewis theory, such as the average energy in the layer and the average number of elastic collisions, are given in Table 5.

Table 5: Multiple-scattering of 2.25 MeV electrons by several materials (Lewis theory results).

Material	Atomic number	Target thickness		Average energy	No. of collisions
		(mg/cm^2)	(μm)	(MeV)	
Al	13	26.60	98.56	2.2296	475.4
Fe	26	15.40	19.56	2.2391	337.5
Cu	29	17.15	19.14	2.2381	310.7
Mo	42	12.40	12.13	2.2416	327.7
Ag	47	11.55	11.00	2.2422	286.5
Sn	50	17.40	23.80	2.2385	466.6
Ta	73	8.90	5.34	2.2431	228.7
Au	79	8.90	4.61	2.2443	216.9
Pb	82	7.90	6.96	2.2449	207.8

Later measurements made by Hanson *et al.* [437] for the angular distributions of 15.7 MeV electrons scattered by ^{79}Au foils confirmed the previous experimental results of Kulchitsky *et al.*. The Lewis calculated angular distributions of 15.7 MeV electrons scattered by two Au foils of thickness 18.66 mg/cm^2 and 37.28 mg/cm^2 are shown in Fig. 58 (*left*). For comparison, simulation results obtained with PENELAST together with the experimental values of Hanson *et al.* [437] are also displayed. It can be seen that the agreement between the three sets of data at small angles, as well as in the part corresponding to the single scattering region, is excellent. An additional comparison, shown in Fig. 58 (*right*), has been done between the calculated and measured ratios of results for the two different Au foils (thick-to-thin). An excellent agreement is seen between the three sets of results - calculated, simulated and experimental.

Although the experimental values were not published, multiple-scattering angular distributions for electrons scattered by ^{4}Be have also been discussed by Hanson *et al.* for two foils of thickness 257.0 mg/cm^2 and 491.3 mg/cm^2, respectively. Figure 58 (*right*) displays for comparison ratios of calculated and simulated results for the two different Be foils mentioned (thick-to-thin).

For both elements, Be and Au, additional data of interest are shown in Table 6. The mean electron energy in the foil and the number of "collisions" events, evaluated from Lewis theory using Eq. (151) and Eq. (152), are compared with results from Molière theory (with the expression for the number of collisions deduced in terms of the Born approximation solution to the scattering for experimental screening [437]). The calculated values for the mean electron energy are in very good agreement, the discrepancy not exceeding 0.2%. However, the number of "collisions" provided by the Lewis algorithm is seen to be significantly greater than that obtained from Molière theory.

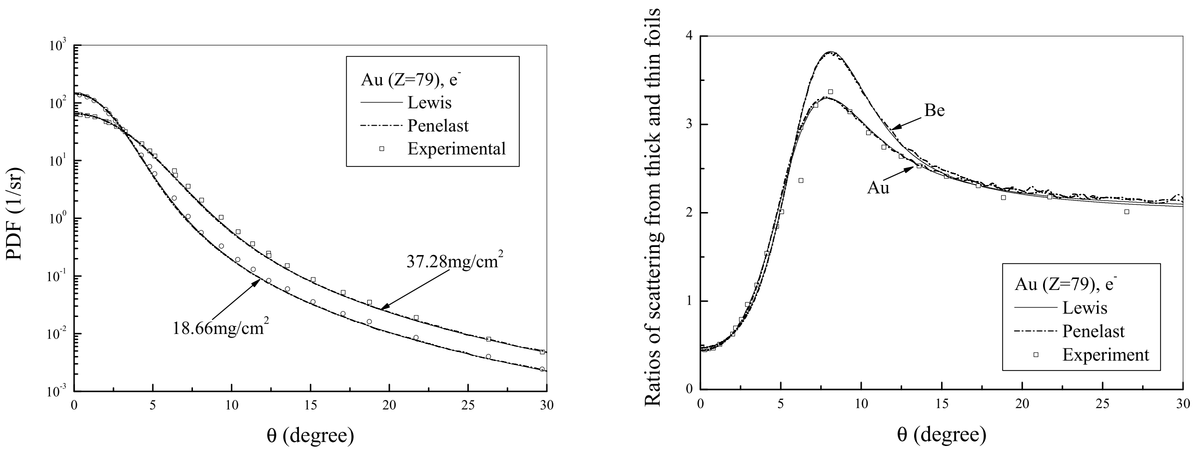

Figure 58: Multiple-scattering angular distributions of electrons after passing through Au foils (*left*) obtained from Lewis calculations (*continuous line*), simulations with PENELAST (*dashed-dot line*) and experiments (*symbols*). Angular dependence for the ratios of scattering for Be and Au (*right*).

Table 6: Multiple-scattering of 15.7 MeV electrons by Be and Au.

Material	Target thickness		Average energy (MeV)		No. of "collisions"	
	(mg/cm^2)	(μm)	Lewis	Molière	Lewis	Molière [437]
Au	18.66	9.6584	15.67	15.69	444	366
	37.28	19.2961	15.64	15.67	888	732
Be	257.0	$1.39 \cdot 10^3$	15.47	15.47	3652	2043
	491.3	$2.66 \cdot 10^3$	15.27	15.24	6981	3907

6.6 Angular Distribution of Electrons after a Given Path Length: Straggling Effects

6.6.1 Comparison of Lewis and PENELAST

Figure 59 (*left*) displays multiple-scattering angular distributions calculated using Lewis theory and those obtained from simulations with PENELAST for 10 MeV electrons in different materials. As previously pointed out, for large deflection angles, especially above 120 degrees, distribution results from the Lewis expansion are systematically lower than those obtained by MC simulation with PENELAST. These deviations increase for increasing atomic-number elements. The same tendency can be observed in Fig. 59 (*right*) which shows angular distributions for lead for different electron incident energies from 1.0 MeV up to 10 MeV. These straggling effects could be due to both the discrete radiative, as well as collisional, energy loss processes, which are simulated in detail in PENELAST, while in Lewis theory they are accounted for by means of the CSDA.

In order to understand the differences in the angular distributions at very large angles, cal-

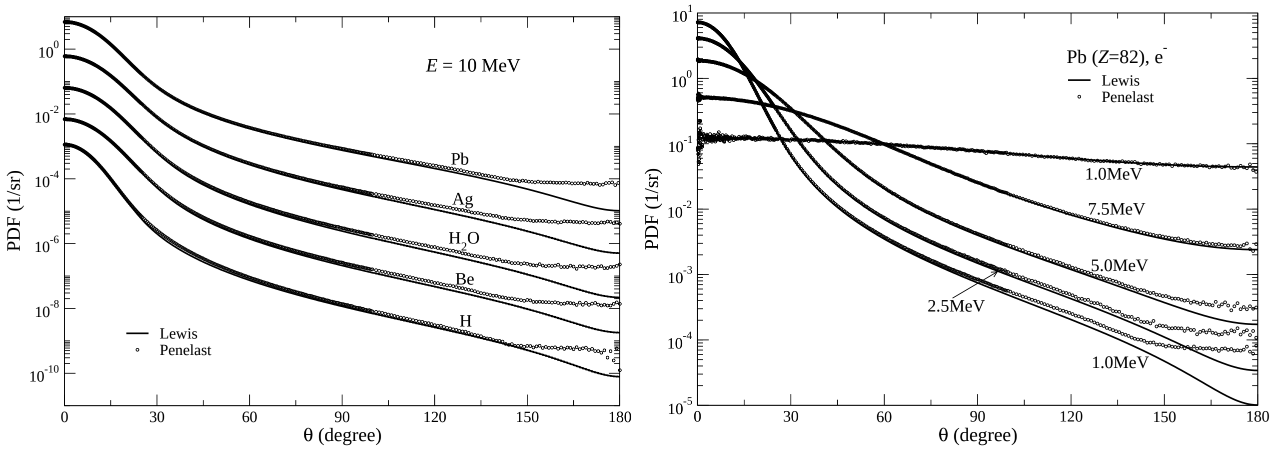

Figure 59: Multiple-scattering angular distributions for 10 MeV electrons after passing through H(x10^{-4}), Be(x10^{-3}), H_2O(x10^{-2}), Ag(x10^{-1}), and Pb foils (*left*). Multiple-scattering angular distributions for electrons with different incident energies after traveling a given path length s=100μm in lead (*right*). The continuous curves represent distributions calculated from the Lewis expansion. The symbols are simulation results obtained with PENELAST. (In order to obtain a relatively good backscattering angular distribution, in particular for low-Z elements, a large number of histories ($2.1{\cdot}10^9$) had been considered in the simulation.)

culated by using Lewis theory and PENELAST, we have disconnected in both calculations the mechanism of energy loss due to bremsstrahlung emission. Figures 60 and 61 show distributions for electrons of various energies in oxygen, water and gold computed with Lewis and PENELAST, with (*left*) and without (*right*) taking into account the energy loss due to bremsstrahlung. In the second case only collisional losses have been considered in both calculations. It is seen that, when bremsstrahlung emission is not accounted for, the differences in the angular distributions obtained using both calculational techniques are significantly reduced, the agreement obtained in this case being resonably good. Since the same radiative stopping power was adopted for the calculation of angular distributions using both the Lewis expansion and PENELAST, the observed differences are attributed to radiative straggling and also, to a lesser extent, to collisional straggling. Indeed, for high-energy electrons, say for energies above 1MeV, radiative energy-loss straggling, not included in the Lewis theory, becomes important and should be taken into account by means of improved mathematical models.

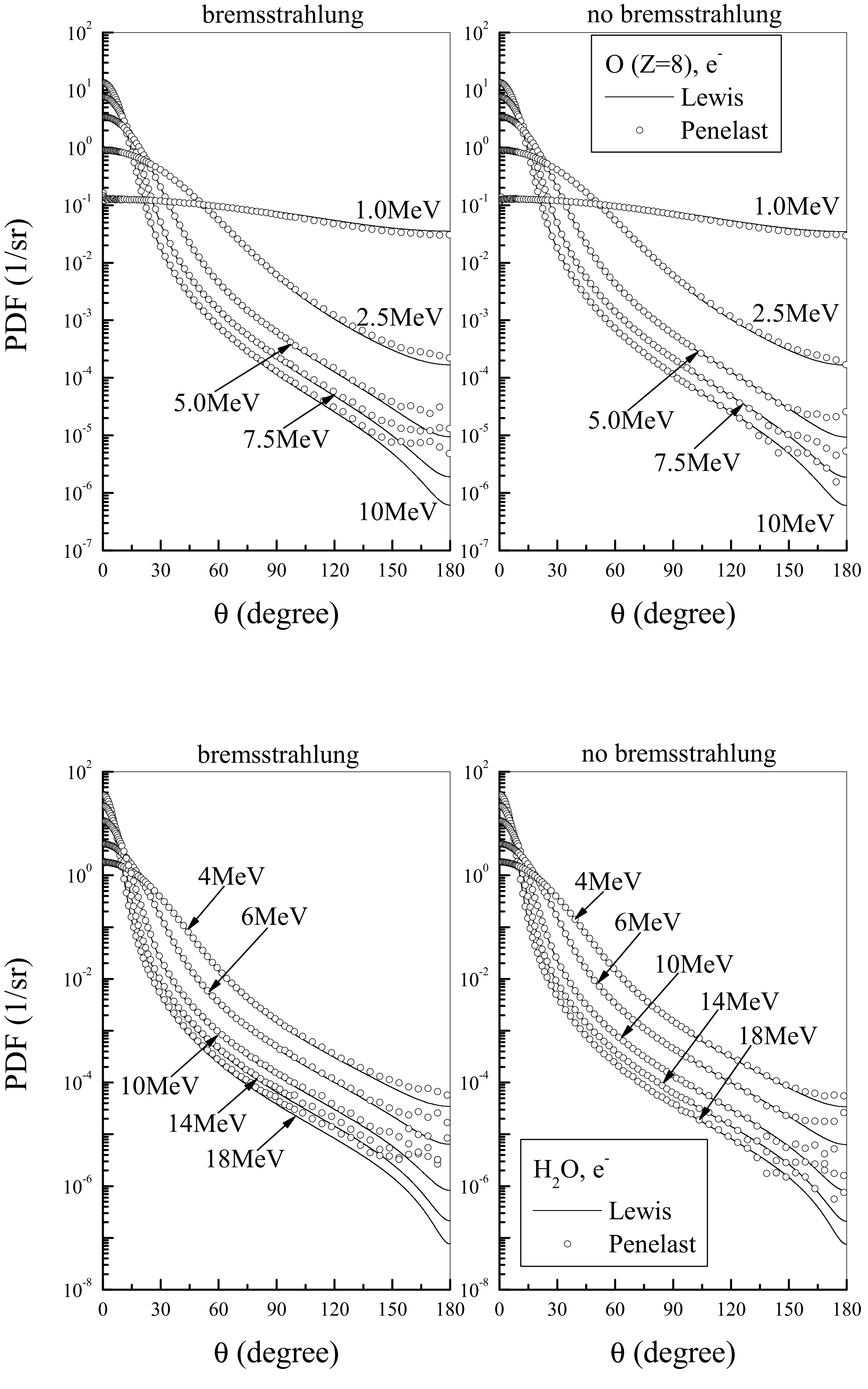

Figure 60: Multiple-scattering angular distributions for electrons of indicated energies after traveling a given path length in oxygen (*upper*) and water (*lower*), with (*left*) and without (*right*) radiative energy-losses being included. The continuous curves represent distributions calculated from the Lewis theory. The symbols are simulation results obtained with PENELAST.

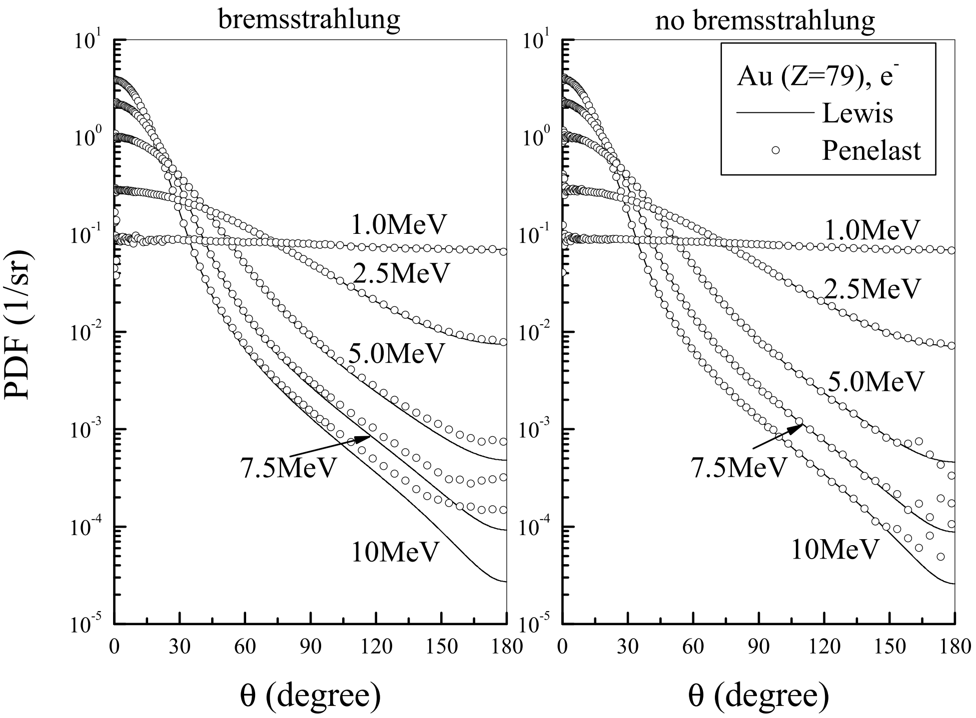

Figure 61: Idem Fig. 60 for gold.

The effect of energy straggling is illustrated in Fig. 62, which shows electron energy spectra for gold for different path lengths (*left*) and incident electron energies (*right*) obtained from PENELAST. The simulation of the energy distribution is a very sensitive test of the multiple-scattering process and of the energy loss computation (dE/dx and its fluctuation). This figure also shows energy spectra calculated with the modified version of PENELAST in which radiative losses are disconnected. We can see that both collisional and radiative straggling increase with increasing incident electron energy and with increasing path lengths. In general, at such high energies, radiative straggling is more important than collisional straggling, although for short path lengths they become similar. Straggling modifies the electron energy spectrum by making it broader and extending it towards low energies. Because of this, the multiple-scattering angular distribution becomes broader, as has been illustrated earlier. Therefore, we conclude that accurate calculations of multiple-scattering angular distributions by using the Lewis theory should incorporate energy straggling, especially radiative. The correct simulation of this quantity becomes very important, for instance, in what concerns backscattering experiments or dose calculations far away from the central axis.

6.6.2 A method to account for straggling effects in Lewis theory

A method to account for straggling effects, both radiative and collisional, is proposed in the following. It consists in the convolution of the two functions, $p_{\mathrm{L}}(\Delta E, \theta)$, the Lewis multiple-scattering angular probability distribution function for charged particles after travelling a

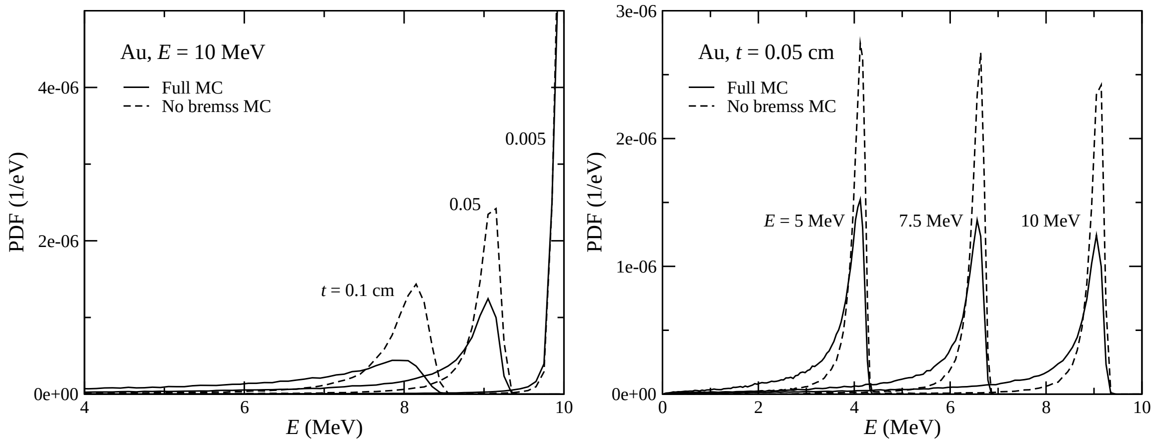

Figure 62: Electron energy spectra for the indicated path lenghts (*left*) and electron incident energies (*right*) in gold. The continuous curves are the results of MC simulation including all the interaction mechanisms. The dashed curves are the results of MC simulation ignoring bremsstrahlung.

given path-length s, and $p_{\mathrm{P}}(s;\Delta E)$, the electron energy probability distribution function of transmitted particles through a foil of the same thickness s. The convolution is done over a finite range ΔE. Explicitly,

$$F_{\mathrm{L_{corr}}}(\theta;s) \simeq \int p_{\mathrm{P}}(s;\Delta E)\, p_{\mathrm{L}}(\Delta E,\theta)\,\mathrm{d}(\Delta E) = \sum_{\mathrm{i}=0}^{\mathrm{N}} \left(\int_{\mathrm{i}} p_{\mathrm{P}}(s;\Delta E)\,\mathrm{d}(\Delta E) \right) p_{\mathrm{L}}(\Delta E_{\mathrm{i}},\theta), \quad (168)$$

where $F_{\mathrm{L_{corr}}}$ is the Lewis multiple-scattering angular distribution corrected with the convolution method, N is the number of energy bins and ΔE_{i} is the discrete energy interval of the transmitted electron energy spectra. The probability function, $p_{\mathrm{P}}(s;\Delta E)$, has been obtained from the MC simulation with the code PENELAST.

It can be seen in the examples given in Fig. 63, for beryllium (*left*) and carbon (*right*) corresponding to two different energy losses, that the method proposed works rather well qualitatively (since the increase in the probability distribution function is obtained), but not quantitatively because it overestimates the results given by PENELAST. Additional investigations need to be done in order to be able to account for straggling effects within the Lewis theory in a more consistent manner.

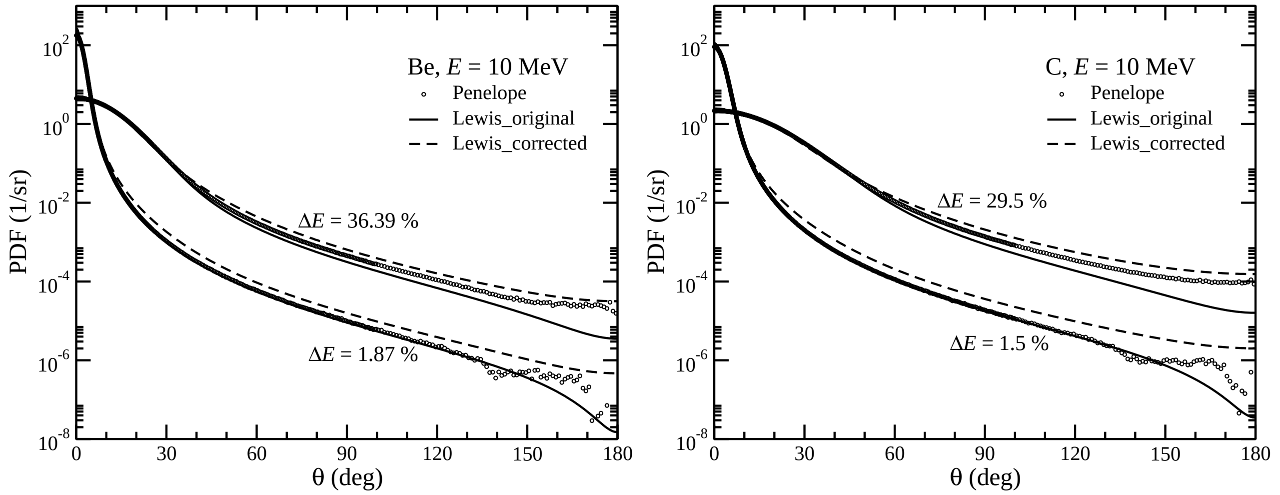

Figure 63: Multiple-scattering angular distributions of 10 MeV electrons in beryllium and carbon for the indicated average energy losses. The continuous lines are the results from the original Lewis expansion; the dashed lines represent distributions obtained from the Lewis expansion convolved by the corresponding energy spectra given by the MC simulation. Symbols are simulation results.

6.7 Angular Distribution of Electrons after a Given Path Length: Effect of Inelastic Scattering on the Angular Deflections

At small angles, the inelastic DCSs as function of the scattering angle, calculated by using the GOS model [229], are found to have a somewhat peaked shape and to be up to a few orders of magnitude larger than the elastic cross sections from the ELSEP database. Moreover, the relative importance of inelastic scattering increases with decreasing atomic number of the material, e.g. in the case of water, the material commonly used for biological applications. In Fig. 64, examples are given for low-Z (^{13}Al) and high-Z (^{49}Au) materials at two different energies. In addition, the total (elastic + inelastic) DCSs have also been displayed.

The contribution of inelastic DCSs to the multiple-scattering probability distribution functions for medium to low energies is investigated in the following, with emphasis on low-Z materials. It should be mentioned that, to date, the effect of inelastic scattering of charged particles by atomic electrons on multiple-scattering angular deflections has been considered in MC codes only by making use of different rough approximations.

6.7.1 Replacing Z by $Z^2 + Z$

For sufficiently high energies (depending on the atomic number of the projectile), both elastic and inelastic DCSs concentrate at very small angles. Therefore, in the high-energy limit, one can invoke the small angle approximation [165] and assume that the inelastic transport cross sections are nearly proportional to the elastic ones, i.e. $\sigma_\ell^{(\mathrm{in})} = \mathcal{C}\sigma_\ell$, and the constant $\mathcal{C}$ is nearly the same for all orders ℓ. Under these circumstances, the effect of inelastic scattering can be accounted for by simply multiplying the DCS by a factor $1+\mathcal{C}$. In several MC simulation codes,

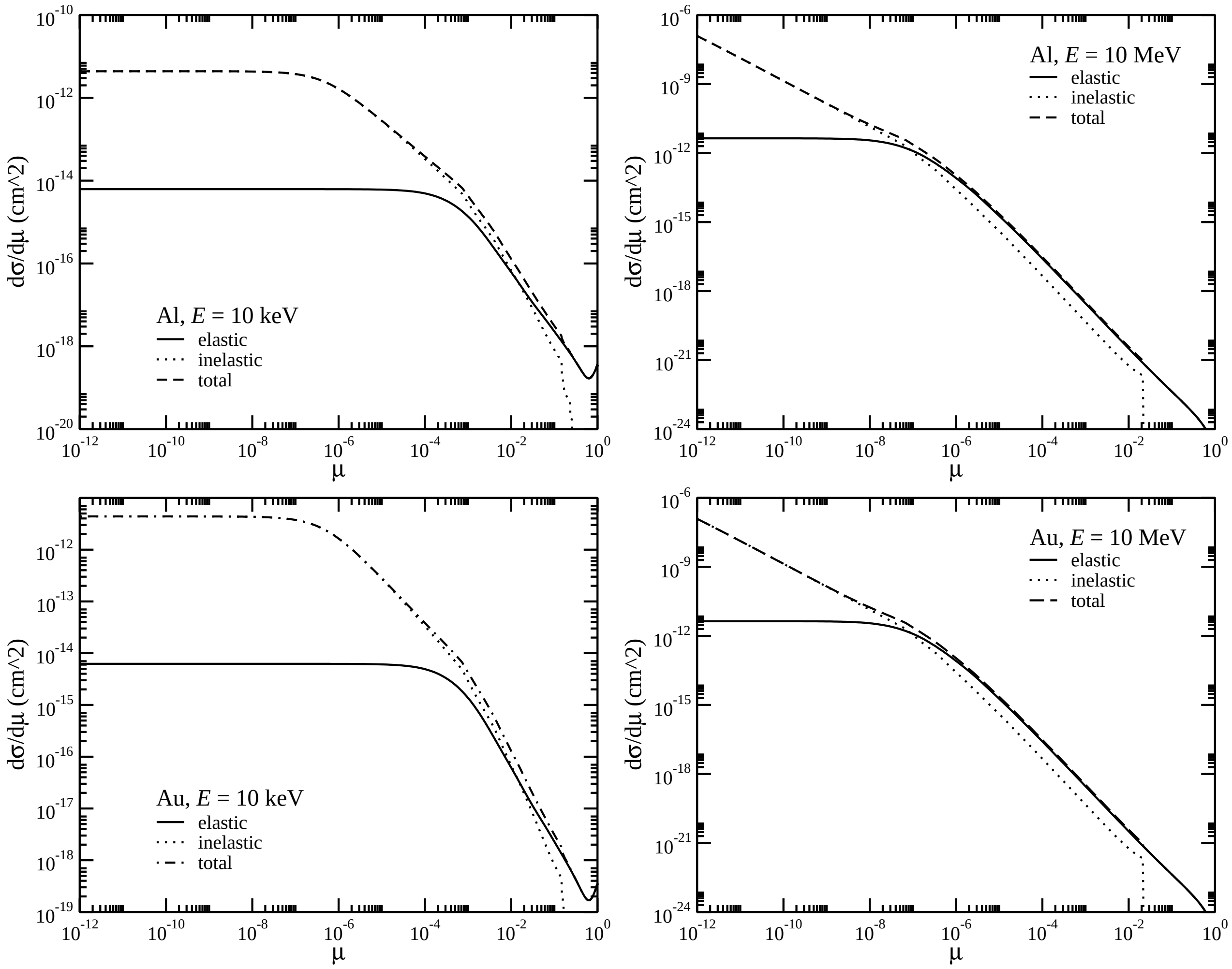

Figure 64: Elastic, inelastic and total (elastic + inelastic) differential cross sections for the scattering of electrons by aluminium and gold for the indicated energies.

inelastic scattering is introduced by multiplying the elastic DCS by $1 + Z^{-1}$ [241], where Z is the atomic number of the material (or the average atomic number in the case of compounds and mixtures). Evidently, this is a rough approximation, which amounts to assuming that the angular distribution in single inelastic events is the same as in elastic collisions, something which applies only at higher energies, of the order of 1 MeV and larger.

Figure 65 (*left*) shows angular distributions of 10 MeV electrons in different materials. To illustrate the contribution of inelastic scattering to the angular distribution, the figure also includes angular distributions calculated by multiplying the elastic DCSs by $1 + Z^{-1}$. Figure 65 (*right*) displays the relative differences between cases with and without the accounting of the inelastic collision contribution to the angular multiple-scattering deflections. We can see that the contribution of inelastic scattering is important for low-atomic number elements and that it decreases for increasing atomic number.

The availability of inelastic DCSs as a function of the scattering angle in numerical form, based on detailed physics models [241, 229], allows us to consider a much more accurate calculation of the inelastic collision contribution to the multiple-scattering angular distributions than by

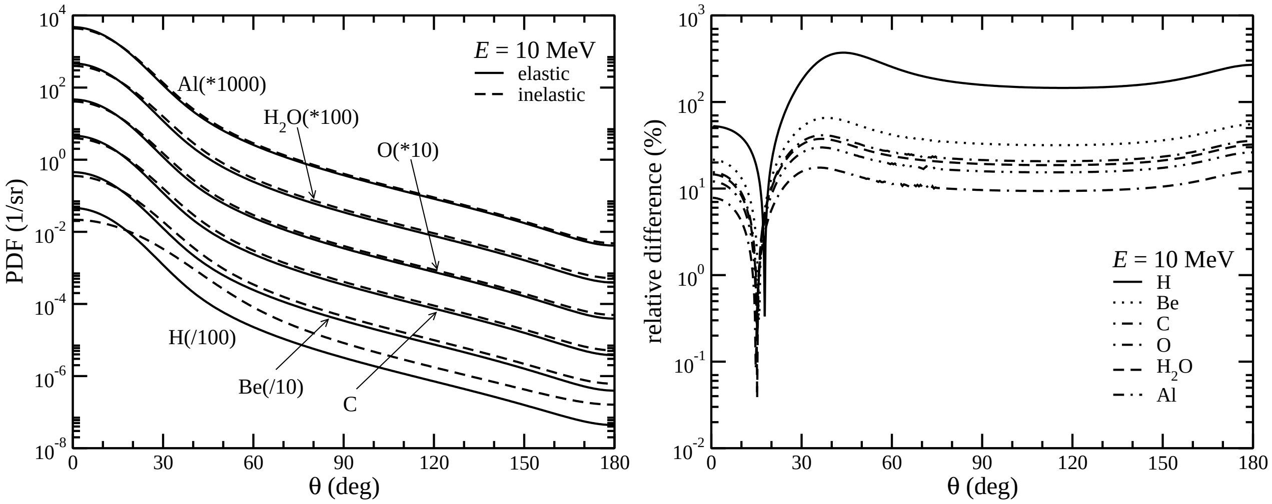

Figure 65: Lewis multiple-scattering angular distributions of 10 MeV electrons in the indicated materials (*left*). The continuous lines represent purely elastic scattering distributions; the dashed lines are distributions calculated by considering the correction factor $1 + Z^{-1}$ to account for angular deflections by inelastic scattering. Relative differences between elastic scattering PDF's, with and without inelastic scattering effects included, for the indicated materials (*right*).

simply using the continuous slowing down approximation, as originally described in the paper of Lewis [49].

6.7.2 Calculation of transport coefficients

To account for the effect of inelastic scattering within the multiple-scattering theories of Goudsmit-Saunderson and Lewis, the transport coefficients G_ℓ given by Eq. (138) must be calculated for the sum of the elastic and inelastic DCSs,

$$G_\ell = \mathcal{N}\, 2\pi \int_{-1}^{1} [1 - P_\ell(\cos\theta)] \left[\frac{\mathrm{d}\sigma_{\mathrm{el}}(\theta)}{\mathrm{d}\Omega} + \frac{\mathrm{d}\sigma_{\mathrm{in}}(\theta)}{\mathrm{d}\Omega} \right] \mathrm{d}(\cos\theta), \tag{169}$$

where $\mathrm{d}\sigma_{\mathrm{el}}/\mathrm{d}\Omega$ and $\mathrm{d}\sigma_{\mathrm{in}}/\mathrm{d}\Omega$ are the elastic and the inelastic DCS, respectively.

For checking purposes, recalculation of the original total (elastic + inelastic) DCS data for both electrons and positrons has been done according to the following Legendre series:

$$\frac{\mathrm{d}\sigma_{\mathrm{tot}}(\theta)}{\mathrm{d}\Omega} = \sigma \sum_{\ell=0}^{\infty} \frac{2\ell+1}{4\pi} F_\ell P_\ell(\cos\theta), \tag{170}$$

where $F_\ell \equiv 1 - G_\ell$ is given by Eq. (169). Results for electrons scattered by aluminium (*left*) and gold (*right*) are displayed in Fig. 66 as a function of the scattering angle ($\mu = (1 - \cos(\theta))/2$). It is seen that, due to the sharply peaked cross section distribution existing at small angles, the convergence of the Legendre series given in Eq. (170) slows down dramatically even at low energies. Thus, the reconstruction of the DCSs of 5 keV electrons in aluminium, using the inelastic DCSs from the GOS model, requires as many as 10,000 terms in order

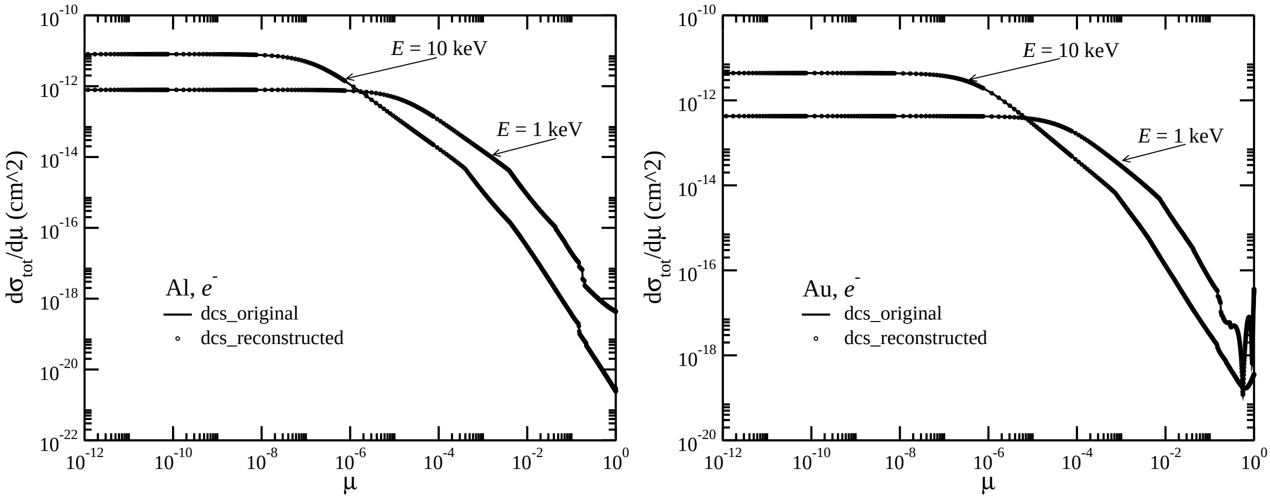

Figure 66: Total (elastic + inelastic) differential cross sections for aluminium (*left*) and gold (*right*), calculated from original models (*continuous lines*) and “reconstructed” using the Legendre polynomials (*symbols*).

to get convergence within 5%; this limit increases with decreasing atomic number. Multiple-scattering angular distributions for low energy electrons that include inelastic contributions and which are calculated on the basis of DCSs given by the GOS model are displayed in Fig. 67.

In order to overcome the problem of calculating a very large number of transport coefficients, methods with additional approximations have been tested. Thus, the small-angle approximation (see e.g. [165]) has been used for the calculation of the G_ℓ coefficients. By considering a limiting form of the Legendre polynomials, $P_\ell(\cos\theta) \simeq 1 - 1/4\ell(\ell+1)\theta^2$, the calculation of the angular distribution is very much simplified, being based only on the first transport mean free path:

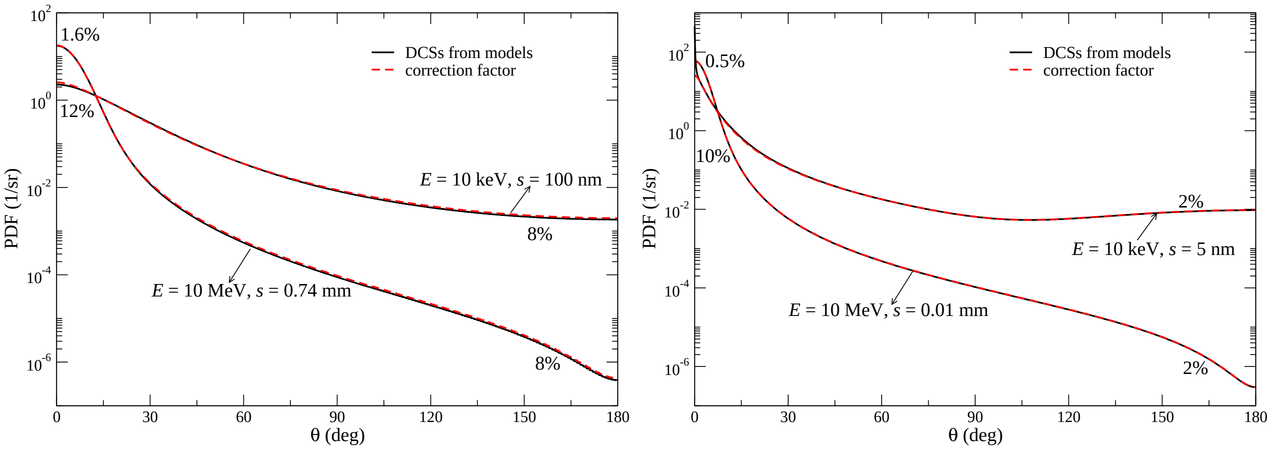

Figure 67: Lewis multiple-scattering angular distributions of 10 MeV electrons in aluminium (*left*) and gold (*right*). To account for angular deflections caused by inelastic scattering, the correction factor $1 + Z^{-1}$ (*continuous lines*) or the inelastic DCSs from the GOS model (*dashed lines*) are used.

$$\frac{1}{\lambda_\ell^{(\mathrm{s})}} \simeq \mathcal{N} 2\pi \frac{\ell(\ell+1)}{4} \int_0^{\theta_\mathrm{s}} \theta^2 \frac{\mathrm{d}\sigma_\mathrm{tot}(\theta)}{\mathrm{d}\Omega} \sin\theta \mathrm{d}\theta \simeq \frac{\ell(\ell+1)}{2} \frac{1}{\lambda_1^{(\mathrm{s})}} \tag{171}$$

where θ_s is a cutoff angle; when θ_s is very small, this approximation can be reliably used for the calculation of angular deflections due to soft collisions.

Finally, the calculation of the transport coefficients for the Wentzel model using Legendre functions of the second kind, $Q_\ell(x)$ as given by Eq. (146), has been considered. In Fig. 68, multiple-scattering probability distribution functions from Lewis theory are shown for electrons that have traveled different path lengths in various elements, considering the inelastic DCSs from both GOS and Wentzel models.

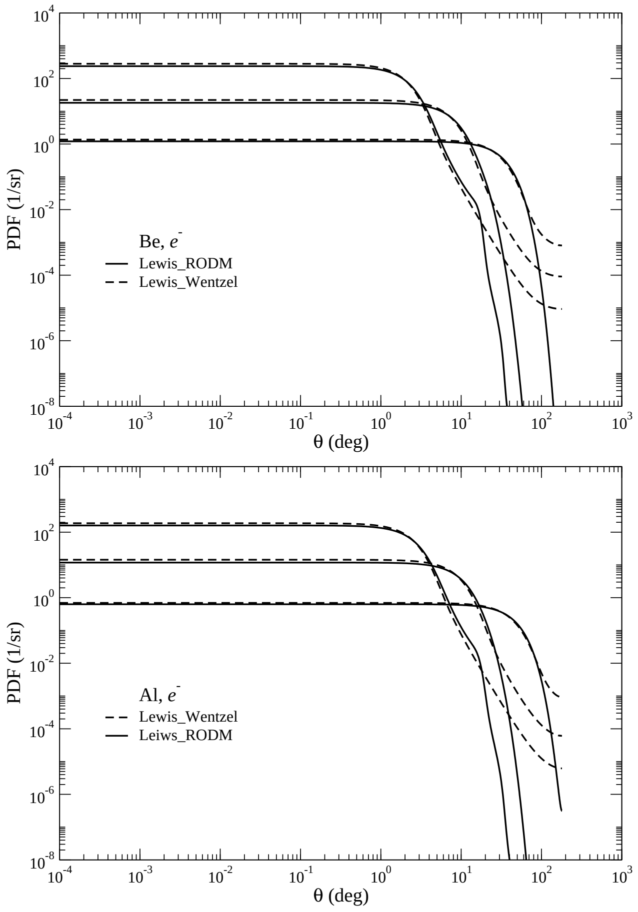

Figure 68: Multiple-scattering probability distribution functions for electron inelastic DCSs from the original GOS model (*continuous line*) and based on the Wentzel model (*dot-dash line*), for beryllium, water, aluminium and gold.

6.8 Summary

In this chapter, a new numerical algorithm for a fast running Monte Carlo code based on Lewis theory, that uses the CSDA to account for the effect of energy loss along the particle path, has been developed. For this purpose, different multiple-scattering algorithms used for the efficient simulation of charged particle transport in matter have first been analysed. The numerical algorithms for the calculation of the transport coefficients have been checked by reconstructing the original elastic DCS data. The calculated multiple-scattering angular distributions of particles, after passing through different materials of various thicknesses, have been compared with simulation results obtained with PENELAST while using the same set of DCSs data, the ELSEP library. In addition, comparisons with experimental data, performed for a wide range of elements at high as well as at medium energies, have shown a very good agreement in all cases.

For higher energies and at large angles, the multiple-scattering angular distributions obtained with LEWIS depart from those simulated with PENELAST due to straggling effects, i.e. collisional and radiative energy losses which Lewis theory takes into account only approximately via the CSDA. For cases in which the bremsstrahlung interaction is not considered, it has been found that the influence of straggling effects reduces significantly such that there is an apparent improvement in the agreement between calculation and simulation. A method has been proposed to account for straggling effects, and this has been shown to provide qualitatively consistent results.

Finally, the effect of inelastic scattering on the multiple-scattering angular deflections has been investigated. A common approximation currently used in all MC codes has been used to highlight the increasing importance of this effect with decreasing atomic number. On the basis of the state-of-the-art inelastic cross section data which have now been made available in numerical form, a new methodology has been implemented and tested so as to ensure more realistic calculations of multiple-scattering angular deflections.

7 Summary, Main Results and Recommendations for Future Work

The correlation between late biological effects and radiation exposure requires the description of both the spatial distribution of low-energy electrons and their energy deposition at cellular and subcellular levels. In relation to these aspects, most of the studies that can presently be done are based on detailed Monte Carlo calculations, due to the severe limitations that exist for direct experimental investigations. The theoretical adequacy of the models currently used by Monte Carlo codes to describe the physics involved can be checked by comparing the results obtained by using different, independently developed particle transport programs which are able to simulate the track structure of ionizing particles in matter. In order to be meaningful and able to provide useful insights, such comparisons must be carried out while ensuring that (a) accurate and identical sets of basic cross section data are employed by the codes used for comparison and (b) the limitations and ranges of applicability of the various particle transport algorithms are well recognized. Such studies are particularly important for the development of reliable Monte Carlo tools that can allow real-time charged particle transport simulations necessary for routine clinical treatment planning. The work described in this thesis has been carried out in the above context and deals, in particular, with the transport of electrons and positrons of low and medium energy.

7.1 Summary

The two introductory chapters have provided a detailed description of the interactions of ionizing radiation with biological matter, particularly from the point of view of radiation induced DNA damage that leads to physiological injury of the cell and even its rapid death. In this context, Chapter 2 has introduced the most plausible theories developed to date to describe the multi-step process of radiation induced carcinogenesis, i.e. initiation, promotion and progression. Special emphasis has been given to the description of the so-called "early interaction events", the direct (physical stage) and the indirect (chemical stage) mechanisms, and to the identification of the areas that still need further investigation in order to fill the knowledge gap about the processes that take place between these two stages. Chapter 2 has also introduced the most important Monte Carlo tools currently used for the simulation of particle transport and which, therefore, are very important for the study of the interactions mentioned above.

The present thesis has made two principal contributions in the latter context, i.e. towards the development of new and improved Monte Carlo calculational tools for charged particle transport in biological materials. These are (i) the provision of up-to-date new cross-section datasets for electron and positron interactions down to 1 eV (Chapters 3-4), and (ii) the development and application of an advanced particle transport method based on a multiple-scattering algorithm for fast simulations in Monte Carlo codes (Chapters 5-6). The new simulation method can make use of input cross section data in numerical format, while fulfilling the requirements of both high accuracy and computational speed. In this calculation, it has been possible to include, for the first time based also on the use of numerical cross sections, the effect of inelastic scattering on the angular distributions of scattered particles.

The work related to cross section generation and validation has been largely based on the consideration of standard models for the analytical description of bremsstrahlung, elastic, and inelastic scattering of electrons and positrons in matter, as described in Chapter 3. For each type of interaction, the physical models presently available together with the developments currently made to describe the very low electron energy domain, as also their implementation into the FORTRAN77 cross section generation code PSICRO, have been discussed. Chapter 4 presents representative results, obtained with the models applied for each interaction type, while carrying carry out an extensive cross section data validation study for a wide range of energies and elements. Thus, this study has centred on comparisons between the newly calculated datasets and a large amount of most recent analytical, and (whenever possible) experimental, cross section data for electrons/positrons of low to medium energy.

The development and application of new tools for stochastic calculations has resulted in PENELAST, a new mixed-algorithm Monte Carlo code developed in the course of this thesis and described in Chapter 5. It effectively represents an extension of the general-purpose code system PENELOPE, and employs up-to-date elastic scattering differential cross sections. These are based on state-of-the-art physics models and have currently been made available in numerical format. The inelastic scattering cross sections employed are based on the PENELOPE generalized oscillator strength model [34]. PENELAST has been used for both mixed and detailed simulations of angular distributions and energy spectra of charged particles after passing through various materials, in particular for low-Z elements and for small distances such as sub-cellular dimensions. Although the code primarily addresses problems related to the simulation of medium to high energy particles, special emphasis has been placed on its capabilities to both correctly handle the implementation of numerical cross section data and to extend the calculation of energy spectra to energies well into the eV range.

The work on developing new, more efficient Monte Carlo methods has also yielded a new multiple-scattering numerical algorithm based on Lewis theory[49] presented in Chapter 6. This algorithm is used for the calculation of angular distributions of charged particles after travelling a given path-length in the medium to high energy range. The implementation of this algorithm into the new FORTRAN77 code LEWIS has been described in detail in the same chapter, and the accuracy of the calculated results has been assessed by comparison with calculated distributions obtained using other multiple-scattering algorithms (such as Molière), with the results of PENELAST simulations, and with available experimental data. The development is completed with methods to account for angular deflections due to the inelastic scattering contribution and to correct for straggling effects, in the calculation of the multiple-scattering angular distributions.

7.2 Main Results

The main results of the present work can be grouped under the following headings: "Cross section data for Monte Carlo codes" and "Monte Carlo methods".

7.2.1 Cross section data for Monte Carlo codes

- Bremsstrahlung:

Various theoretical models, such as the Bethe-Heitler theory, and the Kirkpatrick-Wiedmann-Statham and partial wave analysis methods, have been used for the calculation and comparison of bremsstrahlung emission cross section data. Special emphasis has been placed on the generation of up-to-date low-energy numerical cross sections for bremsstrahlung emission that are needed for the accurate simulation of electron and positron transport in different materials. In the low-energy range, no comparison was possible with experimental values due to the lack of appropriate measurements. The results consist of two sets of bremsstrahlung cross section data and emitted photon energy spectra, viz. for electrons and positrons interacting with neutral atoms of atomic numbers Z=1-100 and for incident energies between 1 eV and 100 GeV.

- Elastic:

The elastic scattering of low to medium energy electrons/positrons by neutral atoms has been considered on the basis of the partial wave analysis method, numerical implementation being carried out into an upgraded version of the code PSICRO. Generation and validation of elastic scattering differential cross section data has been carried out down to 1 eV incident particle energy and, for the first time, assessed against experimental results for this very low energy range. The comparison of the currently calculated cross sections with available experimental data, in particular for low-Z elements, has shown a relatively good agreement for all angles and energies considered. It has thus been demonstarted that the current model considered for the description of the interaction potential used by the partial wave analysis method can adequately describe the elastic scattering process of charged particles by neutral atoms, especially at very low energies. Regarding the calculated differential cross sections for high atomic number elements, certain disagreements have been shown to exist at forward directions (scattering angle smaller than 60° for all energies considered).

- Inelastic:

The validation of shell ionization cross section data generated with the code PSICRO has been done considering the latest experimental and calculated data. In the entire incident energy range over which experimental data are available, the K-shell and L-shell ionization cross sections calculated for electrons using PSICRO's Weizsäcker-Williams method show very good agreement with measured values for a wide range of atoms and incident energies. In addition, good agreement has also been found with values based on more recently developed theoretical models.

For the description of the excitation process from the ground state of neutral atoms (Z=1 to 100), in the energy range from 1 eV to 1 MeV, a model based on many-body theory has been proposed and implemented in the FORTRAN77 code PSICRO. In the high-energy range, the original Lawrence Livermore National Laboratory (LLNL) formalism that corresponds to distant ('resonance') collisions is retained. The program calculates integrated cross sections, energy loss, average angular distributions of the incident particle and the emitted photon for phonon, particle-hole and plasmon excitation for incident electrons/positrons for the free-electron case. In addition, the new model, which employs the free-electron Lindhard dielectric energy-loss function, has been further refined in order to also consider bound-electron particle-hole excitation. The comparison of experimental and calculated (discrete and total) excitation cross sections has been performed for both electron and positron scattering by several rare-gas atoms, with a good agreement being observed in general. Although still not sufficiently detailed for the calculation of differential cross sections, the present model has been found to provide an adequate general description of the excitation mechanism.

In summary, the present theoretical developments and the efforts made to validate results on the basis of available experimental data have yielded new cross sections (elastic and inelastic) for electrons and positrons, covering a large number of materials (Z=1-100) and going down to energies lower than considered to date. As regards the accuracy of the data presently generated for bremsstrahlung emission, elastic scattering, ionisation and excitation, this appears to be quite adeguate for most applications. Thus, for elastic scattering, the comparisons made for various elements have shown that the agreement with measurements is within the experimental errors (not larger than 30%). In particular for low-Z elements and low energies, a very good agreement has been obtained (differences of maximum 5%). Compatisons for ionisation cross sections have also shown that the currently generated data are in very good agreement with measurements, the discrepancies (about 3-5%) being most of the time well within the experimental errors (about 20-30%).

These various cross section types generated, incorporated into two data libraries having the LLNL format, have been made available in electronic form (files) and should help improve the quality of radiation transport modelling by Monte Carlo codes such as GEANT or GEANT-PSI.

7.2.2 Monte Carlo methods

- Monte Carlo code PENELAST:

A new mixed-algorithm Monte Carlo code PENELAST has been written, essentially as an extension of the general-purpose code system PENELOPE (version 2001). The code PENELAST employs up-to-date numerical elastic cross section data currently made available in tabulated format, the ELSEP (ELastic Scattering of Electrons and Positrons) database, and based on state-of-the-art theoretical models. The excellent agreement between the results obtained with PENELAST and PENELOPE, above the 1 keV energy cutoff employed in the latter, has served to confirm the accuracy of algorithms used to prepare the cross section data needed for any energy and scattering angle required. Thus, a fast, computationally efficient and accurate sampling technique is used to link the newly generated cross section databases. The novelty resides in the current extension of computed energy spectra down to energies well into the eV range. The development of such a tool is clearly valuable for radiation protection studies as regards the role of low-energy secondary electrons, obtained in various interaction processes, in leading to specific radiation effect end-points.

Effectively, in addition to the large field of applications for which the Monte Carlo code system, PENELOPE, was originally developed, its current extension to low energies has opened the possibility to address specific applications in environmental health physics and radiation micro- and nano-dosimetry. Furthermore, the wide range of elements, for which reliable low-energy electron and positron data have been made available, makes PENELAST a code which could potentially be used for new applications in condensed matter and radiation science, i.e. basic and applied research on the effects of radiation on materials and devices.

- Multiple-scattering algorithm code LEWIS:

A new FORTRAN 77 computer code for the calculation of the multiple-scattering angular deflection of high-energy charged particles has also been developed. The code is based on the Lewis theory which employs the continuous slowing down approximation to account for the effect of energy loss along the particle path. Comparison of the angular distributions of particles, after passing through different materials of various thicknesses, has been made with experiments, as well as with calculated/simulated results obtained using other multiple-scattering algorithms (such as Molière [26, 425] and Goudsmit-Saunderson [29]), and identical set of elastic differential cross section data. This has clearly brought out the specific ranges of validity of the different methods, the present Lewis theory based calculations being found to be more generally applicable than, for instance, those based on Molière theory [26, 425].

The numerical algorithms employed for the calculation of the transport coefficients have been checked by showing that the original elastic differential cross section data can be succesfully reconstructed. The method proposed to account for straggling effects has been shown to provide qualitatively consistent results. In addition, on the basis of the state-of-the-art inelastic cross sections which have also currently been made available in numerical format, a new methodology which ensures more realistic calculations of multiple-scattering angular deflections based on inelastic data has been implemented and tested.

7.3 Recommendations for further developments

- Cross section data

In the context of bremsstrahlung emission, due to the fact that the information available from the different theoretical models [162] is fragmentary (as shown in Chapter 3), there is a real need for a more complete database able to describe in particular the angular dependence of the differential cross section. In addition, assessment of more recent models for the calculation of bremsstrahlung cross section data at lower energies (such as the distorted-wave Born approximation) is highly recommended.

It has been shown in the course of the present thesis that, for very low energies (down to 1 eV), the models which seem to best fit the experimental data for elastic scattering do so adequately only for specific ranges of energy and target atomic numbers. Accordingly, in order to generate differential cross sections in energy and scattering angle grids dense enough to ensure highly accurate interpolation, further model work is still required. Thus, it is recommended to either develop a single theoretical model of general applicability, or to integrate several different models in a coherent manner to cover the complete range of low energies and atomic numbers. Moreover, the need to link the resulting new differential cross section data to a versatile Monte Carlo code that has low-energy capabilities would have to be addressed.

As regards inelastic scattering, it is recommended that, for inner-shell ionization, studies be conducted on the reliability of advanced models used for the calculation of accurate theoretical cross sections (e.g. distorted-wave Born approximation method), especially near the ionization threshold energy. Despite the fact that the excitation process remains the most important energy loss mechanism below the ionization threshold, accurate differential cross section data for a wide range of materials, particularly in the low-energy range, are not yet available. The development of more refined models is thus needed in this context.

Finally, it must be borne in mind that further work is needed for target generalisation from single atoms to complex biomolecules and condensed media.

- Monte Carlo methods

As indicated earlier, the code PENELAST - based on numerical ELSEP differential cross sections [120], their accurate and rapid interpolation methodology, and the calculation of transport properties - has opened the possibility of addressing radiation protection issues at cellular/sub-cellular levels. The implementation of such algorithms together with appropriately formated low-energy cross sections would, for the first time, provide a detailed description of the spatial distribution of low-energy electrons in biological materials. Further development steps should then consider the succeeding physico-chemical, chemical and biological processes involved in radiation damage.

Connected to the development of accurate multiple-scattering algorithms for the fast simulation of medium and high-energy charged particle transport, the next step would be to develop a methodology for taking straggling effects accurately into account. This, together with a fast running sampling algorithm, will allow the successful development of a complete Class I Monte Carlo code which can then be reliably used in practice, e.g. in radiation treatment planning (complex beam shaping, source shielding, etc.).

A Examples of PSICRO Input and Output Files

A.1 Example of PSICRO input

In this section, an example of the PSICRO code's input files is shown, viz. for the case of positron scattering by silver (Z=47). In the calculation, bremsstrahlung, elastic and inelastic cross section data, and other energy-related quantities can be generated. First, the atomic numbers for elements Z=1-100 are listed, together with the corresponding atomic densities which have to be used in the calculation. The libraries which contain the required data are linked further. Finally, the two output files are also indicated.

```
cd $HOME/wqeldl/job
mkdir $$
cd $$
cat > wqeldl.inp ≪ END OF FILE
EEDL01 020214 2 47 47
  1    1
  2    2
  3    1
  4    1
  5    1
  6    1
  7    1
  8    1
  9    2
 10    2
 11    1
 12    1
 13    1
 14    1
 15    1
 16    1
 17    2
 18    2
 19    1
 20    1
 21    1
 22    1
 23    1
 24    1
 25    1
 26    1
 27    1
 28    1
 29    1
 30    1
 31    1
 32    1
 33    1
 34    1
 35    1
 36    2
 37    1
 38    1
 39    1
 40    1
 41    1
 42    1
 43    1
 44    1
 45    1
 46    1
 47    1
 48    1
 49    1
 50    1
51    1
52    1
53    1
54    2
55    1
56    1
57    1
58    1
59    1
60    1
61    1
62    1
63    1
64    1
65    1
66    1
67    1
68    1
69    1
70    1
71    1
72    1
73    1
74    1
75    1
76    1
77    1
78    1
79    1
80    1
81    1
82    1
83    1
84    1
85    1
86    2
87    1
88    1
89    1
90    1
91    1
92    1
93    1
94    1
95    1
96    1
97    1
98    1
99    1
100    1
END OF FILE
ln -s /afs/psi.ch/user/n/negreanu/libraries/EADL.DIR EADL.DIR
ln -s /afs/psi.ch/user/n/negreanu/libraries/EADL.BIN EADL.BIN
ln -s /afs/psi.ch/user/n/negreanu/libraries/EPDL97.DIR EPDL.DIR
ln -s /afs/psi.ch/user/n/negreanu/libraries/EPDL97.BIN EPDL.BIN
ln -s /afs/psi.ch/user/n/negreanu/libraries/EXDL97.DIR EXDL.DIR
ln -s /afs/psi.ch/user/n/negreanu/libraries/EXDL97.BIN EXDL.BIN
ln -s /afs/psi.ch/user/n/negreanu/libraries/EEDL.DIR EEDL.DIR
ln -s /afs/psi.ch/user/n/negreanu/libraries/EEDL.BIN EEDL.BIN
ln -s $HOME/wqeldl/wqeldl.rho psicro.rho
ln -s $HOME/wqeldl/imrato.potinpre imrato.potinp
$HOME/wqeldl/wqeldln.x < wqeldl.inp > wqeldl.out
mv wqeldl.out $HOME/wqeldl/wqeldln.outelem
mv EEDL01 $HOME/wqeldl/EEDL01m
rm *
```

A.2 Example of PSICRO output

In this section, examples of the PSICRO code's output files are shown, viz. for electron scattering by hydrogen and silver, respectively. The header gives details of the calculation (e.g. model types used for the description of the various interactions considered in the description of the interaction potential). The code PSICRO calculates interaction cross sections (differential and total), angular distributions and average energies for the scattered particle, and other needed quantities.

```
NAME OF GENERATED LIBRARY FILE: EEDL01
PARTICLE TYPE: 3 ELECTRON
ELEMENTS: 1 TO 1
DATE: 211105
Z, ATOMIC WEIGHT, DENSITY (GRAMM/CCM): 1 3.008 1.14000D-04
CUBIC-SPLINE INTERPOLATION OF THE PARTIAL SHIFTS (ISCH=2)
EXCHANGE POTENTIAL: HARA
POLARIZARION POTENTIAL: O'CONNELL, LANE, PADIAL AND NORCROSS
MUFFIN-TIN RADIUS = 4.13278E+01 A.U.
RADIAL CUTOFF OF POLARIZATION POTENTIAL : 3.4 AU
BINDING ENERGY OF THE OUTERMOST SUBSHELL : 13.605 eV

Elastic scattering: Cutoff cross sections                 Elastic scattering: Total cross sections
1 1.00000D-07 1.93634D+09 6.91480D+01 56                  1 1.00000D-07 1.93637D+09 6.91489D+01 7
2 2.59450D-07 1.99275D+09 7.11623D+01 56                  2 2.59450D-07 1.99282D+09 7.11648D+01 10
3 8.70000D-07 1.86917D+09 6.67493D+01 60                  3 8.70000D-07 1.86920D+09 6.67502D+01 15
4 1.20700D-06 1.78237D+09 6.36495D+01 66                  4 1.20700D-06 1.78234D+09 6.36484D+01 18
5 1.59700D-06 1.69165D+09 6.04100D+01 80                  5 1.59700D-06 1.69161D+09 6.04085D+01 20
...                                                       ...
Angular distribution of the scattered particle
1 1 1.00000D-07 1.00000D-06 6.86733D+08
1 2 1.00000D-07 3.16228D-06 6.86733D+08
1 3 1.00000D-07 1.00000D-05 6.86736D+08
1 4 1.00000D-07 3.16228D-05 6.86743D+08
1 5 1.00000D-07 1.00000D-04 6.86765D+08
...
```

```
*****************************************************************************
NAME OF GENERATED LIBRARY FILE: EEDL01
DATE: 211105
PARTICLE TYPE: 3 ELECTRON
ELEMENTS: 47 TO 47
CUBIC-SPLINE INTERPOLATION OF THE PARTIAL SHIFTS (ISCH=2)
EXCHANGE POTENTIAL: HARA
POLARIZARION POTENTIAL: O'CONNELL, LANE, PADIAL AND NORCROSS
Z, ATOMIC WEIGHT, DENSITY (GRAMM/CCM): 47 107.870 1.05000D+01


Bremsstrahlung: Integrated cross sections    Average energy of the secondary photon
1 1.00000E-06 2.78818E+03                    1 1.00000E-06 3.32553E-07
2 2.00000E-06 3.19948E+03                    2 2.00000E-06 5.83929E-07
3 3.00000E-06 3.46765E+03                    3 3.00000E-06 8.11676E-07
4 5.00000E-06 3.83774E+03                    4 5.00000E-06 1.22905E-06
5 7.00000E-06 4.10283E+03                    5 7.00000E-06 1.61531E-06
...                                          ...
```

B Lagrange Interpolation and Cubic Spline Interpolation Methods

Interpolation is a method of constructing new data points from a discrete set of known data points which are monotonically increasing. Interpolation methods are commonly used in two situations: when the results are available for selected conditions, but values are needed for intermediate conditions, and when the functional dependence is so complicated that explicit evaluation is costly in terms of computer time. Extrapolation, a type of interpolation, is the extension of such data beyond the range of the measurements. It is much more difficult, and its results are often invalid or subject to substantial uncertainty if not used and interpreted properly.

The Lagrange method and cubic spline method of interpolation are two different ways to perform curve fitting on a given set of input points. In this section, each interpolation method is briefly explained.

B.1 Lagrange Interpolation

This is a particularly convenient way to interpolate among tabulated values by using polynomials. For a given set of $N+1$ data points

$$\{(x_{\mathrm{i}}, y_{\mathrm{i}}), \qquad i = 0, \ldots, N\} \tag{172}$$

it is possible to construct a polynomial p, of degree at most N with the property that

$$p\,(x_{\mathrm{i}}) = y_{\mathrm{i}}, \qquad i = 0, \ldots, N. \tag{173}$$

The Lagrange polynomials provide a convenient alternative to solving the simultaneous equations that result from requiring the polynomials to pass through the data values. The Lagrange interpolation formula is:

$$f(x) = \sum_{\mathrm{i}=1}^{\mathrm{N}} f\,(x_{\mathrm{i}})\, P_{\mathrm{i}}^{\mathrm{L}}(x), \tag{174}$$

where $f\,(x_{\mathrm{i}})$ are the known values of the function and $f(x)$ is the desired value of the function. The Lagrange polynomial $P_{\mathrm{i}}^{\mathrm{L}}(x)$ is the polynomial of order $N-1$ that has the value 1 when $x = x_{\mathrm{i}}$ and 0 for all $x_{\mathrm{j}\neq\mathrm{i}}$:

$$P_{\mathrm{i}}^{\mathrm{L}}(x) = \frac{\prod_{\mathrm{j}\neq\mathrm{i}}(x - x_{\mathrm{j}})}{\prod_{\mathrm{j}\neq\mathrm{i}}(x - x_{\mathrm{j}})}. \tag{175}$$

An advantage of Lagrange interpolation is that the method does not need evenly spaced values in x. However, there are problems with using the Lagrange interpolation method. For high-order polynomials that match many entries in the table simultaneously, the interpolated curve will begin to oscillate rapidly between the sample points, wildly deviating from the linear interpolation. This will cause undesired effects when the sampling points are very close together.

If used for extrapolation with a high-order polynomial, this method may give serious errors. A high-order polynomial may provide a very good fit to a data set over its range of validity, but if higher powers than needed are included, the polynomial may diverge rapidly from smooth behaviour outside the range of the data.

B.2 Cubic Spline Interpolation

The cubic spline interpolation is used in order to avoid the problems related to the undesirable fluctuations which appear when using polynomial interpolation with higher-order polynomials. The spline provides a technique for obtaining a smoother interpolation formula by fitting a piecewise curve through the sampled points. A cubic spline $s(x)$ is constructed for each interval between data points by determining the four polynomial coefficients as follows. Two requirements are that the endpoints of the polynomial match the data:

$$s\left(x_{\mathrm{i}}\right) = f\left(x_{\mathrm{i}}\right) \qquad \text{and} \qquad s\left(x_{\mathrm{i+1}}\right) = f\left(x_{\mathrm{i+1}}\right) \tag{176}$$

The two other constraints arise from the requirement that the first and second derivatives be the same as in adjoining intervals. These constraints are shared with the nearby data intervals. This is a desired effect, so that the pieces are smooth and continuous with no breaks or sudden changes throughout all pieces of the curve. It is conventional to specify that the second derivatives vanish at the endpoints of the data set, $f''(x_0) = f''(x_1) = \ldots = f''(x_{\mathrm{n}})$. This then specifies a set of simultaneous equations to be solved for the interpolating function:

$$\begin{aligned}
\left(x_{\mathrm{i}} - x_{\mathrm{i-1}}\right) f''(x_{\mathrm{i-1}}) + 2\left(x_{\mathrm{i+1}} - x_{\mathrm{i-1}}\right) f''(x_{\mathrm{i}}) \;+\; \left(x_{\mathrm{i+1}} - x_{\mathrm{i}}\right) f''(x_{\mathrm{i+1}}) = \\
\frac{6}{\left(x_{\mathrm{i+1}} - x_{\mathrm{i}}\right)}\left[f(x_{\mathrm{i+1}}) - f(x_{\mathrm{i}})\right] \;+\; \frac{6}{\left(x_{\mathrm{i}} - x_{\mathrm{i-1}}\right)}\left[f(x_{\mathrm{i-1}}) - f(x_{\mathrm{i}})\right]
\end{aligned} \tag{177}$$

with $\mathrm{i} = 1, 2, 3, \ldots, \mathrm{n} - 1$.

The cubic function for each interval is:

$$\begin{aligned}
f_{\mathrm{i}}(x) = \frac{f''(x_{\mathrm{i-1}})}{6\left(x_{\mathrm{i}} - x_{\mathrm{i-1}}\right)}\left(x_{\mathrm{i}} - x\right)^3 \;+\; \frac{f''(x_{\mathrm{i}})}{6\left(x_{\mathrm{i}} - x_{\mathrm{i-1}}\right)}\left(x - x_{\mathrm{i-1}}\right)^3 \\
+ \left[\frac{f(x_{\mathrm{i-1}})}{\left(x_{\mathrm{i}} - x_{\mathrm{i-1}}\right)} - \frac{f''(x_{\mathrm{i-1}})\left(x_{\mathrm{i}} - x_{\mathrm{i-1}}\right)}{6}\right]\left(x_{\mathrm{i}} - x\right) \\
+ \left[\frac{f(x_{\mathrm{i}})}{\left(x_{\mathrm{i}} - x_{\mathrm{i-1}}\right)} - \frac{f''(x_{\mathrm{i}})\left(x_{\mathrm{i}} - x_{\mathrm{i-1}}\right)}{6}\right]\left(x - x_{\mathrm{i-1}}\right).
\end{aligned} \tag{178}$$

The type of interpolant one should use depends on the characteristics of the data being fit, the required smoothness of the curve, speed considerations, postfit analysis requirements, and so on. Computer routines are readily available to perform these interpolations.

C Properties of the Legendre Polynomials

C.1 Legendre Polynomials

The Legendre polynomials, sometimes called Legendre functions of the first kind, Legendre coefficients, or zonal harmonics, are solutions of the second order differential equation known as the Legendre differential equation:

$$\frac{\mathrm{d}}{\mathrm{d}x}\left[(1-x^2)\frac{\mathrm{d}y}{\mathrm{d}x}\right]+n(n+1)y=0 \tag{179}$$

If n is an integer, the functions are polynomials. The Legendre polynomials, named after Adrien-Marie Legendre, $P_{\mathrm{n}}(x)$, $n=1,2,\ldots$, with $x\in[-1,1]$ are plotted in Figure (69) up to n =5.

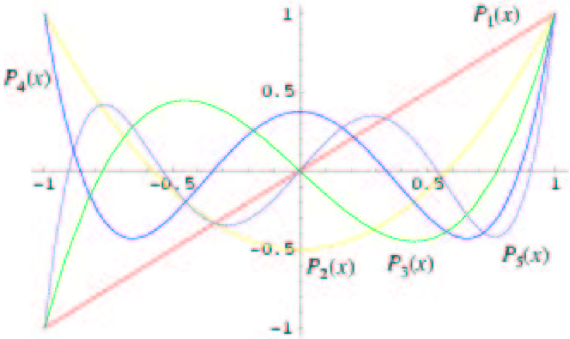

Figure 69: Legendre polynomials up to n =5.

The Legendre ordinary differential equation is frequently encountered in physics and other technical fields. In particular, it occurs when solving Laplace's equation (and related partial differential equations) in spherical coordinates. It may be solved using the standard power series method, in which case the solution is finite (i.e. the series converges) provided $|x|<1$ is satisfied. Furthermore, it is finite at $x=\pm1$ provided n is a non-negative integer, i.e. $n=0,1,2,\ldots$. In this case, the solutions form a polynomial sequence of orthogonal polynomials which constitute the Legendre polynomials.

Each Legendre polynomial $P_{\mathrm{n}}(x)$ is an n^{th}-degree polynomial, that may be expressed using Rodrigues' formula as

$$P_{\mathrm{n}}(x)=(2^{\mathrm{n}}n!)^{-1}\frac{\mathrm{d}^{\mathrm{n}}}{\mathrm{d}x^{\mathrm{n}}}\left[(x^2-1)^{\mathrm{n}}\right] \tag{180}$$

which yields the following generating formula

$$P_{\mathrm{n}}(x)=\frac{1}{2^{\mathrm{n}}}\sum_{\mathrm{k}=0}^{\lfloor \mathrm{n}/2\rfloor}\frac{(-1)^{\mathrm{k}}(2n-2k)!}{k!(n-k)!(n-2k)!}x^{\mathrm{n}-2\mathrm{k}} \tag{181}$$

with $\lfloor n/2\rfloor$ the floor function, i.e. the largest integer resulting from the division.

An important property of the Legendre polynomials is that they are orthogonal with respect to the L^2 inner product on the interval $-1 \leq x \leq 1$, i.e. they satisfy

$$\int_{-1}^{1} P_{\mathrm{n}}(x) P_{\mathrm{m}}(x) \mathrm{d}x = \frac{2}{2n+1} \delta_{\mathrm{mn}} \tag{182}$$

where δ_{mn} denotes the Kronecker delta, equal to 1 if $m = n$ and to 0 otherwise. This property makes it possible to derive the Legendre polynomials by carrying out the Gram-Schmidt orthonormalization process on the polynomials $\{1, x, x2, \ldots\}$ with respect to this inner product, and with unitary weighting coefficients.

Thus, the generating sequence:

$$\begin{aligned}
P_0(x) &= 1 \\
P_1(x) &= \left[x - \frac{\int_{-1}^{1} x \mathrm{d}x}{\int_{-1}^{1} \mathrm{d}x}\right] \cdot 1 = x \\
P_2(x) &= x\left[x - \frac{\int_{-1}^{1} x^3 \mathrm{d}x}{\int_{-1}^{1} x^2 \mathrm{d}x}\right] - \left[\frac{\int_{-1}^{1} x^2 \mathrm{d}x}{\int_{-1}^{1} \mathrm{d}x}\right] \cdot 1 = x^2 - \frac{1}{3} \\
P_3(x) &= \left[x - \frac{\int_{-1}^{1} x \left(x^2 - \frac{1}{3}\right)^2 \mathrm{d}x}{\int_{-1}^{1} \left(x^2 - \frac{1}{3}\right)^2 \mathrm{d}x}\right] \left(x^2 - \frac{1}{3}\right) - \left[\frac{\int_{-1}^{1} \left(x^2 - \frac{1}{3}\right)^2 \mathrm{d}x}{\int_{-1}^{1} x^2 \mathrm{d}x}\right] x = x^3 - \frac{3}{5} x \\
&\ldots
\end{aligned} \tag{183}$$

The polynomials are normalized so that $P_{\mathrm{n}}(1) = 1$.

The first few Legendre polynomials are:

n	$P_{\mathrm{n}}(x)$
0	1
1	x
2	$(1/2)(3x^2 - 1)$
3	$(1/2)(5x^3 - 3x)$
4	$(1/8)(35x^4 - 30x^2 + 3)$
5	$(1/8)(63x^5 - 70x^3 + 15x)$
6	$(1/16)(231x^6 - 315x^4 + 105x^2 - 5)$

A closed formula for these polynomials can be given by Sloane. Some useful properties of these polynomials are given further.

In general

$$P_{\mathrm{n}}(-x) = \begin{cases} P_{\mathrm{n}}(x) & n \quad \text{even,} \\ -P_{\mathrm{n}}(x) & n \quad \text{odd.} \end{cases} \tag{184}$$

The polynomials satisfy the following recurrence relations:

$$x P_{\mathrm{n}}(x) = \frac{1}{2n+1} \left[(n+1) P_{\mathrm{n+1}}(x) + n P_{\mathrm{n-1}}(x)\right] \tag{185}$$

$$\left(x^2-1\right)\frac{\mathrm{d}}{\mathrm{d}x}P_{\mathrm{n}}(x)=n\left[xP_{\mathrm{n}}(x)-P_{\mathrm{n-1}}(x)\right] \tag{186}$$

and the differential equation:

$$(1-x^2)\frac{\mathrm{d}^2}{\mathrm{d}x^2}P_{\mathrm{n}}(x)-2x\frac{\mathrm{d}}{\mathrm{d}x}P_{\mathrm{n}}(x)+n(n+1)P_{\mathrm{n}}(x)=0. \tag{187}$$

Finally, some integrals of the polynomials in the interval $[-1,1]$ are:

$$\int_{\mathrm{x}}^{1}P_{\mathrm{n}}(x)\mathrm{d}x=\frac{(1-x^2)}{n(n+1)}\frac{\mathrm{d}P_{\mathrm{n}}(x)}{\mathrm{d}x} \tag{188}$$

for $n\neq 0$, which as a special cased for $x=0$, gives

$$\begin{aligned}\int_{0}^{1}P_{\mathrm{n}}(x)\mathrm{d}x &= \frac{P_{\mathrm{n-1}}(0)-P_{\mathrm{n+1}}(0)}{2n+1} \\ &= \begin{cases} 1 & \mathrm{m}=0 \\ 0 & \mathrm{m\ even} \\ (-1)^{(n-1)/2}\frac{n!!}{n(n+1)(n-1)!!} & \mathrm{m\ odd}\end{cases}\end{aligned} \tag{189}$$

And the integral of the product of two polynomials

$$\int_{\mathrm{x}}^{1}P_{\mathrm{m}}(x)P_{\mathrm{n}}(x)\mathrm{d}x=\frac{(1-x^2)\left[P_{\mathrm{n}}(x)P'_{\mathrm{m}}(x)-P_{\mathrm{m}}(x)P'_{\mathrm{n}}(x)\right]}{m(m+1)-n(n+1)} \tag{190}$$

for $m\neq 0$, which for $x=0$ is

$$\int_{0}^{1}P_{\mathrm{m}}(x)P_{\mathrm{n}}(x)dx=\begin{cases}\frac{1}{\mathrm{2n+1}} & \mathrm{m}=\mathrm{n} \\ 0 & \mathrm{m}\neq\mathrm{n} \\ f_{\mathrm{m,n}} & \mathrm{m\ even,}\quad \mathrm{n\ odd} \\ f_{\mathrm{n,m}} & \mathrm{n\ even,}\quad \mathrm{m\ odd}\end{cases}$$

with

$$f_{\mathrm{m,n}}=\frac{(-1)^{(\mathrm{m+n+1})/2}m!n!}{2^{\mathrm{m+n-1}}(m-n)(m+n+1)[(\frac{1}{2}m)!]^2\left\{[\frac{1}{2}(n-1)]!\right\}^2} \tag{191}$$

C.2 Associated Legendre Polynomials

The associated Legendre polynomials $P_{\mathrm{n}}^{\mathrm{m}}(x)$ and $P_{\mathrm{n}}^{-\mathrm{m}}(x)$ are solutions of the associated Legendre differential equation, where ℓ is a positive integer and $m\neq 0,\ \ldots,\ \ell$. For positive m, they can be given in terms of the unassociated polynomials by

$$P_{\mathrm{n}}^{\mathrm{m}}(x)=(-1)^{\mathrm{m}}(1-x^2)^{\mathrm{m}/2}\frac{\mathrm{d}^{\mathrm{m}}}{\mathrm{d}x^{\mathrm{m}}}P_{\mathrm{n}}(x)=\frac{(-1)^{\mathrm{m}}}{2^{\mathrm{n}}n!}(1-x^2)^{\mathrm{m}/2}\frac{\mathrm{d}^{\mathrm{m}}}{\mathrm{d}x^{\mathrm{m}}}(x^2-1)^{\mathrm{n}} \tag{192}$$

where $P_{\mathrm{n}}(x)$ are the unassociated Legendre polynomials. The associated Legendre polynomials for negative values of m are then defined by

$$P_{\mathrm{n}}^{-\mathrm{m}}(x)=(-1)^{\mathrm{m}}\frac{(n-m)!}{(n+m)!}P_{\mathrm{n}}^{\mathrm{m}}(x) \tag{193}$$

Associated polynomials are sometimes called Ferrers' functions. If $m = 0$, they reduce to the unassociated polynomials. The associated Legendre functions are part of the spherical harmonics, which are the solution of Laplace's equation in spherical coordinates. They are orthogonal over $[-1, 1]$ with the weighting function 1.

$$\int_{-1}^{1} P_{\mathrm{n}}^{\mathrm{m}}(x) P_{\mathrm{n}'}^{\mathrm{m}}(x) \mathrm{d}x = \frac{2}{2n+1} \frac{(n+m)!}{(n-m)!} \delta_{\mathrm{nn}'} \tag{194}$$

and orthogonal over $[-1, 1]$ with respect to m with the weighting function $(1 - x^2)^{-1}$

$$\int_{-1}^{1} P_{\mathrm{n}}^{\mathrm{m}}(x) P_{\mathrm{n}'}^{\mathrm{m}}(x) \frac{\mathrm{d}x}{1-x^2} = \frac{(n+m)!}{m(n-m)!} \delta_{\mathrm{nn}'} \tag{195}$$

The associated Legendre polynomials also obey the following recurrence relations

$$(n-m) P_{\mathrm{n}}^{\mathrm{m}}(x) = x(2n-1) P_{\mathrm{n-1}}^{\mathrm{m}}(x) - (n+m-1) P_{\mathrm{n-2}}^{\mathrm{m}}(x) \tag{196}$$

Letting $x = \cos\theta$ commonly denoted μ in this context,

$$\frac{\mathrm{d}P_{\mathrm{n}}^{\mathrm{m}}(\mu)}{\mathrm{d}\theta} = \frac{n\mu P_{\mathrm{n}}^{\mathrm{m}}(\mu) - (n+m) P_{\mathrm{n-1}}^{\mathrm{m}}(\mu)}{\sqrt{1-\mu^2}} \tag{197}$$

$$(2n+1)\mu P_{\mathrm{n}}^{\mathrm{m}}(\mu) = (n+m) P_{\mathrm{n-1}}^{\mathrm{m}}(\mu) + (n-m+1) P_{\mathrm{n+1}}^{\mathrm{m}}(\mu) \tag{198}$$

Additional useful identities are:

$$P_{\mathrm{n}}^{\mathrm{n}}(x) = (-1)^{\mathrm{n}}(2n-1)!!(1-x^2)^{\mathrm{n}/2} \tag{199}$$

$$P_{\mathrm{n+1}}^{\mathrm{n}}(x) = x(2n-1) P_{\mathrm{n}}^{\mathrm{n}}(x) \tag{200}$$

References:

[1] Text from Wikipedia On-line Encyclopedia, from Eric W. Weisstein.

[2] "Legendre Polynomial", from MathWorld-A Wolfram Web Resource. http://mathworld.wolfram.com/LegendrePolynomial.html

[3] E.E.Lewis, and W.F. Miller, "Computational Methods of Neutron Transport", ANS Publications, 1993.

[4] Sloane, N. J. A. Sequences A001790/M2508, A002596/M3768, A008316, A008317, A046161, A060818, A078297, and A078298 in "The On-Line Encyclopedia of Integer Sequences".

D Additional Information on the PENELAST Code

Subroutine `EELdR` first recreates the angular and energy grid for which the DCS tables are included in '<material>.mat'. It then reads the values of the DCSs and performs consistency checks for each energy interval by integrating the DCSs with respect to angle and comparing this value with the total cross section for the given energy, which is also included as the first line before each DCS data block. If the comparison is not successful, the data have become corrupted and the program will issue a warning and stop.

If the data have been correctly read, `EELdR` initializes the algorithm for the simulation of e^- and e^+ elastic collisions. This procedure mainly initializes the variables in the common blocks:

`CEELDB` :	`XSE(MAXMAT,NEGP,NP)`	new grid of `NEGP` angular deflection points
	`PSE(MAXMAT,NEGP,NP)`	cumulative probability function for `XSE`
	`ASE(MAXMAT,NEGP,NP)`	
	`BSE(MAXMAT,NEGP,NP)`	

and

`CPELDB` :	`XSP(MAXMAT,NEGP,NP)`	new grid of `NEGP` angular deflection points
	`PSP(MAXMAT,NEGP,NP)`	cumulative probability function for `XSE`
	`ASP(MAXMAT,NEGP,NP)`	
	`BSP(MAXMAT,NEGP,NP)`	

which are the internal databases containing the DCS information for the elastic scattering of e^+ and e^- in the form of cumulative probability distributions for the deflection angle after a elastic collision, suitable for the sampling procedure employed, for instance, during the calculation of hard collisions by subroutines EELd and PELd, also part of the PENELAST implementation.

An additional common block, `COMMON/CICRUE/EELMAX(MAXMAT),PELMAX(MAXMAT)`, containing energy cut-offs for e^- and e^+, respectively, for all materials in the simulation, completes the databases.

The calculation of the variables in `CEELDB` is achieved by the call to two of the new subroutines added in PENELAST, namely `DCSEL0` and `QNRD0`, in the following order:

```
CALL DCSEL0(ET(KE),-1)
CALL QRND0(DCSEL,0.0D0,1.0D0,NP,ERRM,0)
```

where the vector `ET(KE)` conatains a new energy grid created in the original PENELOPE subroutine `EGRID(EMIN,EMAX)` for the interval `EMIN` and `EMAX`. `ET` grid, which is logarithmically spaced in [`EMIN`,`EMAX`] is the basic energy grid in which the transport functions are tabulated. `EGRID`'s generating algorithm creates a grid with a density suitable for accurate linear log-log interpolations. The energy range covered is from 100 eV to 100 MeV, with 200 points (variable `NEGP`). `EELdR` will then generate all the main variables (such as `XSE`, `PSE`), on this grid, by applying the procedures in a loop spanning from `KE`=1 to `NEGP`.

Subroutine `DCSEL0(E,IELEC)` computes a table of DCSs for the energy E and the particle `IELEC` (-1: e^-, 1: e^+) by log-log cubic spline interpolation of the DCS tables prepared by another PENELAST specific subroutine `ELINIT`. The new, interpolated DCS table for E is then stored in the variables `DCS` and `DCSL`, which are used by other subroutines through the common block:

```
CDCSEP: ET(NE),ETL(NE),TH(NA),THR(NA),XMU(NA),XMUL(NA),
ECS(NE),ETCS1(NE),ETCS2(NE),EDCS(NE,NA),
PCS(NE),PTCS1(NE),PTCS2(NE),PDCS(NE,NA),
DCSI(NA),DCSIL(NA),CSI,TCS1I,TCS2I
```

which contains the DCS information from the ELSEP database for e^- and e^+ stored in the matrices `EDCS(NE,NA)` and `PDCS(NE,NA)`, respectively.

In addition, `DCSEL0` also calculates the total energy dependent cross section `CSI`, and the transport cross sections `TCS1I` and `TCS2I`, by log-log spline interpolation for the energy E of the information contained in `ECS(NE)`, `ETCS1(NE)`, `ETCS2(NE)` (or `PCS(NE)`, `PTCS1(NE)`, `PTCS2(NE)` for e^+). This information is then used by the PENELAST specific function `DCSEL(RMU)`, which gives the value of the DCS for a deflection angle θ (`RMU` $= (1-\cos(\theta))/2$) based on the energy interpolated DCS table DCSI(NA) in the shared common block `CDCSEP`.

Thus, after the call to `DCSEL0(ET(KE),-1)` by `EELdR`, PENELAST is ready to compute the variables in the common block `CEELDB` (`CPELDB` for e^+), by calling `QRND0` for all possible deflection angles (`RMU` from 0.0D0 to 1.0D0). This subroutine calculates the cumulative probability distribution for a given PDF included in the call and declared as external in the subroutine. In the case of subroutine `EELdR`'s call, this PDF is the DCS table calculated for energy `ET(KE)` by subroutine `DCSEL0` and represented by function `DCSEL` (see call to `QRND0` above). The cumulative probability distribution is computed in a new non-uniform angular grid that spans the interval [0.0,1.0] (variable `RMU`). The grid points are selected by `QRND0` such that the interpolation error is minimized when the inverse cumulative probability function `X(R)` (i.e. given a probability value R, compute X in the interval X_{i}, $X_{\mathrm{i+1}}$) is interpolated by a rational function:

```
X(R)=X(I)+((1+AI+BI)*R/(1+AI*R+BI*R**2))*(X(I+1)-X(I))            (201)
```

in the interval [`X(I)`,`X(I+1)`]. The grid `XMIN=X(1)` ... `X(N)=XMAX` must be strictly increasing. The interpolation parameters AI and BI are specific for each interval and minimize the interpolation error in each interval.

The output information is given in the common block:

```
CQRND : X(NM),PAC(NM),A(NM),B(NM),F(NM),IA(NM),NP
```

where `X(NM)` is the new angular grid spanning over `NP` points (`NP` $\leq$ `NM`); `PAC(NM)` is the cumulative probability distribution, obtained from the PDF represented by `DCSEL`, which is based on the DCS table for energy `ET(KE)`; and `A(NM)` and `B(NM)` are the interpolation parameters for each of the grid intervals. The vectors `F(NM)` and `IA(NM)` are parameters needed for the selection of a given X interval by Walker's aliasing method of sampling when the distribution is sampled during the MC simulations. Increasing the number of points in the angular grid can reduce the normalized absolute interpolation error, `ERRM`. For `ERRM` <1.0E-5, the influence of the rational interpolation in the sampling algorithms that makes use of the approximation of X and `PAC` is negligible.

This information is passed to the subroutines that make use of it, e.g. `EELdR`, through the same common block, but with a new name for the variables:

```
CQRND : XTI(NM),PACI(NM),AI(NM),BI(NM),FI(NM),IA(NM),NPI
```

These variables are then transferred to the variables that form the elastic scattering database common block `CEELDB` (`CPELDB` for e^+) and are ready to be used by the rest of the simulation subroutines of PENELAST:

```
XSE(M,KE,I)=XTI(I)
PSE(M,KE,I)=PACI(I)
ASE(M,KE,I)=AI(I)
BSE(M,KE,I)=BI(I)
```

for material M, and energy `KE` with `I` $= 1 \ldots$ `NPI`.

In addition to `XSE`, `PSE`, `ASE` and `BSE`, the moments of the PDF represented by the DCS table for energy `ET(KE)` are also obtained in `EELdR`, by making use of the cumulative probability function represented by the table pair (`XTI`,`PACI`). For this, subroutine `QRNDMS` is called,

`CALL QRNDMS(0.0D0,1.0D0,XM0A,XM1,XM2),` (202)

thus spanning all deflection space [0.0,1.0]. The return values are the zero (`XM0A`), first (`XM1`), and second (`XM2`) moments. `QRNDMS` makes use of the common block `CQRND`, and of the PENELAST function `QRNDM(X)`, which provides a rational approximation of the kind described in Eq. (201) of the cumulative probability function `PACI` for a given value X of `XTI` located in the interval [`XTI(I)`,`XTI(I+1)`]:

```
QRNDM=(PACI(I+1)-PACI(I))*(1.0D0+(AI(I)+BI(I)*ETA)*ETA) * *2
1 /((1.0D0-B(I)*ETA*ETA)*CI*(XTI(I+1)-XTI(I)))
```

These moments are stored in the variables `XE0(KE)`, `XE1(KE)`, and `XE2(KE)`:

```
ECS0=CSI
ECS1=CSI*XM1/XM0A
ECS2=CSI*XM2/XM0A
XE0(KE)=ECS0
XE1(KE)=2.0D0*ECS1
XE2(KE)=6.0D0*(ECS1-ECS2)
```

which are included in the common block `CEEL00` containing the total and transport cross sections in the energy grid defined in `ELINIT`:

```
CEEL00 : EIT(NEGP),XE0(NEGP),XE1(NEGP),XE2(NEGP),XP0(NEGP),
         XP1(NEGP),XP2(NEGP),T1E0(NEGP),T2E0(NEGP),T1P0(NEGP),T2P0(NEGP),
         EITL(NEGP),FL(NEGP),A(NEGP),B(NEGP),C(NEGP),D(NEGP)
```

These variables are then used to compute the mean free paths and the cut-off angle for soft elastic collisions, `RMUC`, by using the rational approximation described above, with `XSE` and `RR` depending on the probability distribution `PSE` (`PACI`) calculated by subroutine `QRNDO` based on the ELSEP DCS information:

```
RR=RU-PSE(M,KE,I)
DPRO=PSE(M,KE,I+1)-PSE(M,KE,I)
IF(DPRO.LT.1.0D-10) THEN
    RMUC=XSE(M,KE,I)
ELSE
    CI=(1.0D0+ASE(M,KE,I)+BSE(M,KE,I))*DPRO
    RMUC=XSE(M,KE,I)+(CI*RR/(DPRO**2+(DPRO*ASE(M,KE,I)
        +BSE(M,KE,I)*RR)*RR))*(XSE(M,KE,I+1)-XSE(M,KE,I))
ENDIF
```

With the calculation of `RMUC`, the data necessary for the simulation of soft collisions can now also be prepared by `EELdR` by computing the moments of the DCS based PDF, in a similar manner as that used to calculate `XM0A`, `XM1`, and `XM2`, but extending the integration of `PACI` from 0.0 to `RMUC` only:

```
CALL QRNDMS(0.0D0,RMUC,XM0,XM1,XM2)
```

The new moments are then stored in variables `T1E0` and `T2E2` (for e^-) and `T1P0` and `T2P0` (for e^+):

```
ECS1=CSI*XM1/XM0A
ECS2=CSI*XM2/XM0A
TCS1=2.0D0*ECS1
TCS2=6.0D0*(ECS1-ECS2)
SEHEL(M,KE)=XS0H*VMOL(M)
T1E0(KE)=TCS1
T1E(M,KE)=T1EI(KE)+TCS1*VMOL(M)
T2E0(KE)=TCS2
T2E(M,KE)=T2EI(KE)+TCS2*VMOL(M)
```

which are part of the common block that contains the total and transport cross sections CEEL00 (see above).

Finally, `EELdR` calculates the total mean free paths for soft and hard collisions:

```
FP0=RHO(M)/(XE0(I)*VMOL(M))
FP1=RHO(M)/(XE1(I)*VMOL(M))
HMFP=RHO(M)/SEHEL(M,I)
```

and writes them in the material.dat file.

`EELd` is called by the PENELAST subroutine `KNOCK` (modified from the original version in PENELOPE), used to simulate random hinges and hard interaction events. EELd is called with two parameters CALL `EELd(RNDC,RMU)`, with `RNDC` a cutoff of the uniform random number used for the sampling of hard events, and `RMU` as the output sampled angular deflection. The subroutine receives the ELSEP processed information for electron elastic scattering in the common block `CEELDB` and uses it to generate `RMU` by sampling from the rational inverse cumulative distribution based on the vectors `XSE` (angular deflection) and `PSE` (cumulative probability distribution based on the processed DCS ELSEP information as described above):

```
RR=RU-PSE(M,JE,I)
IF(RR.GT.1.0D-16) THEN
    D=PSE(M,JE,I+1)-PSE(M,JE,I)
    CD=(1.0D0+ASE(M,JE,I)+BSE(M,JE,I))*D
    RMU=XSE(M,JE,I)+(CD*RR/(D*D+(ASE(M,JE,I)*D
        +BSE(M,JE,I)*RR)*RR))*(XSE(M,JE,I+1)-XSE(M,JE,I))
ELSE
    RMU=XSE(M,JE,I)
ENDIF
```

Subroutine `PELd` performs the same procedure for positrons.

E The Code LEWIS

The program LEWIS calculates multiple scattering angular distributions (MSDs) of electrons and positrons in matter after travelling a given path length s, using the Lewis theory.

The input data for LEWIS consists of:

- 272 files which contain the compositions, parameters for inelastic collisions and stopping powers. The files are named 'lewisnnn.mat', with the three digits *nnn* identifying the material.
- Atomic differential cross sections for elastic scattering (DCSs) tabulated in the ELSEP database. These DCSs are interpolated by LEWIS to make them correspond to the energy grid used by the code, by a log-log cubic spline technique.

The effect of inelastic collisions on the MSD can be calculated by the LEWIS code based on three models selected by the user as input options 1, 2 or 3:

1. Correction of the elastic DCS for a given target atom of atomic number Z by multiplying it by the term $1/Z$.
2. Multiplication of the angular DCS for binary collisions with free electrons at rest by the incoherent scattering function.
3. Use of the first Born approximation to obtain the inelastic scattering DCSs. The approximation is based on the generalized oscillator strength (GOS) model of Sternheimer and Liljequist [34], with a single oscillator for each atomic shell and resonance energy. This approach ensures that the adopted value of the mean excitation energy is exactly reproduced.

The structure of LEWIS is based on five main subroutines, namely `LEWIS0`, `LEWIS1`, `ELINIT`, `DCSEL0` and `GSCOEF`. They are contained in the three source files lewis.f, dbread.f and multscat.f. The first file contains the main program and `LEWIS0` and `LEWIS1`. The file dbread.f includes the subroutines needed to read and process the cross section data bases, i.e. `ELINIT` and `DCSEL0`, and associated subroutines and functions. Finally, multscat.f contains the subroutine `GSCOEF` and other additional functions and subprograms to calculate the MSDs based on the information gathered and processed during the input process of LEWIS. The three source files are compiled together to create the executable LEWIS.

LEWIS runs interactively, i.e. the user must enter the input data and options from the keyboard, following the program prompts. This input information includes: the material identity number ID, the type of projectile, the inelastic correction model, and the number $NLEG$ of terms of the Legendre series expansion used to compute the MSDs.

The initialization of the internal databases is carried out by a call from `LEWIS` to `LEWIS0`. This subroutine reads material information from the appropriate 'lewisnnn.mat' files, i.e. material composition, optical oscillator strengths and stopping powers. With this information, `LEWIS0` then generates the necessary tables of transport coefficients and other quantities required for the calculation of the MSDs and stored into so-called dump files (with the extension '.dmp').

To gather the cross section information, `LEWIS0` calls subroutine `ELINIT`, which

- generates the energy grid for 96 energy and 606 angular points,

- reads the ELSEP DCS database in the form of files eeldxZZZ.tab (for e$^-$ and atomic number ZZZ), and peldxZZZ.tab (for e$^+$ and atomic number ZZZ), and

- checks for the consistency of the read DCSs by integrating them over angle, and comparing them to energy dependent DCSs available also in the ELSEP database.

With the cross section data read and processed by `ELINIT`, `LEWIS0` creates the internal databases of inelastic DCSs, in the form of `COMMON/GPLEW0` and `COMMON/GPLEW1`. Finally, `LEWIS0` calls subroutines `DCSEL0` and `GSCOEF` to compute positron and electron DCSs for all the points in the energy grid (stored in the `COMMON/CDCSEL`) and the GS coefficient for the Legendre polynomial expansion of the MSDs (stored in `COMMOM/COEFGS`).

Lastly, the tables of energy-dependent quantities such as the mean and first transport free-paths, the stopping power, the CSDA ranges and the transport coefficients GS, are written to the files ‘lewis0b.dmp’, ‘lewis0b.dmp’ and ‘lewis_table.dat’.

The final piece of information needed by LEWIS is the kinetic energy of the projectile (e$^+$ or e$^-$) and the path length, which are input by the user at the prompt.

After all these calculations have been finalized, and the required cross sections have been processed and used to compute the necessary coefficients for the formulation of the MSD polynomial expansions, `LEWIS` calls `LEWIS1`, which will yields the MSDs for the 96 energy and 606 angular point grid used internally by the code. The MSDs thus calculated are written in a file named ‘lewis_pdf.dat’.

This process can be repeated for a different pair of input particle energy-path lengths. In such a case, the calculation is carried out by direct calls from `LEWIS` to `LEWIS1`, since no re-initialization is required, because the processed cross section data and coefficients are kept in the internal COMMON BLOCK databases. In addition, in order to speed up calculations when LEWIS is applied to the same material and set of input parameters, the transport coefficients are read from the dump files created by `LEWIS0`, ‘lewis0b.dmp’, ‘lewis0b.dmp’ and ‘lewis_table.dat’, without the need for the lengthy initialization procedure carried out by `LEWIS0`. Therefore, the calculation of the MSDs takes only a few seconds.

Figure 70 gives a detailed description of the calls to various subroutines in LEWIS.

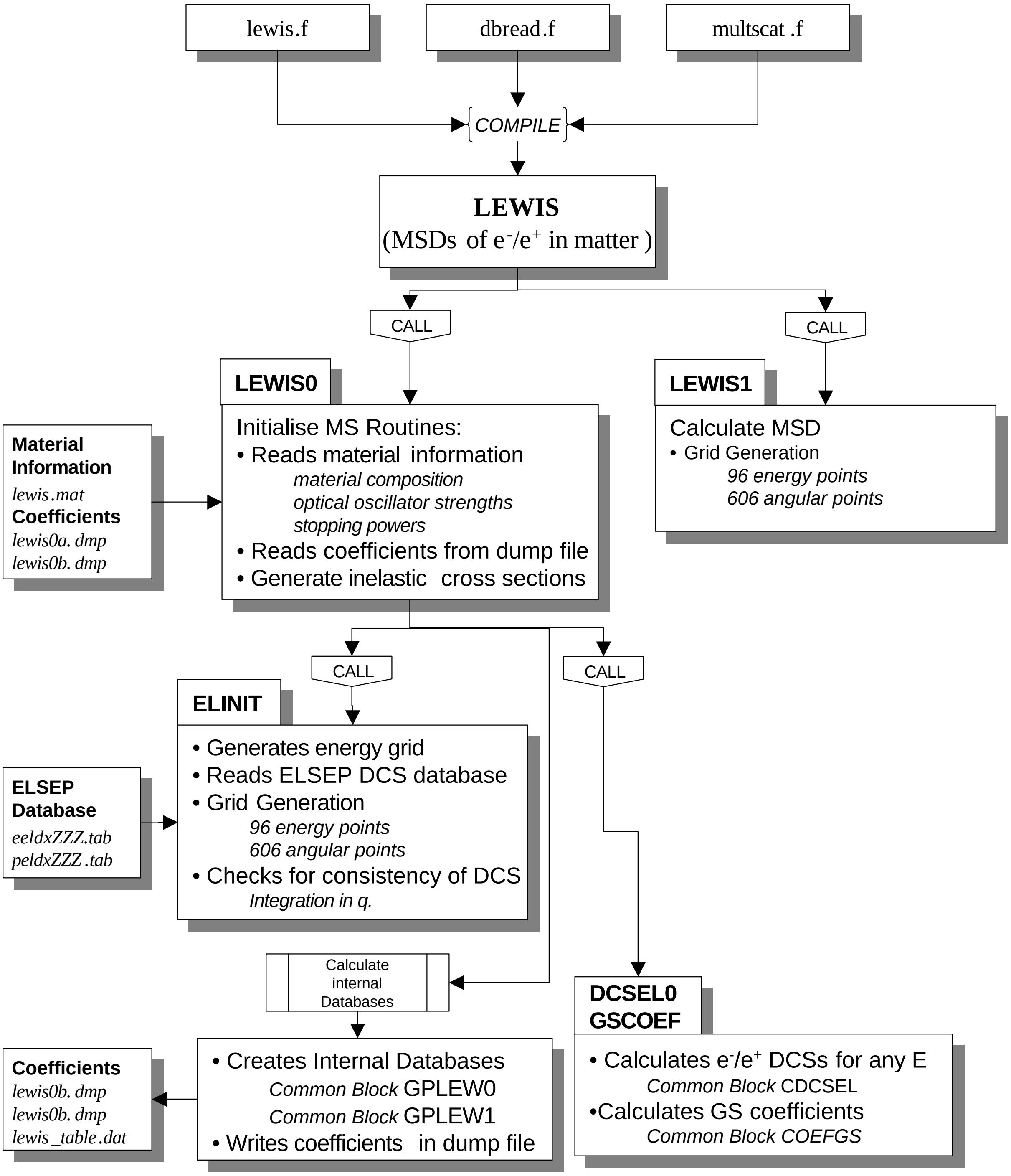

Figure 70: Flowchart diagram of the code LEWIS.

References

[1] Röntgen, W.C., "On a New Kind of Rays", *Sitzgsber. Physik-Med. Ges. Würzburg* **137** (1895); also *Ann. Phys. Chem. N.F.* **64**, 1 (1898).

[2] Becquerel, A.H., "Sur les radiations invisibles émises par phosphorescence", *C. R. Acad. Sci. Paris* **122**, 420 (1896).
Becquerel, A.H., "Sur les radiations invisibles émises par les corps phosphorescents", *C. R. Acad. Sci. Paris* **122**, 501 (1896).
Becquerel, A.H., "Émission des radiations émises par les sels d'uranium", *C. R. Acad. Sci. Paris* **122**, 689 (1896); *ibid.* **122**, 1086 (1896).

[3] Curie, I., Joliot, F., "Émission de proton de grand vitesses par les substances hydrogéné sous l'influence des rayons γ très pénétrants", *C. R. Acad. Sci. Paris* **194**, 273 (1932).

[4] Chadwick, J., "The Existence of a Neutron", *Proc. Roy. Soc. A* **136**, 692 (1932); also *Philos. Mag.* **24**, 594 (1912).

[5] Müller, H.J., "Artificial transmutation of the gene", *Science* **66**, 84 (1927).

[6] Steel, G.G., *Basic Clinical Radiobiology (2nd edition)*, G. Gordon Steel (ed.), Arnold, London (1997).

[7] Bergonié, J., Tribondeau, L., "Actions des rayons X sur le testicle", *Arch. Elect. Med.* **14**, 779 (1906).

[8] Elkin, M.M., Sutton, H., "X-ray damage and recovery in mammalian cells in culture", *Nature* **184**, 1293 (1959).

[9] von Sonntag, C., *The Chemical Basis of Radiation Biology*, Taylor and Francis, London (1987).

[10] Weiland, B., Hüttermann, J., "Free radicals from X-irradiated 'dry' and hydrated lyophilized DNA as studied by electron spin resonance spectroscopy: analysis of spectral components between 77 K and room temperature", *Int. J. Radiat. Biol.* **74**, 341 (1998).

[11] Weiland, B., Hüttermann, J., "Free radicals from lyophilized 'dry' DNA bombarded with heavy-ions as studied by electron spin resonance spectroscopy", *Int. J. Radiat. Biol.* **75**, 1169 (1999).

[12] Weiland, B., Hüttermann, J., "Spin transfer from protein to DNA in X-irradiated 'dry' and hydrated chromatin: an electron spin resonance investigation of spectral components between 77 K and room temperature", *Int. J. Radiat. Biol.* **76**, 1075 (2000).

[13] Nikjoo, H., O'Neill, P., Goodhead, D.T., Terrissol, M., "The influence of track structure on the understanding of relative biological effectiveness for induction of chromosomal exchanges in human lymphocytes", *Int. J. Radiat. Biol.* **71**, 467 (1997).

[14] Ciudad, J., Guirado, D., Sánchez-Reyes, A., Sanjuanbenito, W., Velázquez, S., *Radiobiología Clínica*, Sociedad Espanõla de Física Médica (2003).

[15] Boudaiffa, B., Cloutier, P., Hunting, D., Huels, M.A., Sanche, L., "Resonant Formation of DNA Strand Breaks by Low-Energy (3 to 20 eV) Electrons", *Science* **287**, 1658 (2000).

[16] Inokuti, M., *Physical and Chemical Mechanisms in Molecular Radiation Biology*, W.A. Glass, M.N. Varma (eds.), Plenum Press, New York, p.29 (1991).

[17] Ottolenghi, A., Merzagora, M.,Tallone, L., Durante, M., Paretzke, H.G., Wilson, W.E., "The quality of DNA double-strand breaks: a Monte Carlo simulation of the end-structure of strand breaks produced by protons and alpha particles", *Radiat. Environ. Biophys.* **34** (4), 239 (1995).

[18] Ottolenghi, A., Merzagora, M., *Microdosimetry: an interdisciplinary approach*, P. O'Neill, D.T. Goodhead, H.G. Menzel (eds.), RSC, Thomas Graham House, Cambridge, p.103-110 (1997).

[19] Rossi, H.H., Zaider, M., *Microdosimetry and its Applcations*, Springer-Verlag, Berlin (1996).

[20] Segur, P., Olko, P., Colautti, *Design construction and use of tissue equivalent proportional counters*, T. Schmitz, A. Waker, P. Kliagua, H. Zoetlief (eds.), *Radiat. Prot. Dosim.* (1995).

[21] Grubbe, E.H., "Results and technique in treating epitheliomas with X-rays", *Radiology* **21**, 156 (1933).

[22] Paretzke, H.G., "Radiation track structure theory", in *Kinetics of Non-Homogeneous Processes*, G.R. Freeman (ed.), New York: John Wiley & Sons, p.89-170 (1987).

[23] Swiss Final Report for the EU-Project on "Low Dose Risk Models" in the period 1999-2003.

[24] Boudaiffa, B., Cloutier, P., Hunting, D., Huels, M.A., Sanche, L., "Cross Sections for Low-Energy (10-50 eV) Electron Damage to DNA", *Radiat. Res.* **157**, 227 (2002).

[25] Sanche, L., "Low-Energy Electron Damage to DNA and its Basic Constituents", *Phys. Scripta*, **68** (5), C108 (2003).

[26] Molière, G., "Theorie der Streuung schneller geladener Teilchen II: Mehrfach- und Vielfachstreuung", *Z. f. Naturf.* **3a**, 78 (1948).

[27] Nelson, W.R., Hirayama, H., Rogers, D.W.O., "The EGS4 Code System", Report SLAC-265, Stanford Linear Accelerator Center, Stanford, CA (1985).
Kawrakow, I., Rogers, D.W.O., "The EGSnrc code system: Monte Carlo simulation of electron and photon transport", Report Pirs-701, National research Council of Canada, Ottawa (2001); EGS4 - the Electron Gamma Shower (EGS) Web Page - [http://www.slac.stanford.edu/egs/].

[28] Knespl, D., Reist, H.W., Stepanek, J., *Proceedings of SGSMP/SGBT - Jahrestagung*, 241 (1993).

[29] Goudsmit S., Saunderson, J.L., "Multiple Scattering of Electrons", *Phys. Rev.* **57**, 24 (1940).

[30] Seltzer, S.M., "An overview of ETRAN Monte Carlo methods", in *Monte Carlo Transport of Electrons and Photons*, T.M. Jenkins, W.R. Nelson, A. Rindi, A.E. Nahum, D.W.O. Rogers (eds.), p.153-181, Plenum Press, New York, (1988).

[31] Briesmeister, J.F., *MCNP - A general Monte Carlo N-particle transport code*, Report LA-12625-M Version 4B, Los Alamos National Laboratory, Los Alamos, NM (1997); MCNP - A General Monte Carlo N-Particle Transport Code - [http://laws.lanl.gov/x5/MCNP/index.html].

[32] Fernández-Varea, J.M., Mayol, R., Baró, J., Salvat, F., "On the theory and simulation of multiple elastic scattering of electrons", *NIMB* **73** (4), 447 (1993).

[33] Apostolakis, J., Giani, S., Maire, M., Nieminen, P., Pia, M.G., Urban, L., CERN preprint OPEN-99-034 (1999); GEANT4 Physics Reference Manual on the Web Page - [http://wwwasd.web.cern.ch/wwwasd/geant4/].
Agostinelli, S., *et al*, "GEANT4 - a simulation toolkit", *NIMA* **506** (3), 250 (2003).

[34] Salvat, F., Fernandez-Varea, J.M., Sempau, J., PENELOPE - *A code system for Monte Carlo simulation of Electron and Photon Transport*, *Workshop Proceedings Issy-les-Moulineaux*, France 2003, Nuclear Energy Agency, OECD/NEA Data Bank Report, ISBN 92-64-02145-0 (2003).

[35] Turner, J.E., Magee, J.L., Wright, H.A., Chatterjee, A., Hamm, R.N., Ritchie, R.H., "Physical and chemical development of electron tracks in liquid water", *Radiat. Res.* **96**, 437 (1983).

[36] Hamm, R.N., Turner, J.E., Ritchie, R.H., Wright, H.A., "Calculation of heavy-ion tracks in liquid water", *Radiat. Res.* **8**, S20 (1985).

[37] Turner, J.E., Hamm, R.N., Wright, H.A., Ritchie, R.H., Magee, J.L., Chatterjee, A., Bloch, W.E., "Studies to link the basic radiation physics and chemistry of liquid water", *Radiat. Phys. Chem.* **32**, 503 (1988).

[38] Wilson, W.E., Paretzke, H.G., "Calculations of distributions for energy imparted and ionization by fast protons in nanometer sites", *Radiat. Res.* **87**, 521 (1981).

[39] Wilson, W.E., Metting, N.F., Paretzke, H.G., "Microdosimetric aspects of 0.3- to 20-MeV proton tracks I. Crossers.", *Radiat. Res.* **115**, 389 (1988).

[40] Uehara, S., Nikjoo, H., Goodhead, D.T., "Cross-sections for water vapour for the Monte Carlo electron track structure code from 10 eV to the MeV region", *Phys. Med. Biol.* **38** (12), 1841 (1993).

[41] Terrissol, M., Patau, J.P., Eudaldo, T., "Applications à la microdosimetrie et a la radiobiologie de la simulation du transport des électrons de basse énergie dans l'eau à l'état liquide", in *Sixth symp. on microdosimetry*, J. Booz, H.G. Ebert (eds), Harwood Academic Publishers, London, p.169 (1978).

[42] Friedland, W., Jacob, P., Paretzke, H.G., "Biophysical simulation of DNA fragments from low-LET radiation", *Radiat. Res.* **148**, 486 (1997).

[43] Friedland, W., Jacob, P., Paretzke, H.G., Stork, T., "Monte Carlo simulation of the production of short DNA fragments by low-linear energy transfer radiation using higher-order DNA models", *Radiat. Res.* **150** (2), 170 (1998).

[44] Friedland, W., Jacob, P., Paretzke, H.G., Merzagora, M., Ottolenghi, A., "Simulation of DNA fragment distributions after irradiation with photons", *Radiat. Environ. Biophys.* **38** (1), 39 (1999).

[45] Wilson, W.E., Miller, J.H., Nikjoo, H., "PITS: A code set for positive ion track structure", in *Computational Approaches in Molecular Radiation Biology*, M.N. Varma, A. Chatterjee (eds.), Plenum Press, New York, p.137-150 (1994).

[46] Wilson, W.E., Nikjoo, H., "A Monte Carlo code for positive ion track simulation", *Radiat. Environ. Biophys.* **38**, 97 (1999).

[47] Berger, M.J., "Monte Carlo calculation of the penetration and diffusion of fast charged-particles", in *Methods in Computational Physics*, **1**, B. Alder, S. Fernbach, M. Rotenberg (eds.), Academic Press, New York, p.135-215 (1963).

[48] Inokuti, M., "Basic physical and chemical information needed for development of Monte Carlo codes", *Computational Approaches in Molecular Radiation Biology*, M.N. Varma, A. Chatterjee (eds.), Plenum Press, New York, p.21-31 (1994).

[49] Lewis, H.W., "Multiple Scattering in an Infinite Medium", *Phys. Rev.* **78**, 526 (1950).

[50] Martland, H.S., "Occurrence of malignancy in radioactive persons", *Am. J. Cancer* **15** (4), 2435 (1931).

[51] Court-Brown, W.M., Doll, R., "Expectation of life and mortality from cancer among British radiologists", *Br. Med. J.* **2**, 181 (1958).

[52] Beebe, G.W., Ishida, M., Jablon, S., "Studies of the mortality of A-bomb survivors. I. Plan of study and mortality in the medical subsample (selection 1), 1950-1958", *Radiat. Res.* **16**, 253 (1962).

[53] Hooke, R., *Micrographia: or, Some physiological descriptions of minute bodies made by magnifying glasses (1st edition)*, J. Martyn and J. Allestry (eds.), London (1665).

[54] van Holde, K.E., *Chromatin*, Springer-Verlag New York Inc. (1989).

[55] Thacker, J., "Radiation-induced mutation in mammalian cells at low doses and dose rates", *Advances in Radiation Biology* **16**, 77 (1992).

[56] Natarajan, A.T., A.S. Balajee, A.S., Boei, J.J.W.A., Chatterjee, S., Darroudi, F., Grigorova, M., Noditi, M., Oh, H.J., Slijepcevic, P., Vermeulen, S., "Recent Developments in the Assessment of Chromosomal Damage", *Int. J. Radiat. Biol.* **66** (5), 615 (1994).

[57] Fayard, B., *et al*, "Cell Inactivation and Double-Strand Breaks: The Role of Core Ionizations, as Probed by Ultrasoft X Rays", *Radiat. Res.* **157** (2), 128 (2002).

[58] Ward, J.F., "DNA Damage Produced by Ionizing Radiation in Mammalian Cells: Identities, Mechanisms of Formation, and Reparability", *Progress in Nucleic Acids and Molecular Biology* **35**, 95 (1988).

[59] Stewart, R.D., "A Theoretical Investigation of Cell Cycle Effects and Interspecies Radiosensitivies", *Ph.D. Thesis*, Kansas State University (1997);
[http://www.pnl.gov/berc/staff/rds/epub/phd/abstract.html].

[60] Nikjoo, H., O'Neill, P., Terrissol, M., Goodhead, D.T., "Quantitative modelling of DNA damage using Monte Carlo track structure method", *Radiat. Environ. Biophys.* **38** (1), 31 (1999).

[61] Jallepalli, P.V., Langauer, C., "Chromosome segregation and cancer: cutting through the mystery", *Nature Rev. Cancer* **1** (2), 109 (2001).

[62] Duesberg, P., Li, R., Rasnik, D., Rausch, C., Willer, A., Kraemer, A., Yerganian, G., Hehlmann, R., "Aneuploidy Precedes and Segregates with Chemical Carcinogenesis", *Cancer, Genetics and Cytogenetics*, **119** (2), 83 (2000).

[63] Nikjoo, H., O'Neill, P., Goodhead, D.T., Terrissol, M., "Computational modelling of low-energy electron-induced DNA damage by early physical and chemical events", *Int. J. Radiat. Biol.* **71** (5), 467 (1997).

[64] Green, N.J.B., Bolton, C.E., Spencer-Smith, R.D., "The link between physics and chemistry in track modelling", *Radiat. Environ. Biophys.* **38** (4), 221 (1999).

[65] Ottolenghi, A., Ballarini, F., Merzagora, M., "Modelling radiation-induced biological lesions: from initial energy depositions to chromosome aberrations", *Radiat. Environ. Biophys.* **38** (1), 1 (1999).

[66] Michael, B.D., Prise, K.M., "A multiple-radical model for radiation action on DNA and the dependence of OER on LET", *Int. J. Radiat. Biol.* **69**, 351 (1996).

[67] Moiseenko, V.V., Hamm, R.N., Waker, A.J., Prestwich, W.V., "A multiple-radical model for radiation action on DNA and the dependence of OER on LET", *Int. J. Radiat. Biol.* **74** (5), 533 (1998).

[68] Sachs, R.K., Brenner, D.J., Hahnfeldt, P.J., Hlatkys, L.R., "A formalism for analysing large-scale clustering of radiation-induced breaks along chromosomes", *Int. J. Radiat. Biol.* **74** (2), 185 (1998).

[69] Folkard, M., Prise, K.M., Vojnovic, B., Brocklehurst, B., Michael, B.D., "Critical energies for ssb and dsb induction in plasmid DNA by vacuum-UV photons: an arrangement for irradiating dry or hydrated DNA with monochromatic photons", *Int. J. Radiat. Biol.* **76** (6), 763 (2000).

[70] Schöllnberger, H., Mebust, M.R., Crawford-Brown, D.J., Eckl, P.M., Hofmann, W., "Significance of cell-cycle delay, multiple initiation pathways, misrepair and replication errors in a model of radiobiological effects", *Int. J. Radiat. Biol.* **77** (4), 519 (2001).

[71] Michaels, H.B., Hunt, J.W., "A model for radiation damage in cells by direct effect and by indirect effect: a radiation chemistry approach", *Radiat. Res.* **74** (1), 23 (1978).

[72] Chatterjee, A., Holley, W.R., "Energy deposition mechanisms and biochemical aspects of DNA strand breaks by ionizing radiation", *Int. J. Quantum Chem.* **39**, 709 (1991).

[73] Michael, B.D, O'Neill, P.A., "Molecular biology. A sting in the tail of electron tracks", *Science* **287** (5458), 1603 (2000).

[74] Rutherford, E., "The scattering of α and β particles by matter and the structure of the atom", *Philos. Mag.* bf 21, 669 (1911).

[75] Ramsauer, C., "The cross section of the gas molecule compared to slow electrons", *Ann. d. Phys.* **64** (6), 513 (1921); *ibid.* **66** (22), 546 (1922).

[76] Charlton, D.E., Humm, J.L., "A Method of Calculating Initial DNA Strand Breakage Following the Decay of Incorporated ^{125}I", *Int. J. Radiat. Biol.* **53** (3), 353 (1988).

[77] Holley, W.R., Chatterjee, A., Magee, J.L., "Production of DNA strand breaks by direct effects of heavy charged particles", *Radiat. Res.* **121** (2), 161 (1990).

[78] Pomplun, E., Terrisol, M., "Low-energy electrons inside active DNA models: a tool to elucidate the radiation action mechanisms", *Radiat. Environ. Biophys.* **33** (4), 279 (1994).

[79] Nikjoo, H., Laughton, C.A., Terrisol, M., Panyutin, I.G., Goodhead, D., "A method for radioprobing DNA structures using Auger electrons", *Int. J. Radiat. Biol.* **76** (12), 1607 (2000).

[80] Denifl, S., Ptasinska, S., Cingel, M., Matejcik, S., Scheier, P., Märk, T.D., "Electron attachment to the DNA bases thymine and cytosine", *Chem. Phys. Lett.* **377** (1-2), 74 (2003).

[81] Schwarz, G., "Über Desensibilisierung gegen Röntgen und Radiumstrahlen", *Munchener Med. Wochenschr.* **56**, 1217 (1909).

[82] Schwarz, G., "Zur genaueren Kenntnis der Radiosensibilität", *Wiener Klin. Wochenschr.* **11**, 397 (1910).

[83] Gray, L.H., Conger, A.D., Ebert, M., Hornsey, S., Scott, O.C.A., "The concentration of oxygen dissolved in tissues at the time of irradiation as a factor in radiotherapy", *British J. Radiol.* **26**, 638 (1953).

[84] Schwarz, H.A., "Application of spur diffusion model to the radiation chemistry of aqueous solution", *J. Phys. Chem.* **73** (6), 1928 (1969).

[85] Huels, M.A., Hahndorf, I., Illenberger, E., Sanche, L., "Resonant dissociation of DNA bases by subionization electrons", *J. Phys. Chem.* **108** (4), 1309 (1998).

[86] Brocklehurst, B., Higashimura, T., "Triplet formation in ion recombination in spurs. Comment", *J. Phys. Chem.* **78** (3), 309 (1974).

[87] Green, N.J.B., Pimblott, S.M., Brocklehurst, B., "Spin effects on spur kinetics: analytic models for single-species spur", *J. Chem. Soc. Faraday Trans.* **87**, 2427 (1991).

[88] Green, N.J.B., Pimblott, S.M., Brocklehurst, B., "Spin effects on spur kinetics. Re-encounters and the independent pairs approximation", *J. Chem. Soc. Faraday Trans.* **91** (2), 223 (1995).

[89] Bolton, C.E., Green, N.J.B., "Spin effects on spur kinetics: 4. Incorporating a realistic exchange interaction", *J. Phys. Chem.* **100** (21), 8807 (1996).

[90] Pimblott, S.M., Green, N.J.B., Brocklehurst, B., "Spin effects on spur kinetics: independent pair modelling of two-species spur", *J. Chem. Soc. Faraday Trans.* **87** (22), 3601 (1991).

[91] Crowell, R.A., Bartels, D.M., "Multiphoton Ionization of Liquid Water with 3.0-5.0 eV Photons", *J. Phys. Chem.* **100** (45), 17940 (1996).

[92] Goulet, T., Jay-Gerin, J.P., "Thermalization of subexcitation electrons in solid water", *Radiat. Res.* **118** (1), 46 (1989).

[93] Migus, A., Gauduet, Y., Martin, J.L., Antonetti, A., "Excess electrons in liquid water: First evidence of a prehydrated state with femtosecond lifetime", *Phys. Rev. Lett.* **58**, 1559 (1987).

[94] Long, F.H., Lu, H., Eisenthal K.B., "Femtosecond studies of the presolvated electron: An excited state of the solvated electron?", *Phys. Rev. Lett.* **64**, 1469 (1990).

[95] Kimura, Y., Alfano, J.C., Walhout, P.K., Barbara, P.F., "Ultrafast Transient Absorption Spectroscopy of the Solvated Electron in Water", *J. Phys. Chem.* **98** (13), 3450 (1994).

[96] Keszei, E., Murphrey, T.H., Rossky, P.J., "Electron Hydration Dynamics: Simulation Results Compared to Pump and Probe Experiments", *J. Phys. Chem.* **99** (1), 22 (1995).

[97] Prezhdo, O.V., Rossky, P.J., "Solvent Mode Participation in the Nonradiative Relaxation of the Hydrated Electron", *J. Phys. Chem.* **100** (43), 17094 (1996).

[98] Jonah, C.D., Miller, J.R., Matheson, M.S., "The reaction of the precursor of the hydrated electron with electron scavengers", *J. Phys. Chem.* **81** (17), 1618 (1977).

[99] Pimblott, S.M., LaVerne, J.A., "On the Radiation Chemical Kinetics of the Precursor to the Hydrated Electron", *J. Phys. Chem. A* **102** (17), 2967 (1998).

[100] Chatterjee, A., Magee, J.L., "Theoretical Investigation of the Production of Strand Breaks in DNA by Water Radicals", *Rad. Prot. Dosim.* **13** (1), 137 (1985).

[101] Nikjoo, H., O'Neill, P., Terrisol, M., Goodhead, D.T., "Modelling of Radiation-induced DNA Damage: The Early Physical and Chemical Event", *Int. J. Radiat. Biol.* **66** (5), 453 (1994).

[102] Terrisol, M., "Modelling of Radiation Damage by ^{125}I on a Nucleosome", *Int. J. Radiat. Biol.* **66** (5), 447 (1994).

[103] Ballarini, F., Biaggi, M., Merzagora, M., Ottolenghi, A., Dingfelder, M., Friedland, W., Jacob, P., Paretzke, H.G., "Stochastic aspects and uncertainties in the prechemical and chemical stages of electron tracks in liquid water: a quantitative analysis based on Monte Carlo simulations", *Radiat. Environ. Biophys.* **39** (3), 179 (2000).

[104] Humm, J.L., "Dosimetric aspects of radiolabeled antibodies for tumor therapy", *J. Nucl. Med.* **27** (9), 1490 (1986).

[105] Myers, M.J., "Dosimetry for radiolabelled antibodies–macro or micro?", *Int. J. Cancer suppl.* **2**, 71 (1988).

[106] Metropolis, N., Ulam, S., "The Monte Carlo Method", *J. Am. Stat. Assoc.* **44** (247), 335 (1949).

[107] Jablonski, A., Powell, C.J., "Elastic-electron-scattering effects on angular distributions in x-ray-photoelectron spectroscopy", *Phys. Rev. B* **50** (7), 4739 (1994).

[108] Jablonski A., Jiricek, P., "Dependence of experimentally determined inelastic mean free paths of electrons on the measurement geometry", *Surf. Sci.* **412-413**, 42 (1998).

[109] Dubus, A., Jablonski, A., Tougaard, S., "Evaluation of theoretical models for elastic electron backscattering from surfaces", *Progr. Surf. Sci.* **63** (6), 135 (2000).

[110] Naya, J.E., von Ballmoos, P., Smither, R.K., Faiz, M., Fernandez, P.B., Graber, T., Albernhe, F., Vedrenne, G., "Experimental results obtained with the positron annihilation radiation telescope of the Toulouse-Argonne collaboration", *NIMA* **373** (1), 159 (1996).

[111] Rosenberg, N., Jiang, C.Z., Morin, P., "Monte Carlo simulations of coaxial backscattered electrons in SEM", *Ultramicroscopy* **76** (3), 97 (1999).

[112] Orosz, G.T., Gergely, G., Menyhard, M., Tóth, J., Varga, D., Lesiak, B., Jablonski, A., "Hydrogen and surface excitation in electron spectra of polyethylene", *Surf. Sci.* **566-568** (1), 544 (2004).

[113] Tilinin, I.S., Jablonski, A., Werner, W.S.M., "Quantitative surface analysis by Auger and X-ray photoelectron spectroscopy", *Progr. Surf. Sci.* **52** (4), 193 (1996).

[114] Bräuer-Krisch, E., Bravin, A., Lerch, M., Rosenfeld, A., Stepanek, J., Di Michiel, M., Laissue, J.A., "MOSFET dosimetry for microbeam radiation therapy at the European Synchrotron Radiation Facility", *Med. Phys.* **30** (4), 583 (2003).

[115] Andreo, P., "Monte Carlo techniques in medical radiation physics", *Phys. Med. Biol.* **36** (7), 861 (1991).

[116] Stepanek, J., "Electron and positron atomic elastic scattering cross sections", *Radiat. Phys. Chem.* **66** (2), 99 (2003).

[117] Negreanu, C., Stepanek, J., Joneja, O., Chawla, R., "Validation of new electron and positron data libraries", *NIMB* **213**, 55 (2004).

[118] Negreanu, C., Stepanek, J., Joneja, O., Chawla, R., "Generation and validation of low-energy electron and positron excitation cross section data", *J. Phys. B* (to be submitted for publication) (2005).

[119] Salvat, F., "Optical-model potential for electron and positron elastic scattering by atoms", *Phys. Rev. A* **68**, 012708 (2003).

[120] Salvat, F., Jablonski, A., Powell, C.J., "ELSEPA Dirac partial-wave calculation of elastic scattering of electrons and positrons by atoms, positive ions and molecules", Comput. Phys. Commun. **165** (2), 157 (2005).

[121] Kellerer, A., "The dosimetry of ionizing radiation", K.R. Kase, B.E. Bjängard, F.H. Attix (eds), Academic Press Inc., Orlando, FL, p. 78 (1985).

[122] Terrisol, M., Beaudré, A., "Simulation of Space and Time Evolution of Radiolytic Species Induced by Electrons in Water", *Radiat. Prot. Dos.* **31** (1-4), 175 (1990).

[123] Stepanek, J., "Advanced Method to Determine the Radiation Spectra due to Single Atomic-subshell Ionization by a Particle or due to Decay of Radionuclide", Annual report of SGSMP/SGBT, p. 223 (1993).

[124] IAEA "Atomic and molecular data for radiotherapy and radiation research", IAEA-TECDOC-799, International Atomic Energy Agency, Vienna (1995).

[125] Stepanek, J., "A program to determine the radiation spectra due to a single atomic-subshell ionisation by a particle or due to deexcitation or decay of radionuclides", *Comput. Phys. Communicat.* **106** (3), 237 (1997).

[126] Hayashi, H., Watanabe, N., Udagawa, Y., Kao, C.-C., "The complete optical spectrum of liquid water measured by inelastic x-ray scattering", *Proc. Natl. Acad. Sci.* **97**, 2755 (2000).

[127] Stepanek, J., "Methods to determine the fluorescence and Auger spectra due to decay of radionuclides or due to a single atomic-subshell ionization and comparisons with experiments", *Med. Phys.* **27** (7), 1544 (2000).

[128] Uehara, S., Nikjoo, H., "Monte Carlo Track Structure Code for Low-Energy Alpha-Particles in Water", *J. Phys. Chem. B* **106** (42), 11051 (2002).

[129] Michaud, M., Wen, A., Sanche, L., "Cross Sections for Low-Energy (1100 eV) Electron Elastic and Inelastic Scattering in Amorphous Ice", *Radiat. Res.* **159** (1), 3 (2003).

[130] Emfietzoglou, D., Nikjoo, H., "The Effect of Model Approximations on Single-Collision Distributions of Low-Energy Electrons in Liquid Water", *Radiat. Res.* **163** (1), 98 (2005).

[131] Friedland, W., Dingfelder, M., Jacob, P., Paretzke, H.G., "Calculated DNA double-strand break and fragmentation yields after irradiation with He ions", *Radiat. Phys. Chem.* , **72** (2-3), 279 (2005).

[132] Bernhardt, Ph., Friedland, W., Jacob, P., Paretzke, H.G., "Modeling of ultrasoft X-ray induced DNA damage using structured higher order DNA targets", *Int. J. Mass Spectr.* **223-224**, 579 (2003).

[133] Bernhardt, Ph., Paretzke, H.G., "Calculation of electron impact ionization cross sections of DNA using the DeutschMrk and BinaryEncounterBethe formalisms", *Int. J. Mass Spectr.* **223-224**, 599 (2003).

[134] Nikjoo, H., Uehara, S., Wilson, W.E., Hoshi, M., Goodhead, D.T., "Track structure in radiation biology: theory and applications", *Int. J. Radiat. Biol.* **73** (4), 355 (1998).

[135] Semenenko, V.A., J. E. Turner, J.E., Borak, T.B., "NOREC, a Monte Carlo code for simulating electron tracks in liquid water", *Radiat. Environ. Biophys.* **42** (3), 213 (2003).

[136] Friedland, W., Li, W.B., Jacob, P., Paretzke, H.G., "Simulation of Exon Deletion Mutations Induced by Low-LET Radiation at the HPRT Locus" *Radiat. Res.* **155** (5), 703 (2001).

[137] Friedland, W., Jacob, P., Bernhardt, P., Paretzke, H.G., Dingfelder, M., "Simulation of DNA Damage after Proton Irradiation", *Radiat. Res.* **159** (3), 401 (2003).

[138] Berger, M.J., Wang, R., "Multiple scattering angular deflections and energy-loss straggling", in *Monte Carlo Transport of Electrons and Photons*, T.M. Jenkins, W.R. Nelson, A. Rindi (Eds.), Plenum Press, New York, p.21-56 (1988).

[139] Halbleib, J.A., Kensek, R.P., Mehlhorn, T.A., Valdez, G.D., Seltzer, S.M., Berger, M.J., "ITS version 3.0: the integrated TIGER series of coupled electron/photon Monte Carlo transport codes", *Report SAND91-1634*, Sandia National Laboratories, Albuquerque, NM (1992).

[140] Baró, J., Sempau, J., Fernández-Varea, J.M., Salvat, F., "PENELOPE: An algorithm for Monte Carlo simulation of the penetration and energy loss of electrons and positrons in matter", *NIMB* **100** (1), 31 (1995).

[141] Salvat, F., Fernández-Varea, J.M., Baró, J., Sempau, J., PENELOPE*, An Algorithm and Computer Code for Monte Carlo Simulation of Electron-Photon Showers*, Informes Tecnicos CIEMAT no. 799, Madrid: CIEMAT (1996); also available from the Radiation Safety Information Computational Center, RSICC, as Code Package CCC-682, Oak Ridge National Laboratory, Oak Ridge, TN (1999).

[142] Sempau, J., Acosta, E., Baró, J., Fernández-Varea, J.M., Salvat, F., "An algorithm for Monte Carlo simulation of coupled electron-photon transport", *NIMB* **132**, 377 (1997).

[143] Hartmann Siantar, C.L., Chandler, W.P., Chadwick, M.B., Cox, L.J., Rathkopf, J.A., Resler, D.A., Svatos, M.M., White, R.M., "PEREGRINE^{tm}: The All-Particle Monte Carlo Dose Calculation Code", *Medical Physics* **21** (6), 937 (1994).

[144] Howerton, R.J., Dye, R.E., Perkins, S.T., "Evaluated nuclear data library", LLNL, Livermore, CA, UCRL-50400, Vol.4, Rev.1 (1981).

[145] Cullen, D.E., Hubbell, J.H., Kissel, L., "EPDL97, The evaluated data library, '97 version", LLNL, CA, UCRL-50400, Vol.6 (1997).

[146] Perkins, S.T., Cullen, D.E., Seltzer, S.M., "Tables and Graphs of Electron-Interaction Cross Section from 10 eV to 100 GeV Derived from the LLNL Evaluated Electron Data Library (EEDL), Z=1-100", LLNL, Livermore, California, UCRL-50400, Vol.31 (1991).

[147] Perkins, S.T., Cullen, D.E., Chen, M.H., "Tables and graphs of atomic subshell and relaxation data derived from the LLNL Evaluated Atomic Data Library (EADL), Z=1-100", LLNL, Livermore, CA, UCRL-50400, Vol.30 (1991).

[148] Stewart, R.D., Wilson, W.E., McDonald, J.C., Strom, D.J., "Microdosimetric properties of ionizing electrons in water: a test of the PENELOPE code system", Phys. Med. Biol. **47**, 79 (2002).

[149] Llovet, X., Sorbier, L., Campos, C.S., Acosta, E., Salvat, F., "Monte Carlo simulation of x-ray spectra generated by kilo-electron-volt electrons", *J. Appl. Phys.* **93**, 3844 (2003).

[150] Koch, H.W., Motz, J.W., "Bremsstrahlung Cross Section Formulas and Related Data", *Rev. Mod. Phys.* **31**, 920 (1959).

[151] Tsai, Y-S., "Pair production and bremsstrahlung of charged leptons", *Rev. Mod. Phys.* **46**, 815 (1974).

[152] Pratt, R.H., Feng, I.J., "Atomic Inner-Shell Physics", Bernd Crasemann (ed), Plenum, New York (1985).

[153] Sommerfeld, A., "Diffraction and scattring of electrons", *Ann. d. Physik.* **11**, 257 (1931); "Atombau und Spektrallinien", Vieweg und Sohn, Braunschweig (1939); "Wellenmechanik", Frederick Ungar, New York (1950).

[154] Bethe, H.A., Heitler, W., "On the Stopping of Fast Particles and on the Creation of Positive Electrons", *Proc. Roy. Soc. (London) A* **146**, 83 (1934).

[155] Bethe, H.A., "The influence of screening on the creation", *Proc. Cambridge Phil. Soc.* **30**, 404 (1934).

[156] Heitler, W., "Quantum Theory of Radiation (3rd edition)", Oxford Univ. Press, London (1954).

[157] Bethe, H.A., Maximon, L.C., "Theory of Bremsstrahlung and Pair Production. I. Differential Cross Section", *Phys. Rev.* **93** (4), 768 (1954).

[158] Davies, H., Bethe, H.A., Maximon, L.C., "Theory of Bremsstrahlung and Pair Production. II. Integral Cross Section for Pair Production", *Phys. Rev.* **93** (4), 788 (1954).

[159] Olsen, H., Maximon, L.C., "Photon and Electron Polarization in High-Energy Brems- strahlung and Pair Production with Screening", *Phys. Rev.* **114** (3), 887 (1959).

[160] Furry, W.H., "Approximate Wave Functions for High Energy Electrons in Coulomb Fields", *Phys. Rev.* **46** (5), 391 (1934).

[161] Sommerfeld, A., Maue, A.W., "Approximate adaptation of a solution of the Schrdinger equation to the solution of Dirac's equation", *Ann. d. Physik.* **22**, 629 (1935).

[162] Pratt, R.H., Tseng, H.K., Lee, C.M., Kissel, L., MacCallum, C., Riley, M., "Brems- strahlung energy spectra from electrons of kinetic energy 1 keV - 2000 keV incident on neutral atoms 2 - 92", *At. Data Nucl. Data Tables* **20** (2), 175 (1977); errata in **26** (5), 477 (1981).

[163] Tseng, H.K., Pratt, R.H., "Exact Screened Calculations of Atomic-Field Brems- strahlung", *Phys. Rev. A* **3** (1), 100 (1971).

[164] Kissel, L., Quarles, C.A., Pratt, R.H., "Shape Functions for Atomic-Field Bremsstrahlung from Electrons of Kinetic Energy 1 - 500 keV on Selected Neutral atoms 1 - 92", *At. Data Nucl. Data Tables* **28**, 381 (1983).

[165] Salvat, F., Fernández-Varea, J.M., "Semiempirical cross sections for the simulation of the energy loss of electrons and positrons in matter", *NIMB* **63** (3), 255 (1992).

[166] Borie, E., Maximon, L.C., Olsen, H., "Molecular Coherence Effects in Radiation Processes: Bremsstrahlung", *Phys. Rev. A* **2** (4), 1443 (1970).

[167] Walker, R.L., Berman, B.L., Bloom, S.D., "Coherent bremsstrahlung produced by relativistic positrons and electrons on a single crystal of silicon", *Phys. Rev. A* **11** (3), 736 (1975).

[168] Ohtsuki, Y.H., Yamamura, Y., Yoshimatsu, M., "Axial-channeling radiation of MeV electrons in high-Z materials", *Phys. Rev. B* **28** (7), 3718 (1983).

[169] Seltzer, S.M., Berger, M.J., "Bremsstrahlung spectra from electron interactions with screened atomic nuclei and orbital electrons", *NIMB* **12** (1), 95 (1985).

[170] Haug, E., (unpublished) cf. *Z. Naturforsch.* **30a**, 1099 (1975).

[171] Wheeler, J.A., Lamb, W.E., "Influence of Atomic Electrons on Radiation and Pair Production", *Phys. Rev.* **55** (9), 858 (1939); errata in *Phys. Rev.* **101** (6), 1836 (1956).

[172] Kirkpatrick, P., Wiedmann, L., "Theoretical Continuous X-Ray Energy and Polarization", *Phys. Rev.* **67** (12-12), 321 (1945).

[173] Statham, P.J., "The generation, absorption and anisotropy of thick-target bremsstrahlung and the implications for quantitative energy dispervive analysis", *X-Ray Spectrom.* **5**, 154 (1976).

[174] ICRU 37 "Stopping Powers for Electrons and Positrons", ICRU, Bethesda, MD (1984).

[175] Wentzel, G., "Zwei Bemerkungen über die Zerstreuung korpuskularer Strahlen als Beugungserscheinung", *Z. Phys.* **40**, 590 (1927).

[176] Seltzer, S.M., Berger, M.J., "Bremsstrahlung energy spectra from electrons with kinetic energy 1 keV - 10 GeV incident on screened nuclei and orbital electrons of neutral atoms with Z=1-100", *At. Data Nucl. Data Tables* **35**, 345 (1986)

[177] Brysk, H., Zerby, C.D., Penny, S.K., "Bremsstrahlung Cross Sections at Moderate Energies", *Phys. Rev.* **180** (1), 104 (1969).

[178] Tseng, H.K., Pratt, R.H., Lee, C.M., "Electron bremsstrahlung angular distributions in the 1-500 keV energy range", *Phys. Rev. A* **19** (1), 187 (1979).

[179] Hodes, I., *Ph.D. Thesis*, University of Chicago *(unpublished)* (1953).

[180] Mack, D., Mitter, H., "Calculation of electron-electron-bremsstrahlung cross sections", *Phys. Lett. A* **44** (1), 71 (1973).

[181] Ford, R.L., Nelson, W.R., "The EGS code system (version 3)", Standford Linear Accelerator Report, SLAC-210 (1978).

[182] Kim, L., Pratt, R.H., Seltzer, S.M., Berger, M.J., "Ratio of positron to electron bremsstrahlung energy loss: An approximate scaling law", *Phys. Rev. A* **33** (5), 3002 (1986).

[183] Yates, A.C., "A program for calculating relativistic elastic electron-atom collision data", *Comput. Phys. Commun.* **2** (4), 175 (1971).

[184] Salvat, F., Mayol, R., "Elastic scattering of electrons and positrons by atoms. Schrödinger and Dirac partial wave analysis", *Comput. Phys. Commun.* **74** (3), 358 (1993).

[185] Fink, M., Yates, A.C., "Theorerical Electron Scattering Amplitudes and Spin Polarizations I.", *At. Data* **1**, 385 (1970).

[186] Fink, M., Ingram, J., "Theorerical Electron Scattering Amplitudes and Spin Polarizations II.", *At. Data* **4**, 129 (1972).

[187] Gregory, D., Fink, M., "Theorerical Electron Scattering Amplitudes and Spin Polarizations III.", *At. Data Nucl. Data Tables* **14**, 39 (1974).

[188] Riley, M.E., MacCallum, C.J., Biggs, F., "Theoretical electron-atom elastic scattering cross sections: Selected elements, 1 keV to 256 keV", *At. Data Nucl. Data Tables* **15** (5), 443 (1975); also At. Data Nucl. Data Tables **28**, 379 (1983).

[189] Reimer, L., Lödding, B., "Calculation and Tabulation of Mott Cross Sections for Large-Angle Electron Scattering", *Scanning* **6**, 128 (1984).

[190] Mayol, R., Salvat, F., “Total and transport cross sections for elastic scattering of electrons by atoms”, *At. Data Nucl. Data Tables* **65** (1), 55 (1997).

[191] Czyzewski, Z., MacCallum, D.O., Romig, A., Joy, D.C., “Calculations of Mott scattering cross section”, *J. Appl. Phys.* **68**, 3066 (1990); [http://pciserver.bio.utk.edu/metrology].

[192] Berger, M.J., Seltzer, S.M., “Database of Cross Sections for the Elastic Scattering of Electrons and Positrons by Atoms”, NISTIR 6573, National Institute of Standards and Technology, Gaithersburg MD (2000); [http://www.nea.fr/abs/html/dlc-0208.html].

[193] Jablonski, A., Salvat, F., Powell, C.J., “NIST Electron Elastic-Scattering Cross Section Database - Version 3.0”, National Institute of Standards and Technology, Gaithersburg MD (2002); [http://www.nist.gov/srd/nist64.htm].

[194] Walker, D.W., “Relativistic Effects in Low Energy Electron Scattering from Atoms”, *Adv. Phys.* **20**, 257 (1971).

[195] Zeitler, E., Olsen, H., “Complex Scattering Amplitudes in Elastic Electron Scattering”, *Phys. Rev.* **162** (5), 1439 (1967).

[196] Benedito, E., Fernández-Varea, J.M., Salvat, F., “Mixed simulation of the multiple elastic scattering of electrons and positrons using partial-wave differential cross sections”, *NIMB* **174** (1), 91 (2001).

[197] Salvat, F.,Mayol, R., “Accurate numerical solution of the Schrödinger and Dirac wave equations for central fields”, *Comput. Phys. Commun.* **62** (1), 65 (1991).

[198] Mott, N.F., Massey, H.S.W., “The Theory of Atomic Collisions”, 3rd Edn., Oxford Univ. Press, London (1965).

[199] Salvat, F., Martínez, J.D., Mayol, R., Parellada, “Analytical Dirac-Hartree-Fock-Slater screening function for atoms (Z=1-92)”, *J. Phys. Rev. A* **36** (2), 467 (1987).

[200] Hahn, B., Ravenhall, D.G., Hofstadter, R., “High-Energy Electron Scattering and the Charge Distributions of Selected Nuclei”, *Phys. Rev.* **101** (3), 1131 (1956).

[201] Helm, R.H., “Inelastic and Elastic Scattering of 187-Mev Electrons from Selected Even-Even Nuclei”, *Phys. Rev.* **104** (5), 1466 (1956).

[202] Molière, G., “Theorie der Streuung schneller geladener Teilchen I: Einzelstreuung am abgeschirmten Coulomb-Feld”, *Z. f. Naturforsch.* **2a**, 133 (1947).

[203] Thomas, L.H., “Tables of Statistical Electron Distributions for Atoms with Degree of Ionization Zero to Four and of the Corresponding Electrostatic Potentials”, *J. Chem. Phys.* **22**, 1758 (1954).

[204] Cox Jr., H.L., Bonham, R.A., “Elastic Electron Scattering Amplitudes for Neutral Atoms Calculated Using the Partial Wave Method at 10, 40, 70 and 100keV for Z=1 to Z=54”, *J. Chem. Phys.* **47**, 2599 (1967).

[205] Desclaux, J.P., “A multiconfiguration relativistic DIRAC-FOCK program”, *Comput. Phys. Commun.* **9** (1), 31 (1975); *ibid.* **13** (1), 71 (1977).

[206] Bransden, B.H., McDowell, M.R.C., Noble, C.J., Scott, T., “Equivalent exchange potentials in electron scattering”, *J. Phys. B* **9** (8), 1301 (1976).

[207] Mittleman, M.H., Watson, K.M., “Effects of the Pauli principle on the scattering of high-energy electrons by atoms”, *Ann. d. Phys.* **10**, 268 (1960).

[208] Riley, M.E., Truhlar, D.G., “Approximations for the exchange potential in electron scattering”, *J. Chem. Phys.* **63** (5), 2182 (1975).

[209] Furness, J.B., McCarthy, I.E., "Semiphenomenological optical model for electron scattering on atoms", *J. Phys. B* **6** (11), 2280 (1973).

[210] Bromberg, J.P., "Absolute Differential Cross Sections of Elastically Scattered Electrons. II. A Polarization Scattering Potential for Hg at 500, 400, and 300 eV", *J. Chem. Phys.* **51** (9), 4117 (1969).

[211] Hohenberg, P., Kohn, W., "Inhomogeneous Electron Gas", *Phys. Rev.* **136** (3B), B864 (1964).

[212] Ochkur, V.I., *Zh. Eksp. Teor. Fiz.* **45**, 734 (1963); also *Sov. Phys. JETP* **18**, 503 (1964).

[213] Dirac, P.A.M., "The Quantum Theory of the Electron", *Proc. R. Soc. A* **117**, 610 (1928); *ibid.* **118**, 351 (1928).

[214] Schrödinger, E., "Quantisierung als Eigenwertproblem. I.", *Ann. d. Physik.* **79**, 361 (1926).

[215] Rose, M.E., *Relativistic Electron Theory*, Wiley, New York (1961).

[216] Mott, N.F., "The scattering of fast electrons by atomic nuclei", *Proc. Roy. Soc. (London) A* **124**, 425 (1929).

[217] Wilderman, S., Private communication, University of Michigan, Ann Arbor (1988).

[218] Shadwick, W.F., Talman, J.D., Norman, M.R., "A program to compute variationally optimized relativistic atomic potentials", *Comput. Phys. Commun.* bf 54 (1), 95 (1989).

[219] Talman, J.D., Shadwick, W.F., "Optimized effective atomic central potential", *Phys. Rev. A* bf 14 (1), 36 (1976).

[220] Slater, J.C., "Quantum theory of atomic structure", McGraw-Hill, New York, Vol. 2 (1960).

[221] Hara, S., "The Scattering of Slow Electrons by Hydrogen Molecules", *J. Phys. Soc. Jap.* bf 22, 710 (1967).

[222] O'Connell, Lane, N.F., "Nonadjustable exchange-correlation model for electron scattering from closed-shell atoms and molecules", *Phys. Rev. A* bf 27 (4), 1893 (1983).

[223] Padial, N.T., Norcross, D.W., "Parameter-free model of the correlation-polarization potential for electron-molecule collisions", *Phys. Rev. A* bf 29 (4), 1742 (1994).

[224] Jain, A., "Low-energy positron-argon collisions by using parameter-free positron correlation polarization potentials", *Phys. Rev. A* bf 41 (5), 2437 (1990).

[225] Berger, M.J., Seltzer, S.M., "Stopping Powers of Electrons and Positrons", National Bureau of Stansards, Report NBSIR 82-2550, Washington, (1982).

[226] ICRU Report 37, "Stopping Powers for Electrons and Positrons", ICRU, Bethesda, MD, (1984).

[227] Tanuma, S., Powell, C.J., Penn, D.R., "Proposed formula for electron inelastic mean free paths based on calculations for 31 materials", *Surface Sci.* **192**, L849 (1987).

[228] Fernández-Varea, J.M., Mayol, R., Liljequist, D., Salvat, F., "Inelastic scattering of electrons in solids from a generalized oscillator strength model using optical and photoelectric data", *J. Phys. : Condens. Matter* **5**, 3593 (1993).

[229] Fernández-Varea, J.M., Salvat, F., Dingfelder, M., Liljequist, D., "A relativistic optical-data model for inelastic scattering of electrons and positrons in condensed matter", *NIMB* **229** (2), 187 (2005).

[230] Weizsäcker, C.F., "Ausstrahlung bei Stössen sehr schnellen Elektronen", *Z. Phys.* **88**, 612 (1934).

[231] Williams, E.J., "Correlation of certain collision problems with radiation theory", *Kgl. Danske Videnskab. Matfys. Medd.* **XIII**, 4 (1935); also "Nature of the High Energy Particles of Penetrating Radiation and Status of Ionization and Radiation Formulae", *Phys. Rev.* **45**, 729 (1934).

[232] Powell, C.J., "Microbeam Analysis", J.R. Micahel, P. Ingram (eds.), San Francisco Press, San Francisco, 13 (1990).

[233] Segui, S., Dingfelder, M., Fernández-Varea, J.M., Salvat, F., "The structure of the Bethe ridge. Relativistic Born and impulse approximations", *J. Phys. B* **35** (1), 33 (2002).

[234] Rudge, M.R.H., Schwartz, S.B., "The ionization of hydrogen and of hydrogenic positive ions by electron impact", *Proc. Phys. Soc. (London)* **88**, 563 (1966).

[235] Mayol, R., Salvat, F., "Cross sections for K-shell ionisation by electron impact", *J. Phys. B* **23** (12), 2117 (1990).

[236] Hippler, R., "Plane wave born calculations of K-shell ionization at low velocities", *Phys. Lett. A* **144** (2), 81 (1990).

[237] Segui, S., Dingfelder, M., Salvat, F., "Distorted-wave calculation of cross sections for inner-shell ionization by electron and positron impact", *Phys. Rev. A* **67**, 062710 (2003).

[238] Bethe, H.A., "Zur Theorie des Durchgangs schneller Korpuskularstrahlen durch Materie", *Ann. d. Physik.* **5**, 325 (1930).

[239] Inokuti, M., "Inelastic Collisions of Fast Charged Particles with Atoms and MoleculesThe Bethe Theory Revisited", *Rev. Mod. Phys.* **43** (3), 297 (1971).

[240] Cooper, J.W., "Proceedings of the International Conference on Inner Shell Ionization Phenomena and Future Applications", R.W. Fink, S.T. Manson, J.M. Palms, P.V. Rao (eds.), U.S. Atomic Energy Commission, Oak Ridge, Tenn., CONF-720404, Vol.2, 807. (1973).

[241] Fano, U., "Ionizing Collisions of Very Fast Particles and the Dipole Strength of Optical Transitions", *Phys. Rev.* **95**, 1198 (1954).

[242] Gryzinski, M., "Classical Theory of Atomic Collisions. I. Theory of Inelastic Collis", *Phys. Rev.* **138**, A336 (1965).

[243] McGuire, E.J., "Scaled electron ionization cross sections in the Born approximation", Phys. Rev. A **16** (1), 73 (1977).

[244] Seltzer, S.M., "Cross section for bremsstrahlung production and electron-impact ionisation", Monte Carlo Transport of Electrons and Photons, Plenum Press, New York and London, 81 (1987).

[245] Møller, C., "On the theory of the passage of rapid electrons through matter", *Ann. d. Physik.* **14** (5), 531 (1932).

[246] Bhabha, H.J., "The scattering of positrons by electrons with exchange on Dirac's theory of the positron", *Proc. R. Soc. (London) A* **154**, 195 (1936); also GEANT version 3.15, CERN-data Handling Division, DD/EE/84-1 (1992).

[247] Scofield, J.H., "Theoretical photoionization cross sections from 1 keV to 1500 keV", LLNL Report UCRI-51326 (1973); also "K- and L-shell ionization of atoms by relativistic electrons", *Phys. Rev. A* **18** (3), 963 (1978).

[248] Kim, Y.-K., Inokuti, M., "Generalized Oscillator Strengths of the Helium Atom. I", *Phys. Rev.* **175** (1), 176 (1968).

[249] Clark, R.E.H., Abdallah, Jr.J., Csanak, G., Kramer, S.P., "Electron-impact cross sections and coherence parameters for the 6s^2 ^{1}p ^{1}P transition in neutral barium", *Phys. Rev. A* **40** (6), 2935 (1989).

[250] Bray, I., Stelbovics, A.T., "Calculation of Electron Scattering on Hydrogenic Targets", *Adv. At. Mol. Phys.* **35**, 209 (1995).

[251] Burke, P., Berrington, K., "Atomic and Molecular Processes: An R-Matrix Approach", Institute of Physics Publishing, Bristol (1993).

[252] Kim, Y.-K., "Scaling of plane-wave Born cross sections for electron-impact excitation of neutral atoms", *Phys. Rev. A* **64**, 032713 (2001).

[253] Dingfelder, M., Hantke, D., Inokuti, M., Paretzke, H.G., "Electron inelastic-scattering cross sections in liquid water", *Rad. Phys. Chem.* **53** (1), 1 (1998).

[254] Emfietzoglou, D., "Inelastic cross sections for electron transport in liquid water: a comparison of dielectric models", *Rad. Phys. Chem.* **66** (6), 373 (2003).

[255] Fano, U., "Penetration of protons alpha particles and mesons", *Ann. Rev. Nucl. Sci.* **13**, 1 (1963).

[256] Oliva, J., "New calculational scheme for particle range and an application to a positron entering a metal", *Phys. Rev. B* **21** (11), 4918 (1980).

[257] Oliva, J., "Inelastic positron scattering in an electron gas", *Phys. Rev. B* **21** (11), 4909 (1980).

[258] Lindhard, J., "On the properties of a gas of charged particles", *Kgl. Danske Videnskab. Selskab. Mat.-Fis. Medd.* **28** (8), 57 (1954).

[259] Perkins, A., Carbotte, J.P., "Effect of the Positron-Phonon Interaction on Positron Motion", *Phys. Rev. B* **1** (1), 101 (1970).

[260] Gehenn, L.J., Reichert, E., "Differential Cross Sections for Elastic Scattering of Low Energy Electrons by Sodium", *Z. Phys.* **254**, 28 (1972).

[261] Teubner, P.J.O., Buckman, S.J., Noble, C.J., "Differential cross sections for the elastic scattering of intermediate energy electrons from sodium", *J. Phys. B* **11** (13), 2345 (1978).

[262] Srivastava, S.K., Vuskovic, L., "Elastic and inelastic scattering of electrons by Na", *J. Phys. B* **13** (13), 2633 (1980).

[263] Allen, L.J., Brunger, M.J, McCarthy, I.E., Teubner, P.J.O., "A complex phaseshift analysis for elastic scattering of 54.4 eV electrons from sodium", *J. Phys. B* **20** (18), 4861 (1987).

[264] Marinkovic, B., Pejcev, V., Filipovic, D., Cadez, I., Vuskovic, L., "Elastic and inelastic electron scattering by sodium at 10, 20 and 54.4 eV", *J. Phys. B* **25** (14), 5179 (1992).

[265] Lorentz, S.R., Miller, T.M., "Elastic and inelastic scattering of electrons by sodium: differential cross sections at 20-150 eV", *private communication* (cited by Madison *et al.* [271]) (1992).

[266] Carse, G.D., "Low energy inelastic scattering of electrons by atoms", *J. Phys. B* **5** (10), 1928 (1972).

[267] Issa, M.R., *Ph.D. Thesis*, University of Durham (1977).

[268] McCarthy, I.E., Mitroy, J., Stelbovic, A.T., "Electron scattering from alkali atoms in the one-electron model", *J. Phys. B* **18** (12), 2509 (1985).

[269] Mitroy, S.M., McCarthy, I.E., Stelbovic, A.T., "Electron scattering from sodium at intermediate energies", *J. Phys. B* **20** (18), 4827 (1987).

[270] Balashov, V.V., Grum-Grzhimailo, A.N., Klochkova, O.I., "Inelastic and superelastic scattering of electrons by sodium: the role of the imaginary part of the optical potential in the DWBA analysis of the 3S-3P transition", *J. Phys. B* **22** (24), L669 (1989).

[271] Madison, D.H., Bartschat, K., McEachran, R.P., "Second-order distorted wave calculation for elastic and inelastic electron-sodium scattering", *J. Phys. B* **25** (23), 5199 (1992).

[272] McMillan, J.H., "Elastic Electron Scattering in Potassium", *Phys. Rev.* **46**, 983 (1934).

[273] Gehenn, W., Wilmers, M., "Differential Cross Sections for Elastic Scattering of Low Energy Electrons by Potassium", *Z. Phys.* **244**, 395 (1971).

[274] Eyb, M., "Resonance scattering of low-energy electrons from potassium atoms", *J. Phys. B* **9** (1), 101 (1976).

[275] Rao, M.V.V., Bharathi, S.M., "Elastic scattering of intermediate-energy electrons by sodium, potassium and rubidium atoms", *J. Phys. B* **20** (5), 1081 (1987).

[276] Williams J.F., Trajmar, S., "Electron impact excitation of potassium at 6.7, 16 and 60 eV", *J. Phys. B* **10** (10), 1955 (1977).

[277] Buckman, S.J., Noble, C.J., Teubner, P.J.O., "Intermediate energy electron scattering from potassium", *J. Phys. B* **12** (18), 3077 (1979).

[278] Vuskovic, L., Srivastava, S.K., "Scattering of intermediate-energy electrons by potassium", *J. Phys. B* **13** (24), 4849 (1980).

[279] Gregory, D., Fink, M., *At. Nucl. Data Tables* **14**, 3218 (1974).

[280] Kennedy, J.V., Myerscough, V.P., McDowell, M.R.C., "Electron impact excitation of the resonance transitions of Li, Na and K", *J. Phys. B* **10** (18), 3759 (1977).

[281] Bray, I., "Convergent close-coupling method for the calculation of electron scattering on hydrogenlike targets", *Phys. Rev. A* **49** (2), 1066 (1993).

[282] Bray, I., Fursa, D.V., McCarthy, I.E., "Calculation of electron-potassium scattering", *Phys. Rev. A* **47** (5), 3951 (1993).

[283] Madison, D.H., Lehmann, M., McEachran, R.P., Bartschat, K., "Elastic and inelastic scattering of electrons from potassium", *J. Phys. B* **28** (1), 105 (1992).

[284] Trajmar, S., Williams, W., Srivastava, S.K., "Electron-impact cross sections for Cu atoms", *J. Phys. B* **10** (16), 3323 (1977).

[285] Madison, D.H., McEachran, R.P., Ismail, M., Teubner, P.J.O., "Elastic scattering of electrons from copper at intermediate energies ", *J. Phys. B* **31** (5), 1127 (1998).

[286] Winter, N.W., cited by Trajmar *et al.* [284] (*unpublished*) (1977).

[287] Msezane, A., Henry, R.W., "Angular distributions for electron-impact excitation of Mg II, Zn II, and Cu I", *Phys. Rev. A* **33** (3), 1636 (1986).

[288] Reichert, E., *Z. Phys.* **173**, 26 (1963).

[289] Holst, S., Maue, W., Newjoto, R., Peters, J., "Differential cross sections of atomic Au for electron scattering (30-200 eV)", *J. Phys. B* **23** (17), 2977 (1990).

[290] Holzwarth, G., Meister, H.J., "Elastic Scattering of Relativistic Electrons by Screened Gold and Mercury Nuclei", *Nucl. Phys.* **59**, 56 (1964).

[291] Schonfelder, J.C., "Atomic structures and electron scattering in the relativistic Hartree approximation", *Proc. Phys. Soc.* **87**, 163 (1966).

[292] Townsend, J.S., Bailey V.A., "The motion of electrons in argon and in hydrogen", *Philos. Mag.* **44**, 1033 (1922).

[293] Townsend, J.S., Bailey V.A., *Philos. Mag.* **46**, 661 (1923).

[294] Ramsauer, C., Kollath R., "The cross section effect of noble gase molecules against electrons under 1 volt", *Ann. d. Phys.* **3** (4), 536 (1929).

[295] Zecca, A., Karwasz, G.P., Brusa, R.S., "One century of experiments on electron-atom and molecule scattering: a critical review of integral cross sections; I. Atoms and diatomic molecules", *Riv. Nuovo Cimento* **19** (5) (1996).

[296] Williams, J.F., "Electron scattering from hydrogen atoms. II. Elastic scattering at low energies from 0.5 to 8.7 eV", *J. Phys. B* **8** (10), 1683 (1975).

[297] Williams, J.F., "Electron scattering from atomic hydrogen. III. Absolute differential cross sections for elastic scattering of electrons of energies from 20 to 680 eV", *J. Phys. B* **8** (10), 2191 (1975).

[298] Shyn, T.W., Cho, S.Y., "Angular distribution of electrons elastically scattered from hydrogen atoms", *Phys. Rev. A* **40** (3), 1315 (1989).

[299] Shyn, T.W., Grafe, A., "Angular distribution of electrons elastically scattered from hydrogen atoms. II", *Phys. Rev. A* **46** (5), 2949 (1992).

[300] Gilbody, H.B., Stebbings, R.F., Fite, W.L., "Collisions of Electrons with Hydrogen Atoms. VI. Angular Distribution in Elastic Scattering", *Phys. Rev.* **121** (3), 794 (1961).

[301] Teubner, P.J.O., Lloyd, C.R., Weigold, E., "Differential cross section for elastic scattering of electrons from atomic hydrogen: Low energies", *Phys. Rev. A* **9** (6), 2552 (1974).

[302] Burke, P.G., Schey, H.M., Smith, K., "Collisions of Slow Electrons and Positrons with Atomic Hydrogen", *Phys. Rev.* **129**, (3) 1258 (1963).

[303] Callaway, J., Oza, D.H., "Optical-potential model for electron-atom scattering", *Phys. Rev. A* **32** (5), 2628 (1985).

[304] Klingston, A.E., Walters, H.R., "Electron scattering by atomic hydrogen: the distorted-wave second Born approximation", *J. Phys. B* **13** (23), 4633 (1980).

[305] Temkin, A, Lamkin, J.C., "Application of the Method of Polarized Orbitals to the Scattering of Electrons from Hydrogen", *Phys. Rev.* **121** (3), 788 (1961).

[306] Bullard, E.C., Massey, H.S.W., "The Elastic Scattering of Slow Electrons in Gases.-II", *Proc. R. Soc. A* **133**, 637 (1931).

[307] Gibson, J.R., Dolder, K.T., "Measurements of angular distributions of electrons elastically scattered by helium", *J. Phys. B* **2** (11), 1180 (1969).

[308] Andrick, D., Bitsch, A., "Experimental investigation and phase shift analysis of low-energy electron-helium scattering", *J. Phys. B* **8** (3), 393 (1975).

[309] McConkey, J.W., Preston, J.A., "Differential elastic scattering of electrons by the rare gases. I. Helium", *J. Phys. B* **8** (1), 63 (1975).

[310] Srivastava, S.L., Trajmar, S., "Differential elastic cross sections for high angle electron scattering by He in the intermediate energy region", *J. Chem. Phys.* **64** (9), 3886 (1976).

[311] Shyn, T.W., "Angular distribution of electrons elastically scattered from gases: 2-400 eV on He. I", *Phys. Rev.* **22** (3), 916 (1980).

[312] Brunger, M.J., Buckman, S.J., Allen, L.J., McCarthy, I.E., Ratnavelu, K., "Elastic electron scattering from helium: absolute experimental cross sections, theory and derived interaction potentials", *J. Phys. B* **25** (8), 1823 (1992).

[313] Mott, N.F., “The Scattering of Electrons by Atoms”, *Proc. R. Soc. (London) A* **127**, 658 (1930).

[314] Kim, Y.-K., Inokuti, M., “Atomic Form Factor and Incoherent-Scattering Function of the Helium Atom”, *Phys. Rev.* **165** (1), 39 (1968).

[315] Nesbet, R.K., “Variational calculations of accurate e^--He cross sections below 19 eV”, *Phys. Rev. A* **20** (1), 58 (1979).

[316] LaBahn, R.W., Callaway, J., “Differential Cross Sections for the Elastic Scattering of 1- to 95-eV Electrons from Helium”, *Phys. Rev. A* **2** (2), 366 (1970).

[317] Shi, X., Burrow, P.D., “Differential scattering cross sections of neon at low electron energies”, *J. Phys. B* **25** (20), 4273 (1992).

[318] Williams J.F., “A phaseshift analysis of experimental angular distributions of electrons elastically scattered from He, Ne and Ar over the range 0.5 to 20 eV”, *J. Phys. B* **12** (2), 265 (1979).

[319] Brewer, D.F.C., Newell, W.R., Harper, S.F.W., Smith, A.C.H., “Elastic scattering of low-energy electrons by neon atoms”, *J. Phys. B* **14** (22), L749 (1981).

[320] Register, D.F., Trajmar, S., “Differential, integral, and momentum-transfer cross sections for elastic electron scattering by neon: 5 to 100 eV”, *Phys. Rev. A* **29** (4), 1785 (1984).

[321] Gulley, R.J., Alle, D.T., Brennan, M.J., Brunger, M.J., Buckman, S.J., “Differential and total electron scattering from neon at low incident energies”, *J. Phys. B* **27** (12), 2593 (1994).

[322] Saha, H.P., “Accurate ab initio calculation of scattering length and phase shifts at very low energies for electron-neon scattering”, *Phys. Rev. Lett.* **65** (16), 2003 (1990).

[323] O’Malley, T.W., Crompton, R.W., “Electron-neon scattering length and S-wave phaseshifts from drift velocities”, *J. Phys. B* **13** (17), 3451 (1980).

[324] Bromberg J.P., “Absolute differential cross sections of electrons elastically scattered by the rare gases. I. Small angle scattering between 200 and 700 eV”, *J. Chem. Phys.* **61**, 963 (1974).

[325] Lewis B., Furness J.B., Teubner P.J.O., Weigold E., “The elastic scattering of electrons from argon”, *J. Phys. B* **7** (9), 1083 (1974).

[326] DuBois R.D., Rudd M.E., “Differential cross sections for elastic scattering of electrons from argon, neon, nitrogen and carbon monoxide”, *J. Phys. B* **9** (15), 2657 (1976).

[327] Jansen R.H.J., de Heer F.J., Luyken H.J., van Wingerden B., Blaauw H.J., “Absolute differential cross sections for elastic scattering of electrons by helium, neon, argon and molecular nitrogen”, *J. Phys. B* **9** (2), 185 (1976).

[328] Vuskovic, L., Kurepa, M.V., “Differential cross sections of 60-150 eV electrons elastically scattered in argon”, *J. Phys. B* **9** (5), 837 (1976).

[329] Andrick, D., Langhans, L., “Measurement of the free-free cross section of e^--Ar scattering”, *J. Phys. B* **11** (13), 2355 (1978).

[330] Srivastava, S.K., Tanaka, H., Chutjian, A., Trajmar, S., “Elastic scattering of inter- medi- ate-energy electrons by Ar and Kr”, *Phys. Rev. A* **23** (5), 2156 (1981).

[331] Wagenaar R.W., de Boer A., van Tubergen T., Los J., de Heer F.J., “Absolute differential cross sections for elastic scattering of electrons over small angles from noble-gas atoms”, *J. Phys. B* **19** (19), 3121 (1986).

[332] Iga I., Mu-Tao L., Nogueira J.C., Barbieri R.S., “Elastic differential cross section measurements for electron scattering from Ar and O_2 in the intermediate-energy range”, *J. Phys. B* **20** (5), 1095 (1987).

[333] Weyhreter M., Barzick B., Mann A., Linder F., "Measurements of differential cross sections for *e*-Ar, Kr, Xe scattering at E=0.05-2 eV", *Z. Phys. D* **7**, 333 (1988).

[334] Furst J.E., Golden D.E., Mahgerefteh M., Zhou J., Mueller D., "Absolute low-energy e^--Ar scattering cross sections", *Phys. Rev. A* **40** (10), 5592 (1989).

[335] Walker, D.W., "The effect of atomic distortion on electron scattering from mercury", *J. Phys. B* **3** (6), 788 (1970).

[336] Lewis B., McCarthy I.E., Teubner P.J.O., Weigold E., "The elastic scattering of electrons from krypton, neon and xenon", *J. Phys. B* **7** (18), 2549 (1974).

[337] Williams J.F., Crowe A., "The scattering of electrons from inert gases. II. Absolute differential elastic cross sections for neon, krypton and xenon atoms", *J. Phys. B* **8** (13), 2233 (1975).

[338] Heindörff T., Hofft J., Dabkiewicz P., "Elastic electron scattering from krypton and xenon for collision energies up to 10.5 eV", *J. Phys. B* **9** (1), 89 (1976).

[339] Jansen R.H.J., de Heer F.J., "Absolute differential cross sections for elastic scattering of electrons by krypton and xenon", *J. Phys. B* **9** (2), 213 (1976).

[340] Danjo A., "Electron scattering from Kr. I. Differential cross section for elastic scattering", *J. Phys. B* **21** (22), 3759 (1988).

[341] Register, D.F., Vuskovic, L., Trajmar, S.,"Proc. 7th Int. Conf. on Atomic Physis", Boston, D. Kleppner et al. (eds), Cambrige, MA, MIT, Abstracts p. 38 (1980).

[342] Wehyreter, M., Barzick, B., Linder, F., "Proc. 13th Int. Conf. on the Physics of Electronic and Atomic Collisions", Berlin, J., Eichler et al. (eds), Amsterdam, North-Holland, Abstracts p.78 (1983).

[343] Holtklamp, T., Jost, K., *private communication*, cited by Zecca *et al.* [295] (1983).

[344] Register, D.F., Vuskovic, L., Trajmar, S., "Elastic electron scattering cross sections for Xe in the 1-100 eV impact energy region", *J. Phys. B* **19** (11), 1685 (1986).

[345] Mehr, J., "Winkelverteilungen elastisch an Edelgas-Atomstrahlen gestreuter Elektronen; Spinpolarisation eines an Argon gestreuten 40 eV Elektronenstrahls", *Z. Phys.* **198**, 345 (1967).

[346] Heindorff, T., Hofft, J., Dabkiewicz, P., "Elastic electron scattering from krypton and xenon for collision energies up to 10.5 eV", *J. Phys. B* **9** (1), 89 (1976).

[347] Klewer, M., Beerlage, M.J.M., van der Wiel, M.J., "Angular distributions of electrons elastically scattered from xenon at energies between 2 and 300 eV", *J. Phys. B* **13** (3), 571 (1980).

[348] McCarthy, I.E., Noble, C.J., Phillips, B.A., Turnbull, A.D., "Optical model for electron scattering from inert gases", *Phys. Rev. A* **15** (6), 2173 (1977).

[349] Berg, H., "The elastic scattering of low energy electrons from Xenon", *Phys. Lett. A* **88** (6), 292 (1982).

[350] McEachran, R.P., Stauffer, A.D., "Elastic scattering of electrons from krypton and xenon", *J. Phys. B* **17** (12), 2507 (1984).

[351] Kemper, K., Awe, B., Rosicky, F., Feder, R., "Elastic scattering of slow electrons from Ar and Kr atoms", *J. Phys. B* **16** (10), 1819 (1985).

[352] He, F.Q., Long, X.G., Peng, X.F., Luo, Z.M., An, Z., "K-shell ionization of iron by electron bombardment", *Acta Phys. Sin.* **5** (7), 499 (1996).

[353] Luo, Z.M., "Improved bipartition model of electron transport. I. A general formulation", *Phys. Rev. B* **32** (2), 812 (1985); "Improved bipartition model of electron transport. II. Applications to inhomogeneous media", **32** (2), 824 (1985).

[354] Luo, Z.M., An, Z., He, F.Q., Li, T.H., Long, X.G., Peng, X.F., "Correction of the influence of the substrate upon the measurement of K-shell ionization cross sections", *J. Phys. B* **29** (17), 4001 (1996).

[355] Tang, C.H., "Measurements of germanium K-shell ionization cross sections and tin L-shell x-ray production cross sections by electron impact", *J. Appl. Phys.* **91** (10), 6739 (2002).

[356] Long, X.G., Liu, M., He, F.Q., Peng, X.F., "Cross sections for K-shell ionization by electron impact", *At. Data Nucl. Data Tables* **45** (2), 353 (1990).

[357] Joy, D.C., "A Database on Electron-Solid Interactions", *Scanning* **17** (5), 270 (1995).

[358] Luo, Z.M., *Ph.D. Thesis* (1994).

[359] Shevelko, V.P., Solomon, A.M., Vukstich, V.S., "K-shell Ionization of Free Metal Atoms K, Ca, Rb, and Sr by Electron Impac", *Phys. Scripta* **43**, 158 (1990).

[360] An, Z., Tang, C.H., Zhou, C.G., Luo, Z.M., "Measurement of scandium and vanadium K-shell ionization cross sections by electron impact", *J. Phys. B* **33** (18), 3677 (2000).

[361] Jessenberger, J., Hink, W., *Z. Physik. A* **275**, 331 (1975).

[362] He, F.Q., Peng, X.F., Long, X.G., Luo, Z.M., An, Z., "K-shell ionization cross sections by electron bombardment at low energies", *NIMB* **129** (4), 445 (1997).

[363] Llovet, X., Merlet, C., Salvat, F., "Measurements of K-shell ionization cross sections of Cr, Ni and Cu by impact of 6.5-40 keV electrons", *J. Phys. B* **33** (18), 3761 (2000).

[364] An, Z., Tang, C.H., Luo, Z.M., "Measurement of K-Shell Ionization Cross Sections of Cr, Ni and Cu Atoms by 7.5-25 keV Electron Impact", *Chin. Phys. Lett.* **18** (11), 1460 (2001).

[365] Shima, K., "Mn and Cu K-shell ionization cross sections by slow electron impact", *Phys. Lett. A* **77** (4), 237 (1980).

[366] Luo, Z.M., An, Z., Li, T.H., Wang, L.M., Xia, X.Y., "Measurement of K-shell ionization cross sections of Fe and Mn by electron impact", *J. Phys. B* **30** (11), 2681 (1997).

[367] Tang, C.H., An, Z., Li, T.H., Luo, Z.M., "Measurement of zinc and manganese K-shell ionization cross sections by electron impact", *NIMB* **155** (1-2), 1 (1999).

[368] Llovet, X., Merlet, C., Salvat, F., "Measurements of absolute cross sections for K-shell ionization of Fe and Mn by electron impact", *J. Phys. B* **35** (4), 973 (2002).

[369] An, Z., Li, T.H., Wang, L.M., Xia, X.Y., Luo, Z.M., "Correction of substrate effect in the measurement of 825-keV electron-impact K-shell ionization cross sections of Cu and Co elements", *Phys. Rev. A* **54** (4), 3067 (1996).

[370] Pockman, L.T., Webster, D.L., Kirkpatrick, P., Harworth, K., "The Probability of K Ionization of Nickel by Electrons as a Function of Their Energy", *Phys. Rev.* **71** (6), 330 (1947).

[371] Davis, D.V., Mistry, V.D., Quarles, C.A., "Inner shell ionization of copper, silver and gold by electron bombardment", *Phys. Lett. A*, **38** (3), 169 (1972).

[372] Shima, K., Nakagawa, T., Umetani, K., Mikumo, T., "Threshold behavior of Cu-, Ge-, Ag-K-, and Au-L_3-shell ionization cross sections by electron impact", *Phys. Rev. A* **24** (1), 72 (1981).

[373] Zhou, C.G., Fu, Y.C., An, Z., Tang, C.H., Luo, Z.M., "Measurement and Correction of K-Shell Ionization Cross Sections for Copper and Gallium by Electron Impact", *Chin. Phys. Lett.* **18** (6), 759 (2001).

[374] Zhou, C.G., An, Z., Luo, Z.M., "Measurement of K-shell production cross sections for Ga, Ge and Zr elements by electron impact", *J. Phys. B* **35** (4), 841 (2002).

[375] Merlet, C., Llovet, X., Salvat, F., "Measurements of absolute K-shell ionization cross sections and L-shell x-ray production cross sections of Ge by electron impact", *Phys. Rev. A* **69**, 032708 (2004).

[376] Luo, Z.M., Tang, C.H., An, Z., He, F.Q., Peng, X.F., Long, X.G., "Selenium and yttrium K-shell ionization cross sections by electron impact", *Phys. Rev. A* **63**, 034702 (2001).

[377] Peng, X.F., He, F.Q., Long, X.G., Luo, Z.M., An, Z., "Cross sections for K-shell ionization of niobium by electron impact", *Phys. Rev. A* **58** (3), 2034 (1998).

[378] He, F.Q., Long, X.G., Peng, X.F., Luo, Z.M., An, Z., "K-shell ionization of molybdenum by electron bombardment", *NIMB* **114** (3-4), 213 (1996).

[379] Rester, D.H., Dance, W.E., "K-Shell Ionization of Ag, Sn, and Au from Electron Bombardment", *Phys. Rev.* **152** (1), 1 (1966).

[380] Schneider, H., Tobehn, I., Ebel, F., Hippler, R., "Absolute cross sections for inner shell ionization by lepton impact", *Phys. Rev. Lett.* **71** (17), 2707 (1993).

[381] Lennard, W.N., Schultz, P.J., Massoumi, G.R., Logan, L.R., "Observation of the Difference between $e^- - e^-$ and $e^+ - e^-$ Interactions", *Phys. Rev. Lett.* **61** (21), 2428 (1988).

[382] Nagashima, Y., Saito, F., Itoh,Y., Goto, A., Hyodo, T., "Measurement of Cu K-Shell and Ag L-Shell Ionization Cross Sections by Low-Energy Positron Impact", *Phys. Rev. Lett.* **92** 223201 (2004).

[383] Hansen, H., Flammersfeld, A., "Messung des Wirkungsquerschnitts für K-Ionisierung durch Stoss niederenergetischer Negatonen und Positonen", *Nucl. Phys.* **79** (1), 135 (1966).

[384] Gryzinski, M., Kowalski, M., "Theory of inner shell ionisation by positrons", *Phys. Lett. A* **183** (2-3), 196 (1993).

[385] Peng, X.F., He, F.Q., Long, X.G., An, Z., Luo, Z.M., "Measurement of L-shell ionization cross sections for niobium by electron impact", *Chin. Phys.* **10** (1), 31 (2001).

[386] Tang, C.H., Luo, Z.M., An, Z., He, F.Q., Peng, X.F., Long, X.G., "L-shell ionization study of indium, tin, and rhenium by low-energy electron impact", *Phys. Rev. A* **65**, 052707 (2002).

[387] Luo, Z.M., Fu, Y.C., An, Z., Peng, X.F., He, F.Q., Long, X.G., "Ionization of Hafnium L-Shell by Electron Impact", *Chin. Phys. Lett.* **19** (11), 1610 (2002).

[388] Peng, X.F., He, F.Q., Long, X.G., An, Z., Luo, Z.M., "L-Shell Ionization Study of Tungsten by Electron Impact", *Chin. Phys. Lett.* **18** (1), 39 (2001).

[389] Yang, D.L., Luo, X.B., Fu, Y.C., He, F.Q., Long, X.G., Peng, X.F., Luo, Z.M., "Ionization for Hf- and W-L-shell by electron impact", *Chin. Phys.* **13** (5), 670 (2004).

[390] Wu, Z.W., Yang, D.L., Luo, X.B., He, F.Q., Peng, X.F., Luo, Z.M., "L-Shell X-Ray Production Cross Sections of Au and Ir Atoms by Electron Impact near the Threshold Region", *Chin. Phys. Lett.* **20** (9), 1485 (2003).

[391] Carvalho, M.L., Ferreira, J.G., Salgueiro, L., "L-subshell-ionization cross sections of tungsten by electron impact near the threshold region", *Phys. Rev. A* **37** (1), 106 (1988).

[392] Salgueiro, L., Ferreira, J.G., Carvalho, M.L., Ramos, M.T., "L subshell ionisation of tungsten by low-energy electrons", *J. Phys. B* **13** (19), 3849 (1980).

[393] Huizinga, W.J., "On the relative probability of excitation of the three L-levels of tungsten as a function of the velocity of the cathode rays", *Physica* **4** (4), 317 (1937).

[394] Chang, C.N., "L-subshell ionization cross sections for tungsten at low electron energies", *Phys. Rev. A* **19** (5), 1930 (1979).

[395] Campos, C.S., Vasconcellos, M.A.Z., Llovet, X., Salvat, F., "Measurements of L-shell x-ray production cross sections of W, Pt, and Au by 1030-keV electrons", *Phys. Rev. A* **66**, 012719 (2002).

[396] McCue, J.J.G., "The Ionization Cross Section of the Silver L_{III} State", *Phys. Rev.* **65** (5-6), 168 (1944).

[397] Llovet, X., Merlet, C., Fernández-Varea, J.M., Salvat, F., "Relative Cross Sections for L- and M-Shell Ionization by Electron Impact", *Mikrochim. Acta* **132** (2-4), 163 (2000).

[398] Salem, S.I., Moreland, L.D., "L_{II} and L_{III} ionization cross sections in gold at very low energies", *Phys. Lett. A* **37** (2), 161 (1971).

[399] Park, Y.K., Smith, M.T., Scholz, W., "Cross sections for L x-ray production and L-subshell ionization by MeV electrons", *Phys. Rev. A* **12** (4), 1358 (1975).

[400] Middleman, L.M., Ford, R.L., Hofstadter, R., "Measurement of Cross Sections for X-Ray Production by High-Energy Electrons", *Phys. Rev. A* **2** (4), 1429 (1970).

[401] Khare, S.P., Saksena, V., Wadehra, J.M., "K-shell ionization of atoms by electron and positron impact", *Phys. Rev. A* **48** (2), 1209 (1993).

[402] Khare, S.P., Wadehra, J.M., "K-, L- and M-shell ionization of atoms by electron and positron impact", *Can. J. Phys.* **74**, 376 (1996).

[403] Krause, M.O., "Atomic radiative and radiationless yields for K and L shells", *J. Phys. Chem. Ref. Data* **8** (2), 307 (1979).

[404] Chen, M.H., Crasemann, B., Mark, H., "Widths and fluorescence yields of atomic L-shell vacancy states", *Phys. Rev. A* **24** (1), 117 (1981).

[405] Puri, S., Mehta, D., Chand, B., Singh, N., Trehan, P.N., "L shell fluorescence yields and Coster - Kronig transition probabilities for the elements with 25< Z <96", *X-Ray Spectom.* **22** (5), 358 (1993).

[406] Scofield, J.H., "Relativistic Hartree-Slater values for K and L X-ray emission rates", *At. Data Nucl. Data Tables* **14** (2), 121 (1974).

[407] Trajmar, S.J., Kanik, I., "Atomic and Molecular Processes in Fusion Edge Plasmas", R.K. Janev (ed), New York, Plenum Press, 31 (1995).

[408] Mori, S., Sueoka, O., "Excitation and ionization cross sections of He, Ne and Ar by positron impact", *J. Phys. B* **27** (18), 4349 (1994).

[409] de Heer, F.J., Jansen, R.H.J., van der Kaay, W., "Total cross sections for electron scattering by Ne, Ar, Kr and Xe", *J. Phys. B* **12** (6), 979 (1979).

[410] Zecca, A., Karwasz, G.P., Brusa, R.S., *Riv. Nuov. Cimento* **18** (1996).

[411] Perdew, J.P., Zunger, A., "Self-interaction correction to density-functional approximations for many-electron systems", *Phys. Rev. B* **23** (10), 5048 (1981).

[412] Buhring, W., *Z. Phys.* **187**, 180 (1965).

[413] Bethe, H.A., "Bremsformel für Elektronen relativistischer Geschwindigkeit", *Z. Phys.* **76**, 293 (1932).

[414] Allison, W.W.M., Cobb, J.H., "Relativistic charged particle identification by energy loss", *Ann. Rev. Nucl. Part. Sci.* **30**, 253 (1980).

[415] Inokuti, M., "Addenda: Inelastic collisions of fast charged particles with atoms and molecules The Bethe theory revisited", *Rev. Mod. Phys.* **50** (1), 23 (1978).

[416] Sternheimer, R.M., "The density effect for the ionization loss in various materials", *Phys. Rev.* **88**, 851 (1952).

[417] Liljequist, D., "A simple calculation of inelastic mean free path and stopping power for 50 eV - 50 keV electrons in solids", *J. Phys. D: Appl. Phys.* **16**, 1567 (1983).

[418] Rester, D.H., Derrickson, J.H., "Electron Transmission Measurements for Al, Sn, and Au Targets at Electron Bombarding Energies of 1.0 and 2.5 MeV", *J. Appl. Phys.* **42** (2), 714 (1971).

[419] Cosslett, V.E., Thomas, R.N., "The plural scattering of 20 keV electrons", *Brit. J. Appl. Phys.* **15**, 235 (1964).

[420] Lencinas, S., Burgdörfer, J., Kemmel, J., Heil, O., Kroneberger, K., Keller, N., Rothard, H., Groeneveld, K.O., "Transport of fast electrons through thin foils", *Phys. Rev. A* **41** (3), 1435 (1990).

[421] Landau, L., "On the energy loss of fast particles by ionization", *J. Phys. U.S.S.R.* (Moscow) **8**, 201 (1944).

[422] Negreanu, C., Llovet, X., Chawla, R.,Salvat, F., "Calculation of multiple-scattering angular distributions of electrons and positrons", *Rad. Phys. Chem.* , *accepted for publication* (2005).

[423] Kawrakow, I., Bielajew, A.F., "On the condensed history technique for electron transport", *NIMB* **142** (3), 253 (1998).

[424] Bielajew, A.F., Salvat, F., "Improved electron transport mechanics in the PENELOPE Monte-Carlo model", *NIMB* **173** (3), 332 (2001).

[425] Bethe, H.A., "Molière's Theory of Multiple Scattering", *Phys. Rev.* **89** (6), 1256 (1953).

[426] Bielajew, A.F., "Plural and multiple small-angle scattering from a screened Rutherford cross section", *NIMB* **86** (3-4), 257 (1994).

[427] Kawrakow, I., Bielajew, A.F.,"On the representation of electron multiple elastic-scattering distributions for Monte Carlo calculations", *NIMB* **134** (3-4), 325 (1998).

[428] Berger, M.J., Wang, R., "Monte Carlo transport of electrons and photons", T.M. Jenkins, W.R. Nelson, A. Rindi (eds.) Plenum Press, New York, p.21-56 (1989).

[429] Spencer, L.V., "Theory of Electron Penetration", *Phys. Rev.* **98** (6), 1597 (1955).

[430] Liljequist, D., Ismail, M., "Transport mean free path related to trajectory patterns: Comparison of nonrelativistic and highly relativistic electron penetration through matter", *J. Appl. Phys.* **62**, 342 (1987).

[431] Spencer, L.V., "Calculation of Peaked Angular Distributions from Legendre Polynomial Expansions and an Application to the Multiple Scattering of Charged Particles", *Phys. Rev.* **90** (1), 146 (1953).

[432] Abramowitz, M., Segun, I., "Handbook of Mathematical Functions", Dover, New York, (1974).

[433] Gauss, C.F., "Methodus nova integralium valores per approximationem inveniendi", *Commentationes Societatis Regiae Scientarium Gottingensis Recentiores* **2** (III), 163 (1814).

[434] Jacobi, C.G.J., "Ueber Gausss neue Methode, die Werte der Integrale näherungsweise zu finden" *J. Reine Angew. Math.* **1**, 301 (1926).

[435] Press, W.H., Teukolsky, S.A., Vetterling, W.T., Flannery, B.P., *Numerical Recipes in Fortran. The Art of Scientific Computing*, Cambridge University Press, Cambridge (1992).

[436] Kulchitsky, L.A., Latyshev, G.D., "The Multiple Scattering of Fast Electrons", *Phys. Rev.* **61** (5-6), 254 (1942).

[437] Hanson, A.O., Lanzl, L.H., Lyman, E.M., Scott, M.B., "Measurement of Multiple Scattering of 15.7-MeV Electrons", *Phys. Rev.* **84** (4), 634 (1951).

Acknowledgements

> *"Yet do I fear thy nature;*
> *It is too full o' the milk of human kindness.*
> – William Shakespeare –
> "Macbeth", Act 1 scene 5

I would like to acknowledge the special support and dedication shown constantly by Professor Rakesh Chawla, the director of this thesis, the head of reactor physics and systems behaviour research at PSI/EPFL; the many discussions and suggestions provided by my supervisor, Dr. Om Joneja, which made this work a unique experience; as well as the contributions provided by Dr. Jiri Stepanek, the consultant of the first part of this thesis work.

I would like to express my most sincere gratitude to Professors Michael Dingfelder (East Carolina University, USA) and Francesc Salvat (University of Barcelona, Spain), for their concern, guidance and valuable help during the first and second part of this thesis work, respectively. I would also like to acknowledge the cooperation from Professor José Maria Fernández-Varea and Dr. Xavier Llovet, both of the University of Barcelona, for carefully reading the thesis manuscript and for their constant offer of help.

It is a pleasure to thank all my colleagues from the LWR-PROTEUS and STARS projects, in particular Dr. Fabian Jatuff and Martin Zimmermann, for their kindness, encouragement and support throughout the years and for providing a nice and stimulating working atmosphere.

I would also like to thank Professors Ion Munteanu (University of Bucharest, Romania) and Ion Chipara (University of Indiana, USA) for their efforts to motivate and develop my scientific curiosity and to make learning a nice experience for me.

I wish to express special thanks to Mrs. Ruth Ringele and Mr. Philippe Jacquemoud for their constant availability for solving, respectively, administrative and computer related problems.

Thanks to my friends and office-mates, Catherine Pralong-Fauchere and Stefano Caruso, and their families, for all the moments we shared together, and to all my friends from here (Klaus Reichlin, Laura Heyderman, Christine Guesdon, Christina Reynolds, Thierry Sengstag, and Michael Plaschy) and from abroad (Roma Šiugždaite from Lithuania, Camille Guillerminet from France, Stéphane Chauvie from Italy, Manuel Ballester from Cuba, and Andrei Micu, Ioana Dima, Costin Anghel and Oana Dobrescu from Romania). I am particularly grateful to Dr. Mahdi Zareaahmadabadi (Ohio University, USA) from whom I had the chance to learn so many things, both on the scientific and human side.

The financial support from the 5^{th} EU project on "Low Dose Risk Models", on which I had the privilege of working with colleagues from several countries, is gratefully acknowledged. I would also like to thank Professors M. Q. Tran, R. Chawla, M. Dingfelder, O. Schneider and M. Terrissol, and to Dr. O. Joneja for accepting to form the jury for the thesis.

Finally, my deepest thanks to my family, Rafael and Alexander, my godparents, Dr. Ecaterina Taralunga and Professor Vladimir Rasvan, and to my parents, for their support, understanding and tolerance during these years of work.

CURRICULUM VITAE

> *"...we must refrain from all explanations of the design of nature,*
> *drawn from the will of a Supreme Being, because*
> *this would not be natural philosophy, but*
> *an admission that we have come to its end."*
> – Immanuel Kant –
> "Prolegomena to Any Future Metaphysics"

Cezarina Elena NEGREANU-MACIAN
Place of birth: Zimnicea, Teleorman, Romania;
Date of birth: 29.09.1972;
Romanian Citizenship.

Address: Breite 2,
5210 Windisch, AG

PROFESSIONAL EXPERIENCE AND EDUCATION

October 2000 - September 2005	Doctoral candidate, physics: *EPFL, Lausanne, & PSI, Villigen, Switzerland.*
September 1999 - September 2000	Diploma program degree, physics: *Abdus Salam International Centre for Theoretical Physics, Trieste, Italy.* Thesis: "Generation of an Action Potential in a Motor Neuron".
January 1998 - August 1999	Associate Junior Assistant Professor, biophysics; *University "Carol Davila" of Medicine and Pharmacy, Bucharest, Romania.*
October 1997 - July 1998	Master in Science, physics; *University of Bucharest, Bucharest, Romania.* Thesis: "FMR Studies on Thin Amorphous Layers".
November 1996 - August 1999	Researcher, physics; *ICPET R&D Institute for Thermopower Equipment, Bucharest, Romania.*
October 1991 - July 1996	Bachelor in Science, physics; *University of Bucharest, Bucharest, Romania.* Thesis: "Study on the Influence of Neutron Irradiation on the Features of Double Injection Semiconducting Devices".
September 1987 - July 1991	Certificate of maturity, mathematics-physics; *Lyceé "Alexandru Ghica", Alexandria, Romania.*

CONFERENCE AND JOURNAL PUBLICATIONS

Negreanu, C., Stepanek, J., Joneja, O., Chawla, R., "Generation and validation of low-energy electron and positron excitation cross section data", *to be submitted for publication*, J. Phys. B (2006).

Negreanu, C., Llovet, X., Chawla, R.,Salvat, F., “Calculation of multiple-scattering angular distributions of electrons and positrons”, *accepted for publication*, Rad. Phys. Chem. (2005).

Negreanu, C., Stepanek, J., Joneja, O., Chawla, R., “Validation of new electron and positron data libraries”, NIMB **213**, 55 (2004).

Joneja, O.P., Negreanu, C., Stepanek, J., Chawla, R., “Comparison of Monte Carlo simulation of photon/electron dosimetry in microscale applications”, Australasian Physical & Engineering Sciences in Medicine **26** (2), 12 (2003)

Negreanu, C., Stepanek, J., Joneja, O.P., Chawla, R., “Electron and positron excitation cross-section data”, *XXIII*rd *International Conference on Photonic, Electronic and Atomic Collisions (ICPEAC)*, Stockholm, Sweden, 23-29 July 2003.

Negreanu, C., Stepanek, J., Joneja, O.P., Chawla, R., “Validation of new electron and positron data libraries”, *V*th *International Topical Meeting on Industrial Radiation and Radioisotope Measurement Applications*, Bologna, Italy, 9-14 June 2002.

Joneja, O.P., Negreanu, C., Stepanek, J., Chawla, R., “Comparison of Monte Carlo simulations of photon/electron dosimetry in microscale applications”, *International Workshop on Micro- and Mini-Dosimetry and Its Applications*, Sydney, Australia, 16-20 December 2001.

Negreanu, C., Radulet, D., Doaga, O., Caplanusi, A., Katona, L., Eremia, D., Tanos, E., Katona, E., “Computer Assisted Experimental Set-up for Cell Suspension Irradiation with Variable Coherency 685nm Light”, Romanian Journal of Biophysics **4** (1998).

Chipara, M.I., Galatanu, A., Morariu, M., Munteanu, I., Negreanu, C., Negreanu, B., “A FMR Study on $Fe_{80}m_3B_{17}$ (m=Co, Cr, Fe, Mn, Ni) amorphous ribbons”, *XVII*th *Conference of the Turkish Physical Society*, Alanya, Turkey, October 1998.

Katona, L., Barbu, E., Patica, A., Negreanu, C., “Gaseous/Liquid Burning Stage in Recirculated O_2/CO_2 Atmosphere with Increasing the CO_2 Concentration in Flue Gases”, Energetica Revue **46**, 9 (1998).